NANYANG TECHNOLOGICAL UNIVERSITY

FABRICATION OF 3D MICROFEATURES ON THIN METAL FOILS USING LASER-INDUCED SHOCK PRESSURE

BALASUBRAMANIAN NAGARAJAN

SCHOOL OF MECHANICAL AND AEROSPACE ENGINEERING

2015

FABRICATION OF 3D MICROFEATURES ON THIN METAL FOILS USING LASER-INDUCED SHOCK PRESSURE

BALASUBRAMANIAN NAGARAJAN

School of Mechanical and Aerospace Engineering

A thesis submitted to the Nanyang Technological University in partial fulfillment of the requirement for the degree of Doctor of Philosophy

2015

Acknowledgements

First and foremost, I would like to express my heartfelt gratitude to my supervisor, Prof. Sylvie Castagne for her extensive guidance, constructive discussions, and motivation all these years. I deeply value her trait of being kind and patient even in tough times, which helped me in great deal to weather the storms.

I am very grateful to my co-supervisor, Dr. Wang Zhongke for his invaluable comments and encouragement throughout the candidature. I thank Dr. Zheng HongYu for his support and frequent discussions.

At this occasion, I mark my special thanks to Prof. Sathyan Subbiah, who encouraged me to pursue PhD and assisted through.

I express my gratitude to Prof. Shiv Kapoor, Prof. Li Lin, and Prof. Murukeshan for providing their sound feedbacks regarding this thesis.

My special thanks to Dr. Rajaneesh, Dr. Sathiyamoorthy, and Dr. Rathi for being an inspiration.

I would like to thank NTU and SIMTech for the scholarship and assistance. I appreciate all the help provided by the technical staff in MAE, Ms. Mei Yoke especially for her unwavering help in doing countless EBSD measurements, Mr. Leong, Mr. Chan, Mr. Martin, Ms. Sandy, Mr. Yew, Ms. Esther, and Ms. Jacelyn for the assistance.

I extend my gratitude to Dr. Xu Song for his enthusiastic assistance, Dr. Lim, Dr. Gary, Dr. Xincai, Mr. Chee Wai, Mr. Teh, Ms. Yong Wei, Mr. Ang, and Mr. Jeffrey for their help.

I am indebted to a plethora of folks in the school, Dinesh, Pradeep, Mani,

Arvind, Sudhan, Karthik, Raja, Sathya, Ganapathy, Taureza, Buddhika, Kush, Ranjith, Bindhu, Indira, Monir, and Shinoj for facilitating the smooth sailing across.

Special thanks to roommates and all my friends, naming each of them could flood the pages I fear, for shouldering me all along.

Finally, I am grateful to my sisters, Nivethini and Nishanthini, and parents, Nagarajan and Vijayalakshmi, for their love and support.

Abstract

The increasing demand in the metallic microfabrication in recent times highlights the significance of microforming process due to its compliance with mass production, customization, materials, and formability. Nevertheless, the existing microforming processes are limited by a number of factors including fabrication of micromolds/punches, friction and wear of contact surfaces, size effects, and process flexibility. This thesis attempts to address these limitations by developing a new microforming process for fabricating 3D microfeatures on metallic foils.

A novel mold-free microforming technique, Flexible Pad Laser Shock Forming (FPLSF), which uses laser-induced shock pressure and a flexible pad to fabricate microscale features on metal foils is developed and demonstrated. FPLSF uses laser-induced shockwaves as the deformation force to induce plastic deformation on metal foils, where flexible pad acts as the backing support. Hemispherical microcraters of depth $\sim$ 15 μm to 300 μm and radius $\sim$ 150 μm to 1 mm with excellent surface quality are produced on copper, nickel, and stainless steel foils (25 μm thickness). The formed features experience beneficial uniform thickness distribution and material strengthening.

In order to understand the effect of various process parameters on foil deformation characteristics, a detailed parametric study is performed. The process parameters include laser fluence, number of pulses, laser system, ablative overlay, ablative overlay thickness, confinement medium, confinement thickness, flexible pad material and its thickness. The correlations between the process variables and deformation features are established.

As FPLSF is a new process, it is necessary to understand the process mechanisms involved. In FPLSF, the principle mechanism behind laser-induced shock pressure is the formation and propagation of plasma upon laser irradiation. Therefore, a detailed investigation of laser-induced plasma characteristics is carried out using a high speed camera. The plasma lifetime and plasma expansion during FPLSF are studied initially. Moreover, the effects of laser fluence, number of pulses, confinement medium, and confinement thickness on the plasma characteristics are analyzed and correlated with the corresponding plastic deformation of metal foils.

FPLSF is a high-strain rate forming process involving strain rates of $10^5\ s^{-1}$, where the deformation mechanisms are possibly influenced by high-strain rate effects. To study the underlying plastic deformation mechanism during FPLSF, mechanical properties and microstructure of copper foil are studied. Initially, thickness distribution of the deformed foils along the cross section at different positions is examined. Hardnesses at the cross-section, top surface, and bottom surface of the crater are examined subsequently. The microstructure variation on copper foil surfaces due to FPLSF is investigated using Electron BackScatter Diffraction (EBSD) technique. The microstructure of the foil is characterized using grain size distribution, grain boundary misorientation angle, and texture. Strain hardening is identified to be the prominent plastic deformation mechanism in FPLSF rather than the typical adiabatic softening effect known to be occurring at high strain rates for processes such as electromagnetic forming, explosive forming, and laser dynamic forming. This significant difference in deformation mechanism with FPLSF is attributed to the concurrent reduction in plastic strain, strain rate and the inertia effects, resulting from the FPLSF process configuration.

Finally, finite element analysis (FEA) of FPLSF is performed to study the deformation characteristics of metal foil and flexible pad. A 3D finite element model is developed to simulate the high strain rate plastic deformation of metal foil and hyperelastic deformation of flexible pad in the commercial FE package, ABAQUS. FE model is validated first by comparing the shape, depth, and diameter of the

deformation features between experiments and simulation. A time-resolved analysis of stress and strain distributions at different positions along the foil is carried out. The stress-strain distributions are correlated with the experimental results to understand the observed process behaviors. Furthermore, several process variables, laser fluence, material and thickness of the metal foil, and flexible pad are investigated using FEA.

Table of Contents

List of Figures

List of Tables

List of Symbols

α	Absorption coefficient
α_a	Coefficient of asymmetry
α_t	Thermal diffusivity
β	Slowing coefficient
δ'	Skin depth or penetration depth
$\dot{\varepsilon_0}$	Reference strain rate
$\dot{\varepsilon}$	Strain rate
λ_i	Principal stretch
μ_m	Magnetic permeability
μ_i	Shear modulus
ν	Frequency
ρ	Density of the state
σ	True stress
σ_e	Electrical conductivity
τ	Pulse duration
ε	True strain

ξ_0 Constant based on specific heat of ambient gas

A, B, C, m, n Johnson-Cook material constants

B_P Constant depending on the irradiated material

C_P Specific heat capacity

D Shock velocity

d Vaporization depth

E Laser energy

e Engineering strain

e_c Electron charge

e_m Critical thickness

F Deformation gradient tensor

G Shear modulus

HV Vickers hardness

I Laser intensity

I_0, I_1, I_2 Laser intensity at different stages

I_i Cauchy-Green tensor invariants

K Bulk modulus

k Thermal conductivity

K_1 Specific heat ratio

$L(t)$ Plasma thickness

L_v Latent heat of fusion and vaporization

m_e	Electron mass
n	Refractive index
n	Strain hardening exponent
n_e	Electron number density
P	Shock pressure
R	Reflectivity
R	Shockfront propagation distance
r	Radial distance from beam center
r_0	Laser beam radius
R_{max}	Plume stopping distance
S	Stiffness
T_b	Boiling temperature
T_m	Melting temperature
T_r	Reference temperature
u	Shockwave velocity
v	Deformation speed
W	Strain energy density
W_e	Plasma electron oscillation frequency
Y	Yield stress
Z	Shock impedance

List of Abbreviations

EBSD	Electron BackScatter Diffraction
SEM	Scanning Electron Microscope
FE-SEM	Field Emission - Scanning Electron Microscope
TEM	Transmission Electron Microscope
LSF	Laser Shock Forming
LDF	Laser Dynamic Forming
LPF	Laser Peen Forming
RPF	Rubber Pad Forming
MEMS	Micro-Electronic Mechanical Systems
LIGA	Lithography, Electroplating, and Molding
BCC	Body Center Cubic
HCP	Hexagonal Close Packed
ASB	Adiabatic Shear Band
IPF	Inverse Pole Figure
RD	Rolling Direction
TD	Transverse Direction
fps	frames per second
ICCD	Intensified Charged Coupled Device

Chapter 1

Introduction

This chapter discusses the motivation for this research followed by the objectives and scope of the present work. The outline of the thesis is also presented.

1.1 Microfabrication

Microfabrication is defined as producing microlevel systems and components or creating microsized features on macroparts where at least two dimensions are in sub-millimeter range [1]. There is an increasing demand for the fabrication of micro systems and devices in several sectors including electronics, energy, automobile, medical equipments, communications, MEMS (Micro-Electro Mechanical Systems) and optics [2, 3]. Numerous products and components including microactuators, micro-mechanical devices, sensors and probes, micro-fluidic components, medical implants, micro-switches, optical devices, memory chips, micro-motor, magnetic hard-drive heads, computer processors, inkjet printing heads, lead frames, electrical connectors, and micro fuel cells are made by microfabrication techniques [2, 4–6]. Few examples of microcomponents or microfeatures are displayed in Fig. 1.1.

The manufacturing of these microsystems is achieved by a number of different fabrication techniques. Fig. 1.2 classifies the typical micromanufacturing processes based on their working mechanism [3]. However, it is more appropriate to classify the processes into MEMS-based (or lithography-based) and non-MEMS-based (or

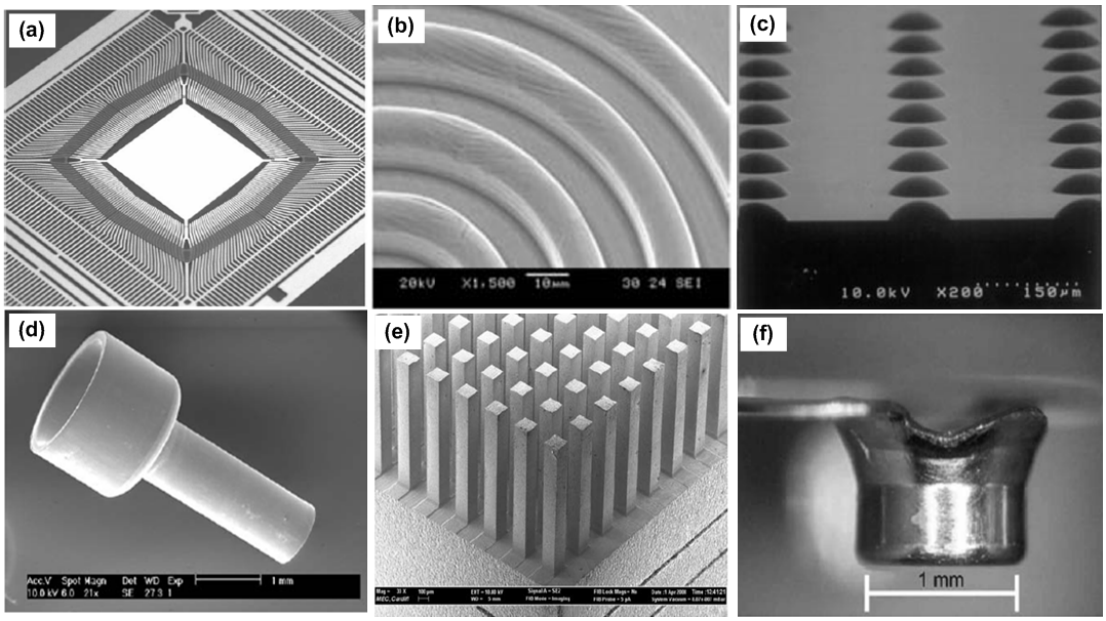

Figure 1.1: Typical examples of microcomponents/features (a) Leadframe by stamping [7] (b) Micro fluidic channels by isostatic pressing [8] (c) Microlens arrays by compression molding [9] (d) Micromotor shaft by extrusion [10] (e) Micropillars by micro-wire EDM [11] (f) Electron gun cup by deep drawing [10]

non-lithography-based) techniques in microfabrication industry [6]. Lithographic processes are found to be the predominant techniques by which micro and submicron features are fabricated for MEMS devices. Lithography involves a series of processes that facilitate the transfer of required patterns from a mask into a silicon material through polymer resist by means of chemical treatments [12]. Despite its enormous popularity and well-developed process knowledge, these techniques are largely limited by their quasi three dimensional (2D or 2.5D) fabrication principle. Another significant limitation has been their ability to process only silicon-based materials. In addition, it is difficult to produce high aspect ratio features using these processes [11]. LIGA, laser fabrication, etching, and plating are other MEMS-based techniques that have limitations such as 1D processing and increased process complexity [11]. Injection moulding, casting, and deposition techniques such as SDM, CVD and electrochemical deposition are some other methods used to manufacture micro components [6].

In recent times, the micromanufacturing industry identified a tremendous emergence of non-silicon materials namely metals, glass, ceramics, and polymers due

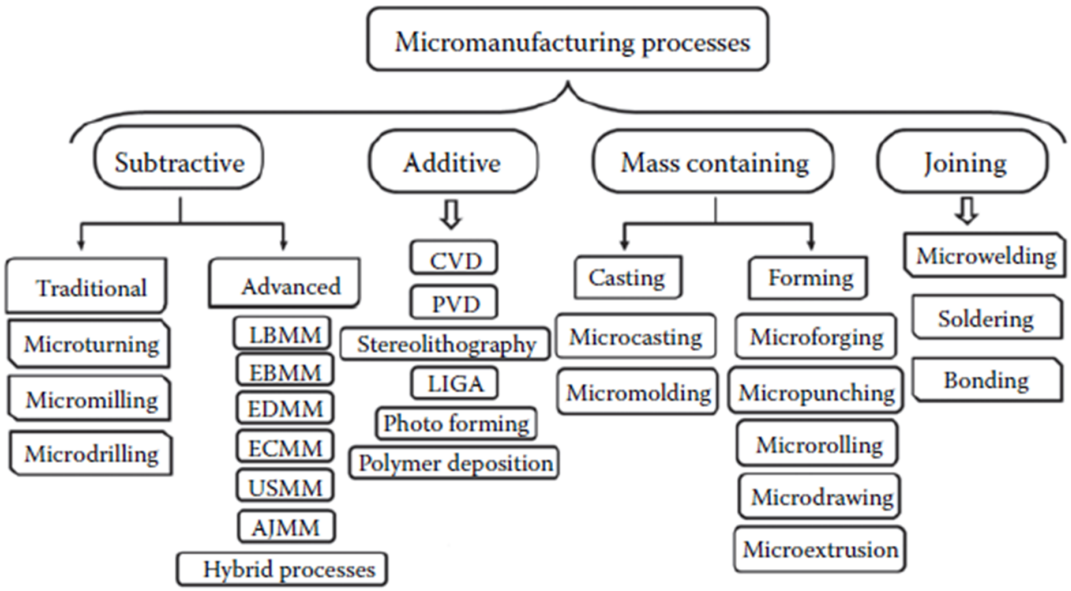

Figure 1.2: Classification of micromanufacturing processes [3]

to their applicability in the microsystems, which is illustrated in Fig. 1.3 [13]. Specifically, the utilization of metallic materials in microcomponents is gaining momentum, largely because of their applicability due to the mechanical and electrical properties (strength, ductility, electrical conductivity, etc). Also, the formidable progress in the research of metal processing techniques towards miniaturization, for which extensive process knowledge is available only on macroscales, encourages the industry to adopt metallic materials [10, 14].

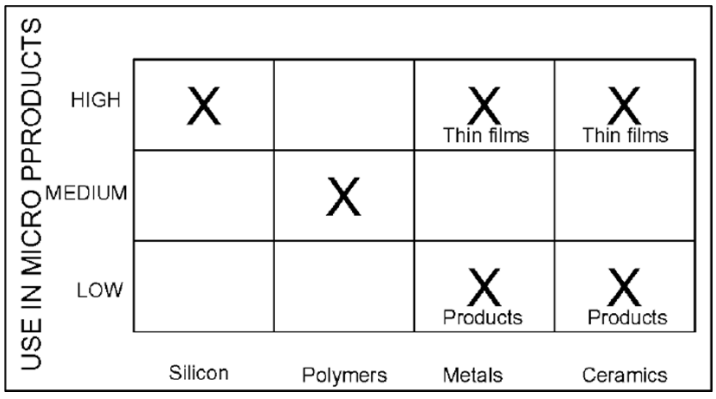

Figure 1.3: Materials in microsystems [13]

The processing of metals in microfabrication is commonly achieved by non-lithography based techniques. Micromanufacturing processes related to metals can

be classified into additive, machining, forming, and joining processes as seen in Fig. 1.2. However, micromachining and microforming processes enjoy large significance due to their wide range of processes compatible for various materials. These techniques are typically characterized by their ability to produce 3D microfeatures with high aspect ratio. Micromachining processes consist of mechanical cutting (turning, milling, drilling, grinding, and polishing), Electro chemical machining (ECM), Electric discharge machining (EDM), laser machining, electron beam machining, and ion beam machining. Micromachining processes are found to have one or more of the following limitations: microtool fabrication, larger machining force, chip removal, high tool wear, 2D material removal, relatively lower material removal rate [13]. High aspect ratio tooling experience structural damages, requiring high strength materials [15]. The larger cycle time and relatively lower production rate of micromachining processes reduces their applicability in mass production. Whereas, another category of micromanufacturing, namely the microforming processes gained prominence in microfabrication industry due to their propensity for mass production of components/features. The further attention of this chapter is turned towards microforming.

1.2 Microforming

Microforming is defined as a manufacturing process to produce metallic parts or structures in microscales in minimum two dimensions by plastic deformation without any material removal or addition[10]. The suitability of microforming for mass production is supported largely by the short process cycle time and the cheap production cost. In addition, several factors including net shape production, better mechanical properties of final components, and high production rate make microforming an attractive option compared to the material removal or additive techniques in microfabrication [14]. Microforming is further categorized into bulk forming and sheet metal forming based on the product type (i.e) the geometry of the workpiece and the required microfeatures.

1.2.1 Bulk metal forming

Bulk forming processes involve large shape changes, low surface area to volume ratio, compressive stress in all directions, large plastic deformation, and considerable modification in cross section and shape [16]. It is broadly classified into forging, extrusion, rolling and drawing processes [4, 16].

- Forging: A deformation process in which the plastic deformation of the workpiece occurs by compressive forces applied through tool and dies. Forging is further classified into open-die forging, impression-die forging, closed-die forging, radial forging, orbital forging, upsetting, coining, hobbing, etc.
- Extrusion: It is a forming process by which the metal is squeezed through a die opening by compression to form a long product of constant cross section.
- Rolling: It is a deformation process of reducing the thickness or modifying the cross-section of workpiece by compressive forces exerted by a set of rollers.
- Drawing: It is a process in which reduction or change in cross-section of a wire, rod or bar is achieved by pulling it through a die opening.

The various efforts for the forming of microparts by various bulk metal forming processes has been reviewed by Geiger and Jesweit [10, 17]. In one of the earlier attempts, Saotome and Inoue [18] demonstrated the microforging of amorphous and superplastic materials by fabricating V-grooves of width ranging between 1 and 20μm. Cold forging has long been used to create metal parts of minimum diameter up to 300 μm [10]. More recently, Li et al. [19] used radial forging to create inner micro grooves on thin copper tubes. In case of microextrusion process, Geiger et al. [10] achieved an extrusion of copper pins of 800 µm shaft diameter with a wall thickness of 125 μm by a multi-stage forming operation. Extrusion of amorphous alloys into microgear shafts up to 100 µm pitch circle and 10 µm module were obtained through superplastic backward extrusion by Saotome and Iwazaki [20]. Meanwhile, Wang et al. [21] developed a floating die design for forming microgear through filling the die cavities by converting the frictional resistance

force into a useful force through upsetting [21]. Krishnan et al. [22] developed a forward extrusion technique to fabricate circular brass pins of diameter ranging from 0.57 mm to 1.33 mm. Bohm et al. [23] demonstrated the cold embossing of 500 μm thick metals such as copper, aluminum, steel, and brass to fabricate features of 10 μm minimum and micro channels of 2.5 and 1 μm using silicon dies, where the wear and failure of dies are apparent. Bulging of the material at the structure rims and the inability of silicon dies to be used for high compressive stresses are the few limitations of this process. Microprojections of 100 - 200 μm diameter and 5 - 50 μm depth were made on the aluminum sheets of 2 mm thick using the coining process by Ike and Plancak [24]. This process is limited by the insufficient filling of the material and the surface damage. In these processes, the common limitations are the precise alignment of the die and punch, difficulty in making intricate die features, and the handling of components. As most of the microsytems involved are made of sheets or foils as highlighted from Fig. 1.3, the further emphasis is shifted to sheet metal forming.

1.2.2 Sheet metal forming

Sheet metal forming processes typically involve planar workpieces, high surface area to volume ratio, localized deformation, and invariant cross-section. The deformation is usually achieved by the tensile forces in the plane of sheets [25]. They can be broadly classified into bending, drawing, and shearing which hence comprise of following processes: punching, blanking, deep drawing, bending, stretch forming, creep forming, bulging, roll forming, stamping, embossing, vacuum forming, hydroforming, peen forming, spinning, rubber-die forming, superplastic forming, and high-energy rate forming [26]. Schematic of a few sheet metal forming processes are presented in 1.4. The following paragraphs describe some of the processes:

- Bending: A plastic deformation process by which metal is strained around a straight axis. Some typical bending processes are V-bending, edge bending, flanging, seaming, curling, hemming, corrugating, air bending, offset bending,

tube bending, etc.

- Deep drawing: It is one of the most common sheet metal forming techniques that is performed by placing the flat sheet metal over a die cavity and forcing the metal into the die using a punch.
- Shearing: A metal cutting process involving shear force to cut the material without the production of chips.
- Stretch forming: It is a process in which the sheet is clamped on its edges and stretched to form a shape.
- Spinning: It is a process to create axisymmetric parts using a mandrel and rounded rollers or tools.
- Rubber pad forming (RPF): Process by which the sheet is deformed between a rigid tooling and a rubber pad.
- Hydroforming: Drawing of materials using a pressure medium (fluids) as punches or dies.
- High-energy rate forming (HERF): Processes in which large amount of energy is released in a very short duration to produce material deformation.

The theory and application of above-mentioned sheet metal forming processes are well-established in mesoscale range. The applicability of various sheet metal forming processes in manufacturing microcomponents and the associated process-related issues have been investigated extensively in recent years. The major challenge towards miniaturization effort is identified to be "size effects", a behavior that induces deviation in process characteristics as a result of scaling down the dimensions of geometry [27]. Size effects are generally due to the following factors: surface to volume ratio, microstructure, surface topography, surface tension, and adhesion force. The miniaturization affects a wide range of characteristics related to the material and process including flow stress, forming limit, anisotropy, formability, fracture, process scatter, elastic recovery, tribology, and formed product surface quality [10, 27, 28].

A major review of the microforming processes was communicated first by Geiger et al. [10], which has been further expanded by various researchers [7, 28, 32–34]. Highlights of few important processes are discussed further below.

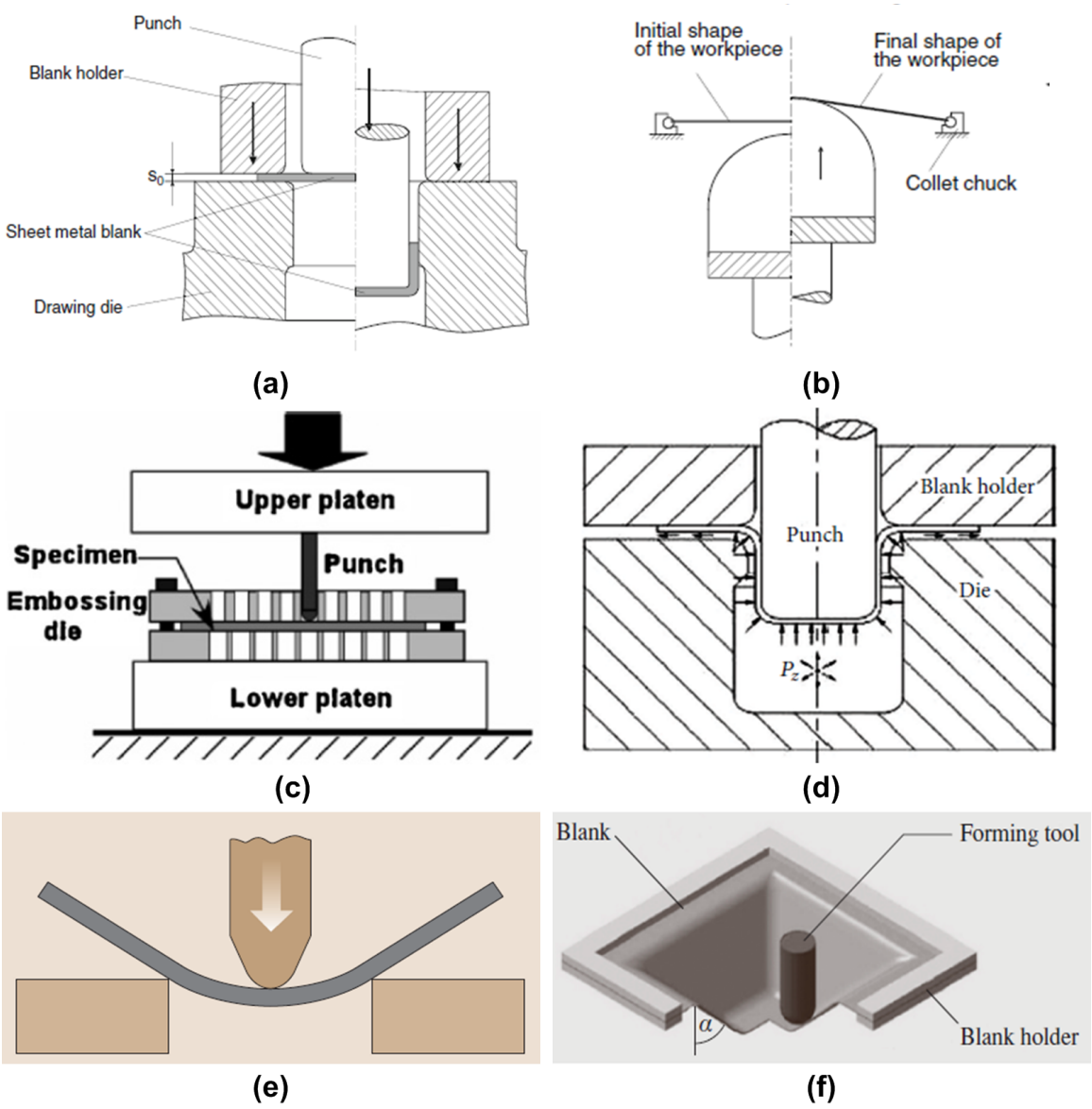

Figure 1.4: Schematic of some common sheet metal forming processes (a) Deep drawing [29] (b) Stretch drawing [29] (c) Embossing [30] (d) Hydromechanical deep drawing [31] (e) Bending [25] (f) Incremental forming [25]

Micro deep drawing is a significant sheet metal forming process used to create box, cup, and complex shapes. Saotome et al. [35] demonstrated the deep drawing of steel sheets with 50 μm thickness using micropunch with diameters as small as 500 μm. Vollertsen et al. [34, 36] established deep drawing of aluminum and stainless steel cups of 1 mm diameter and 0.5 mm depth using a metal punch . Microcups of 0.95 mm diameter were produced on 40 μm thick copper alloy using micro deep drawing by Gong et al. [37]. Chen et al. [38] achieved micro deep drawing of SUS 304 stainless steel sheets with thicknesses ranging between 20 μm

and 150 μm using 2 mm punch diameter. Meanwhile, deep drawing of same SUS 304 sheets (20 μm thick) into microcups of 150 μm was achieved in two sequential stages by Manabe et al. [39]. Erhardt et al. [40] proposed additional heating of the blank to increase the material formability in deep drawing. Wrinkling of components has been a major limitation in deep drawing, which is caused by the compressive hoop stresses developed in the flange region. Hence, the control of blank-holder pressure with respect to the drawing ratio is required to suppress the wrinkling but the friction increases due to the blank holder pressure. Also, the contact between the die and circumference of the blank-holder, which is non-uniform, increases the wrinkling. In an attempt to eliminate wrinkling, resin dies, blank-holder and an auxiliary sheet were used in the deep drawing of copper foils by Marumo et al. [41]. This auxiliary resin sheet resisted the deformation and prevented the wrinkling of drawn blank wall and flange. Friction in deep drawing is typically higher due to the large surface area to volume ratio, especially at the die radius and the flange, which affects the process performance [34]. In addition, size effects increase the friction between the components in lubricated conditions. Thus, Gong et al. [37] used DLC coating of dies and blank holders in micro deep drawing of copper alloys to facilitate an increment of limit drawing ratio (a ratio of maximum blank diameter to punch diameter) and a reduction in forming force. High equipment and tooling cost has also been a major limitation with drawing process.

Cold isostatic pressing of 3 μm thick copper and 2.5 μm thick AISI 304 stainless steel to produce channels of curved, straight, concentric circles, and cross shapes using silicon and resin dies, where black plasticine was used as the pressure transmitting medium, has been investigated by Joo et al. [8]. Incomplete forming, wrinkling, and plastic deformation of dies were observed while forming with the resin dies. Microchannels of 10-20 µm width and 5-10 µm depth were achieved using the silicon die but with limitations such as slip marks on stretched surfaces, line traces along the side wall, thinning at narrow inter-channel distance, surface

dents, and foil tearing due to sharp die edges. Single-point incremental forming has been developed by Jeswiet et al. [42] using a spherical forming head and a blank holder to induce local plastic deformation gradually and create complex shapes in sheet metals. However, this process has limitations in terms of forming steep angles, uncontrolled plastic deformation in processed areas, springback, complexity of multiple tools, long cycle time, and the lack of accuracy.

The alternatives to the deep drawing are identified to be hydroforming and rubber-pad forming. Hydroforming of sheets, where the rigid tooling is replaced by the pressure medium is classified further into fluid forming and hydromechanical deep drawing, in which the pressurized fluid replaces the punch and die respectively [25]. The pressure medium in hydroforming results in the reduction in friction, wrinkles, and fracture as observed in case of rigid punches with conventional deep drawing. An improvement in formability and uniformity of formed components is another characteristic of the hydroforming process. Forouhandeh et al. [31] conducted an overview of hydroforming process in both macro and microscales. In an earliest attempt to deploy hydroforming in microapplications, Koc and Mahabunphachai [43] formed microchannels of fuel cell bipolar plates (width - 0.46 to 1.33 mm; height - 0.15 to 0.98 mm) on 51 μm thick SUS304 steels. The limitation of producing larger aspect ratio features (greater than 0.5) due to the large amount of required hydrostatic pressure was addressed by Hung and Lin [44] through designing a two stage high pressure hydroforming system to fabricate microchannels of 0.75 mm width and height on 100 μm thick SUS304 steels. Most recently, Forouhandeh et al. [31] demonstrated microhydroforming of 300 μm thick CuBe2% alloy to produce microcups of about 5 mm diameter. Though one of the rigid tooling in conventional deep drawing is eliminated with hydroforming, the process cycle still remains large due to the increased complexity with changing the dies [25].

Rubber-pad forming replaces either one of the rigid tooling, die or punch, with a flexible rubber material. Though the application of rubber pad forming in mi-

croscales appears to be limited, few attempts are reported in the literature. Specifically, the issues with hydroforming to fabricate asymmetric microchannel features of bipolar plates have been addressed better by the rubber pad forming. Liu and Hua [45] produced bipolar plates having microchannels of 500 μm depth and 800 μm width on SUS304 stainless steel sheets of 100 μm with rubber pad in place of female die. Peng et al. [46] achieved the similar forming capabilities by introducing a rubber pad between the rigid punch and the die over the metal sheet. Rubber pad forming was extended to other materials, Al 1050 alloy [47, 48] and titanium [49] (channel width - 800 μm, depth - 400 μm) as well. In spite of the improved formability and reduced tooling cost with rubber pad forming, it is largely limited by the low production rate. It is also noticed from the above processes that the typical deformation sizes were approximately 500 μm, which are quite large for the emerging microfabrication needs. In addition, the process knowledge of rubber pad forming in microscales is limited despite its availability in macroforming (as detailed in chapter 2).

This discussion of potential microforming techniques highlighted significant issues that should be addressed for the improvement, implementation, or development of microforming techniques in microfabrication applications. The further section summarizes the forming issues.

1.2.3 Limitations of existing forming processes

This section compiles the common limitations with the sheet metal forming processes pertinent to the deformation in microscales. The fundamental failure modes of sheet metal forming are determined to be fracture, wrinkling, springback, and surface defects [25, 50]. It is identified that deep drawing and its derived processes are amongst the most commonly used techniques to produce microcomponents. Generally, the following defects are experienced in deep drawing of sheet metals: earing, distortions, wrinkles in the flange and wall, tearing, bucking, scratches, folding, and excessive thinning, as shown in Fig. 1.5 [25, 29, 50, 51]. It is apparent

from the discussion in section 1.2.2 that, these failure modes were also observed during the microforming efforts, as seen from Fig. 1.6.

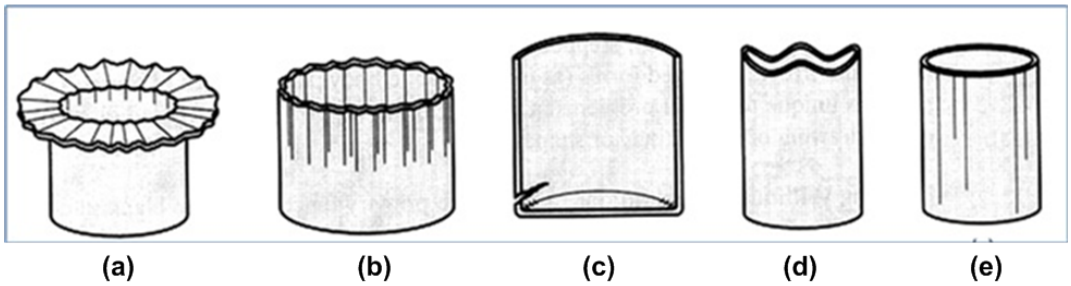

Figure 1.5: Common defects in sheet metals during forming process [50] (a) Wrinkling (Flange) (b) Wrinkling (Wall) (c) Tearing (d) Earing (e) Surface defects

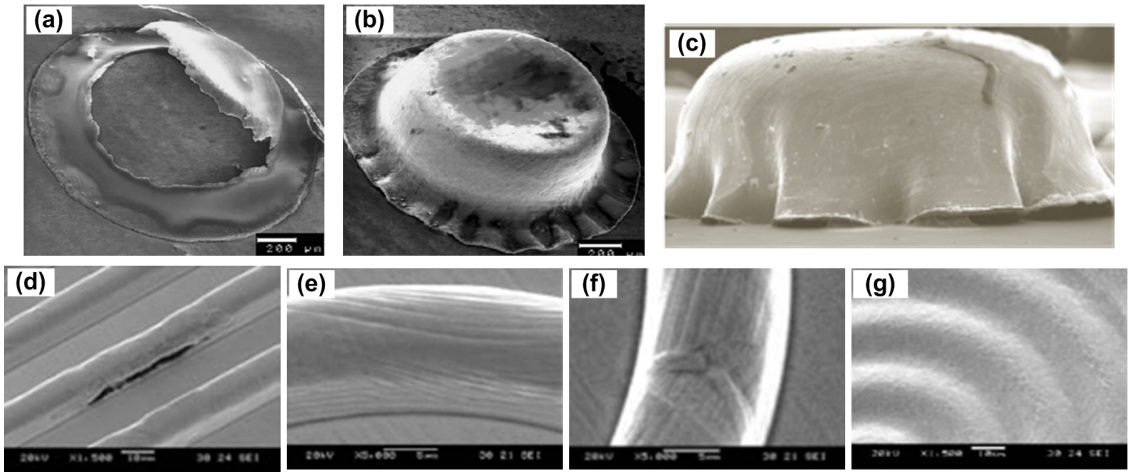

Figure 1.6: Limitations in microforming processes [8, 36, 52] (a) Bottom fracture (b) Flange wrinkling (c) Wall wrinkling (d) Tearing (e) Slip marks (f) Dented ridges (g) Incomplete filling

Friction between the process components is another major limitation with the forming processes as the friction and wear of parts have detrimental effects on the process outcome. For example, in deep drawing process, the friction is developed between the following interactions: punch and workpiece, blankholder and workpiece, and die and workpiece, which induces undesirable residual stresses on the formed surface and so the flow stress. Friction also affects the surface finish of the work surface after forming. Significantly, expensive forming tools experience wear due to friction causing dimensional inaccuracy on the formed parts [16]. In order to increase the wear resistance of dies and punches, either specific coatings (DLC) [37, 53] or surface finishing of dies using ion beam irradiation [53, 54] are

required, which are expensive and time-consuming. In addition, with friction being system and size-dependent, predicting the process outputs through simulation will be difficult especially when frequent changes in substrate materials and geometry are required. Springback is another significant limitation that is observed in most of the sheet forming processes affecting the dimensional accuracy of the formed part.

In reference to the forming at microscales, the above-mentioned forming issues show significant prominence as a result of the size effects. An increase in friction is observed with the reduction in the blank size due to the size effects [10, 16]. Miniaturization typically increases sheet thinning due to the decreased material anisotropy, reduction in flow stress, and increase in friction [10, 13]. Large number of influential factors on miniaturization increases the process complexity. The other issues existing with sheet metal forming processes used for microfabrication are listed below:

- It is hard to make intricate contours by forming processes like cutting and casting operations.
- At micro levels, machines and tools are required to possess high precision with narrow tolerances.
- Handling and alignment (accurate positioning) of dies and punches.
- Accurate feeding of sheets to sub-micron accuracy is challenging, especially in case of progressive forming.

In summary, the limitations with the sheet metal forming processes can be broadly classified into manufacturing-related and the process-related issues as represented in Fig. 1.7. Typical manufacturing issues are related to the process flexibility, cycle time, fabrication of tools, tool wear, and handling and alignment of process components. The limitations with thickness distribution, elastic recovery, component failure, friction and wear, and process modeling can be termed as process-based or material based issues.

A holistic analysis of the limitations in these two categories revealed that the source for most of the identified issues can be narrowed down to two factors: process formability and effect of dies and punches. Firstly, the issues such as material failures, springback, thinning, surface integrity of formed components, and difficulty in forming high strength materials are partially attributed to the formability issues corresponding to the process and material.

Secondly, but significantly, the influence of die/punch is identified with the fact that most of the listed processes involve die/punch patterns of required geometry, and the components are formed by replicating the patterns.the effect of dies/punches. The following points details the pertinent issues related to die and punches:

1. Primarily, the manufacturing of tools, especially the complex inner geometries of dies, has always been a problem with forming processes [6, 10, 15, 16, 51, 55]. Moreover, the fabrication of microdies and micropunches, especially the intricate or inner features, is one of the key challenges in the microfabrication industry [33, 34]. Typically, microtool fabrication is achieved by the techniques including: Ultra-Precision Micromachining (UPM), electron beam lithography, micro-Electrical Discharge Machining (EDM), LIGA, and laser ablation [6, 7, 56]. Not only that the tool fabrication is time consuming and expensive, it is increasingly difficult in case of complex microstructures.

2. In addition to the fabrication factors, the friction in the system is largely dictated by the contact of blank with die and punch, which further influences the flow stress and material formability. The influence of tool wear significantly affects the formed surface quality. Though processes like hydroforming and rubber pad forming eliminates either die or punch to produce features, the processes still involve large amount of interaction involving blank with die/punch.

3. In the emerging microfabrication industry, the flexibility of the process to

produce different components/features in short time with reduced cost has been a major requirement. The expensive and time-consuming fabrication of dies/punches will probably affect the process flexibility.

4. The process cycle time is significantly larger with the usage of dies and punches due to the increased complexity in the alignment of tools, in addition to the tool fabrication duration.

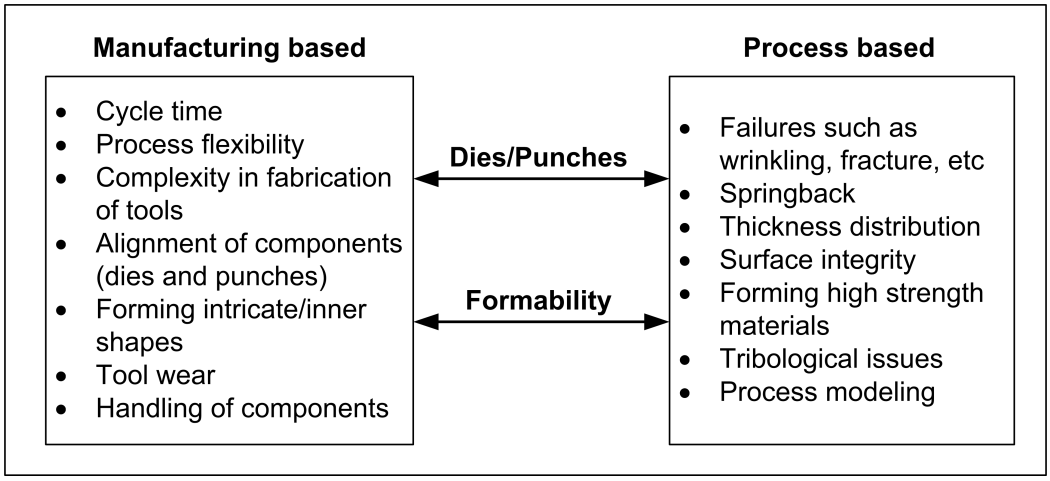

Figure 1.7: Summary of limitations with sheet metal microforming processes - Research motivation

The development of new fabrication techniques requires attention on the discussed aspects.

There is a comparatively newer branch in sheet metal forming, high velocity or high strain rate forming, in which deformation of materials is achieved at strain rates typically greater than $10^4 s^{-1}$ [57]. These processes are classified by the electrical, chemical, or mechanical means of energy source. A significant improvement in material formability is demonstrated by these processes (explosive forming, electromagnetic forming, electrohydraulic forming) mainly due to the difference in deformation mechanisms at high strain rates, in comparison to quasi-static forming techniques reported earlier. However, the capabilities of high velocity processes have so long been restricted to deformation only at macroscales. Meanwhile, with the advent of lasers as the energy sources recently, the high velocity forming embarks into microfabrication applications [58, 59]. As laser technology has been

reliable, easily controllable, and precise, it is an ideal choice for microscale fabrication. Despite the benefits with high strain rate forming with laser systems, the process still requires the die patterns to fabricate microfeatures, which introduces the limitations mentioned previously in Fig. 1.7. Hence, there is a necessity to develop new techniques/processes without dies or punches, that are fast, reliable, flexible, and suitable for variety of materials to produce microdeformation features. It forms the motivation for this research work.

1.3 Research Objectives

The major objectives of this research work are as follows:

- Developing a novel mold-free forming process for the fabrication of three dimensional micro-features on a variety of thin metallic materials.
- Studying the underlying process mechanisms and predicting the process behavior.

1.4 Scope

1. Development of a microforming process without rigid tooling (die/punch) using laser energy as the source for the plastic deformation of metals. The feasibility and flexibility of the proposed technique to fabricate microsize features on metal foils are examined to establish the process.

2. Detailed parametric analysis of the process to understand the influence of different process variables on the characteristics of the final deformation features, that is essential for the improvement of process capability and process modeling.

3. Analysis of different process mechanisms involved in the process

   (a) The evolution of laser-induced plasma with time was studied using a high-speed camera visualization as the principle mechanism behind the loading energy is the formation and propagation of plasma upon laser irradiation.

   (b) The formability of the material at the high strain rate forming process is investigated through characterizing the deformation features, percentage thinning and hardness at the surface and the cross-section.

   (c) Microstructural characterization of formed features to study the plastic deformation mechanism experienced.

4. Process modeling using computational simulation methods for the prediction of system response to the input variables and to study the process behavior that are difficult to observe by experimental techniques.

1.5 Thesis Outline

Following the introduction of research background in this chapter, the thesis starts with the critical review of various high strain rate sheet metal microforming processes and their potential applicability in the microscales in Chapter 2. Chapter 2 also discusses process mechanisms involved and the process modeling approach. Chapter 3 examines the feasibility of the proposed microforming technique, Flexible Pad Laser Shock Forming (FPLSF) to fabricate microfeatures with different sizes and geometry through plastic deformation of thin metallic foils. In addition, the influence of different process variables on the process outputs are investigated in detail. In chapter 4, the laser-induced plasma evolution, which is one of the significant process mechanisms in the developed process is evaluated with respect to the significant process parameters. Then, the plastic deformation characteristics of metal foils in the high strain rate FPLSF is studied through the mechanical properties and microstructural characterization in chapter 5. Finally, the modeling strategy using finite element simulation for the process prediction and analysis is explored at chapter 6. The major conclusions of this thesis along with the suggestions for the further research are presented in chapter 7.

Chapter 2

Literature Review

This chapter reviews the relevant literature on sheet metal forming at high strain rates, in particular the processes using lasers as the energy source. The corresponding process variables and process mechanisms are discussed further. Subsequently, the modeling aspects of high strain rate processes are reviewed.

2.1 Rubber pad forming

As the objective of this research work focuses on developing processes without rigid tooling, it will be beneficial to study the existing processes which successfully replaced at least one of the rigid tools in the forming. Apart from the high strain rate techniques, the other such processes are hydroforming and rubber pad forming which were discussed briefly in chapter 1. Rubber pad forming provides considerable scope for compliance and further improvement in comparison to the hydroforming process. Thus, RPF is reviewed for process behavior, advantages, and limitations, which can be reflected upon the new process development.

Rubber pad forming, also called as Guerin process, is the process in which conventional male or female die is replaced by a flexible rubber material to form sheet metals into shapes corresponding to the die pattern. The process setup is illustrated in Fig. 2.1 [60]. Rubber pad forming has long been used in manufacturing industry through embossing, bulging, shearing, and forming [61]. The application

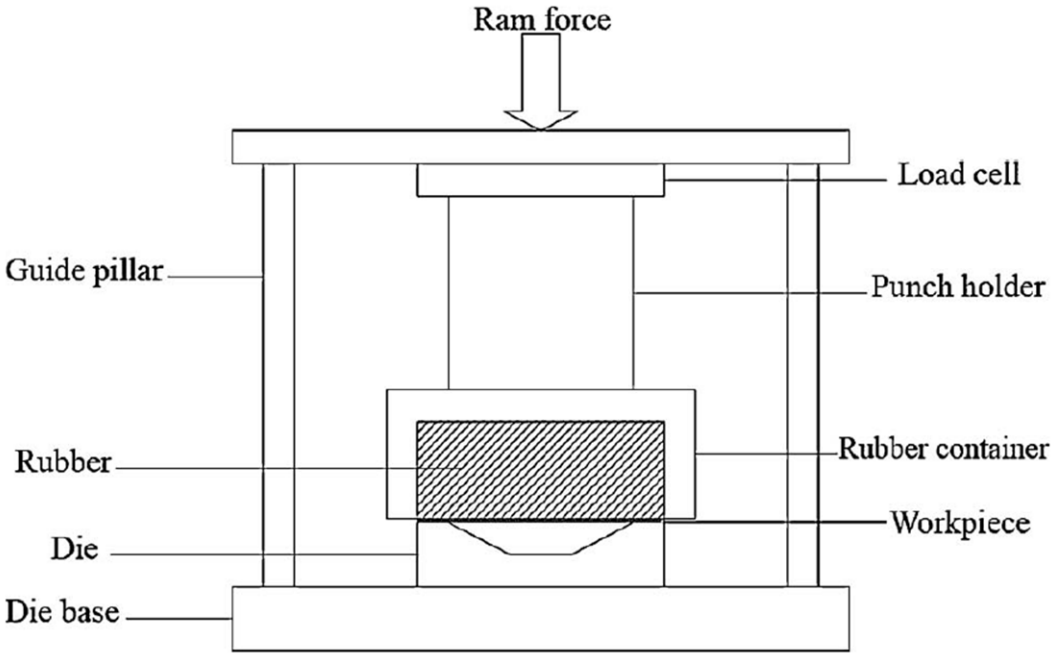

Figure 2.1: Schematic of Rubber pad forming process [60]

of this process ranges from the production of aircraft panels in the early days using polychloroprene pads to the fuel cell bipolar plates in the recent times. In RPF, the incompressibility of the flexible material plays a significant role in the deformation of sheets. Thiruvarudchelvan [62] used urethane pad, which can withstand maximum of 150°C temperature as the male die, to produce ashtrays from copper, brass and aluminum sheets. The two significant process variables, namely the hardness and thickness of the rubber pad material, are analyzed further.

2.1.1 Rubber pad material

In rubber pad forming, materials such as natural rubber, silicone rubber, and polyurethane rubber are commonly used as the rubber pad [45, 60, 61]. Ramezani et al. [60] compared these different materials and identified that the silicon rubber required lower punch load but is limited by its lifetime and inability to make sharp edges. Polyurethane rubber has a larger lifetime and produced sharper blank edges with lower thinning of sheets, thus making it appropriate for larger number of loading cycles. Thiruvarudchelvan [62] observed that the drawing was dominant compared to stretching for softer pads, but wrinkling of sheets occurred due to the

insufficient blank holding force.

Liu et al. [45] revealed that the hardness of rubber plays no significant role in the formability of blank, when testing two different grades hardness of polyurethane rubber. The von Mises stress distribution in the blank and the die filling ratio remain unchanged with the change in hardness. Peng et al. [63] observed in flexible punching process that the stress profile and thickness distribution of formed blank did not vary significantly with the rubber hardness. A similar behavior was also identified with the flexible forming of stainless steel sheets using polyurethane rubber pads [46]. In contrary to the previous findings of insignificant influence of rubber hardness on deformation process, Dirikolu and Akdemir [64] found the maximum von Mises stress of the blank to increase along with the increase in rubber hardness.

Recently, Wang et al. [65] developed laser dynamic flexible forming, in which a rubber pad is placed between the ablative overlay and the substrate. Contrary to Liu's [45] results, it was found that the filling capacity of rubber increases at the lesser hardness resulting in higher deformation depth. However, if the rubber is too soft, the surface quality of the blank will be affected due to the reduction of homogeneous pressure [65]. Lim et al. [48] also observed an increase in forming depth with the reduction in rubber hardness as the corresponding increase in counter pressure facilitated the metal flow into the die. In sheet metal punching using urethane elastomers, an optimum urethane hardness was prescribed by Watari et al. [66] due to the insufficient punching with the hardness either too small or too high. Del Preta et al. [67] found that, though the variation in hardness had no influence on plastic strain distribution, it affected the fillet radii formation significantly. In rubber-assisted hot embossing of ABS film by Nagarajan and Yao [68], the rubber pad hardness played a significant role in the embossed film uniformity as an increase in shore hardness of rubber pad improved the uniformity of the film thickness.

Though the effect of rubber pad hardness on the deformation depth in rubber

pad forming processes has been studied extensively, there were only few studies on the thickness distribution of the formed features. Son et al. [47] observed a reduction in thinning of aluminum sheets with increase in rubber hardness. Contrarily, more thinning of sheets was observed with the increase in rubber hardness during the rubber pad forming of aluminum sheets by Ramezani et al. [60]. It is evident from the results that the hardness of the rubber pad affects the thickness distribution of the formed feature.

From the above mentioned research works, the hardness of the flexible rubber material is found to have significant influence on the stress-strain distribution of metal blanks, deformation feature geometry, and the mechanical properties of the deformed workpiece.

2.1.2 Rubber pad thickness

The thickness of the rubber pad is a significant process parameter in the rubber pad forming processes. The minimum thickness of the rubber pad is prescribed to be 2 or 3 times greater than the forming depth in rubber pad forming [61, 69]. In laser dynamic flexible forming, the deformation depth on the metal foil decreased with increase in rubber pad thickness [65]. However, if the thickness is too thin, both the formed workpiece and rubber pad experienced damage, which was attributed to the reduction in laser energy deposition smoothing. Similarly, in flexible punching process, optimum thickness of rubber is required to achieve an efficient punching [66]. The deformation depth was found to be increased along with the increase in rubber pad thickness up to a certain threshold after which the deformation is saturated [48]. Thus, it is evident that there exists an optimum pad thickness to maximize the deformation depth.

2.1.3 Advantages and limitations

The advantages of using flexible dies are [45, 60, 62],

- Improved formability due to the flexible contact between the die and rubber.

- Uniform pressure distribution because of the hyper-elastic properties of rubber.
- High part dimensional accuracy and excellent surface finish.
- Ability to fabricate various feature shapes using the same flexible pad, increasing the process flexibility.
- Easy alignment and replacement of dies.
- Reduction in sample thinning and friction.
- Low tooling cost.

The limitations of rubber pad forming are listed below:

- The major disadvantage of this process is its low production rate and ineptness for mass production [70].
- Inability to fabricate sharp and deep features [70].
- Compression of the rubber is an influential parameter whereas severe compression will lead to the fracture of forming sample [71].
- Non-uniform thickness distribution was observed when there was an excessive friction between the workpiece and the rigid die [45].
- The other limitations include lower working temperature, lesser number of cycles the rubber pad can be used, and the need for higher press capacity as compared to rigid dies.
- Despite the elimination of one of the die/punch, the friction between the blank and the rigid tool produces undesirable effects on deformation profiles and their surface quality.

2.2 High strain rate metal forming

Manufacturing processes such as machining and forming are characterized by different terminologies such as cutting speed, deformation velocity, stroke rate, and

strain rate, depending on the process attributes. The forming processes are typically characterized by strain rates as opposed to cutting speeds in machining processes. Thus the term "high strain rate" is used commonly to define the forming processes instead of "high energy-rate" or "high velocity". The strain rate is defined by the rate of change of strain, $\dot{\varepsilon} = d\varepsilon/dt$ which is related to the deformation speed (v) as $\dot{\varepsilon} = v/h$ where h is the instantaneous height of the deforming sample. A classification of forming processes based on the strain rate is displayed in Fig. 2.2 [57]. Processes that involve strain rates of 10^2 - 10^7 s^{-1} such as electromagnetic forming, explosive forming, and laser shock forming are termed as high strain rate processes. High speed forming possess significant advantages to the low ($\dot{\varepsilon}< 10^{-1}$ s^{-1}) and intermediate ($\dot{\varepsilon} \sim 10^{-1}$ - 10^2 s^{-1}) strain rate forming processes in terms of formability and process time.

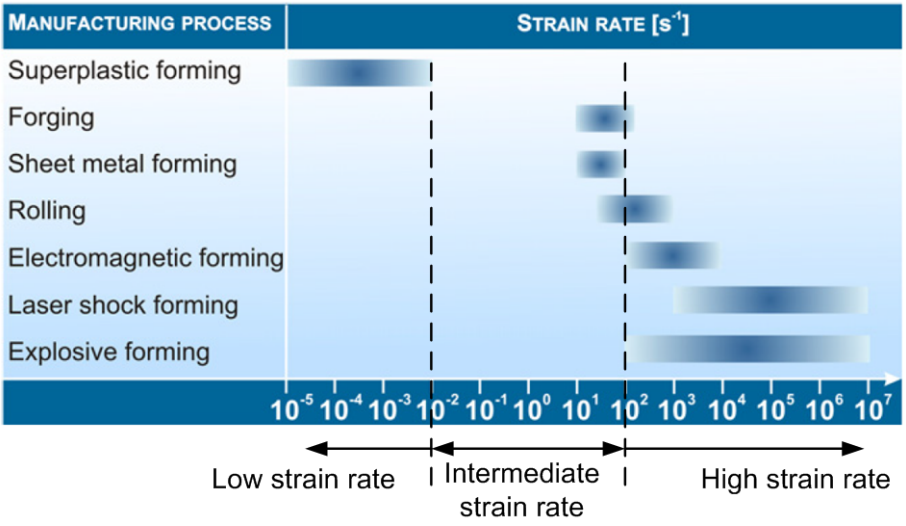

Figure 2.2: Comparison of strain rates of forming processes [57]

The conventional forming processes are classified as intermediate strain rate forming where the loading is assumed to be quasi-static. The flow stress of the material typically increases after yielding due to the concurrent material strengthening in quasi-static conditions. The flow stress increases with an increase in strain rate due to which localized necking is inhibited and the material undergoes large elongation before fracture [16].

Electromagnetic forming is a process that uses a pulsed magnetic field interacting

with the induced eddy current to produce Lorentz force, which acts as the loading force on the sample [72], as shown in Fig. 2.3. The current passing through the actuator coil generates a magnetic field around it which results in the formation of eddy currents and hence magnetic fields in the workpiece. These two magnetic fields repulse each other and force the sample in the opposite direction. This process is limited to the electrically conductive materials such as aluminum and copper. However, low conductive materials can be formed with the aid of a conductive band [73]. Hybrid processes, combining electromagnetic forming with deep drawing to fabricate high aspect ratio features on aluminum sheets have been developed by Risch et al. [74]. Recently, Shang et al. [75] implemented electromagnetic forming to fabricate bipolar plates with stainless steel foil using a conductive driver plate and the compliant layer. Nevertheless, it has limitations in terms of process flexibility, loading of tool coil, poor efficiency, and safety aspects.

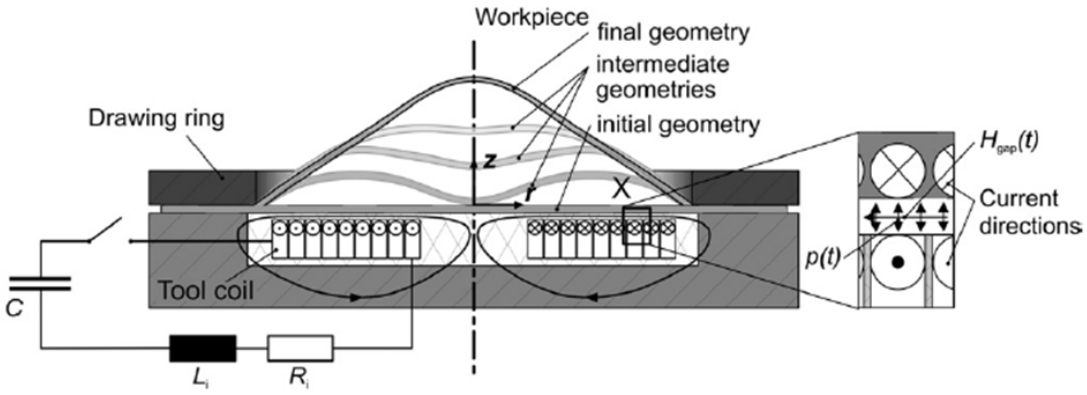

Figure 2.3: Schematic of electromagnetic forming [72]

Explosive forming uses explosive charges to create high-energy rate and forces metal sheets into a die cavity by a generated shockwave, as shown in Fig. 2.4 [4]. Despite its suitability for flexible shapes, it has longer cycle time compared to electromagnetic forming and is suitable only for low volume production of large parts. Safety of this process has been its obstacle. Furthermore, failure and wear of dies is found to be a significant process limitation. Electrohydraulic forming is another high strain rate forming process in which the shockwave is generated through a rapid discharge of energy between two electrodes.

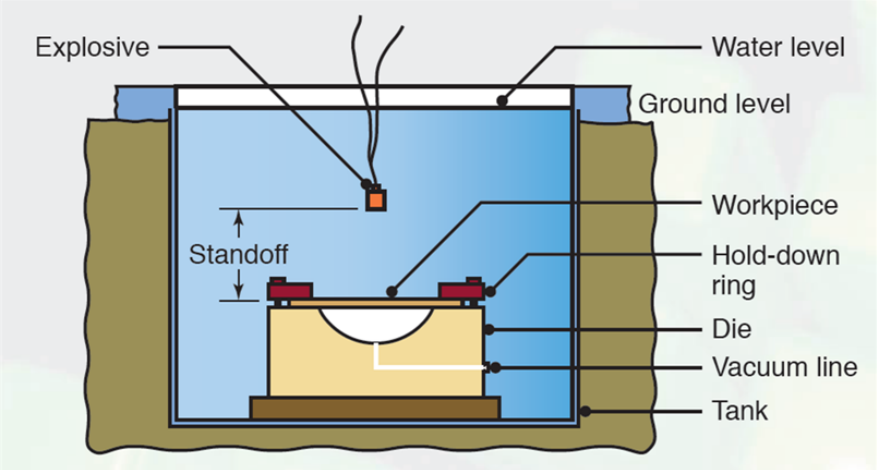

Figure 2.4: Schematic of explosive forming [4]

2.2.1 Advantages and limitations

A major advantage with forming at high strain rates is the elimination of springback effect, which is a common issue with the quasi-static forming processes. Springback of formed components will be reduced when the sheets impact the rigid die at high velocities, due to the relaxation of elastic strains as a result of propagation of plastic waves through the sheet thickness [76]. The mechanisms occurring at the micro and atomic levels during plastic deformation are detailed in the latter part of this chapter. The other benefits of high strain rate forming are summarized below [57, 72, 76–78]:

- Improved formability and ability to make intricate and fine features.
- Suitable for forming large components, resulting in cost reduction.
- High-strength materials that are difficult to be processed by quasi-static processes can be formed.
- Reduction of sample wrinkling due to momentum of sheets during forming.
- High accuracy of the formed features.
- Restriction to imperfections growth due to the inertia.
- Improved strength after forming.
- Reduced cycle time and higher productivity.

- Increase in fatigue strength.

However, there are limitations with extremely high velocity, as it will induce dimensional inaccuracies due to the rebouncing off the parts [76]. Especially, the sudden deceleration of material upon impact with dies causes inadvertent elastic recovery affecting the final component geometry [57].

2.3 Laser-induced plastic deformation

The application of laser system as the energy source in high energy-rate process has been a major breakthrough in both high strain rate forming and laser material processing fields. Laser systems have been extensively used for various applications over the past decades. In terms of forming processes, laser induced shockwaves act as the main driving force in material deformation. Laser induced shock waves serve to cater applications such as fatigue behavior improvement, bending, and plastic deformation of metallic materials.

The mechanism of laser-induced shockwave formation is identical irrespective of the intended application of the shockwaves. An introduction of the mechanism is given as follows: The target material is coated with a sacrificial coating. A high-power laser beam is irradiated on the coating, which is vaporized instantaneously into high-pressure plasma. The expansion of plasma induces shockwaves towards the target, which undergoes deformation once the yield limit of the target material is reached. The plasma expansion is restricted by a confinement medium, increasing the shock pressure magnitude and duration. Depending upon the thickness and backing support of the target, the processes using laser-induced shock waves can be categorized generally into laser shock peening or laser shock forming. If the material is bulk and the plastic deformation of few layers of the surface is experienced, the process is called as laser shock processing or laser shock peening or laser peening. Meanwhile, if the material is a sheet or a foil having small thickness, it is termed as laser shock forming, where the shockwave propagates through the sample thickness

and the plastic deformation of an entire thickness is observed similar to conventional sheet metal forming processes like deep drawing or bending. To deform the sheet metal into a required shape and size, the sample is placed over a die pattern such that the die cavity is covered by the sample. Laser-induced shock processes will be discussed in detail in the following sections.

2.3.1 Laser shock processing

Laser shock processing/ laser shock peening (LSP) of sheet metals is a well-established process using laser induced shock pressure in manufacturing industry, for fatigue strength improvement of components (eg: aerospace components). Laser shock peening is a technique to induce compressive residual stress distributions in the bulk metal surface as illustrated in Fig. 2.5. With the emergence of MEMS field, LSP has been used in microcomponents to improve the fatigue and wear resistance of components. Zhang et al. [79] used 90 μm thick copper foils for laser shock processing where the compressive residual stresses were induced up to 70 μm into the foil. Furthermore, Zhang et al. [80] achieved an improvement in compressive residual stress on 1 to 3 µm thin copper films through microscale laser shock peening.

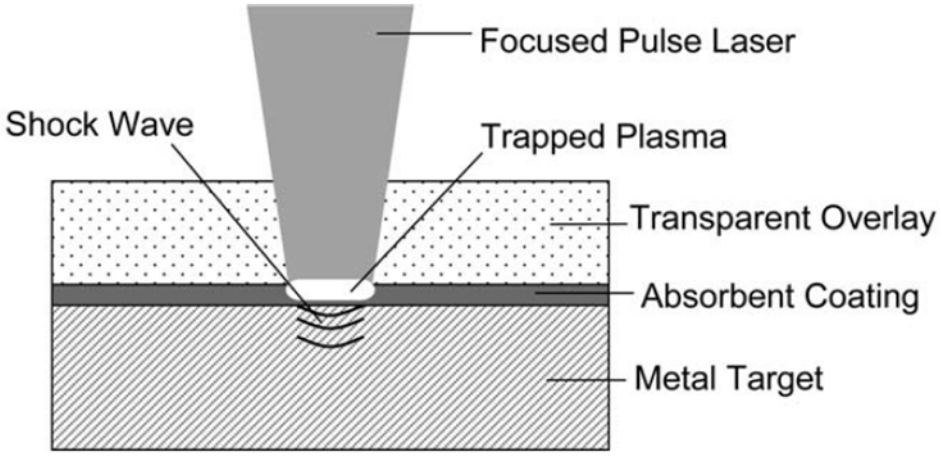

Figure 2.5: Schematic of laser shock peening process [81]

The deformation of metal targets upon laser shock loading is a result of two

subsequent different modes of deformation, elastic or early deformation mode and late or large deformation mode, which depend upon the laser energy, confinement, and the specimen thickness [82]. Fig. 2.6a illustrates the propagation of various elastic waves, dilatational wave, shear wave, von Schmidt wave, and Rayleigh wave into the target thickness upon uniform loading conditions. It can be observed that the reflected dilatational wave causes elastic deformation of rear surface along its propagation direction. The region envelops the shear waves possess highest distortional energy, causing the onset of yielding from this region. Fig. 2.6b illustrates the late deformation mode in pure-plastic (top) and elastic-plastic (bottom) conditions. Dilatational plastic wave propagates first and causes change in volume. This dilatational wave is then coupled to the transverse plastic wave, causing a change in shape. In elastic-plastic conditions, both the dilatational and transverse plastic waves have corresponding elastic counterparts.

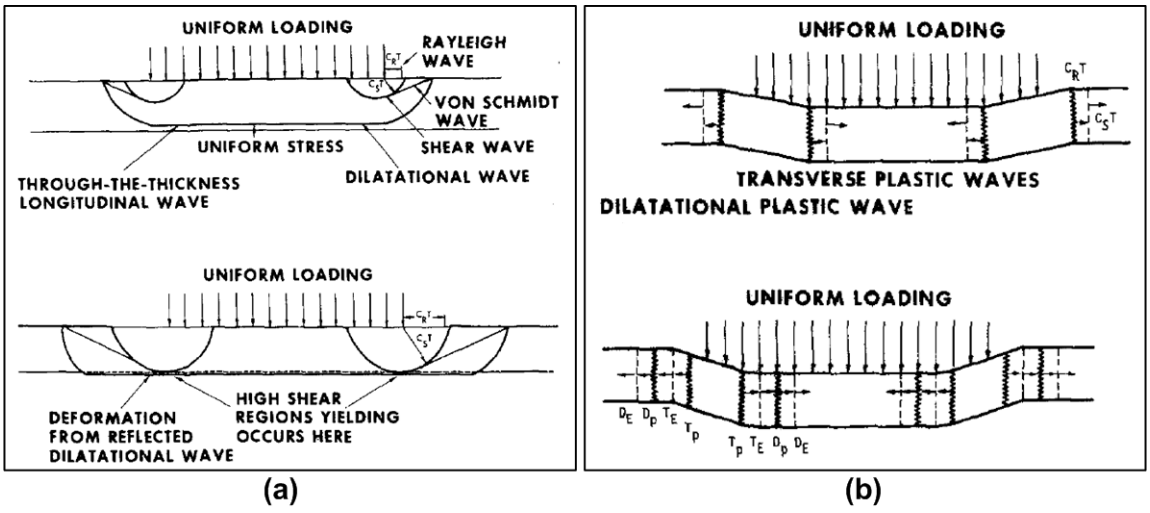

Figure 2.6: Deformation modes in thin material (a) Elastic wave propagation (b) Plastic wave propagation [82]

2.3.2 Laser-induced shock pressure forming

The technology of laser shock wave is used not only for surface modification or strength enhancement but also for creating 3D shapes. Forming of 3D micro components using laser-induced shock waves has attracted attention in recent times due to its microscale precision, localized laser beam control, repeatability, flexibil-

ity, and compatibility with a variety of materials. This section reviews the sheet metal forming efforts using laser-induced shockwaves as the loading source.

Zhou et al. [59] first implemented the laser-induced shock wave in sheet metal forming to create 3D features. The mechanism of laser shock forming is similar to laser shock peening except that the bulk target material is replaced with a thin metal sheet and is supported by an open die. The schematic of laser shock forming process is shown in Fig. 2.7. A high strain rate (10^7 –$10^9 s^{-1}$) forming process using laser shock waves was demonstrated for 0.3 – 0.9 mm thick austenitic and ferritic stainless steel sheets by the same research group [83, 84]. A high power Nd:YAG laser with 8 to 30 J pulse energy was used to deform the sample which contained black paint as the sacrificial layer. In addition to plastic deformation, laser shock forming introduces strain hardening and compressive residual stresses on both surfaces of the deformed samples, resulting in an obvious improvement in fatigue and corrosion resistance [83].

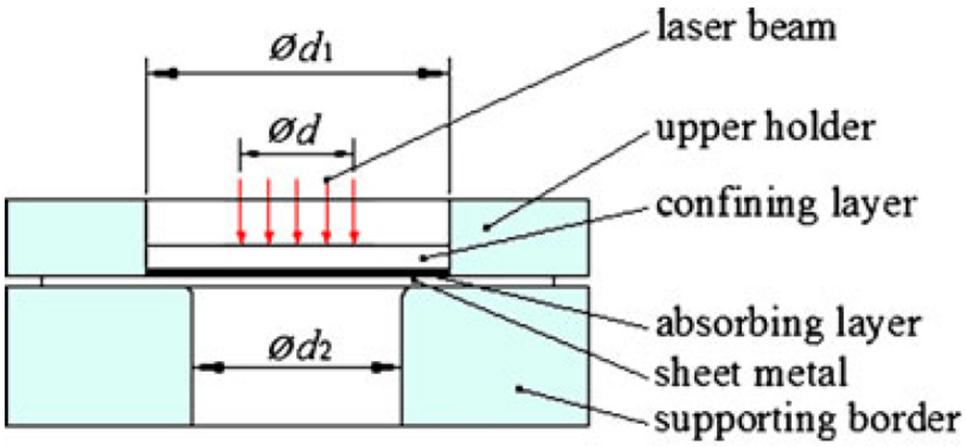

Figure 2.7: Schematic of Laser Shock Forming [85]

Niehoff and Vollertsen [86] demonstrated similar forming processes, laser deep drawing and laser stretch forming, to obtain plastic deformation of metal sheets. The difference with laser deep drawing compared to LSF is that, no sacrificial coating is used for plasma formation in this process. The laser is irradiated directly on the metal sheet surface and ablation of few layers on the irradiation side is vaporized into plasma. Initially, aluminum sheets of 50 μm were formed into domes

with 1.4 mm diameter and height up to 250 μm, as seen in Fig. 2.9a [86]. Later, the process was used to form copper, aluminum and stainless steel sheets of 20 μm thickness into a spherical cup of 1 mm depth using a TEA-CO_2 laser [87]. Higher ductility of copper resulted in lower strain rate, crack initiation delay, and 1.5 times smaller cup than aluminum for the same process parameters. In addition, for similar processing conditions, aluminum foils experienced deep drawing whereas copper and stainless steel samples experienced stretch forming. This behavior can be attributed to their difference in mechanical properties. For 50 μm thick stainless steel, irradiated surface was damaged with no deformation even at 700 pulses, due to higher yield strength of the material. Undercut features were also produced using this technique, in which the die diameter had an influential role [88].

Gary et al. [89] broadened the application of laser shock forming with their technique, Laser Dynamic Forming (LDF), by employing mold cavity behind the metal sheets instead of open dies in laser shock forming and laser deep drawing. The schematic of LDF is presented in Fig. 2.8a. Deformation of metallic foils into a micromold of size ranging from 10 to 250 μm has been observed where the microfeatures conformed to the mold size [89]. Different feature sizes and shapes can be fabricated by employing the corresponding die patterns [90, 91]. During LDF, material is subjected initially to bending and shearing, followed by stretching and necking. Maximum von Mises stress in the foil was observed around the periphery of mold cavity as the flow of material was confined at the edges. When the material collides with the bottom of the mold, it undergoes hardening and the transient strain rate is greater than 1 x $10^6 s^{-1}$ [90]. After LDF, a significant increase in high dislocation density regions, grain size uniformity, and subgrain structures were observed, resulting in an improved mechanical properties [89]. An example of features produced by LDF, micro square array patterns is shown in Fig. 2.9b. LDF can be used to realize the fabrication of micro and nano scale features on brittle and ductile metallic materials, functional materials with elastomeric layers, and graphene films [90, 92–94].

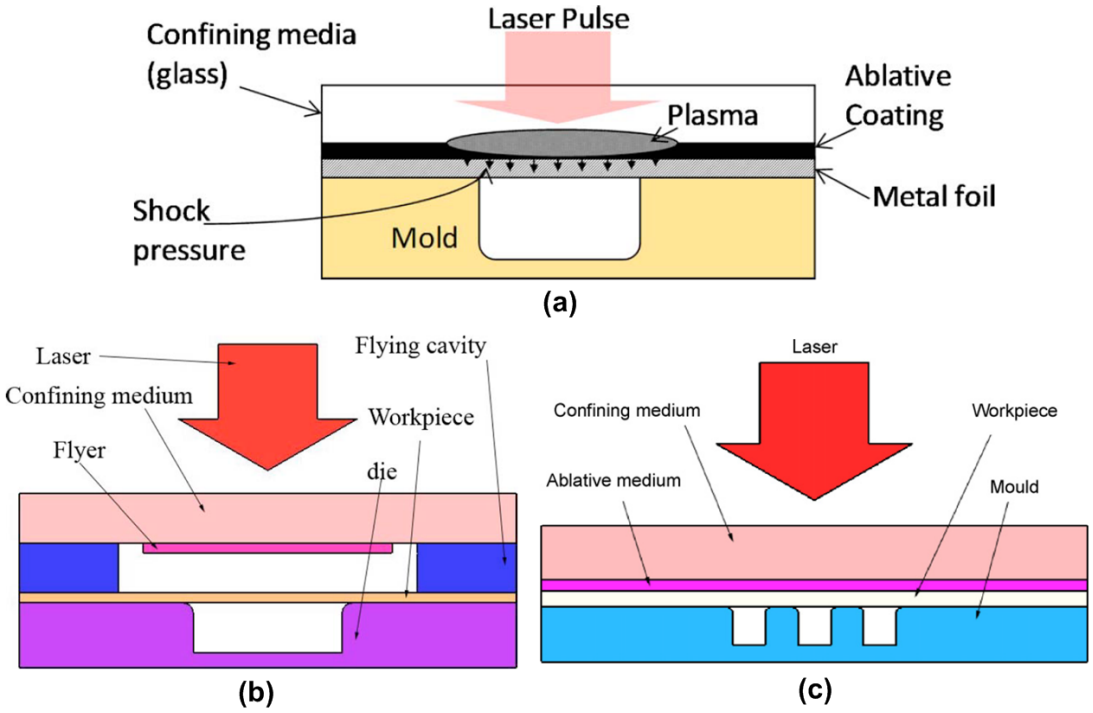

Figure 2.8: Schematic of (a) Laser dynamic forming [91](b) Laser shock forming using flyer system [95] (c) Laser shock embossing [96]

Zhou et al. [97] implemented a novel flyer system over the laser shock forming process. In the new development as illustrated in Fig. 2.8b, a laser driven flyer has been used to impact the sample with high acceleration due to the ultrahigh pressure developed by the thermodynamic irradiation of the laser pulse on the flyer surface. Submicron features (~1 μm) were replicated on a 15 μm thick aluminum foil using a micromold. Simulation results revealed that the deformation velocity of the workpiece increased as a result of the impacted flyer [95]. high laser powers could lead to the damage of sample and mold, which will prevent the mold from further utilization. Though a sharp-edged micromold was used, the process could not replicate the sharp edges as identified from Fig. 2.9c. Another limitation with the flyer system is the difficulty in maintaining a close contact between the flyer and the confinement. Another technique, laser shock embossing [2.8c], which is similar to laser dynamic forming, was developed by Liu et al. [96] to form micro channels of 260 μm x 59 μm and complex 3D microstructures on 10 μm thick copper foils using a micromold, as seen in Fig. 2.9d. Deformation features with high spatial

resolution and non-thermal loading are characteristics of this technique.

There exists another category of laser-induced shock process, Laser Peen Forming

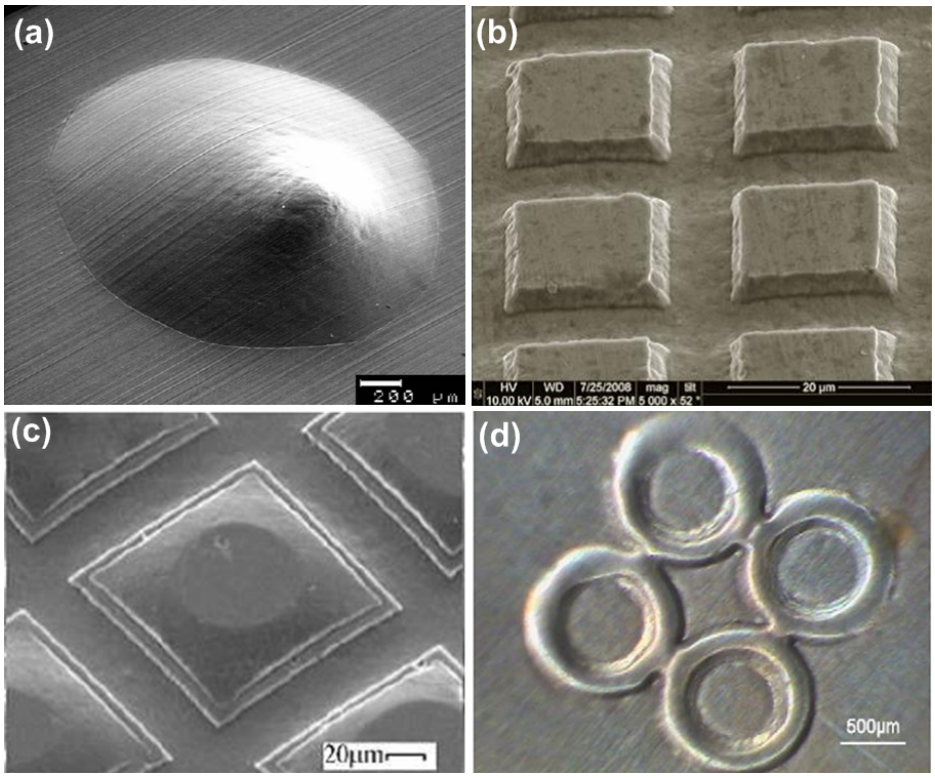

Figure 2.9: Microfeatures produced by various processes (a) Laser deep drawing [86] (b) Laser dynamic forming [91] (c) Laser-driven flyer system [97] (d) Laser shock embossing [96]

(LPF), an athermal process, in which the moment induced by the residual stress acts as the deformation force. The process has similar components such as an absorptive layer and confinement layer, shown in Fig. 2.10 as energy transforming medium. The distribution of the stress field on both surfaces of the metal sheet upon ablation of few layers with laser irradiation induces a bending moment that deforms the metal, as illustrated by Ocana et al. [98] in Fig. 2.11. Bending angle up to 20° was achieved progressively on 75 μm thick steel sheets without a confinement upon irradiation of the graphite overlay using Nd:YAG laser with energy densities ranging from 4.8 - 6.5 GW/cm^2 [99]. An increase in bending angle was observed with an increase in laser wavelength and number of passes initially and saturates later due to the absence of coating and the strain hardening effect [100]. Compared to the laser forming, LPF is a non-thermal process as it causes

no heat affected zones and no metallurgical changes after the process. This process requires lesser laser pulse energy compared to that of LSF as there is no plastic deformation of the entire thickness but only few irradiated surface layers.

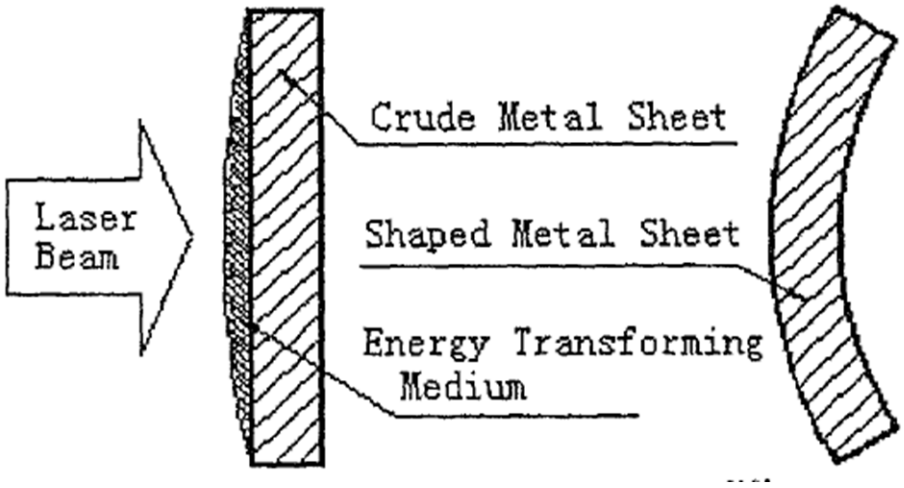

Figure 2.10: Schematic Laser Peen Forming mechanism [101]

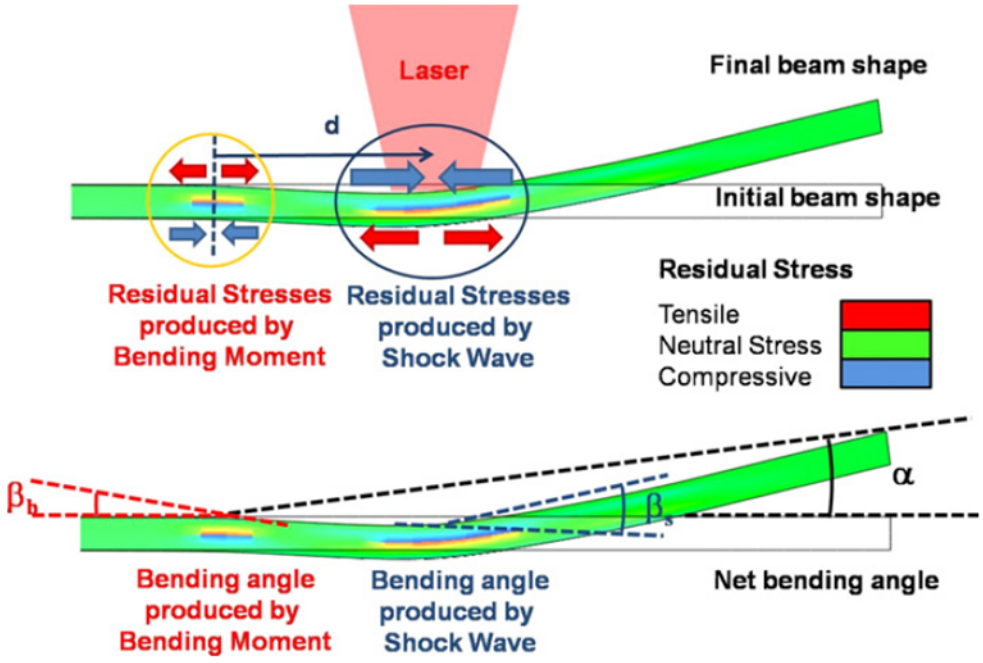

Figure 2.11: Bending of sheets by laser forming [98]

Laser peen forming can be used for shape and position adjustments of micro-components made of temperature sensitive materials. Another application of laser shock processing is precise metal shape-righting, e.g. the correction of the curvature

of sheet metals. When the stress of upper surface is larger than that of bottom surface there will be convex deformation, otherwise it will be concave [102]. However, LPF is limited by its inability to produce complex features.

A flexible forming process to produce shallow 3D features (2.5 mm deformation depth) on Al alloy sheets (700 μm thick) using laser shock energy was reported by Zhang et al. [103]. Laser shots are overlapped to produce the structures as shown in Fig. 2.12. This process follows two sequential steps to achieve the required feature shape: a) Rough forming, during which total forming with depth equivalent to h-ΔZ is realized, b) Fine forming, during which the laser head shocks on the protruding area step by step along the vertical axis. The distance moved by the laser head (ΔZ) is found to control the deformation depth. However, no information on the backing support for the sheets was provided. Without any support, this process may not be suitable for thinner foils as it may induce wrinkling of foils.

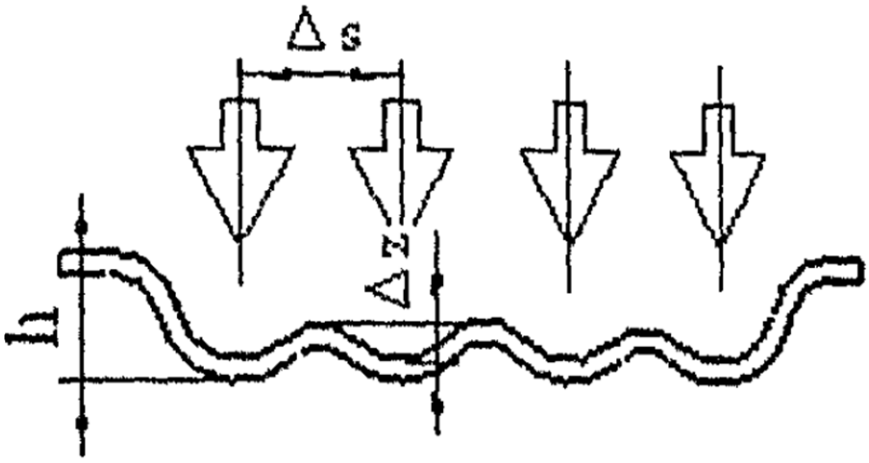

Figure 2.12: Flexible laser shock forming with overlapped laser shots [103]

2.3.3 Advantages and limitations of existing processes using laser-induced shock pressure

The laser-induced processes possess almost all the benefits of high strain rate processes as mentioned in section 2.2.1. In addition, with lasers being precise, fast,

controllable, and repeatable, the process flexibility and cycle time are greatly improved. Also, micro and nanoscale deformation are easily controllable with lasers which are difficult with conventional high strain rate processes.

Comparing all sheet metal forming processes that works based on the principle of laser-induced shock pressure including laser shock forming, laser dynamic forming, laser shock embossing, laser deep drawing, and laser shock forming using laser-driven flyer system, the following common limitations are observed:

- Using laser shock wave as the deformation force, only one of the rigid tooling is replaced in comparison to conventional forming processes as the microfeatures are replicated from the die pattens. The presence of rigid dies involves a vast range of problems as detailed earlier in chapter 1 include primarily the fabrication of microdie patterns, large process cycle time, surface integrity, and tool wear. Though the friction between the sample and punch is eliminated by the non-contact shock force, the friction is still present in the system due to the interaction between the die surfaces and material, which could influence the quality of formed features, die wear, and the process modeling. In addition, the process flexibility is significantly affected which will restrict the process to be deployed in mass customization environment where a frequent change in product features is required.
- When the feature size becomes much smaller, the alignment of microdies and laser spot is increasingly difficult. It also adversely affects the process cycle time.
- There is a possibility of damage to the die patterns and feature surface at higher laser powers.

The motivation to create a new flexible forming process without die patterns using laser-induced shock energy has been complemented by the aforementioned limitations. So, it is imperative to develop a process to produce reliable microfeatures on metallic surfaces using laser shock pressure as a forming tool.

2.4 Laser material processing

For better understanding of the laser shock forming process and its parameters, the process is classified based on different mechanisms involved.

2.4.1 Absorption

The processing of materials using laser beam depends upon various process variables, which can be broadly classified into laser-based and target material-based parameters, as illustrated in Fig. 2.13 [104]. Upon contact with the opaque surface, the consumption of laser beam energy is split into absorption, reflection, and transmission. Especially, absorption of laser beam by the target is influenced by the following factors [105]: material properties, surface roughness, oxide formation, laser beam properties such as the pulse energy, pulse duration, and the beam wavelength, etc. During the irradiation, absorption of only a small layer of surface occurs, which is called as the skin depth or characteristic penetration depth. Skin depth is the thickness of the target up to which the electromagnetic radiation penetrates with a reduction in intensity of the light by a factor of e from its initial value [105]. Skin depth is defined as,

$$\delta' = W = \frac{1}{\pi \sigma_e \mu_m \nu} \tag{2.1}$$

where, σ_e is the electrical conductivity (s/m), μ_m the magnetic permeability (H/m), and ν the frequency (Hz). The penetration depth can also be defined as $W = C/2\nu n$ where $C = 3$ x 10^8 m/s and n the refractive index [106].

At constant wavelength, the absorption increases with an increase in temperature. If the roughness of the target surface increases, the reflectivity will be reduced and there will be more diffusion. Though the materials have high reflectivity initially, it will reduce after the laser irradiation starts which is due to the better coupling with the material [107].

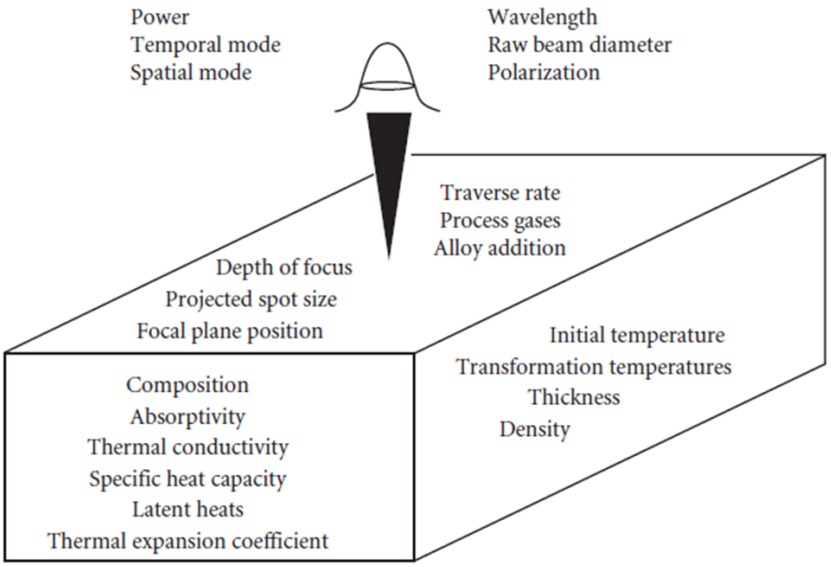

Figure 2.13: Laser Material Processing - process parameters [104]

2.4.2 Heating, melting and vaporization

The resultant process on the target due to laser irradiation depends on the induced temperature at the target surface. If the temperature is less than the melting temperature, only heating of the surface will occur. If the temperature is between the melting point and boiling point, melting of the target surface will happen. The melt depth increases with an increase in laser intensity and pulse duration [108]. At shorter pulses (femto and picosecond), there is no time for the conduction of heat into the target, which is useful for precise machining.

Vaporization of the surface occurs if the temperature reaches the boiling point. The vaporization depth depends upon the power density, pulse duration and material parameters. The vapor formed at the surface induces the recoil pressure on the target surface, which plays a significant role in material removal from the irradiation region [108]. At high intensity and the interaction time (pulse duration), vaporization occurs only when a small amount of material has melted. If the laser intensity is less than 1 GW/cm^2, thermal properties of the absorbent material affects the peak pressure [109]. Usually, temperatures up to 10000°F are generated when the high power laser beam hits the target, causing instant vaporization of material with laser irradiation [110].

2.4.3 Plasma formation

Interaction of laser beam with the vapor results in an ionization of vapor, inducing plasma. The formation of plasma depends on the intensity of the laser beam as explained below [111]:

- At low intensity, laser beam penetrates the vapor that acts like a thin medium, created by the leading edge of the beam, without losing its energy. The laser beam hits the target, and subsequently conducts the heat, melts and vaporizes the material.
- At high intensity, the temperature of the formed vapor is higher which induces excitation of atoms and hence ionization. The laser energy is absorbed by the vapor causing vapor breakdown and plasma formation due to avalanche ionization and multiphoton ionization mechanisms.

The intensity (I_p) at which the plasma ignition occurs for pulse width (τ) ranging between $10^{-8} < \tau < 10^{-3}$ s is given by the following relation [112, 113] :

$$I_p \tau^{1/2} \approx B_P \tag{2.2}$$

where B_P is a .

A thin melt layer is produced when the high temperature plasma contacts the target surface [110]. Compared to plasma layer thickness, the thickness of melting layer, Knudsen layer, and the transition layer between vapor and plasma can be neglected.

2.4.4 Plasma-Laser interaction

During interaction with infrared wavelengths, the plasma plume absorbs laser energy through the inverse bremsstrahlung process [106]. Two different waves, laser-supported absorption wave and laser-supported combustion wave, occurs depending upon the irradiance of the laser beam.

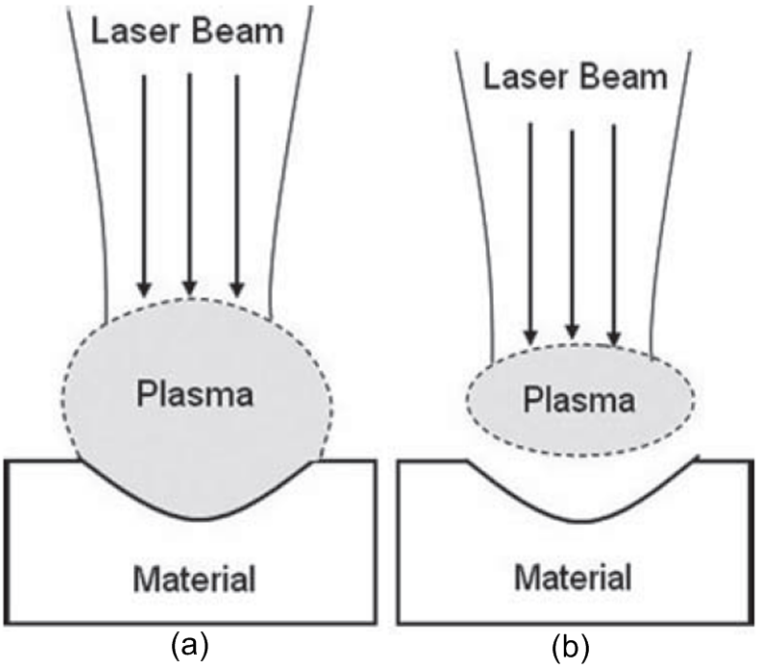

Figure 2.14: Plasma - laser interaction effects [108] (a) Plasma coupling (b) Plasma shielding

The formed plasma remains close to the target surface if the laser intensity (I_p) is just above the limit that causes the plasma formation. This behavior is called as plasma coupling as shown in Fig. 2.14a, due to which the absorption of laser beam by the material increases [108].

When the laser beam passes through the plasma plume, a minor reduction in the laser intensity at the focus is expected due to the defocussing of laser beam by the plume [114]. When the laser passes through the plasma, plasma oscillation affects the propagation of plasma [105]. The plasma electron oscillation frequency (W_e) is defined as, $W_e^2 = n_e\ e_c^2\ /\ \mu_m m_e$, where, n_e is the electron number density (m^{-3}), m_e the electron mass (kg), and e_c the electron charge (C).

If the plasma oscillation frequency is less than the beam frequency, the propagation of laser beam through the plasma occurs. Else, the beam will be reflected back. In case of similar plasma oscillation frequency and beam frequency, there will be resonant absorption of the beam. It is noted that the dense ionized plasma formed at the interface between the confinement and the target reflects back a substantial amount of incident laser light [109]. This behavior will reduce the peak shock

pressure at higher laser intensities along with the dielectric breakdown behavior.

2.4.5 Plasma expansion

Dynamic interaction between laser beam and plasma at the surface for intensities much greater than the intensity threshold for plasma formation causes the expansion and propagation of plasma. The pressure difference between the hot plasma region and the surrounding region causes the plasma to expand [115].

The shape of the plasma plume was observed to be perfectly hemispherical as shown in Fig. 2.15 during its expansion in the atmospheric pressure, in an experiment by Barthelemy et al. [116]. The plume expands with time in both the radial and longitudinal directions. The plasma plume created during ablation of metals by 1064 nm wavelength laser beam at atmospheric pressure is classified into two different regions: plume core and plume periphery, which are identified as the ionized ablation matter and the ionized atmospheric air respectively, as illustrated in Fig. 2.15 [106]. Cirisan et al. [106] identified several processing variables including laser intensity, spatial and temporal profiles of the beam, beam diameter, and ablation environment, to be influential to plasma plume characteristics.

At much higher intensity, plasma expands rapidly and starts moving away from the target surface. Then, there will be no transfer of energy from the plasma to the dense phase. This effect, plasma shielding, is illustrated in Fig. 2.14b [108]. Plasma expansion is adiabatic, occurs at a supersonic velocity, which hence creates shockwaves preceding the plasma [117].

2.4.6 Plasma and shockwave characterization

In laser-ablation processes and laser-induced shock processes, it is necessary to understand the formation and propagation of plasma to study the process mechanisms. Plasma can be characterized by both quantitative and qualitative methods.

Visual observation of plasma/plume in laser-material interaction has been achieved by different methods in the literature: dye laser resonance absorption photography

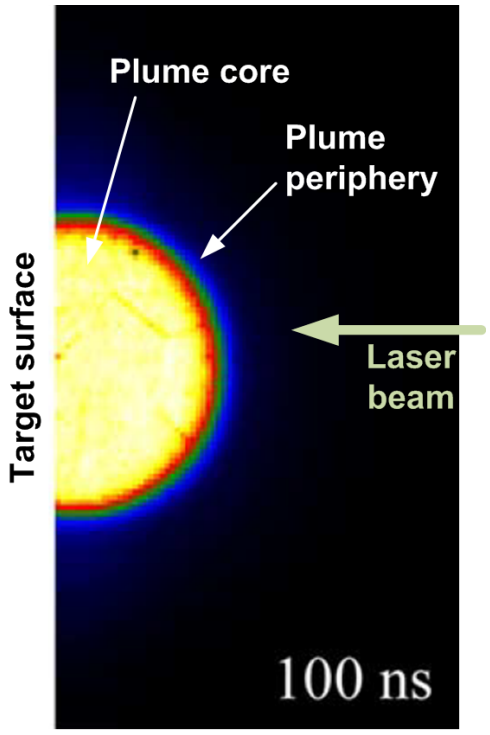

Figure 2.15: Plasma plume during the expansion (aluminum target irradiated by 10 J/cm^2 laser fluence) [116]

[118, 119], time-integrated photography, shadowgraphy [120, 121], speckle photography [122], frame and streak photography [123], and high-speed photography [111, 124, 125] . Fast schlieren photographs are captured using an ICCD (Intensified charged coupled device) camera [126, 127]. Franco et al. [128] used Streak photography technique to study the spatial and temporal evolution of laser-induced plasma by measuring the plasma absorption, initiation time, lifetime, and axial column length of the plasma. The shock wave propagation speed within first 400 ns was measured to be 4000 m/s using images from 20 x 10^6 frames/sec high speed camera. Barthelemy et al. [116] used Fast photography by an ICCD camera to analyze the expansion of plasma produced by the excimer laser ablation of aluminum target in ambient conditions. The similar characterization method was adopted to examine the change in length and diameter of the plume core and plume periphery regions with time at different laser fluences [106]. Seto et al. [124] used two ultrahigh speed cameras (1125fps) to analyze the plasma shape and the keyhole formation in laser welding. A CCD camera was used by Yilbas et al. [129]

to investigate the laser material interaction in laser shock processing by which the formation and expansion of the evaporation front were captured. Chen et al. [117] used an optical beam deflection based fiber-optic sensor to investigate the laser-induced shockwave propagating inside the water . In comparison, high-speed photography is found to be an effective method to visualize and characterize the plasma to study its evolution with time [124, 125].

Typical quantitative characterization parameters include plasma plume size, plume edge position, plume velocity, and the plasma lifetime [111, 130]. In most cases, the geometry of the plasma has been characterized to understand the plasma evolution behavior. The velocity of the plume and shockwave are also used to characterize the plasma expansion. Plume velocity is calculated from the position of the shockwave edge and the corresponding time. Gilgenbach et al. [118] characterized plume velocity by plotting the plume edge position against the delay time between the dye laser pulse and the excimer laser pulse using dye laser resonance absorption photography. Laser drilling of stainless steel with He:Ne laser was examined by Nowakowski [131] using a high speed camera with a frame rate of 18000 frames/sec to calculate the velocity of the ejected particles.

Cirisan et al. [106] defined the plasma expansion using shockwave and drag models. The shockwave model is based on the assumption that the plasma plume and the shockwave induced by the plume due to the differential pressure with ambient medium are propagating with identical speeds. The plume expansion corresponding to the shockfront distance (R) as a function of time (t) is given as [130],

$$R = \xi_0 \left(\frac{E}{\rho_0}\right)^{0.2} t^{2/5} \tag{2.3}$$

where E is the laser energy, ρ_0 the ambient gas density, and ξ_0 the constant based on specific heat of ambient gas.

The decaying of plasma plume due to the drag resistance provided by the ambient medium is modeled using the drag model. The plume position (R) is defined

by,

$$R = R_{max}[1 - exp(-\beta t)] \tag{2.4}$$

where R_{max} is the plume stopping distance and β the slowing coefficient.

There are three models dedicated to explain the expansion of plasma towards the laser beam [128]: (a) Ionization wave model (b) Radiation-supported detonation wave model (c) moving breakdown model.

2.5 Plastic deformation of metal foils

In macroscopic scale, plastic deformation is the permanent, irreversible change in the material upon loading. When the metal is subjected to a tensile load, it undergoes reversible, elastic deformation initially where the stress is proportional to the strain. Once the applied stress reaches the yield strength of the metal, the plastic deformation is initiated. During this stage, a uniform elongation of the material occurs. Plastic deformation stage is defined from the initiation of yield to the end of uniform elongation, before the localized necking stage starts. The corresponding behaviors at microscopic or atomic scales for the macroscopic properties discussed previously need to be studied in order to understand the process mechanisms.

2.5.1 Deformation modes

Elastic deformation of metals is caused by the stretching or compression of the interatomic bonds, causing a temporary change in the interatomic spacing [132]. Whereas, the plastic deformation of metals is realized generally by the movement of dislocations, which are the inherent imperfections present in the crystalline materials. In metal forming processes, the plastic deformation and the inducing mechanisms depend upon various factors. The modes of plastic deformation include slip, twinning, diffusion creep, grain boundary sliding, shear band formation, and phase transformation [133]. The difference between these modes is illustrated in Table.

2.1.

- Slip - It is the motion of dislocations due to which the plastic deformation is realized. Slip occurs on the most densely packed crystallographic planes and along the directions having the greatest atomic packing in those planes. Dislocations moving along a particular slip plane in a grain cannot go directly into another grain in a straight line. Slip lines change their directions at grain boundaries. Dislocations carry a stress field, either compressive, tensile, or shear based upon the position of dislocations in the crystal lattice. Slip occurs due to the interaction of dislocations having identical stress fields, which will cause a repulsion, inducing the plastic deformation (more stress needed to move dislocations). This interaction dislocations with similar stress fields leads to dislocation multiplication which causes an increased interaction and work hardening. Dislocations are characterized by dislocation density, which is defined as the total dislocation length per unit volume, varying from $10^3 mm^{-2}$ to $10^{12} mm^{-2}$ depending upon the intensity of deformation. Due to the plastic deformation, an increase in dislocation density is observed.

- Twinning - Deformation twinning is a homogenous shear of the lattice plane where atoms displace along the twinning direction. The twin structure forms the mirror image of parent structure along the twinning plane. Twinning occurs generally with large shear loading, low stacking-fault, and low temperatures. Mechanical twinning occurs in metals that have HCP and BCC structures, on specific twinning planes and directions. Twinning occurs at low temperatures and at high rates of loading conditions where the slip is restricted. It causes reorientation of crystallographic slip systems, thereby generating new slip systems. This behavior tends to promote the movement of dislocations. Typically, there exists a threshold pressure to obtain twinning. Twinning usually occurs at higher strain rates ($\dot{\varepsilon} > 10^5$ s^{-1}) due to the following reasons [134]:

  (a) When the deformation speeds are high, dislocations do not have enough

time to respond and hence the slip is suppressed.

(b) At higher strain rates, the stress increases locally to reach the critical twinning stress, a condition favorable for twinning.

- Shear band formation - It is a limited non-homogenous deformation which occurs especially under high strain rates inducing large localized strain levels.

Slip and twinning deformation modes usually occurs at the quasi-static loading conditions. Grain boundary sliding, dislocation glide, dislocation creep, and diffusion creep are proportional to loading conditions and temperature, and occur during warm forming, where the deformation is at elevated temperatures [135]. Fatigue loading usually causes the formation of dislocation cell structures. The difference between the deformation modes is illustrated in Table. 2.1.

Table 2.1: Comparison between different deformation mechanisms

Slip	**Twinning**	**Shear band formation**
Homogenous deformation	Localized deformation	Limited non-homogenous deformation
Occurs under static loading	Occurs under shock loading, where slip is restricted	Occurs at high strain rates
More prominent with FCC structure	More prominent with HCP and BCC	
	It makes crystallographic reorientation thus creating new slip systems	

2.5.2 Formability and deformation mechanisms

The main objective of forming processes is to increase the formability of the material by extending the uniform elongation and delaying the onset of necking. The process formability depends upon various factors/mechanisms including strain hardening, strain rate sensitivity, temperature, thermal softening, dislocation density, grain

size, substructures, and inertia effects. Generally, increase in flow stress is experienced with increase in strain rate and reduction in temperature. The strain rate sensitivity increases sharply for strain rates greater than $10^4\ s^{-1}$ due to the change in dislocation formation rate [136]. Smaller grain diameter causes an increase in flow stress according to Hall-Petch equation [133]. Two significant mechanisms occur during the plastic deformation, strain/work hardening and adiabatic/thermal softening have an influence in the formability.

2.5.2.1 Strain hardening

Strain hardening or work hardening is the behavior in which the flow stress increases with increase in strain. The mechanism behind this behavior is the movement of dislocations during the plastic deformation resulting in entanglement and multiplication of dislocations. This will restrict the further movement of dislocations and hence the flow stress increases. The work-hardened material will have an increase in yield strength along with the reduction in ductility. Strain hardening typically increases the dislocation density and creates low-angle subgrain boundaries.

2.5.2.2 Adiabatic Softening

Adiabatic/work/thermal softening occurs at high temperature and high strain rates. When the metal is deformed during the quasi-static loading conditions, the heat generated due to the deformation will dissipate. However, at high-strain rates, there is insufficient time for the generated heat to dissipate. Due to this, localized adiabatic heating of few narrow regions (adiabatic shear bands) will occur followed by either dynamic recrystallization or dynamic recovery of grains. High temperatures results in the annihilation and realignment of dislocations. This behavior is called as "Adiabatic softening".

The softening effect at high strain rates is interrelated with the amount of plastic strain the material experiences during forming. At low strains ($\varepsilon\sim$ 0 to 0.5), the temperature effects are confined to the diffusion of dislocations. Whereas, at high

strains ($\varepsilon\sim$ 3 to 4), the mechanism behind the strain softening is found out to be the combination of migration and rotation behaviors of dynamic recrystallization as illustrated in Fig. 2.16 [136]. Migration recrystallization occurs by the nucleation and growth of new strain-free grains when the critical strain is reached. Rotation recrystallization alters the boundaries of cells into sub-grains and then grains by increasing the misorientation. Upon shock loading, rotation recrystallization occurs first with the gradual breakdown of initial grain structure (Fig. 2.16a) into elongated subgrains (Fig. 2.16b and Fig. 2.16c), which further break into small recrystallized grains (Fig. 2.16d). The obtained microstructure is then subjected to migration recrystallization.

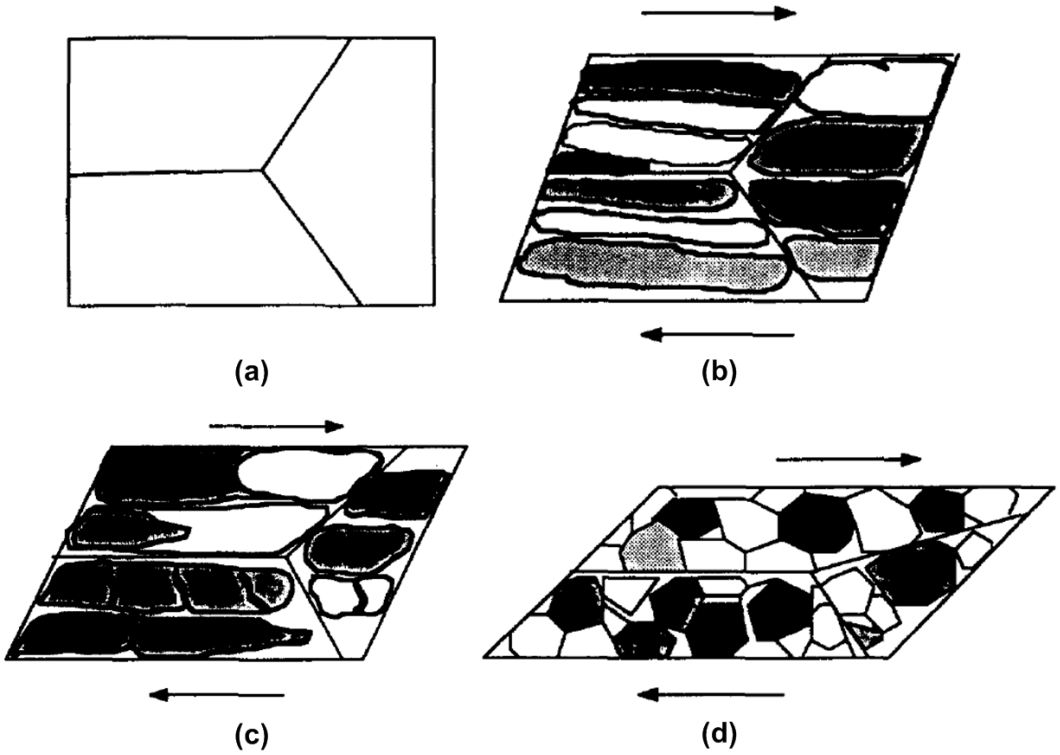

Figure 2.16: Dynamic recrystallization of shock-loaded copper [136] (a) Initial cell structure (b) Elongation of subgrains and cells (c) Breakdown of cells (d) Small recrystallized grains

The formability of the material increases due to the adiabatic softening behavior as there is a reduction in flow stress during the deformation. If the reduction in flow stress due to softening is greater than the increase in flow stress due to the strain hardening, then the localization of shear bands will take place [135]. Restriction

of dislocations on a slip plane by obstacles will induce excessive strain and hence Adiabatic Shear Bands (ASB) [137]. The formation and propagation of adiabatic shear bands are attributed to the following mechanisms:

- Elongation and fragmentation of grains.
- Alternative hardening and softening.
- Dynamic recovery of grains – Realignment and annihilation of dislocations at elevated temperatures during the deformation, causing a reduction in dislocation density.
- Dynamic recrystallization of grains – Large misorientations causes high angle grain boundaries which leads to grain nucleation.
- Phase transformation.

For torsion of pure copper at high strain rates ($\dot{\varepsilon} > 10^3$ s^{-1}), grain reorientation inside the shear bands and formation of equiaxed grains were observed by Yazdani et al. [137]. In case of pure copper, twin formation and stresses with the dislocation structures are observed to cause the adiabatic shear bands. These shear bands can act as a potential crack initiation zones [138]. Andrade et al. [136] observed during shock loading of copper that the shear localization area contained equiaxed grains where the adjacent region consisted of elongated cells, due to the change in strain between different regions. The typical temperature at the adiabatic shear region is predicted to be greater than $0.4*T_m$, an ideal condition for the recrystallization of most of the metals.

A comparison between the strain hardening and adiabatic softening is presented in Table 2.2.

2.5.3 High-strain rate plastic deformation

Metal forming at high strain rates has been reported in processes such as electromagnetic forming, explosive forming and laser shock processing, where adiabatic softening has been the dominant deformation mechanism. This section reviews

Table 2.2: Comparison between strain hardening and adiabatic softening

Strain hardening	**Adiabatic softening**
Dislocations in the grain displace during plastic deformation (slip). The moving dislocations tangle and impede the motion.	At high strain rates, there is no heat dissipation and localized plastic deformation within thin regions (adiabatic shear bands). Dispersion of dislocations during loading.
Increase in flow stress	Reduction in flow stress
Multiplication of dislocations	Diffusal of dislocations
Creates low-angle subgrain boundaries	Increase in subgrain structures
Reduction in formability	Increase in formability
Cold-worked material will experience: • Increase in yield strength • Increase in hardness, due to the dislocations tangle (high dislocation density)	Materials formed by high strain rate will experience: • Increase in hardness , due to subgrain formation and uniform grain sizes

the plastic deformation behavior induced by the laser shock wave in processes such as laser shock peening and laser shock forming. The observed phenomenon in macroscopic and microscopic scales is reviewed. Plastic deformation is usually characterized by different parameters: formability of the sheets, material thinning, change in hardness at the surfaces of the formed features, and the microstructural changes.

2.5.3.1 Formability

An increase in formability at high strain rates is a common phenomenon observed at most of the high velocity processes [57, 58, 72, 76–78, 91]. During shock loading of copper, Andrade et al. [136] found the mechanical twinning to cause an increase in flow stress. The twin boundaries restrict the movement of dislocations, enhancing the material strength. After laser dynamic forming (LDF), a significant increase in material formability was confirmed by the high dislocation density regions and subgrain structures of the formed metal foil [89]. This high dislocation density and

subgrain structures impede void nucleation and growth thereby leading to increased formability [91].

During the shock loading, the propagating shock front acts as dislocation nucleation zones when the shock pressure reaches the critical shear stress [58]. These dislocations move at subsonic speeds to smaller distances generating new dislocation interfaces. Formation of new dislocations tends to increase the formability.

2.5.3.2 Thickness distribution

Thickness distribution or thinning of formed components is one of the significant variables to define the formability in sheet metal forming. Non-uniform thickness distribution leads to irregular stress levels and localized necking, which will lead to the failure of the component. Uniform thickness distribution is crucial in the micro-manufacturing field when the assembly of different sheet components is required.

In quasi-static deep drawing, which is a major sheet metal forming process, high thinning occurs in the sidewalls and the region around the rigid punch radius due to the tensile stresses in both the longitudinal and circumferential directions [139]. Ramezani et al. [60] observed a reduction in maximum thinning from 17% to 11.3% while replacing the rigid metallic punch with a flexible rubber punch made of natural rubber. In this rubber-pad forming process, equal pressure was applied on the sheets by the rubber while pushing the metal into the die thereby minimizing the thinning. Though the maximum thinning ratio was reduced by using flexible punches, the thickness distribution was not uniform. In high strain rate laser dynamic forming, where a metallic die was used along with the laser shock loading, despite an improvement in formability, non-uniform thinning of up to 50% was observed with high plastic strains at the die fillets [89, 140]. This is attributed to an excessive localized necking at the die fillets when the material flow was constrained while being pushed into the die cavity. The friction between the rigid die surface and the deforming metal was also responsible for the variation in thickness distribution [45].

2.5.3.3 Inertia effects

Another significant factor influencing the formability of the material in high strain rate conditions has been the inertia effects. During tensile loading of material, a rapid velocity gradient occurs with the initiation of necking. The change of state induces nonuniform inertia forces, causing uniform elongation outside the neck region. Due to this effect, necking is delayed and uniform extension of material is enhanced. Thus, the inertia effects are found to improve the material formability. Balanethiram and Daehn [78] observed a 100% to 500% increase in ductility of IF iron, copper, and aluminum at high strain rates during electrohydraulic forming, in comparison to the lower strain rates. The velocity of the sample was found to influence the material formability significantly. An increase in ductility was experienced at the optimum velocity in tensile conditions, where the ductility had linear relationship with velocity in electromagnetic forming of ring [76]. Neugebauer et al. [57] showed that the formability of the material increases when forming the metal sheets at high strain-rates, due to the combined behavior of adiabatic softening and inertia effects.

2.5.3.4 Microstructure

The microstructure modification in the sample at high strain rates is different from that with quasi-static deformation. When copper is subjected to high strain rates ($\dot{\varepsilon} \sim 10^4$ s^{-1}) and high plastic strains (~ 3 to 4), grain sizes of about 0.1 µm was formed due to the dynamic recrystallization, as observed by Andrade et al. [136]. During shock loading, high temperatures are developed in the deforming region, causing dynamic recrystallization of grains. After laser dynamic forming of copper, Cheng et al. [89] observed a significant increase in high dislocation density regions, grain size uniformity, and subgrain structures. After microscale laser shock processing of copper, there was no significant change of average grain size, but a reduction of standard deviation was observed by Zhang and Lawrence [58], indicating an increase in uniformity of grains. Zhang et al. [58] also observed an increase in substructures and high deformation regions in laser shock processing of copper and nickel. During laser shock forming of stainless steel, no significant modification of grain boundaries both at the shocked surface and its rear side was observed by Luo et al. [141]. However, the microstructural change with grains was confirmed by the

observation of slip bands, stacking faults and compression of twins at the shocked surface. In laser shock peening, an increase in twinning and dislocation structures was observed by Murr [142].

Ye et al.[134] found significant differences in microstructures between specimens shocked with nanosecond (ns) and femtosecond (fs) laser pulses. The defining parameters between the laser systems have been strain level, strain rate, and pressure, the combination of which influences the deformation mechanism. From ns to fs laser conditions, the shock pressure increased from 0.65 GPa (ns) to 35.4 GPa (fs) and the strain rate increased from 1.8 x 10^6 $s^{-1}$to 1.4 x 10^8 s^{-1}. The surface processed with ns lasers showed larger dislocation density regions along with evidences of grain refinement. High density dislocations with ns lasers induced thicker dislocation walls while producing smaller cell size compared to that with fs lasers, due to the larger strain with the former case. Meanwhile, a large amount of stacking faults and twins were identified with fs lasers along with the reduction in dislocation density. This behavior was attributed to the increase in strain rate and shock pressure with the fs laser, causing the suppression of dislocation slip and enhancement of twinning condition respectively. These results highlighted that the increase in strain rate from 10^6 s^{-1} for ns pulses to 10^8 s^{-1} for fs pulses causes a significant change in the mechanisms involved in the plastic deformation. Meyers et al. [143] also demonstrated the effect of pressure on resultant microstructure, in which the stacking fault and twinning as the primary mechanisms at 40 GPa was shifted to subgrain elongation and microtwinning at 60 GPa. Interestingly, the number of laser pulses also significantly influences the microstructure of the deformed material [134]. Dislocation slip acts as the dominant plastic mechanism for copper, followed by smaller amount of stacking faults with single laser pulse. Whereas, for two pulses, along with an increase in dislocation density, large number of twins and stacking faults were observed due to the larger strains involved in the latter case. The formation of stacking faults and twins at higher strains were attributed to partial dislocation sweeping mechanism, in which partial dislocations with higher density sweeps to form stacking faults, and then transformed to twins

by further sweeping.

Due to high strain rates, the following microstructural effects occur [89, 91, 144, 145]:

- Dislocation nucleation, propagation and annihilation occur instantaneously due to the high dislocation velocity.
- High dislocation density region increases due to the uniform nucleation of dislocations and grain structures.
- Dislocation movement by viscous phonon drag.
- Suppression of dynamic recovery, which depend on cross-slip.
- Restriction to the discrete dislocation cell formation.
- Reduction in dislocation cell size.

2.5.3.5 Residual stress distribution

Laser shock processing induces a beneficial compressive residual stresses on the irradiated surface. In laser bulging of sheets, residual stresses on the convex surface (irradiation side) always remained compressive as seen in Fig.2.17a due to the springback effect whereas the nature of the residual stress at the concave surface was depending on the sheet thickness and laser energy [59]. However, compressive residual stresses were also induced at both surfaces (Fig. 2.17b) with several processes [83, 89, 146]. Despite the through-thickness compressive stress, the magnitude of stress was larger on the surface at which the shock loading was applied. The deformation behavior can be explained as follows:

(i) When the laser is irradiated on the coating material, shockwaves propagate into the target. It induces a dilation of the surface layers and the stretching of the shocked area in the directions normal to the axial impact direction.

(ii) After the end of the laser pulse, the region around the impact area generates the compressive residual stress. Therefore, the residual stresses formed on the surface layers of the impact area have been compressive.

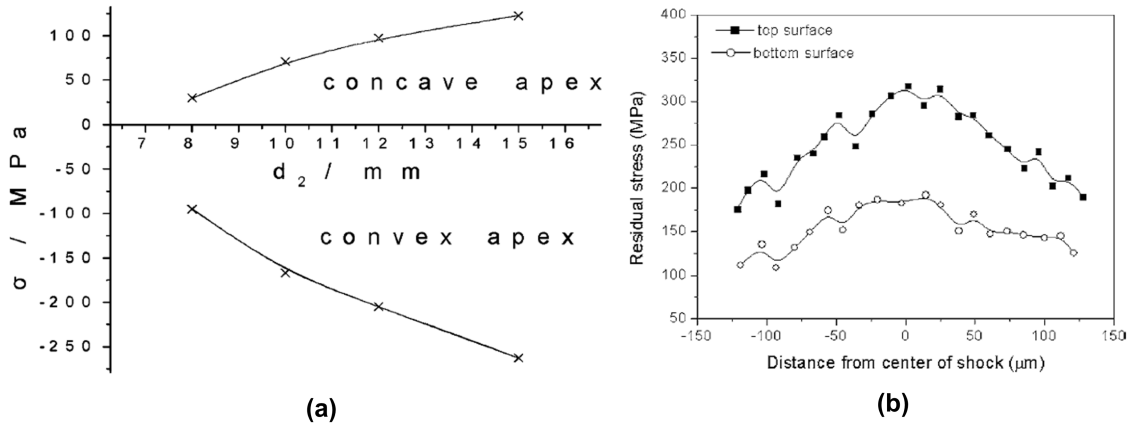

Figure 2.17: Residual stress distribution after laser shock processing (a) Residual stress profiles over the steel surface after laser shock bulging [59] (b) Residual stress distribution on copper after laser dynamic forming [89]

2.5.3.6 Mechanical properties

The mechanical properties of the formed material have also been modified as a result of high strain rate loading. During laser shock peening of 10 *mm* thick aluminum by Montross et al. [147] using Q-switched near-IR laser (1064 nm wavelength, 40 ns FWHM), an increase in surface hardness of 7 to 15% and a reduction in elastic modulus of 5 to 12% was observed, whereas the depth of hardness change varied between 1 *mm* to 2 *mm* from the surface. The change in elastic modulus was reported to be due to the dislocation tangles in shockwave loading. After laser shock forming of SUS304 and SUS430 sheets of 0.3 *mm* to 0.9 *mm* thickness using a Q-switched pulsed Nd:Glass laser (1064 nm wavelength, 20 ns FWHM), an increase in surface hardness was observed by Zhou et al. [84]. Hardness was maximum at the surface, whereas it was reduced away from the surface in the thickness direction [83]. The similar behavior was observed by Wang et al. [148] during laser shock forming of 1.2 *mm* thick brass sheets Q-switched pulsed Nd:YAG laser (1064 nm wavelength, 30 ns FWHM), where the hardness enhancement occurred up to 200 μm thickness from the irradiated surface. High dislocation density, compressive residual stress, and refined microstructure have been attributed to the increase in hardness and yield strength after laser shock loading using a Nd:YAG laser[89]. Increased hardening in FCC metals at high strain rates can also be attributed to

the increased dislocation interactions and subsequent tangling as a result of nucleation of dislocations together with the restriction of the dynamic recovery [145]. A summary of the above mentioned results is presented in Table. .

Table 2.3: Effect of laser shock forming on mechanical properties

Processes	**Material**	**Surface hardness**	**Hardness depth**	**Other properties**
Laser shock peening [147]	Al (10 mm)	Increase by 7 to 15%	Up to 1 mm to 2 mm	Reduction in elastic modulus by 5 to 12%
Laser shock forming [84]	SUS304/ SUS430	Increase in hardness	Maximum at the surface	N.A
Laser dynamic forming [89]	Cu (15 μm)	Increase in hardness by 600% to 800%	N.A	Increase in yield strength
Laser shock forming [148]	Brass (1.2 mm)	Increase in hardness by 20%	Up to 200 μm	N.A

Formability of the material is also influenced by the texture orientation. In most of the forming processes, strong textures are formed on the deformed material, which could affect the material properties. In laser shock processing of copper and nickel by Zhang and Lawrence [58] using a Q-switched Nd:YAG laser, though an increase in $\{0\ 0\ 1\}$ lattice directions was observed on both copper and nickel after forming, no strong textures were formed.

2.6 Influence of process variables

The various relevant parameters in the processes using laser-induced shock waves such as laser system, process components, and materials are discussed to understand their relationship with process output characteristics.

2.6.1 Material properties

Laser shock processing has been successfully employed with wide range of materials including copper, aluminum, brass, stainless steel, titanium, high strength

alloys, elastomeric laminated composites, and graphene thin films were plastically deformed by various processes [83, 92–94, 149]. The plastic deformation is obviously influenced by the mechanical properties of the material involved, as evidenced from various experimental results [58, 87, 150].

In addition to mechanical properties of the substrate material, the influence of parameters such as material thickness and its initial microstructure needs to be understood. Material thickness influences the shock pressure propagation time and the entire plastic deformation [90]. If the thickness of the foil is lesser than a critical value (e_m), the shock wave reflects back from the free surface causing a reduction in peak pressure. The critical thickness is given by $e_m = 0.5\tau D$, where τ is the laser pulse width and D the shock velocity (m/s) [151]. Meanwhile, the acceleration of the foils increases if the thickness is lesser than the critical thickness. In addition, the material thickness affects the residual stress distribution of the formed components. After laser shock bulging of 0.3 mm thick stainless steel sheets, the residual stress was compressive in the convex side whereas it was tensile in the concave side. With increase in sheet thickness to 0.6 mm, through thickness compressive stresses have been experienced [59].

Grain size of blank plays a significant role in microforming as there are only few grains in the thickness direction. Grains in some regions, such as those in contact with the rigid bodies experience more deformation [63]. Generally, larger grain sizes are preferable for plastic deformation as the moving dislocations are interrupted at the grain boundaries. It was observed in LDF of copper foils that the initial grain structures do not affect the dislocations and subgrain structures of formed features [89].

2.6.2 Laser System

The various processing parameters relevant to lasers significantly influence the process outcomes including deformation geometry and shape in shock forming, plastically affected depth in case of shock peening, and mechanical properties such as

hardness and residual stress distribution of the deformed substrate.

2.6.2.1 Laser energy

Laser pulse energy has been a significant process parameter in the processes using laser-induced shockwaves as it influences the ablation of overlay/coating and the amplitude of induced-shock pressure [87, 146].

The increase in laser energy is observed to increase the height and radius of the formed bulge in laser shock forming of stainless steel sheets [59], the deformation depth in laser dynamic forming of copper [90], embossing depth in laser shock embossing of copper [96], and deformation depth in laser shock forming of brass [148]. The increase in pulse energy also improves the surface hardness [148] and the compressive surface residual stress magnitude [83].

In addition, the laser energy influences the interaction of the laser beam with the dielectric mediums. In laser shock processes, the dielectric breakdown at the surface of the confinement medium interrupts the laser beam towards the target, resulting in the saturation of the induced shock pressure [125, 146]. The mechanism behind the dielectric breakdown is identified to be avalanche electron ionization process. The dielectric breakdown and subsequent pressure saturation is comprised of the following sequences [152]:

(a) The breakdown of the dielectric medium is initiated by one of the following behaviors: surface impurities, reflectivity of the target, and collision of metal plasma with the rear surface of the confinement.

(b) The avalanche ionization process occurs, in which an increase in electron density and absorption of laser energy are experienced.

(c) The ionization wave will propagate towards the laser beam ceasing the laser irradiation of the target surface.

The breakdown can be observed in Fig. 2.18 where the luminous portion represents the plasma. At smaller laser intensity (Fig. 2.18a), the plasma was visible

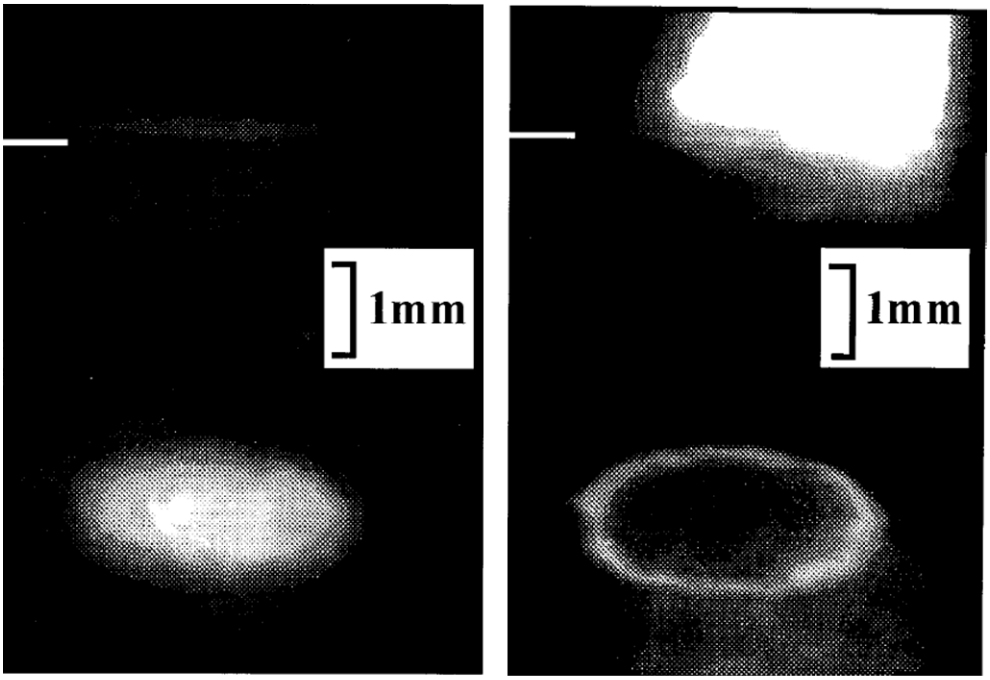

Figure 2.18: Plasma visualization in water confinement using a fast frame camera [125] (a) Plasma formation at the metal surface at 1.8 GW/cm^2 laser intensity (b) Dielectric breakdown at the water surface at 28 GW/cm^2 laser intensity

only at the irradiating surface as shown in Fig. 2.18a. Whereas, at higher intensity (Fig. 2.18b), the breakdown of water at the surface caused the formation and expansion of plasma in the air, which hence absorbed the laser irradiation and reduced the shock pressure. In addition to the reduction in pressure amplitude due to the breakdown, a reduction in pressure pulse duration was also experienced with increasing laser intensity. It was observed that, at 1064 nm wavelength, the duration of the pressure pulse was reduced from 60 ns at 2.5 GW/cm^2 to about 40 ns at 20 GW/cm^2 [146]. If the plasma irradiation is primarily in the extreme UV wavelength (<200nm), multiphoton ionization mechanism of confinement water breakdown becomes dominant [58]. Thus, it is necessary to choose the optimum laser intensity to enhance the plastic deformation and mechanical properties.

2.6.2.2 Laser beam profile (spatial and temporal)

The spatial intensity distribution of the laser beam plays an influential role in laser-shock processes. Gaussian beam (TEM_{00} mode) has been commonly used in laser

shock processing. With circular laser spots, the radial release wave from the edges of the impact, converge at the center causing a reduction in plastic stress and strain magnitudes [85, 153]. This drop can be avoided by overlapping of laser pulses or using non-circular (square or elliptical) beam profiles [85, 146]. Yang et al. [85] used elliptical beam profiles for the laser shock forming of stainless steel sheets. Masse and Barreau [154] eliminated the residual stress drop with square impact in their experiments. Square shaped laser beams were also used by few researchers [110, 155, 156]. In addition, the deformation shape and the thickness distribution are also influenced by the laser beam profile.

The temporal profile of the laser pulse is influential to the pressure pulse amplitude and duration [108, 152]. The peak pressures measured between Gaussian pulse (30 ns duration) and Short Rise Time (SRT) pulse (25 ns duration) were approximately similar for laser intensity lesser than 3 GW/cm^2 and 4 GW/cm^2 with glass and water confinements respectively. After these intensity levels, the peak pressure with SRT pulse was higher than with Gaussian pulse. At higher intensities, the peak pressure occurs earlier than the peak laser pulse with both SRT and Gaussian pulses due to the occurrence of dielectric breakdown. It was found that compressive residual stress magnitude and depth were larger with the temporal pressure pulse profile having sharp increase in pressure than with the Gaussian pulse [110].

2.6.2.3 Spot size

Laser beam diameter is another parameter that affects the deformation profile such that deformation area increases along with the beam diameter despite a concurrent reduction in shockwave pressure [157]. An increase in the shockwave attenuation rate was observed with small impacts of about 0.5 mm to 1 mm compared to larger impacts (4 mm to 5 mm) [110]. The spot size was observed to influence the shockwave propagation, such that the shockwave expansion was spherical with smaller beams whereas planar propagation was experienced with larger beams [81].

2.6.2.4 Wavelength

Shorter wavelengths facilitate better absorption as absorption coefficient of materials is inversely proportional to the wavelength. Also, the absorption density of plasma is high during the confinement at shorter wavelengths [146]. Therefore, the shock pressure is higher at the smaller wavelength. However, the higher absorption properties at shorter wavelengths causes early occurrence of dielectric breakdown effect even at the lower laser intensities [108]. As the threshold intensity for breakdown decreases with decreasing wavelength, higher peak pressures cannot be achieved. Also, the duration of pressure pulse is reduced with the shorter wavelength. If the intensity is smaller (lesser than the threshold), shorter wavelength is better whereas longer wavelengths are preferred if the intensity is large.

2.6.2.5 Pulse duration

The laser pulse duration influences the amplitude and duration of the pressure pulse and the plastically affected depth. Moreover, with shorter pulses, dielectric breakdown threshold increases, resulting in higher peak pressure [108]. The peak pressure of 10 GPa was observed at 0.6 ns pulse duration whereas it was only 6 GPa at 10 ns duration [146]. It is also noted that the shockwave may be absorbed within the absorptive overlay if the pulse duration is less than 1 ns. For constant pressure, the magnitude of surface residual stress increased with the shorter pulse duration. The other benefits of ultra short pulses have been the reduction of mechanical effects such as cavitation bubble expansion and shockwave emission [123]. Furthermore, the transmission of laser beam through the confining medium was influenced by the laser pulse duration.

2.6.2.6 Number of pulses

The number of laser pulses is another significant parameter in laser material processing. In laser deep drawing, the deformation depth of metal sheets increased with an increase in number of pulses whereas the sheets fractured after reaching a

deformation threshold [87]. In this process, the first pulse produced 60% of final deformation and a conical form, whereas further pulses create a spherical form. In laser dynamic forming, multiple pulses effectively reduced the foil bounce off effect, thereby achieving an accurate control of the final shapes [158]. The behavior behind this observation had been the distributed laser energy within multiple pulses to contain the sheet forming velocity below the critical forming velocity of the material, which restricted the local thinning and subsequent fracture. Though the increase in number of pulses reduced the workpiece necking, the bottom of the deformed profile was stretched. Furthermore, the magnitude of compressive residual stresses in the material increased with multiple laser pulses during laser shock processing [81]. Thus, it is understood that there is an optimum level of number of pulses to achieve the maximum and uniform deformation over the entire surface in laser shock forming process.

2.6.2.7 Defocussing

The distance between the laser beam focal point and the sample, called defocussing, influences the shock pressure such that maximum pressure is applied at zero defocussing distance [159]. An optimum defocussing distance has been examined for the favorable vaporization of ablative coating in laser shock embossing of copper foils by Liu et al. [96], where an increase in ablation depth was observed with a reduction in defocussing.

2.6.3 Ablative overlay

The ablative overlay serves to generate the shockwave pressure to deform the workpiece. The material properties and the thickness of the ablative overlay are considered to be the significant process parameters in laser shock forming processes.

2.6.3.1 Ablative overlay material

Ablative coating or overlay is a sacrificial component in laser shock processing, which is vaporized due to high temperature and pressure of laser irradiation. The main purpose of this coating layer is to prevent the material from ablation and increase the shock pressure. In addition, the presence of coating induces beneficial compressive residual stresses on the substrate surface in comparison to the tensile stresses on sample with direct target irradiation [81]. If no coatings are applied on sample, a small volume of work piece as much as about skin depth is heated, vaporized, and ionized, affecting the fatigue behavior [160]. Graphite, aluminum foils, black paint, black tape are typically used as the coating materials [147, 161–164].

Montross et al. [147] compared black paint and self-adhesive aluminum foils as coating materials in laser shock peening. Despite the spallation or debonding of paint, better surface hardness enhancement was observed on samples coated with black paint, in comparison to aluminum foils. However, the aluminum foils demonstrated better adhesive properties than the black paint. Fabbro et al. [146] investigated Al-based paint and metallic (Ta, Cu, Al, and Mo) coatings on aluminum foil of 250 μm thickness at 1 GW/cm^2 and 4 GW/cm^2 during laser shock processing, where no significant difference in peak pressure with change in coatings was observed. However, employing 100 μm thick Al based coating over 316L steel sample increased the peak pressure by 50% compared to the pressure without the coating. This behavior was attributed to the impedance mismatch effect which arises due to the difference in impedance between target and coating materials.

The impedance mismatch effect is eventuated while the shockwaves traverse between materials with different shock impedance [146, 165, 166]. When a shockwave propagates from a material having impedance Z_1 to another material with impedance Z_2 such that $Z_2 > Z_1$, the amplitude of the shockwave will be increased. If the impedance of the coating is lesser than that of metal, the amplitude of shock wave will be higher. This effect is used in laser shock processes to increase the

shock pressure generated upon irradiation.

Zhou et al. [83] applied TiN absorbing layer on the rear surface in addition to the ablative layer on the laser irradiation surface, to protect the sample from spallation effect due to the reflective tensile stress wave .

The selection of ablative overlay depends upon the following factors:

- Absorption properties of material at particular wavelength.
- Thermal conductivity and heat of vaporization of the target.
- Impedance of the material (should be less than the base material).
- Adhesiveness to the substrate, especially when employing multiple pulses or irradiation at the near spots.
- Ease of application.

2.6.3.2 Ablative overlay thickness

The thickness of the overlay should be sufficient enough to avoid thermal effects on the target surface. However, if the overlay thickness is much higher than the ablation depth upon irradiation, the shockwaves tend to attenuate within the overlay before reaching the target. Thus the coating must have a certain maximum thickness to form into plasma completely and a minimum thickness to resist the ablation of the work sample. However, no study on the effect of ablative coating thickness on the deformation characteristics has been reported so far.

2.6.4 Confinement layer

2.6.4.1 Confinement layer medium

Confinement layer is a transparent material used to restrict the plasma expansion. The confinement layer increases the intensity of the laser-induced shock pressure by about two orders of magnitude as compared to the plasma expansion in the vacuum [167]. The induced shock pressure depends upon the shock impedance of

the confinement material [160]. Usually, a glass or water is used as the confinement medium. Materials such as K9 glass, perspex, quartz glass, silicon rubber, and Pb glass were investigated for their effect on induced shock-wave pressure and a difference in shock pressure for different confinement medium was observed by Hong et al. [164]. Using water as the confinement resulted in a 10 fold increase of plasma pressure as compared to the direct ablation, and subsequently the bending angle of the stainless steel sheets was increased [168]. In addition, the confinement prolongs the duration of the shock pressure, thereby adequate momentum can be acquired by the material during deformation [90]. The disadvantages of using water are scattering and absorption of laser, possible corrosion, and water photolysis [169, 170]. Ye et al. [171] used a new medium, gum water, which consisted of polyvinyl alcohol as the confinement layer for femtosecond laser shock forming of metal foils. However, nonlinear absorption of laser energy was observed within the confinement layer, that could lead to a reduction in shock pressure amplitude and shock duration. Ye et al. [134] also used an adhesive tape containing polypropylene as the major constituent as the confinement layer. The shock impedance of adhesive tape (0.19 x10^6 $gcm^{-2}s^{-1}$) is larger than that of the gum water (0.16 x 10^6 $gcm^{-2}s^{-1}$). However, the adhesive tape and gum water have limitations when multiple laser pulses are applied in terms of insufficient material for confinement.

2.6.4.2 Confinement layer thickness

As the shockwave generating at the target-confinement interface is propagating towards the confinement layer as well [160], the critical thickness as mentioned for material thickness will also be applicable for confinement layer thickness. When the shockwave emanating from the irradiation zone reaches the top surface of the water confinement, the water will be detached from the target surface and hence there will be no confinement of plasma [172]. This effect will cause a reduction in plasma pressure if the shockwave reaches the top water surface before the arrival of the peak laser pulse. Therefore, the confinement of plasma depends upon

the confinement thickness and shockwave velocity. Ocana et al. [173] found using numerical simulation that the plasma pressure increases with the increase in confinement thickness.

2.6.5 Temperature

Forming at elevated temperatures is an effective way to minimize the size effects as it facilitates geometric accuracy, uniform forming forces, and enhanced formability due to the improved homogeneity and thermally activated dislocation movements [174]. At elevated temperatures, there is a change in microstructures and plastic deformation behavior [175]. Performing laser dynamic forming on copper samples which are heated above their recrystallization temperature, produced refined grain sizes and reduced high dislocation density regions due to recrystallization and reduction in strain hardening rate [89]. Preheating of the sample can be helpful to form brittle materials through ductility improvement.

2.6.6 Desired microfeatures

For laser shock forming processes where required microfeatures are obtained using mold patterns, parameters such as aspect ratio and fillet ratio affect the deformation characteristics significantly. In LDF, the occurrence of maximum von Mises stress depends upon the fillet ratio of the mold. Increase in fillet ratio leads to higher material flow acceleration and vertical displacement [90]. After an upper limit of aspect ratio, material failure occurs as its formability reaches its maximum.

2.7 Modeling and simulation

The major phenomena involved in the laser-induced shock processes that need to be modeled are shock pressure, material deformation, and material failure characteristics.

2.7.1 Shock pressure modeling

Modeling of shockwave pressure induced by laser-produced plasma in confining conditions has been presented by Fabbro et al [160]. Fabbro's model has been extensively used in laser-induced shock pressure simulations. The shock pressure depends on the following factors: plasma layer thickness, shock impedance of ablative medium and confining layer, laser pulse energy, and fraction of absorbed laser energy used for increasing the plasma thermal energy [160]. The entire process with confinement contains the following steps in sequence: shockwave generation and propagation into confining layer and the metal due to plasma pressure, adiabatic cooling of plasma after the laser switched off, and complete recombination of plasma for prolonged duration. The formulation of shock pressure starts with the assumption that two shockwaves are generated and subsequently propagate inside the target and confinement with fluid velocities behind the shockwave taken as $u_1(t)$ and $u_2(t)$ respectively. The interfacial plasma thickness $L(t)$ is a function of time as given by,

$$L(t) = \int_0^t [u_1(t) + u_2(t)]dt \tag{2.5}$$

From the shockwave relation for pressure $P = u_i Z_i$ with $i = 1$ or 2,

$$\frac{dL(t)}{dt} = \frac{2}{Z}P(t) \tag{2.6}$$

where, $2/Z = 1/Z_1 + 1/Z_2$; Z_1 and Z_2 are shock impedance of target and confinement materials respectively. The incident laser energy $I(t)$ is converted into work to increase the plasma interface and its internal energy, which is formulated as,

$$I(t) = \frac{dL(t)}{dt}P(t) + \frac{3}{2\alpha}\frac{d}{dt}[P(t)L(t)] \tag{2.7}$$

in which α is the fraction of the internal energy in the form of thermal energy used to increase the plasma pressure. If mass transfer between plasma-confinement and plasma-target is considered, there is no need to include the parameter 'α' [58].

Considering constant laser intensity (I_0), the peak shock pressure P(GPa) can be calculated from,

$$P = 0.01\sqrt{\frac{\alpha}{3+2\alpha}}\sqrt{I_0 Z} \tag{2.8}$$

Peyre et al. [176] approximated the peak shock pressure to be the square root of laser intensity as $P = 1.02\sqrt{I_0}$.

It is observed that the peak pressure of the shockwave increases along with the laser intensity [90]. Fabbro's model is based on the assumption of uniform laser irradiation and one-dimensional shock propagation. This assumption is inappropriate when the laser beam diameter is small and follows a Gaussian distribution. This spatial variation in laser beam profile has been modeled by Zhang et al. [58] as given below.

$$P(r,t) = P(t)\exp(-\frac{r^2}{2r_0^2}) \tag{2.9}$$

where, $P(t)$ is the shock pressure from Fabbro's model, r_0 is the laser beam radius, and r is the radial distance from the beam center.

Based on explosive gas dynamics, an alternative calculation for peak shock pressure (P) as a function of laser pulse intensity (I_0), target absorptive coefficient, specific heat ratio (K_1) and the density of the mixture of vapor, absorptive layer and confinement (ρ_0) is devised as [84],

$$P = \left(\frac{K_1+1}{2K_1}\right)^{2K_1(K_1-1)} \frac{[2(K_1^2-1)]^{2/3}}{K_1+1}\left[\rho_0(\alpha I_0)^2\right]^{1/3} \tag{2.10}$$

The above mentioned shock pressure formulations consist of free variables that need to be calculated from the experiments. Wu and Shin [177] developed a self-closed thermal model to calculate the shock pressure induced on the target. This model has no free variables as it considers all the physical mechanisms involved in the process. This confined-plasma model was used to simulated the laser shock peening process with overlapping [178]. Wu and Shin [179] also devised a predictive

2D axisymmetric model using the hydrodynamic equations, along with appropriate equations of state for the water and coating material. With this model, 2D spatial distribution of stress profiles in laser shock peening was predicted [180].

A 1D hydrodynamic Lagrangian finite-difference code, including a Mie-Gruneisen equation of state and elastic-plastic properties for target materials has been used to simulate the laser-induced shock wave interaction with the materials [151].

2.7.2 Constitutive models

The laser shock forming process is associated with ultra-high strain rates. Therefore, the constitutive models need to accommodate the strain rate effects. Johnson-cook model is a constitutive model for materials subjected to large strains, high temperature and high strain rates [181]. Von-Mises flow stress (σ) from this model is calculated as follows,

$$\sigma = \left[(A + B\varepsilon^n)\left(1 + Cln\left(\frac{\dot{\varepsilon}}{\dot{\varepsilon_0}}\right)\right)[1 - T*^m]\right] \tag{2.11}$$

Where, the homologous temperature $T^*$is given by $T* = (T - T_r)/(T_m - T_r)$ in which T is the temperature and T_r and T_m are reference and melting temperatures respectively. A, B, C, m, and n are material constants in which A is the yield stress, B and n to incorporate the work hardening effect, C to include the strain-rate effect and m to include the temperature effect on the flow stress. These material constants are generally calculated using tension, torsion and Hopkinson bar tests.

Hopkinson bar test conducted for OFHC copper, Armco iron and 4340 steel with varying strain rates revealed that the specimen temperature increases with increase in strain rate [181]. As a result, true tensile stress is reduced, confirming the occurrence of adiabatic softening effect. This effect tends to rise with the increase in strain rate. At higher strain rates ($\dot{\varepsilon} > 10^3\ s^{-1}$), flow stress of the material increases rapidly compared to low strain rates ($\dot{\varepsilon} < 10^3\ s^{-1}$), which is attributed to the different dislocation motions at high and low strain rates [91], as detailed in the section 2.5.2. In laser dynamic forming, the material flow stress behavior has been

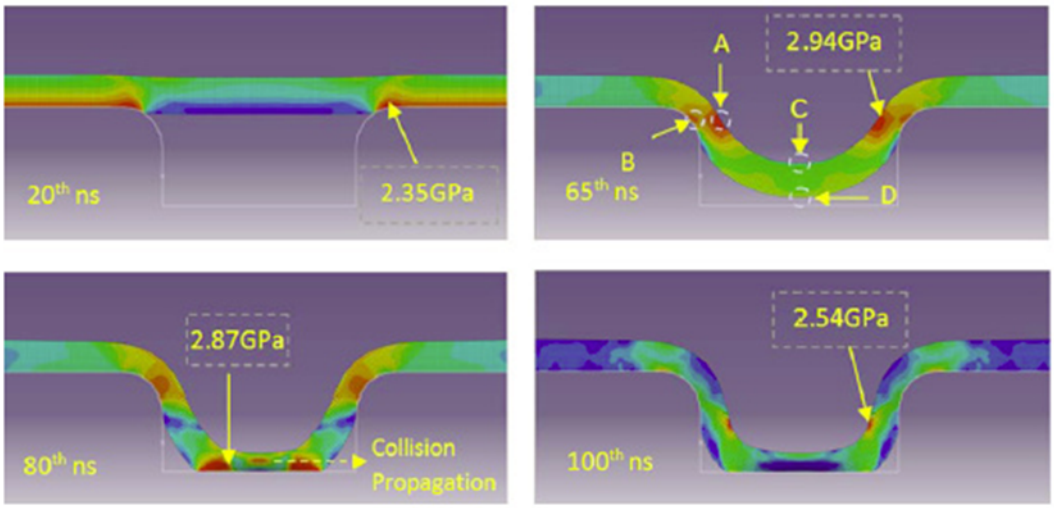

Figure 2.19: Simulation of Laser dynamic forming process [90] - Different stages of deformation

modeled by a modified Johnson-Cook model and the process sequence at various time steps is illustrated in Figure 2.19 [90]. 3D Discrete Dislocation Dynamics (DDD) simulation of LDF was performed by Gao and Cheng [144] including high strain rate and size effects to derive the constitutive model.

A significant difference in results between experiments and simulation using Fabbro and Johnson-Cook (JC) models was observed for Laser shock embossing [96]. Johnson-Cook model is a phenomenological model and is formulated using experiments with maximum strain rates of the order 100 s^{-1}. So, this model may not be accurate at strain rates higher than 10^5 s^{-1} as observed in laser shock forming. In addition, JC model ignore pressure effects which have a significant role in LSF. Inertia effects which delay void growth and necking are also neglected in modeling and simulation thereby resulting in overestimated results [91]. Also, energy dissipated in the ablative material was not considered in the simulation and this might have also caused the deviation. In spite of these limitations, Johnson-Cook model has been extensively used to model the materials that experience strain rates up to10^5 s^{-1} during deformation.

Steinberg proposed a constitutive equation that is applicable at high strain-rates ($\dot{\varepsilon} > 10^5$ s^{-1}) considering ultrahigh-pressure effects [182]. But this model is strain-rate independent considering the fact that strain-rate effect is insignificant at

pressures greater than 10 GPa. So, a constitutive model considering both ultrahigh pressure and strain-rate effects has been proposed by Zhang [79] as formulated below:

$$G = G_0 \left[1 + \left(\frac{G_P^{'}}{G_0}\right) P + \left(\frac{G_T^{'}}{G_0}\right) (T - 300)\right] \tag{2.12}$$

$$Y = Y_0[1 + Cln\dot{\varepsilon}][1 + B\varepsilon]^n \left[1 + \left(\frac{Y_P^{'}}{Y_0}\right) P + \left(\frac{G_T^{'}}{G_0}\right) (T - 300)\right] \tag{2.13}$$

$$G_p^{'} = \frac{dG}{dP}, G_T^{'} = \frac{dG}{dT}, Y_p^{'} = \frac{dY}{dP}, \frac{Y_p^{'}}{Y_0} \approx \frac{G_p^{'}}{G_0} \tag{2.14}$$

where G is the shear modulus, Y the yield stress, P the pressure, and T the temperature. The primed variables with subscripts P and T denote the derivative of that variable with respect to the corresponding subscript parameter at the reference state ($\varepsilon = 0$, $P = 0$, $T = 300K$), and B,C and n are similar to Johnson-Cook model (Eqn 2.11).

2.8 Summary

The following inferences can be derived from the literature survey:

- Various existing high strain rate microforming processes, specifically processes using laser-induced shock pressure are reviewed in detail. Despite exhibiting improvement in material formability, the high strain rate processes still possess similar issues with die/mold as discussed in the previous chapter: die fabrication, process flexibility, friction, die wear, etc. Furthermore, it has been noted that the geometry of the fabricated microfeatures is dependent not only on the microdie geometry but also on the different process parameters such as the laser fluence, pulse duration, spot size, and the number of pulses. As the microdie is not the only factor to determine the feature geometry formed on metal sheets, the rationale to develop new mold-free technique

is further enhanced, with lasers demonstrating large amount of flexibility.

- It is revealed from the review that the thickness distribution of the formed components with existing conventional and high strain rate sheet metal forming processes is still non-uniform which is attributed to the rigid punch and/or die that causes non-uniform stress distribution by restricting the material flow.
- At high velocity forming, sudden deceleration of the deforming material and nonuniform velocity distribution need to be addressed as they influence the final deformation characteristics.
- Despite the significance of plasma formation and expansion in laser shock forming processes, there are inadequate experimental investigations of few major process variables including confinement medium thickness.
- The deformation mechanism in laser shock processing is identified to be a complex interaction between various parameters including strain level, strain rate, and pressure amplitude. The development of new process will exhibit a range of process capabilities in terms of strain and strain rate limits. Therefore, it will be necessary to analyze the deformation mechanisms involved in the developed process to understand and predict the process behaviors.
- The process variables in laser shock processes significantly influence the plastic deformation mechanisms in addition to the deformation geometry profiles. As the resultant mechanical properties of the deformed components depend upon the deformation mechanisms, the relationship between the input parameters, process mechanisms, and output variables need to be established.

The further parts of this thesis intend to address these concerns.

Chapter 3

Flexible Pad Laser Shock Forming - Process Development and Parametric Study

This chapter details the development strategy of the proposed microforming technique, Flexible Pad Laser Shock Forming (FPLSF). The feasibility of the proposed technique to fabricate microfeatures through plastic deformation of thin metallic foils is examined. Subsequently, the mechanisms involved in the process are briefly discussed. The capability and flexibility of the process to fabricate microfeatures with different sizes and geometry are investigated further.

3.1 Process development

A schematic representation of the proposed technique, FPLSF is shown in Fig. 3.1. A high-power pulsed laser is used to generate the shock pressure required for the metal foil deformation. The metal foil to be deformed is placed over a uniform flexible pad surface which is expected to play the role of master micromold. A hyperelastic polymer that can undergo large elastic deformation under loading is used as the flexible pad. The metal foil is covered with a uniform thin layer of an ablative overlay which absorbs the incident laser energy and generates plasma.

It also acts as a thermo-protective layer to prevent the metal foil from thermal damages. A medium, transparent to the laser beam, is placed over the ablative overlay. This transparent medium is called confinement layer as it is used to restrict the plasma diffusion and direct the shockwave towards the foil surface. Typically the magnitude of the laser-induced shock pressure and the duration of shock wave are increased due to the confinement layer [160]. The different process components can be identified in Fig. 3.1.

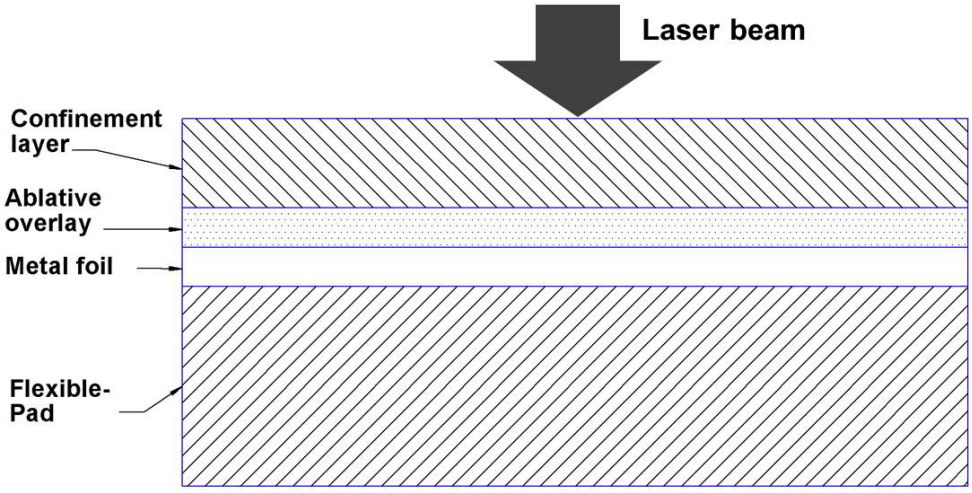

Figure 3.1: Schematic of Flexible Pad Laser Shock Forming (FPLSF) process

The selection of different process variables for this experimentation were based upon the literature study and a preliminary analysis. A detailed investigation of process parameters will be presented in 3.10.

Selection of metals for MEMS devices is based upon their mechanical and electrical properties in addition to their compatibility for processing [183]. Due to the extensive popularity in the microindustry, copper and nickel became the natural choice of substrate materials in this thesis. In addition, stainless steel, especially AISI316, has been used in plethora of applications owing to its structural strength [167, 184]. Thus, the following three materials are used as the substrate metal foils in this thesis: pure copper (99%), pure nickel (99.9%), and stainless steel AISI 316 (Fe/Cr18/Ni10/Mo3). Another reason for choosing the above mentioned materials has been the extensive information available for laser shock processing, which hence can be used for comparison purpose in the later stages. The materials are received

after annealing. The thickness of the metal foil was chosen as 25 μm in order to realize the plastic deformation of the entire sheet thickness as in sheet metal forming, instead of bulk forming with thicker metals. Mechanical properties of the substrate metal foils, pure copper, pure nickel, and AISI 316 stainless steel, are presented in Table. 3.1. True stress-strain curves from the literatures for copper [16] and AISI 316 [17] is given in .

Table 3.1: Material properties of metal foils

Material properties		Cu [181]	Ni [185]	AISI316 [186]
Density (Kg/m^3)		8920	8890	7800
Young's modulus (GPa)		126	207	202
Poisson's ratio		0.34	0.31	0.3
Johnson-Cook parameters	A (MPa)	90	163	514
	B (MPa)	292	648	514
	C	0.025	0.006	0.042
	n	0.31	0.33	0.508
	$\dot{\varepsilon}_0$	1	1	0.001

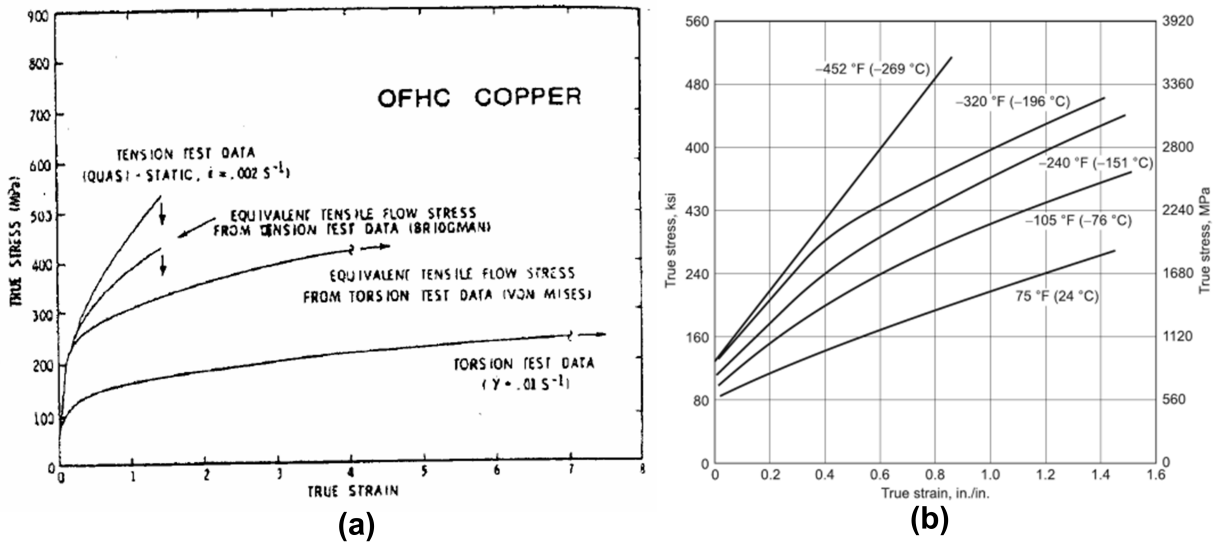

Figure 3.2: True stress versus true strain curve for (a) Copper [181] (b) AISI 316 [187]

For the sacrificial ablative overlay material, graphite-based black paint and aluminum foils are chosen for this analysis based on the literature review (section 2.6.3) and the preliminary FPLSF analysis with black tape and aluminum foil as the overlay materials (3.10.3.1). In laser material processing, the optical proper-

ties of the materials are prominent for the selection of suitable laser parameters. The reflectivity of the ablative overlay target and the substrate foils at different wavelengths are measured using a spectrophotometer and compared in Fig. 3.3a.

For plasma confinement, water and glass are commonly used in laser shock processing (section 2.6.4), which are adopted in this work. Fig. 3.3b shows the transmittance of the confinement layer materials for a range of wavelengths. The ablative overlay and confinement medium are compared in Table. 3.2 based on their shock impedance, which is a significant parameter for the shockwave propagation.

Table 3.2: Shock impedance of materials [152]

Material	**Shock impedance** (Z) ($gcm^{-2}s^{-1}$)
Glass	1.3 x 10^6
Water	0.165 x 10^6
Aluminum	1.5 x 10^6
Copper	4.2 x 10^6

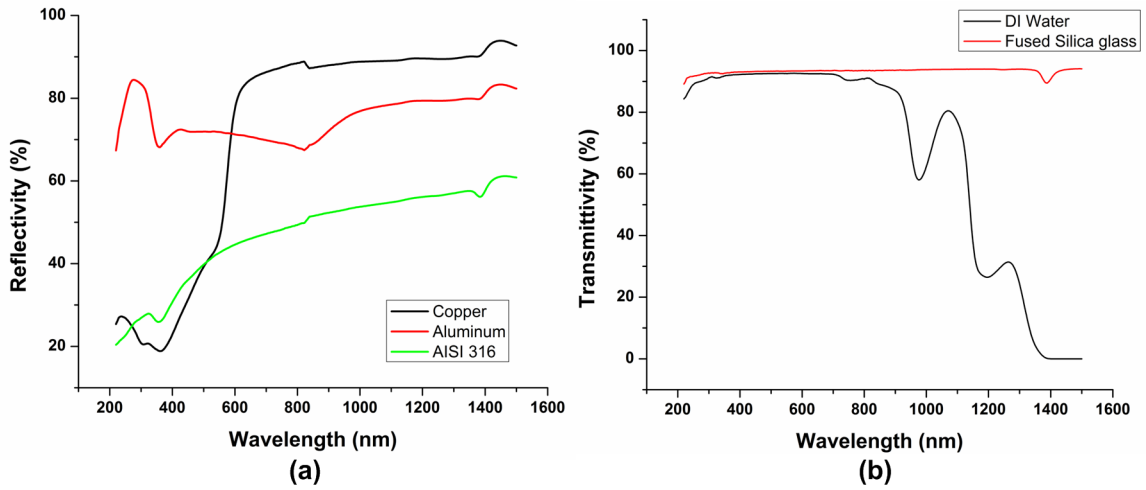

Figure 3.3: (a) Reflectivity of materials at different wavelengths (b) Transmittance of confinement materials at different wavelengths

The selection of laser system is associated with the absorptivity of the target material at the particular wavelength. A Q-switched Nd:YAG pulsed-laser is used for the laser irradiation in this analysis with specifications as listed in Table. 3.3 as the target aluminum overlay shows reasonably good absorption at the corresponding wavelength. Absorptivity of the irradiated surface is expected to increase in

the subsequent pulses due to melting and plasma coupling. The laser beam has a squared energy profile with a focused size of 0.6 mm x 0.6 mm after a focal lens of 80 mm in focal length.

Table 3.3: Laser system parameters

Laser type	System	Wavelength (nm)	Beam profile	Pulse duration (ns)	Repetition rate (Hz)	Max. pulse energy (J)	Output power (W)
Nd:YAG	Rofin DQ x 50S	1064	Flat Top-Hat	38	6000	75 x 10^{-3}	500

3.2 Surface topography characterization

Topography of the deformed feature surfaces were characterized using a surface profiler, Talyscan 150 contact profilometer (Taylor Hobson). Talyscan 3D surface profiler was used to measure the deformation geometry and the surface topographies. An inductive gauge (diamond tip with a radius of 2 μm) with a resolution of 7.35 nm was used to scan the surface of the features with a scanning speed of 1000 $\mu m/s$. The measured surface profiles were filtered for waviness with a cut-off length of 0.025 mm. The typical profiles produced from the developed process are hemispherical craters, as will be discussed in the next chapter. Scanning was performed on either top or bottom surface of the features, and the corresponding depth measured from the cross-section at the center are termed as bulge height and crater depth respectively, as illustrated in Fig. 3.4. The diameter of the deformation profile was measured as illustrated in Fig. 3.4. Crater depth can be defined as the maximum depth of the crater measured from the irradiated side of the foil surface.

Alicona Optical 3D non-contact profiler, based on confocal microscopy, was also used to measure the deformation profiles and the surface topographies. However, due to the higher reflectivity of copper, Alicona results was observed to be less

accurate. Therefore, the surface topography was measured using Talyscan surface profiler throughout this thesis. To visualize the sample features, an optical microscope (Zeiss Axioskop2 MAT) and Scanning Electron Microscope (JEOL 5600 LV) were used.

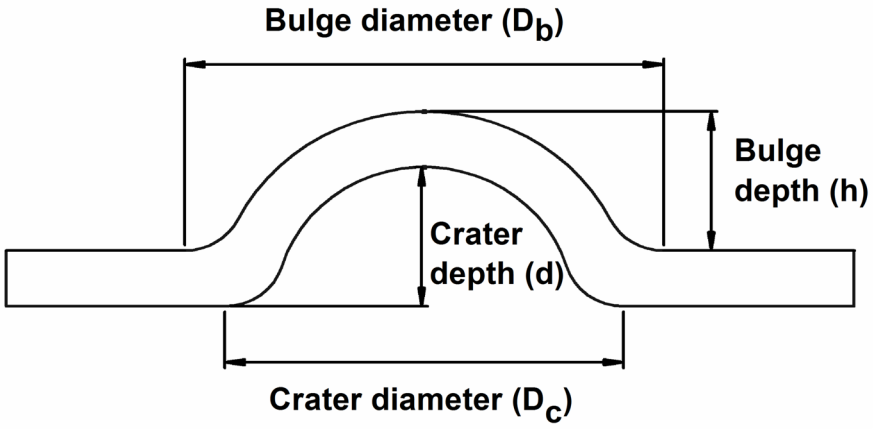

Figure 3.4: Measurement strategy of deformation depth and diameter from the surface profiler

3.3 Formation of microcraters

In this study, annealed 99.9% pure copper foil ($25\mu m$) was used as the specimen. Aluminum foil with a thickness of $15\mu m$ was used as the ablative overlay. A thin layer of vacuum grease was applied between the aluminum foil and the copper foil in order to provide an accurate sealing. Deionized water was used as the confinement layer in this study as water is one of the commonly used confining mediums. The entire setup was placed in a container with water filled up to 4.2 mm above the copper foil. The selection of confinement thickness is attributed to the following analysis: The critical thickness (e_m) of the confinement layer, the minimum thickness required, is given as $e_m = 0.5\tau D$, where τ is the laser pulse duration and D is the shock velocity, is calculated to be 31.35 μm at τ of 38 ns and D of 1650 ms^{-1} [151]. However, when the confinement thickness of water layer was smaller than 3 mm, copper surface was observed to be damaged under the laser shock in this analysis. On the other hand, when the confinement water layer was

too thick, it led to a significant reduction in the laser intensity due to the strong absorption of the water to the laser energy. Thus, an optimum thickness of 4.2 mm was used in this experiment.

Silicone rubber of 300 μm thickness was used as the flexible pad against which the sheet deformation occurs. The thickness of the rubber pad is prescribed to be at least 1.5 to 2 times greater than the depth of the forming cup in the rubber pad forming process [69]. The maximum depth of craters was measured to be about 150 µm in our FPLSF experiments. Thus, a silicone rubber with a thickness of 300 μm which was the double of the maximum crater depth was used.

Experiments were conducted at a laser fluence of 13.6 J/cm^2 with 45 pulses to investigate the feasibility of FPLSF for fabricating micro-deformation craters in copper foils. Fig. 3.5a and Fig. 3.5b compare the SEM image of the bottom and top surfaces of the formed crater respectively. The corresponding 3D topography of the bottom and top crater profiles, measured from the Talyscan surface profiler is compared in Figs. 3.6a and 3.6b respectively. In this study, the deformation depth and diameter of the formed sample are characterized by the parameters, bulge height (h) and bulge diameter (D_b) as indicated in Fig. 3.4. The bulge height (h) and the crater depth (d) are related to the difference in copper foil thickness ($\Delta t = h - d$) before and after FPLSF.

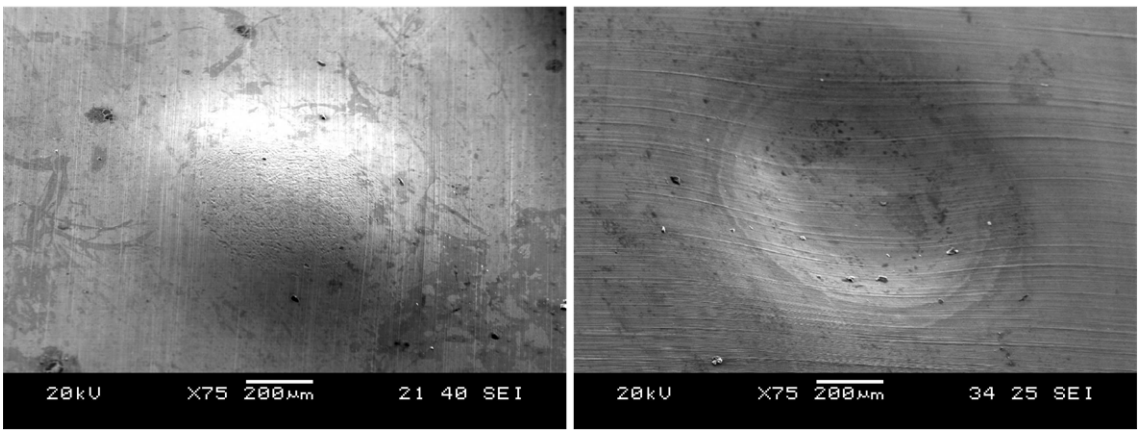

Figure 3.5: Crater formation on copper foil through FPLSF under the laser fluence of 13.6 J/cm^2 (a) SEM image of the crater bottom surface (b) SEM image of the crater top surface

It can be observed from Figs. 3.5 and 3.6 that the shape of the deformation crater was hemi-spherical.This hemispherical crater formation in FPLSF despite the flat-top beam can be attributed to the spherically propagating shockwave from the top surface of the copper foil upon irradiation [155].

The maximum deformation depth was observed at the center of the crater. Thus, the depth and diameter were measured at the crater cross-section at the center as shown in Fig. 3.6c. The deformation depth (h) of the formed sample for the laser fluence of 13.6 J/cm^2 is measured as 95.6 μm. The deformation force that is exerted on the metal foil which is placed over the silicone rubber depends upon the laser-induced shock loading. The maximum laser-induced shock pressure (P) is calculated from the Fabbro's model [160] as given in Eqn. 2.8. The calculated peak shock pressure for 13.6 J/cm^2 laser fluence is calculated to be 270 MPa. As the induced shock pressure (270 MPa) upon irradiation is much higher than the yield strength of the copper (90 MPa), the metal foil experienced plastic deformation.

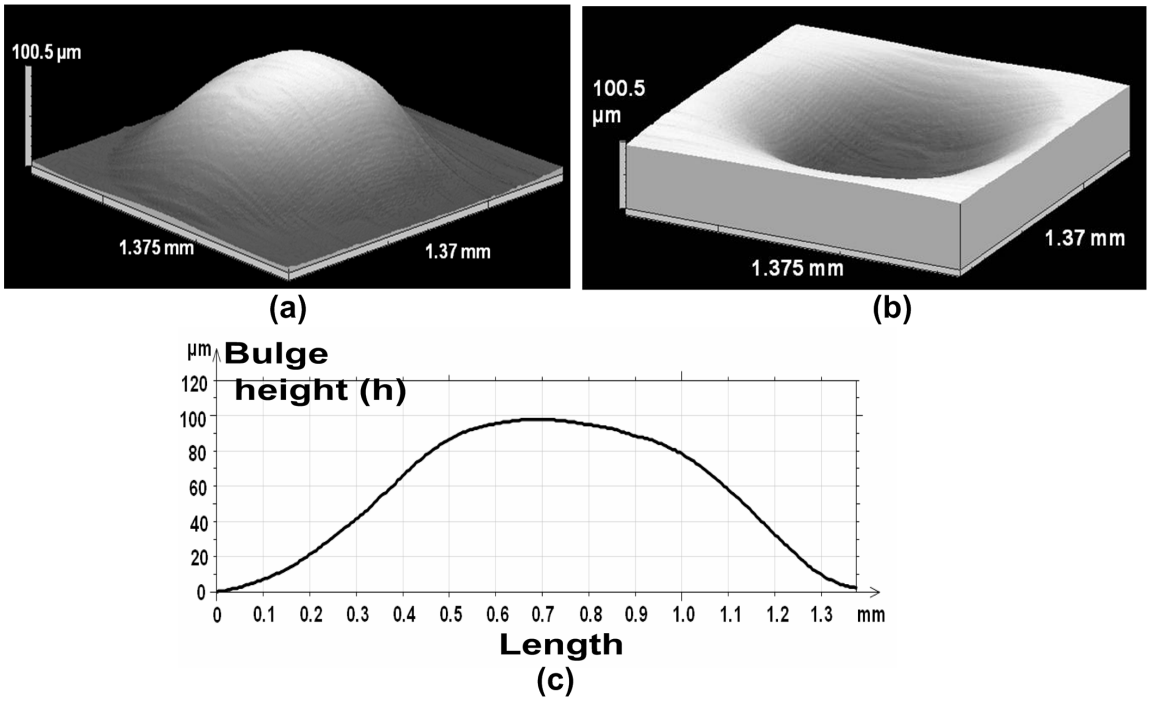

Figure 3.6: Crater profiles measured by the stylus profilometer (a) 3D topography of the bottom crater surface (b) 3D topography of the top crater surface (c) Cross-sectional profile of the crater

The deformation diameter (D_b) of the formed sample was 1.3 mm as shown in

Fig. 3.6c. It can be noted that the observed deformation diameter is greater than that of square beam size of 0.6 mm side. This behavior can be attributed to one or more of the following behaviors, which will be examined in the following chapters:

(a) When the thermal energy generated by the laser irradiation is much higher, the ablative overlay will be vaporized over an area much larger than the actual irradiation area.

(b) The shockwaves emanating from the loading surface tend to propagate spherically outwards [119, 155]. This shockwave propagation tend to increase the plastic deformation region on copper foil.

(c) Typically, hyperelastic polymers experience deformation over a region much larger than the loading area [65]. As the flexible pad is not constrained in FPLSF, the rubber is expected to extend its active deformation area under shock loading and have larger crater diameter.

These hypotheses on larger crater diameter will be explored in the upcoming chapters of this thesis. Silicone rubber was found to retract to its initial position once the deformed metal foil is removed from the rubber surface. In addition, no damage on the rubber surface was observed after using the same rubber for several experiments.

3.4 Process capability

Previously, the feasibility of FPLSF to induce plastic deformation on thin copper foils has been demonstrated. However, the capability of FPLSF to produce different deformation geometries has to be examined. It is understood from the literature that the different deformation profiles can be achieved by controlling the process variables. Laser pulse energy is found to be one of the most significant process parameters that influence the deformation profile in laser shock forming processes with mold [83, 84, 90]. Thus, experiments were performed initially with different

laser fluence values ranging from 1 J/cm^2 to 21 J/cm^2 to analyze the corresponding deformation on metal foils in FPLSF.

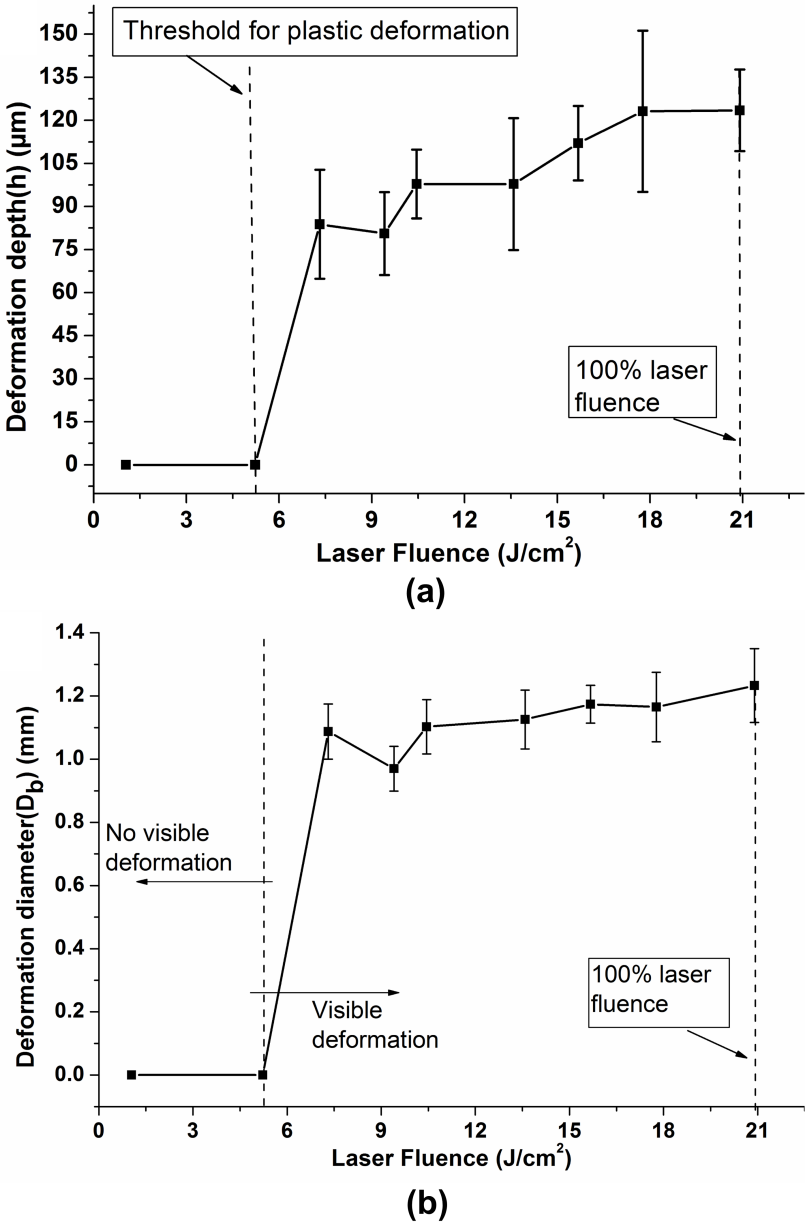

Figure 3.7: Effect of laser fluence on the geometry of craters formed on copper foil (a) Deformation depth (h) (b) Deformation diameter (D_b)

The deformation depth (h) and diameter (D_b) of the formed craters are illustrated in Fig. 3.7. It is found that microcraters of depth ranging between 80 µm and 130 µm were formed on copper foils for the laser fluence varying between 7.3 J/cm^2 and 20 J/cm^2. The relationship between the laser fluence and the deformation depth is approximately linear with the depth increasing along with the fluence

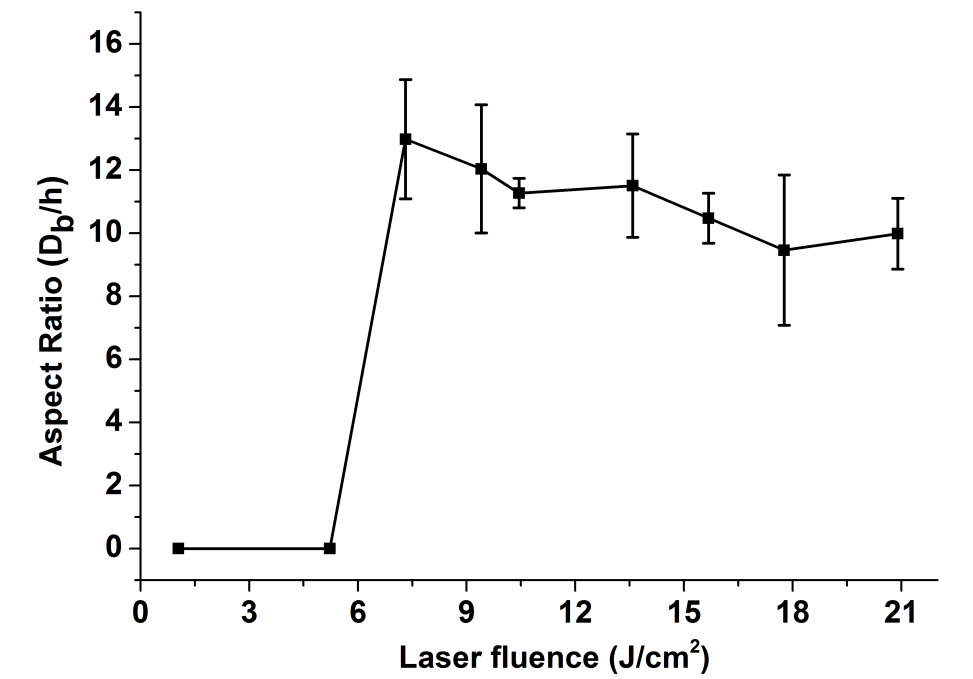

Figure 3.8: Effect of laser fluence on the aspect ratio (D_b/h) of the craters formed on copper foil

(Fig. 3.7). According to Fabbro's model, the plasma-induced shock pressure is dependent on the laser intensity [160]. Therefore, the increase in depth can be attributed to the increase in shock pressure exerted on the metal foil.

Experimental results as shown in Fig. 3.7 illustrate that copper foil experienced no plastic deformation until a certain threshold of laser fluence (5.2 J/cm^2) is exceeded. The rationale behind this non-existing plastic deformation is limited to the following two aspects:

(i) The absorbed laser energy is insufficient to vaporize the aluminum foil so that no plasma and shockwave formation are experienced.

(ii) The shock pressure induced at the applied laser fluence is lesser than the yield strength of copper to induce the plastic deformation of metal foils.

The second hypothesis related to the shock pressure was examined first. The induced shock pressure calculated from Fabbro's model (Eqn. 2.8) for 5.2 J/cm^2 is 167 MPa, which is nearly twice the yield strength of copper (90 MPa). Thus, it is evident that the plastic deformation threshold was not influenced by the shock

pressure in this experiment. Henceforth, the first hypothesis of ablative overlay vaporization was verified further by examining the aluminum foil surface. The vaporization behavior of aluminum foil and copper foil crater formation at 5.2 J/cm^2 laser fluence is illustrated in Fig. 3.9. It is clear from Fig. 3.9a that no melting/vaporization of aluminum foil was experienced and hence no crater formation at 5.2 J/cm^2 fluence.

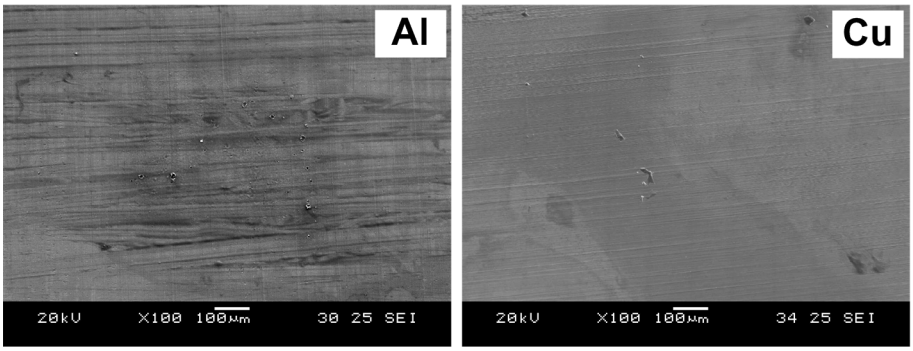

Figure 3.9: Influence of aluminum foil vaporization on crater formation in copper foil at 5.2 J/cm^2 (a) SEM image of aluminum foil top surface (b) SEM image of copper foil top surface

The diameter of the deformation craters (D_b) was also found to increase along with the laser fluence as shown in Fig. 3.7b. The minimum deformation diameter obtained was approximately 1 mm for the lowest laser fluence that induced plastic deformation (7.3 J/cm^2). With increase in laser fluence, combined occurrence of following behaviors are expected: heat conduction to non-irradiated regions, increase in shockwave amplitude along with propagation to a wider distance, and larger deformation of flexible pad. These behaviors can also be attributed to the increase in deformation depth along with the laser fluence. It is observed from Fig. 3.7 that the maximum deformation depth and diameter were experienced for 20.9 J/cm^2 fluence which is the maximum laser output energy, i.e. 100% laser fluence. A minor deviation of deformation diameter from the increasing trend was observed at 9.4 J/cm^2 fluence. This effect can be attributed to the unstable first laser pulse and the non-uniform vacuum grease thickness. However, while considering the standard deviation of the diameter values, the increasing tendency of the average

deformation diameter can be still detected.

It is noticed from Fig. 3.8 that the aspect ratio (D_b/h) of the craters reduced with the increase in laser fluence. Comparing Fig. 3.7a and Fig. 3.7b, it can be identified that the increase in depth (h) was greater than the increase in diameter (D_b) for the increase in laser fluence. The most significant parameters for the deformation depth and diameter are found to be laser fluence and beam profile respectively. As laser fluence is changing and beam profile is constant, it is obvious that the variation in depth is larger than that of diameter. Also, in FPLSF, as the shockloading is applied on the foil surface along the axial direction, the shockwave propagation is expected to be faster axially than in radial directions, causing large increase in depth.

The topographic surface integrity of the fabricated components is a major requirement in the microfabrication industry. The top surfaces of the formed crater at two different laser fluences are compared in Fig. 3.10. It is evident that the crater surface is free of ablation, debris, melt zones, or wear marks, highlighting the competence of FPLSF to produce damage-free surfaces.

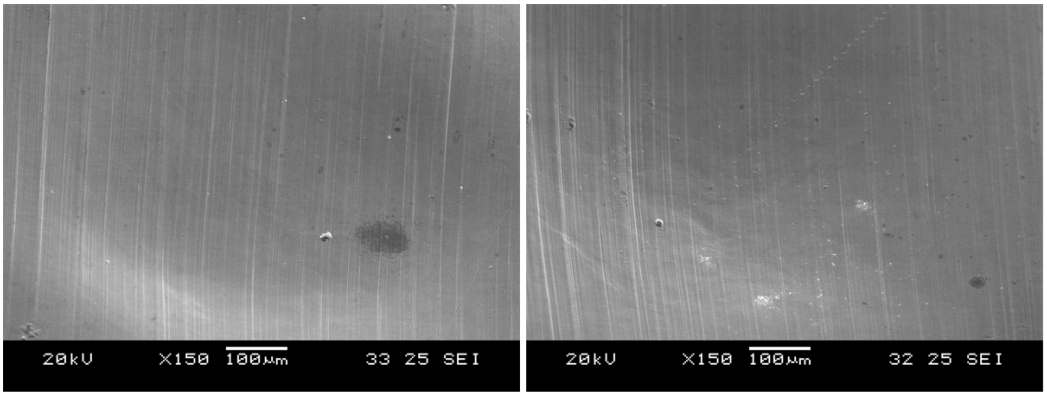

Figure 3.10: Topographic Surface integrity of the crater surfaces at different laser fluences (a) 7.3 J/cm^2 (b) 20.9 J/cm^2

3.5 Fabrication of crater arrays

The reproducibility of FPLSF is demonstrated by fabricating an array of craters on copper foils. Fig. 3.11 shows the surface topography and SEM images of the craters at the laser fluence of 7.3 J/cm^2. Smallest laser fluence of 7.3 J/cm^2 for which deformation is minimum and pitch length of 1.5 mm were used to fabricate the craters as the 3x3 array. The standard deviation of deformation depth between the individual craters of the formed array was measured to be 19.8 μm. Thus, it is evident that the formed craters were uniform in shape and size indicating the controllability of FPLSF process to produce uniform microfeatures on thin metal sheets. As the crater diameter was greater than 1 mm, the pitch length of 1.5 mm was used between the array craters to avoid the interference of shockwaves propagating from adjacent irradiation spots. By reducing the beam sizes, generation of crater arrays with narrow pitch length is feasible due to the reduction of individual crater diameter. The deviation between the formed craters was due to the instability of the first pulse, minor variation in focus and the non-uniform thickness of the vacuum grease applied between copper foil and the ablative overlay.

3.6 Process flexibility

The ability of the process to fabricate different crater sizes was demonstrated earlier by varying the laser fluence. However, only a minor difference in crater diameter was observed as it depends mainly on the laser beam size. Therefore, different beam profiles have been tested to study the capability of the process to fabricate different feature shapes and sizes.

In this experiment, FPLSF process was conducted using a fiber laser (wavelength - 1090 nm, Gaussian beam, pulse duration - 42 ns, frequency - 12KHz, output power- 200W). Fig. 3.12 shows the 3D profile of the craters measured by the confocal scanning microscope and the optical microscopic image of the crater bottom surface. It is evident that the craters with depth less than 30 μm and

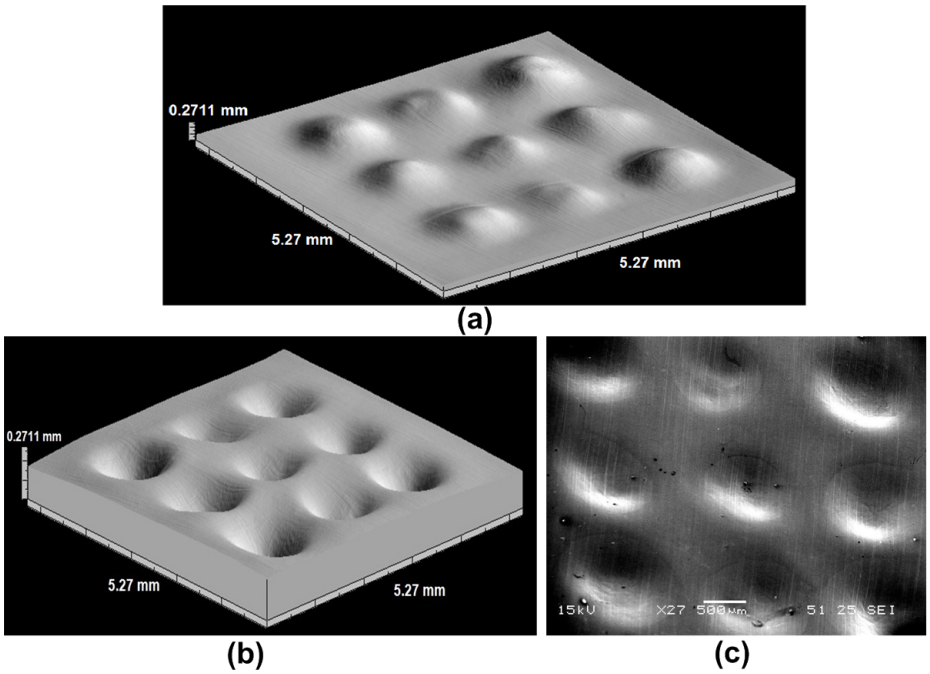

Figure 3.11: Crater arrays on copper foil at the laser fluence of 7.3 J/cm^2; (a) Topography of the formed craters at the bottom surface (b) Topography of the formed craters at the top surface (c) SEM image (30° tilt) of the top surface of the craters

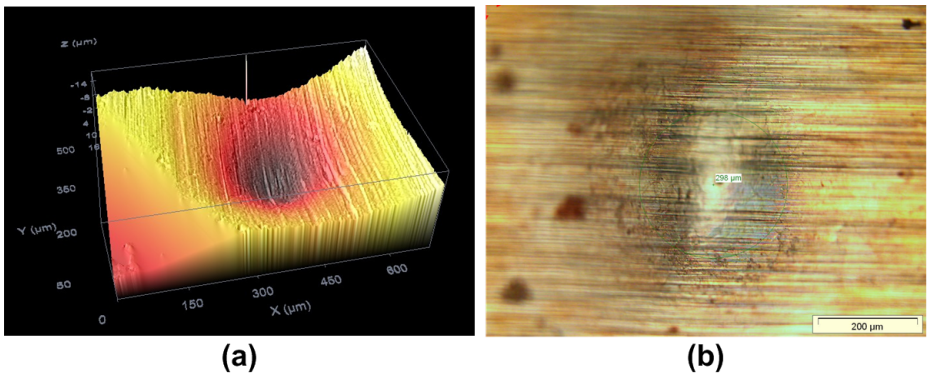

Figure 3.12: Craters formed on copper foils using Fiber laser (a) 3D profile of the crater (b) Microscopic image of crater bottom surface

diameter smaller than 250 μm were produced on copper foils.

In addition to copper, FPLSF produced microcraters on other substrate materials such as nickel and high strength stainless steel, which will be discussed in later part of this chapter. The process capability can also be improved with in-depth knowledge on the different process parameters, which will be explored in the remaining parts of this thesis.

3.7 Process mechanisms

Fabrication of deformation features in FPLSF involves different process mechanisms as summarized in Fig. 3.13. The entire FPLSF process can be classified mainly into two different mechanisms:

1. Laser-material interaction that induces shockwaves

2. Plastic deformation of metal foils and elastic deformation of flexible pad.

These two behaviors, shockwave formation and deformation of metal and flexible pad are mostly independent. Fig. 3.14 represents the sequence of mechanisms involved in FPLSF. The different processes involved at each stage is detailed below:

- Once the laser is applied, it passes through the confinement layer which is placed at the top of the process configuration. The intensity of the laser beam (I_1) after passing through the confinement is expressed by Beer-Lambert law, $I_1 = I_0 e^{-\alpha x}$, where I_0 is the initial laser intensity(W/cm^2), α is the absorption coefficient of the confinement medium ($m^{-1)}$) , and x is the thickness of the confinement (m) . The typical confinement mediums are almost transparent to the laser beam at the wavelengths used in this analysis, as evidenced from the transmittance of different materials at various wavelengths (Fig. 3.3b).

- The laser beam exiting the confinement layer hits the ablative overlay surface. A part of the beam is reflected from the surface (as indicated from the reflectivity (R) of materials at Fig. 3.3a) whereas the remaining energy is absorbed by the material. The intensity of the beam absorbed by the ablative overlay material is given as, $I_2 = I_1(1 - R)$.

  The temperature (T) generated at the top surface at time t is calculated from the following formulation [188]:

$$T(0,t) = \frac{2I_2}{k}\left[\frac{\alpha_t t}{\Pi}\right]^{0.5} \tag{3.1}$$

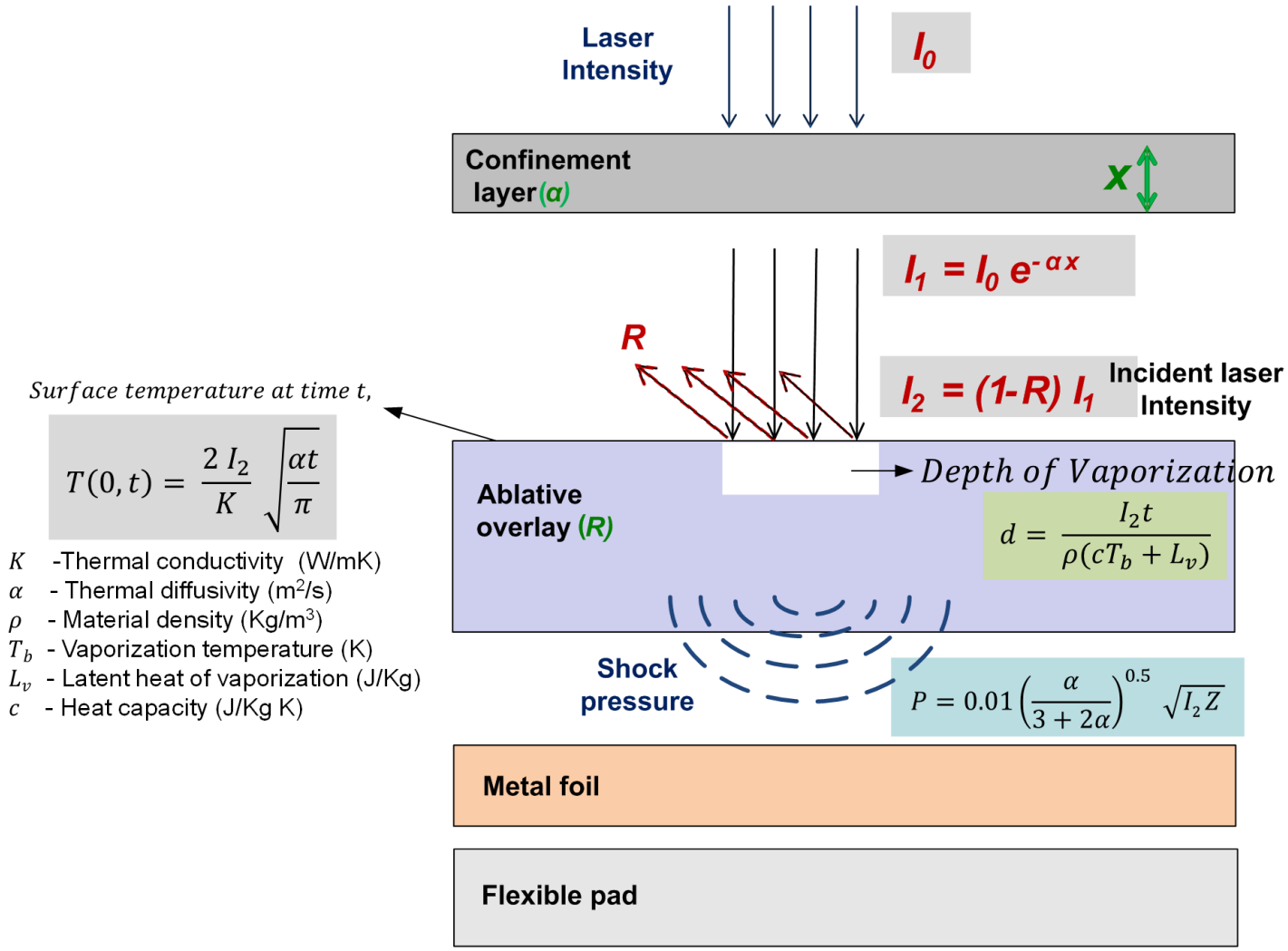

Figure 3.13: Schematic illustration of different process mechanisms involved in FPLSF (The spaces between the process components are exaggerated for the illustrative purpose)

where I_2 is the absorbed laser intensity by the ablative overlay, k is the thermal conductivity (W/mK), and α_t is the thermal diffusivity of overlay (m^2/s). If the temperature generated on the top surface reaches the boiling point, the material starts vaporizing. The depth of the vaporization (d) on target material can be measured from [108],

$$d = \frac{I_2 t_p}{\rho[C_P(T_b + L_v)]} \tag{3.2}$$

where t_p is the laser pulse duration (s), ρ is the material density (kg/m^3), C_P is the specific heat capacity (J/kgK), T_b is the boiling temperature (K), and L_v is the latent heat of vaporization (J/kg). It is noted that the vaporization depth depends upon the laser intensity and the pulse duration in addition to the inherent material properties.

- Once the generated vapor along the overlay surface is further heated by the laser beam, it is transformed into high pressure, high temperature plasma rapidly. In high power laser conditions, as used in this experiment, vaporization occurs instantaneously due to the excessive laser energy. The intensity of plasma formation is a factor of the volume of vaporization.
- Subsequently, the pressure difference between the inner and outer plasma regions results in the expansion of the plasma along the available region between the confinement and the ablative overlay. The plasma expansion depends upon various factors as discussed in section 2.4.5.
- As the plasma expansion is constricted by the confinement layer and the metal foil, shockwaves are induced in both the directions axially [160]. The shockwave directed towards the metal transfers the momentum to the foil.
- The plastic deformation of the metal foil is initiated once the induced shock pressure on the top surface exceeds the yield strength of the material. As the flexible pad is an elastic polymer, it deforms readily along with the displacing metal foil. Once the deformation is started at room temperature, its yield

stress tends to increase due to the hardening behavior (as discussed in section 2.5.2). Thus, the further plastic deformation is possible only if the shock pressure is greater than the dynamic yield strength of the material.

- As a result of its elastic properties, the flexible pad retracts to its original position once the metal foil is removed from the pad or loading is stopped, whereas a permanent deformation is induced on the metal foil.

The sequence of the mechanisms involved in FPLSF is illustrated in Fig. 3.14. The schematic of the plastic deformation in FPLSF is illustrated in Fig. 3.15.

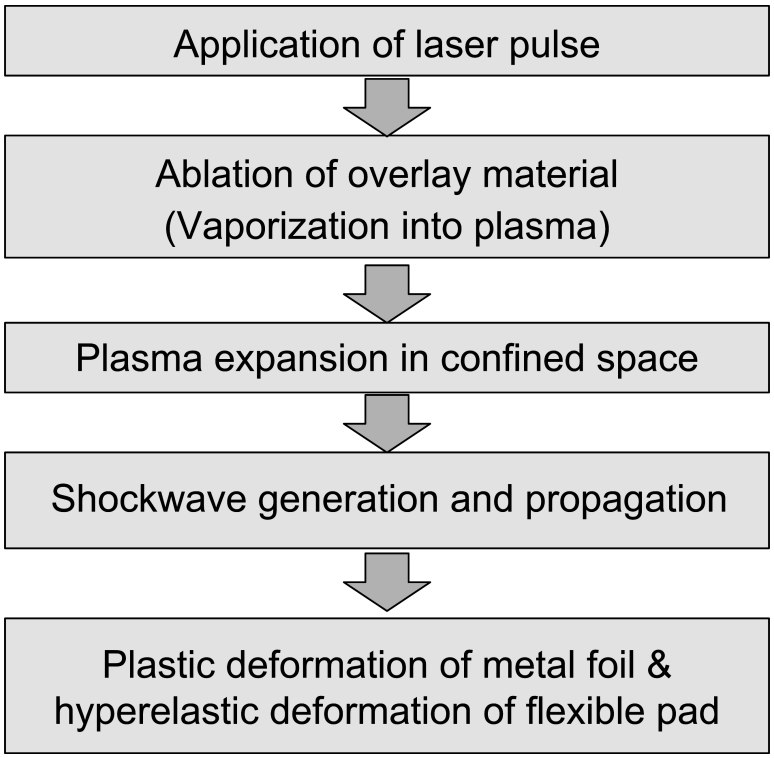

Figure 3.14: Process sequence of FPLSF

3.8 FPLSF - Advantages

The major objective of this thesis has been the elimination or replacement of micro-molds to produce simple 3D microfeatures on metallic materials. While successfully demonstrating the capability to fabricate microfeatures on thin metal foils, the developed technique possesses significant advantages as follows:

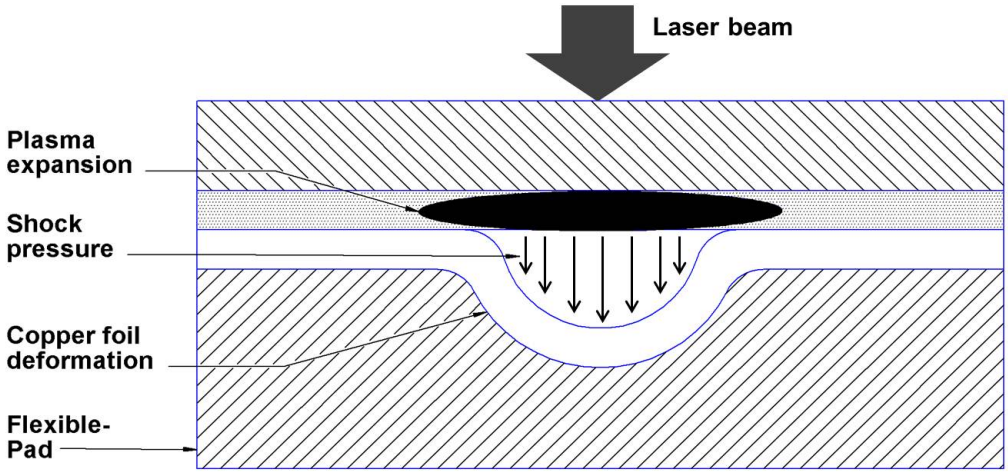

Figure 3.15: Schematic of deformation mechanism in FPLSF

- Primarily, FPLSF does not require the expensive and time-consuming process of mold/punch fabrication to realize the plastic deformation on metal foils while producing microdeformation features
- FPLSF enhances the process flexibility in the microforming domain as different features can be fabricated using simple flat flexible pad through controlling the process parameters, especially laser fluence and beam profiles.
- Though the process cycle time of FPLSF compared to existing microforming processes is largely reduced owing to the elimination of micromold fabrication, the following factors cause a further reduction in the cycle time:
  - No alignment is needed between the process components in FPLSF as required between the dies and punches in deep drawing, and between laser beam and dies in laser dynamic forming processes.
  - As the pulse duration of laser beam is in nanoseconds, the entire deformation process is expected to complete within few nanoseconds/microseconds.
  - As no damage to the flexible pad is observed after shock pressure application, the same pad can be reused for large number of cycles.
- FPLSF involves no major friction between the process components during the deformation of metal foils, which contributes the following benefits:

- Fabricated features has excellent surface integrity as damage-free surfaces are produced with FPLSF, as seen in Fig. 3.10.
- Modeling of the process requires no consideration of frictional effects, which is complicated especially with the microforming due to the presence of size effects.

- The replacement of micromold with the flexible pad in FPLSF provides following significant advantages to the deformation behavior of metal foil:
  - While deforming the metal foils using micromolds, material fracture occurs in the mold fillet region, where the local plastic strains are high [90]. As a flat flexible pad is used in this process, the possibility of stress localization will be reduced thereby minimizing the occurrence of foil fracture.
  - If the forming velocity of the metal foil is higher than a critical velocity, fracture of material takes place [158]. For processes with the micromolds, the forming velocity of the material may reach the critical velocity, as the deformation is not restricted until it reaches the mold bottom. In FPLSF, as the deformation of the metal foil is controlled by the stiffness of the flexible pad, forming velocity of the metal foil is restricted and the occurrence of fracture will be reduced.

In addition to the above-mentioned advantages of FPLSF, significant benefits regarding the material formability, mechanical properties of the deformation features, and the microstructural modifications are expected, which will be investigated in the following chapters.

FPLSF is limited by its incapability to fabricate intricate feature shapes as produced by the processes using micromolds. Nevertheless, the range of feature geometries pertaining to FPLSF can be comparable to a substantial number of existing applications. The benefits of microtexturing, especially micro-dimple surfaces, has been well established in various applications including aerospace, automobile,

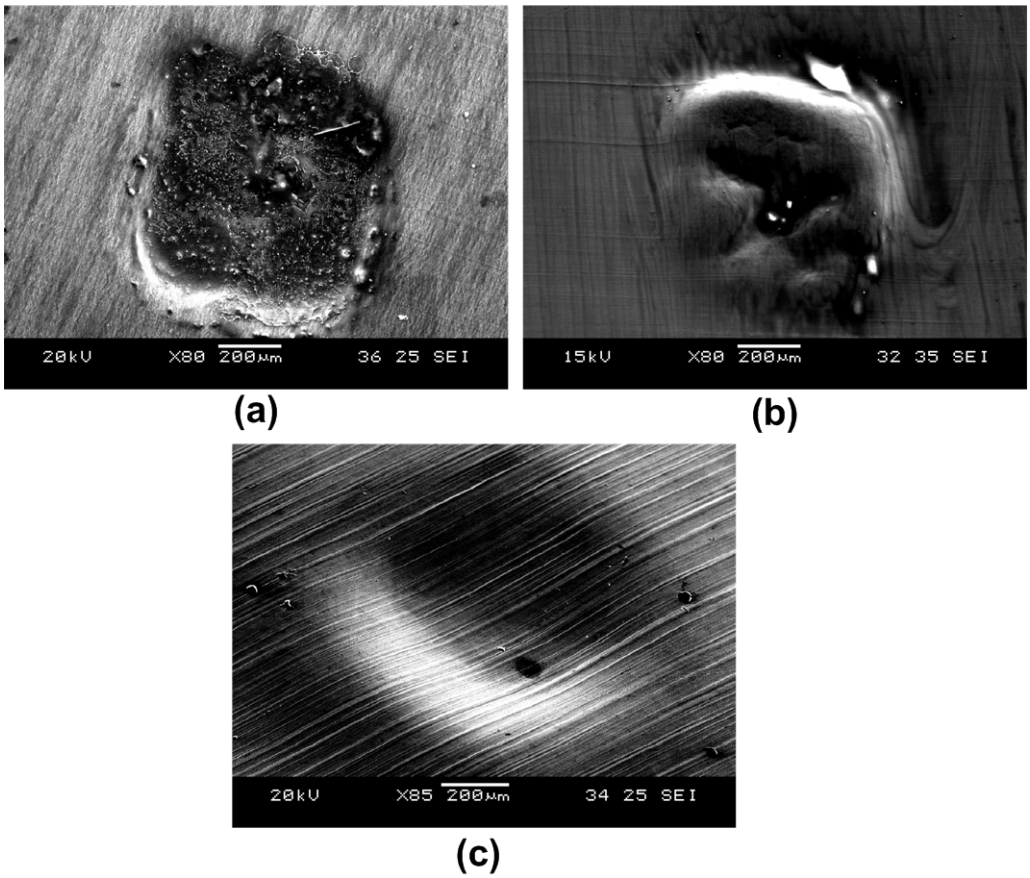

Figure 3.16: Aluminum foil vaporization behavior at laser fluence of 7.3 J/cm^2; SEM image of aluminum foil after FPLSF (a) Top surface (b) Bottom surface ; (c) Crater top surface on copper foil

MEMS devices, and fluidics for their tribological properties [189–191]. Recently, the microtextures acquire an extensive applicability in bioimplants as the dimples and grooves enhance the biocompatibility of implant surfaces due to the improved adherence of the tissues [184]. The fabrication of microsized craters/dimples on metal foils using FPLSF could be deployed for the aforementioned applications. Furthermore, the fabrication of fuel cell components, especially bipolar plates, are produced using processes including rubber pad forming and hydroforming [43, 46, 48]. Due to the similarity of FPLSF to these processes, but with improved process capabilities, the microcomponents can also be fabricated using FPLSF with controlled laser processing parameters. Large area processing of functional components is rapidly growing in recent times using processes like roll-to-roll embossing of large surfaces, where metallic materials are employed as the dies. As FPLSF is an ideal

technique to fabricate identical microfeatures (microdimples) on large surfaces at a faster rate, it can be used to produce metallic microdies for embossing polymer substrates.

3.9 Inferences

Following inferences can be deduced from FPLSF experimentation:

1. Vaporization depth of ablative overlay is identified to be an important parameter in producing the deformation features. Fig. 3.17 illustrates different possible cases of overlay vaporization and the corresponding influence on shockwave propagation. If the entire thickness of ablative overlay is not vaporized, shockwave propagates from the irradiated overlay surface rather than at the metal foil surface, as seen in Fig. 3.17a. Vaporization of only the top portion of aluminum foil at 7.3 J/cm^2 can be observed from Fig. 3.16a. Shockwave propagating from aluminum foil also induced plastic deformation on aluminum foils as seen in Fig.3.16b. This partial vaporization of ablative overlay is the reason for the formation of crater with no thermal damage to the copper surface at 7.3 J/cm^2 fluence (Figs. 3.16c and 3.10a). This behavior will be investigated in detail at section 3.10.3.1.

2. For higher laser fluence (20.9 J/cm^2), the entire thickness of the aluminum foil was ablated as shown in Fig.3.18a. It is interesting to observe from Fig.3.18 that the craters were formed on copper foil with no significant thermal damage despite the direct exposure of copper surface to the laser beam (as illustrated in Fig. 3.17b). This damage-free copper surface at 20.9 J/cm^2 as witnessed from Figs. 3.18 and 3.10b could be attributed to the following aspects:

   (a) High reflectivity of copper at 1064 nm wavelength (88%) may reduce the absorption of laser by copper surface and any possible melting or vaporization.

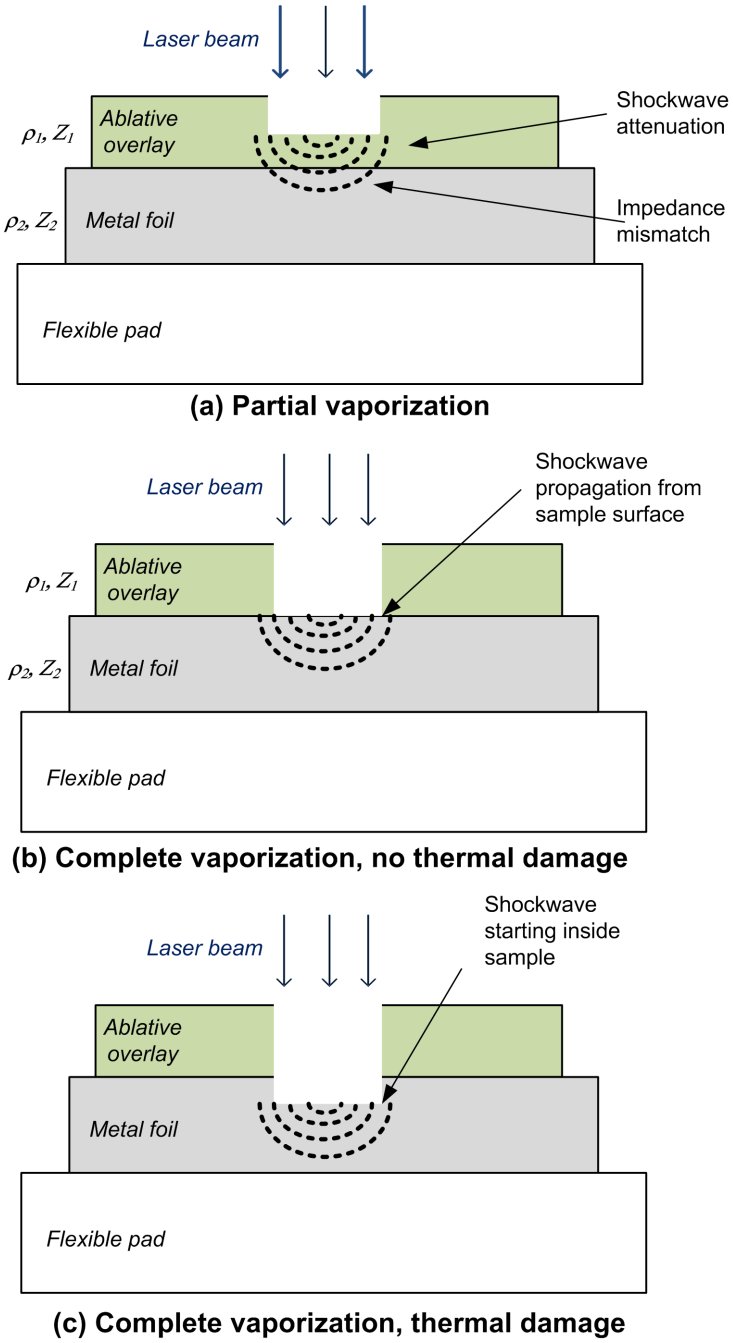

Figure 3.17: Different cases of overlay vaporization and the corresponding shockwave propagation (a) Partial vaporization of overlay thickness (b) Complete vaporization of thickness, with no thermal damage (c) Complete vaporization of thickness, with thermal damage

(b) Any possible melt debris of aluminum foil on the copper surface will be solidified instantaneously as the melting point of aluminum (660.4°C) is lesser than the melting point of copper (1085°C).

(c) Vacuum grease which is present between the copper and aluminum foils

prevents the aluminum debris to contact the copper surface and also vaporized upon interaction with the laser

Therefore, it is understood that the vaporization of aluminum foil has a significant role in FPLSF to produce damage-free surface of the deformation features.

3. The absence of plastic deformation as a result of insufficient shock pressure is due to one or more of the following two behaviors:

   (a) At smaller fluence, vaporization volume is lesser causing a reduction in plasma density and hence the insufficient shock pressure.

   (b) The shockwave attenuation within the thickness of ablative overlay (Fig. 3.17) results in a larger reduction of shock pressure.

4. It has to be highlighted that the plasma formation, expansion, and the shockwave propagation occurs simultaneously during the process. Once the shockwave is impacted on the material, the metal foil starts deforming. As the overlay is sealed to the metal foil, it displaces along with the foil. This displacement of overlay surface could induce the following effects:

   (a) Once the overlay is repositioned, the interface between the overlay and confinement is enlarged, allowing the expansion of plasma to occur more easily. This effect may reduce the magnitude and the duration of the shockpressure.

   (b) Alternatively, instead of spreading over a larger area (similar to the beam area), the plasma could be trapped inside the hemispherical crater adopted by the displaced overlay. This entrapment may provide effective confinement for plasma, thereby increasing the magnitude and duration of the shockpressure.

   (c) There will be defocussing of ablative overlay surface upon its displacement due to the first laser pulse. When the next pulse is irradiated, the

defocussed beam may not induce enough vaporization for the plasma formation.

5. The entire deformation process is completed within few microseconds (also confirmed by the finite element analysis as discussed in Chapter 6). The behavior of metal deformation during subsequent laser pulses is intriguing to explore.

The rest of the thesis will explore some of the above-mentioned behaviors/hypotheses in order to understand the developed process.

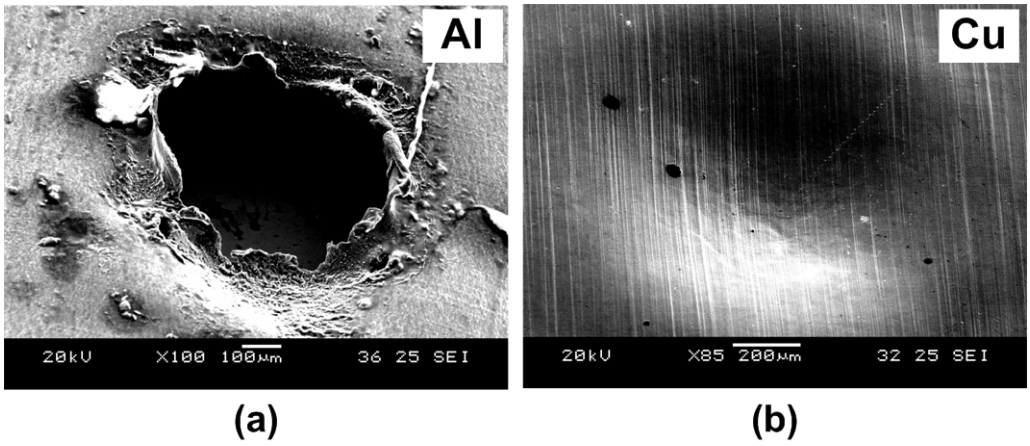

Figure 3.18: (a) SEM image of aluminum foil (thickness - 15 μm) top surface at 20.9 J/cm^2 (b) Copper foil (thickness - 25 μm) top surface

3.10 FPLSF - Parametric Study

The significance of various process variables on the fabrication of deformation features in FPLSF is investigated in this section.

3.10.1 Effect of foil material

The influence of substrate foil material on the crater formation in FPLSF is analyzed at the following conditions: foil thickness - 25 μm; confinement - water (4 mm); ablative overlay - aluminum (15 μm); flexible pad - silicone rubber (0.3 mm); number of laser pulses - 45. The crater depth at various laser fluences has been

compared for copper and stainless steel in Fig. 3.19a. For the laser fluence varying from 7.3 J/cm^2 to 20 J/cm^2, the deformation craters with depth ranging between 29 μm and 48 μm were formed on stainless steel foils, in comparison to craters deeper than 80 μm with copper foils. It is obvious that the amount of plastic deformation reduces with the increase in material strength. However, the diameter of the craters showed little variation between copper and stainless steel foils as seen in Fig. 3.19b. This behavior can be attributed to the fact that the vaporization of the ablative overlay and the subsequent shockwave propagation are identical in both the cases.

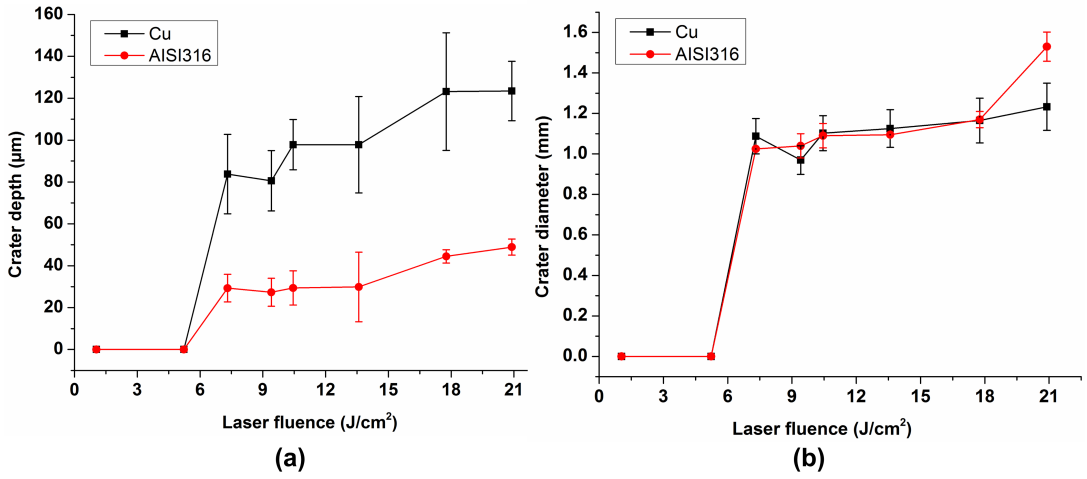

Figure 3.19: Effect of substrate foil material on (a) Crater depth (b) Crater diameter at different laser fluences

3.10.2 Effect of number of pulses

The crater formation on copper foil between single pulse and 45 pulses has been compared with the following parameters in this analysis: confinement - water (4 mm), flexible pad - silicone rubber (0.9 mm); ablative overlay - aluminum (15 μm). Fig. 3.20 compares the top surfaces of the aluminum foil ablative overlay and the deformation crater on copper foil between one pulse and 45 pulses. It is evident from the observations that the single pulse irradiation had been sufficient to produce the deformation crater. The deformation feature size is found to increase along with an increase in number of pulses. When the number of pulses was increased to 45,

the crater diameter increased by about 25 % to that of one pulse as witnessed from Figs. 3.20b and 3.20c. The increase in crater diameter was corresponding to the larger depth and area of aluminum foil vaporization with increase in laser pulses to 45, which is shown in Fig. 3.20a. Multiple pulses vaporizes more overlay material, resulting in an increased plasma formation and subsequent propagation along the radial direction. This phenomenon is attributed to the larger crater diameter at 45 pulses.

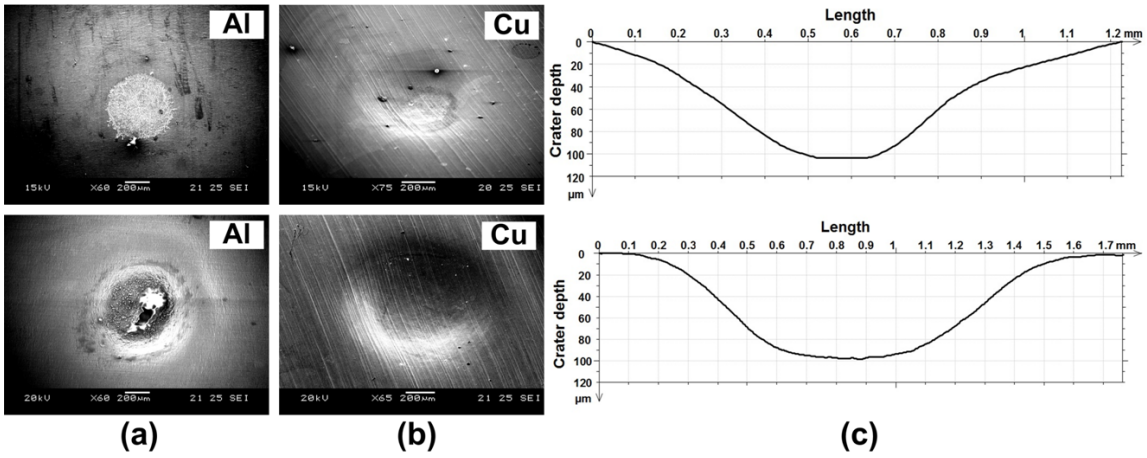

Figure 3.20: Comparison of crater formation on copper foil between single pulse (top) and 45 pulses (bottom) irradiation at 13.6 J/cm^2 laser fluence: (a) SEM image of aluminum foil top surface (b) SEM image of the crater top surface on copper foil (c) Cross-sectional profile of the crater at its center

The comparison of deformation depth and top surface hardness (measurement procedure as detailed in 5.2.2) of the craters between one pulse and 45 pulses for various laser fluences is presented in Fig. 3.21. For the laser fluence of 20.9 J/cm^2, the crater depth was observed to increase from 113.2 μm to 123.5 μm with the increase in number of pulses from single to 45 pulses, as seen in Fig. 3.21a. Thus, it is evident that more than 90% of the final depth of the formed crater was achieved during the first pulse itself. This behavior of smaller increase (<10%) in crater depth during subsequent laser pulses is attributed to one or more of the following effects:

- Once the foil deformation is initiated upon the first pulse, yield stress of the material increases due to workhardening behavior. This effect is evident from

Fig. 3.21b where the hardness of the top crater surface after the first pulse is higher than the hardness after multiple pulses. The reduction in hardness with the multiple pulses could be due to the direct heating of copper surface as the overlay aluminum foil was completely vaporized. Due to workhardening of foils after the first pulse, further plastic deformation during the subsequent pulses is restricted and only a small increase in crater depth was observed.

- During foil deformation with the first pulse, the aluminum foil overlay displaces along with the copper foil as both foils are firmly sealed together using the vacuum grease. This movement of aluminum foil provides a defocussing effect during subsequent pulses and reduces the laser intensity on the aluminum foil surface. This would have caused lesser vaporization and hence smaller increase in crater depth after the first pulse.

3.10.3 Ablative Overlay

3.10.3.1 Ablative overlay material

The selection of ablative overlay, the sacrificial coating, is based on several material properties including absorption coefficient (higher is better), heat of vaporization (low), thermal conductivity (low), and acoustic impedance (high). The literature review identified the graphite based materials, especially, the black paint coating as one of the commonly used absorbent coatings/layers in laser shock processing. Thus, commercially available black paint was tested initially. The paint was manually applied over the metal foil, with thicknesses ranging between 15 μm to 45 μm. It is evident from Fig. 3.22a that the black paint coating demonstrates better absorption behavior as the effective area of vaporization (~ 1500 μm) was observed to be almost 2.5 times larger than the beam size of 600 μm. However, following limitations are identified with black paint as the ablative overlay in FPLSF:

- As the diameter of the deformation feature depends upon the vaporization area of the overlay, maintaining the feature diameter closer to the laser beam

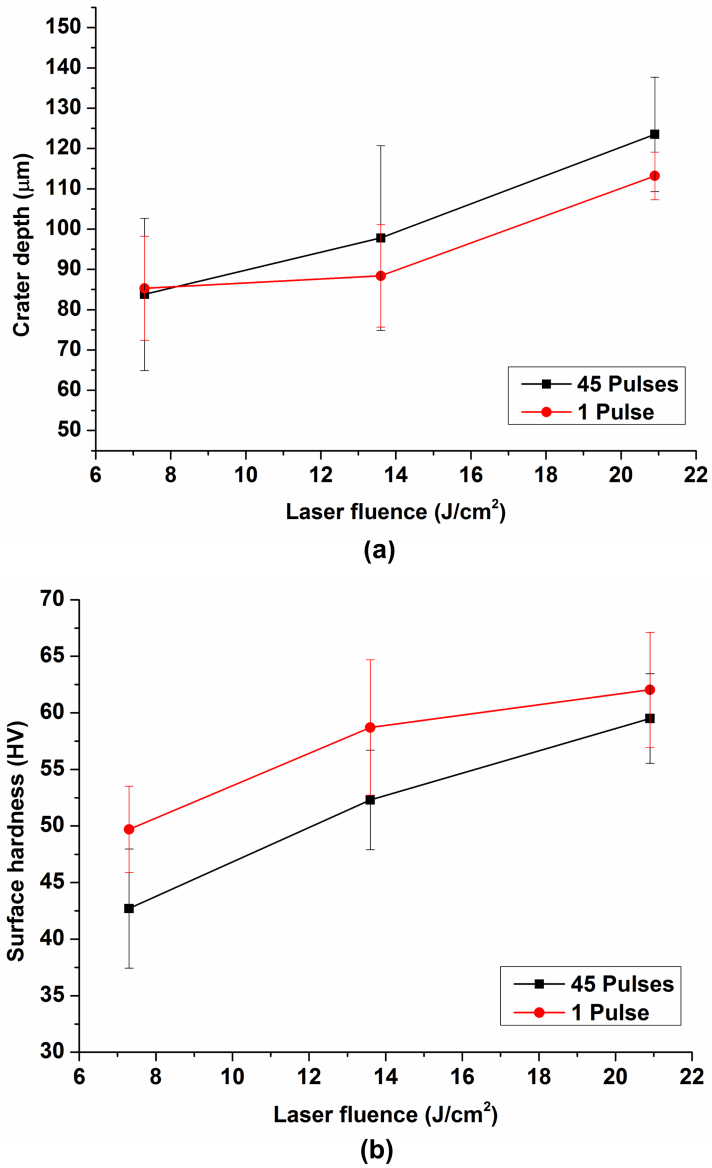

Figure 3.21: Comparison of deformation craters between one pulse and 45 laser pulses (a) Crater depth (b) Crater top surface hardness

size is difficult with black paint due to the larger vaporization.

- Fabrication of closer-distance features, such as arrays or continuous patterns, is not possible as the enlarged vaporization hinders the irradiation at adjacent regions.
- Multiple pulse irradiation require thicker coatings or reapplication of paint between successive pulses.
- Practical limitations were encountered with controlling the thickness of the paint and its uniformity.

- Chemical cleaning is required to remove the black paint from the formed component.

Aluminum foil has also been used as the sacrificial layer in laser-induced shock processes. Thus, aluminum foil with thicknesses ranging between 15 μm and 25 μm thickness has been tested as the ablative overlay in this study. As evident from Fig. 3.22b, aluminum foils have the vaporization area close to the laser beam area of 600 μm x 600 μm during laser irradiation. In comparison, the extent of vaporization with aluminum foil has been at least two times lesser than with black paint as compared in Fig. 3.22. Thus, smaller craters can be produced with aluminum foil. In addition, aluminum foil is optimum to produce features adjacently, as demonstrated in the fabrication of arrays (3.5). More importantly, aluminum foil can be peeled off easily from the deformed foil surface after the completion of the laser shock forming, unlike other ablative materials, paint coatings and black tape, which are hard to remove from the foil surface.

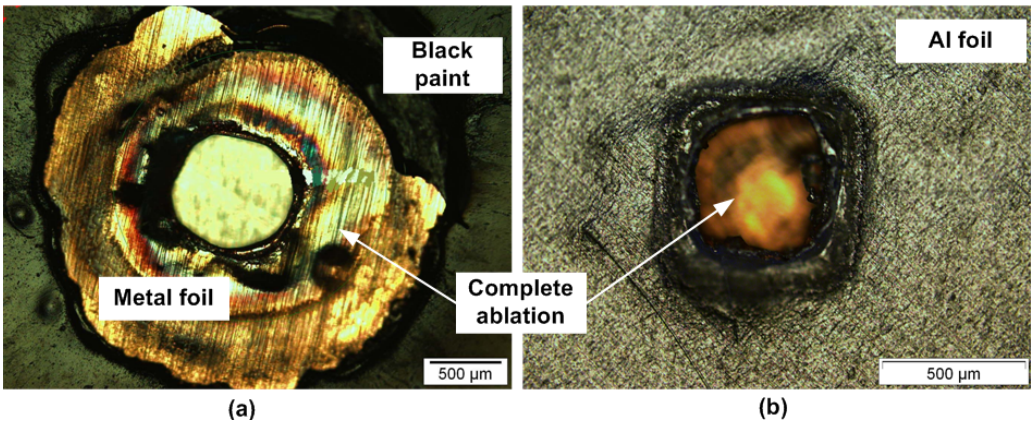

Figure 3.22: Comparison of vaporization behavior between different ablative overlay materials (a) Black paint (b) Aluminum

3.10.3.2 Ablative overlay thickness

Investigation of ablative overlay thickness was conducted at the following conditions: substrate - copper (15 μm); confinement - water (4 mm); flexible pad - silicone rubber (0.9 mm); ablative overlay - aluminum (15 μm); defocussing - +1 mm; number of laser pulses - 45. Fig. 3.23 compares the crater depth on copper foil

between two different thicknesses of ablative overlay with change in laser fluence. Interestingly, two different behaviors corresponding to the ablative overlay thickness were observed over the range of laser fluence tested. For the smallest laser fluence of 7.3 J/cm^2, larger crater depth occurred with the thicker 25 μm overlay thickness. Whereas, with increase in laser fluence (greater than 13.6 J/cm^2), deeper craters were produced with smaller overlay thickness of 15 μm. In order to analyze these results further, it is essential to outline the behaviors pertinent to the overlay thickness vaporization. When the laser is irradiated on the ablative overlay, either complete or partial vaporization of its thickness is observed depending upon the laser fluence, as discussed in the section 3.8. When the entire thickness of ablative overlay occurs, the shockwaves are directly applied on the substrate foil (Figs. 3.17b and c). Meanwhile, as illustrated in Fig. 3.17a, the partial vaporization of thickness imparts two contrasting mechanisms which occur concurrently, as follows:

1. When the shockwave passes through the remaining thickness of the overlay, there will be attenuation of shockwaves before reaching the metal foil. Additionally, a part of the induced shock pressure is also consumed by the plastic deformation of aluminum foils. The shockwave attenuation causes a reduction in shock pressure and hence a reduction in the deformation size.

2. When the shockwave propagating through the overlay contacts the substrate material, the difference in impedance of the materials will impart the "impedance mismatch" effects. In FPLSF conditions, the impedance of aluminum overlay (Z_1= 1.5 x 10^6) is lesser than the copper substrate (Z_2= 4.2 x 10^6), an increase in pressure magnitude is expected when the shockwave reaches the copper surface which will increase the deformation size subsequently.

These two contradictory behaviors, shockwave attenuation and pressure enhancement as a result of partial vaporization of ablative overlay, influence the process outcomes. It is obvious that the vaporization depth of overlay upon irradiation is

identical, irrespective of its thickness. Thus, with thicker overlays, the shockwaves pass through the remaining thickness, causing a reduction in shock pressure and hence crater depth. The aforementioned shockwave attenuation resulted in the reduction of crater depth with 25 μm overlay thickness as observed in Fig. 3.23.

Larger crater depths at 7.3 J/cm^2 fluence for 25 μm could be possible only if two following behaviors occur simultaneously:

- The thinner overlay is completely vaporized and shock pressure applied directly on the metal foil.
- Partial vaporization with thicker overlay results in pressure enhancement larger than the shockwave attenuation.

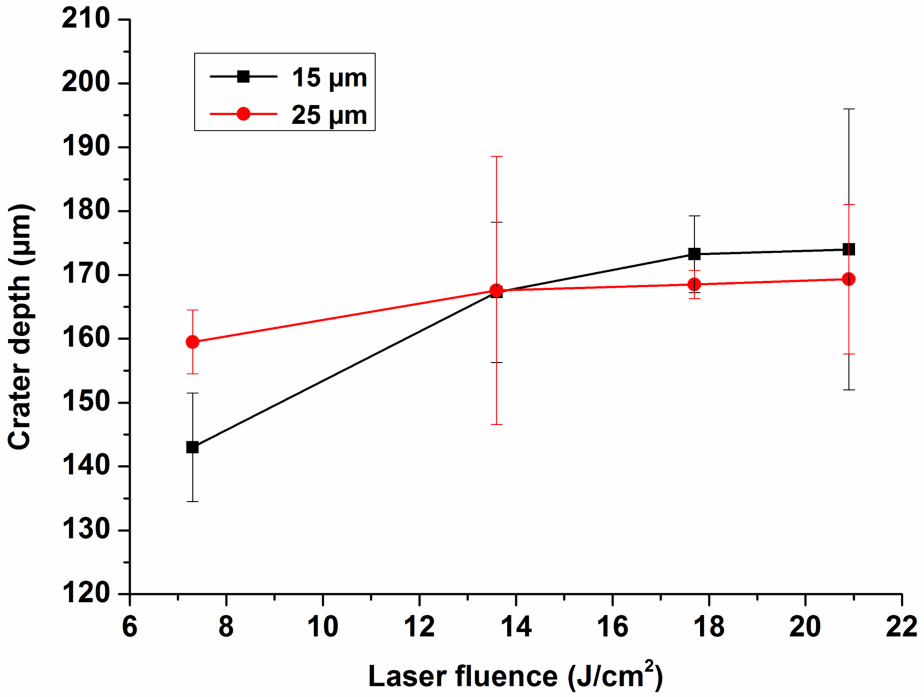

Figure 3.23: Effect of ablative overlay thickness on crater depth

3.10.4 Confinement Layer

3.10.4.1 Confinement medium

Fused silica glass and deionized water confinements were investigated at three different laser fluence values (7.3 J/cm^2, 13.6 J/cm^2 and 20.9 J/cm^2) . The thick-

nesses of glass and water confinements were 4 mm and 6 mm respectively. The other processing conditions are as follows: flexible pad - silicone rubber (0.9 mm); defocussing - +1 mm; number of pulses - 45. The depth, diameter, and shape of the deformation craters are compared between glass and water confinements in this analysis.

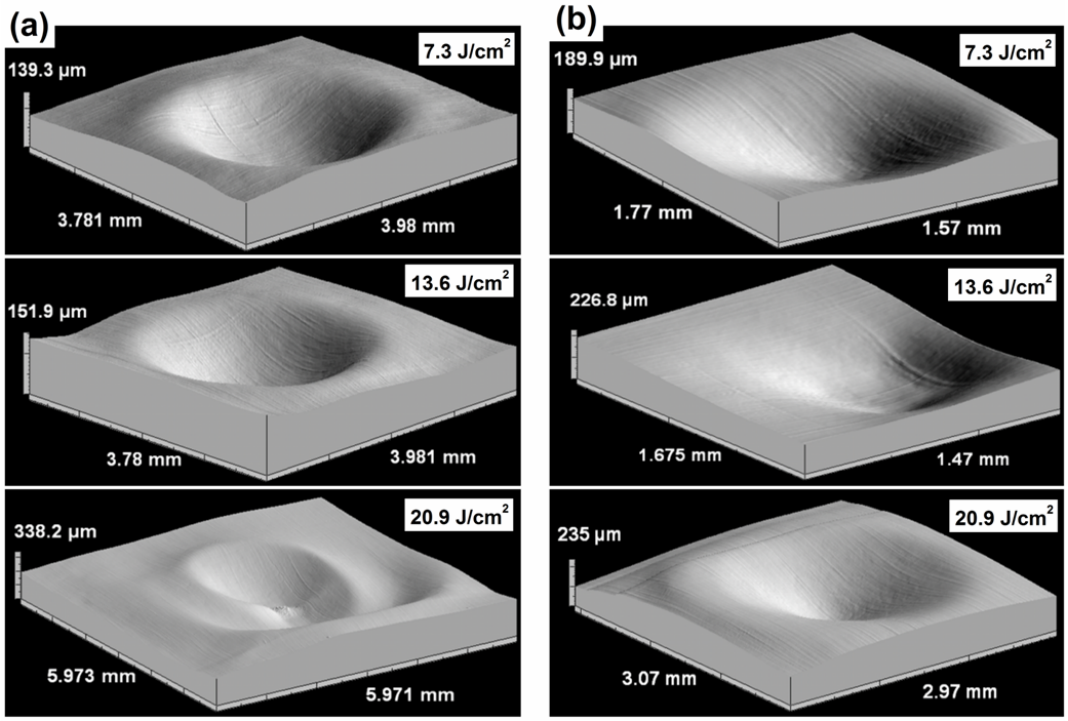

Figure 3.24: Surface topography of the craters formed by FPLSF with (a) Glass confinement (b) Water confinement

The surface topography of craters formed at different laser fluences for water and glass confinements is compared in Fig. 3.24. It is evident that, hemispherical craters were formed at all laser fluence levels tested when using the water confinement. In case of glass confinement, though the lesser laser fluence (7.3 J/cm^2 and 13.6 J/cm^2) produced hemispherical craters, feature shapes identical to shockwave ripples were formed on the copper foils at 20.9 J/cm^2 fluence as shown in Fig. 3.24a. This behavior is identified to be influenced by the difference in vaporization behavior of aluminum overlay between water and glass confinements, which is shown in Fig. 3.25. As the transmittance of fused silica glass (94%) is higher than that of water (81%), incident laser energy on the ablative overlay is higher with

glass. As a result, the aluminum foil overlay was completely ablated for all laser fluences, as shown in Fig. 3.25a, exposing the copper foil to the laser beam. This induced the vaporization of the copper foil top surface, as shown in Fig. 3.26a for 13.6 J/cm^2 and Fig. 3.26b for 20.9 J/cm^2. Severe vaporization of the copper foil surface at 20.9 J/cm^2 with glass (Fig. 3.26b) induces the shockwaves to propagate starting from the vaporized depth of the copper foil, instead of propagating from the surface. This behavior could have resulted in the the difference in feature shapes, especially the shockwave ripples with glass confinement. This formation of shockwave structures on the copper foil can also be attributed to the wave guidance of the shockwave by the glass. Furthermore, the plasma propagation will have a significant impact on the foil deformation features, the effect of which will be analyzed in the next chapter. Meanwhile, damage-free crater surface was produced with water confinement even at the maximum laser fluence of 20.9 J/cm^2 (Fig. 3.26d).

The depth and diameter of the craters for water and glass confinements are compared in Fig. 3.27. For both water and glass confinements, an expected increase in depth and diameter of the craters along with the laser fluence was identified in correlation with laser-induced shock pressure. When comparing crater depth between water and glass, larger depth was observed with water confinement for laser fluences 7.3 J/cm^2 and 13.6 J/cm^2 as seen in Fig. 3.27a. This is an interesting observation as deeper craters were expected with glass confinement due to the following factors:

- According to Fabbro's shock pressure model, induced shock pressure is directly proportional to shock impedance of the target and confinement materials [160]. As shock impedance of glass (1.3 x 10^6 $gcm^{-2}s^{-1}$) is greater than shock impedance of water (0.165 x 10^6 $gcm^{-2}s^{-1}$), induced-shock pressure is higher with glass, hence deeper craters are expected.
- Due to the higher transmittance of glass than water, incident laser energy is larger at the ablative overlay surface with glass confinement. Thus, higher

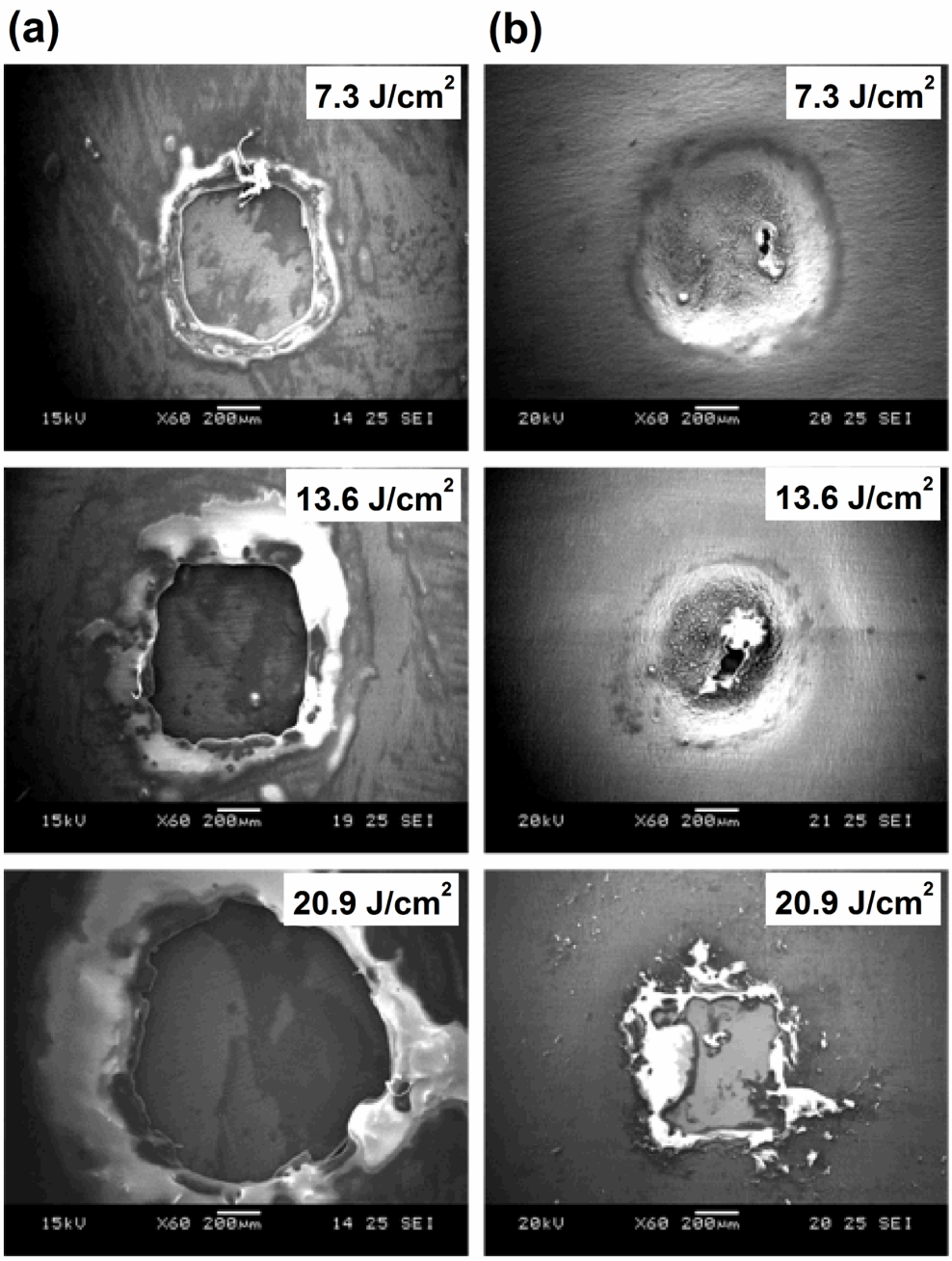

Figure 3.25: Effect of laser fluence on aluminum foil irradiation in FPLSF with (a) Glass confinement (b) Water confinement

shock pressure is expected subsequently.

Despite these factors, water confinement produced deeper craters owing to the following behaviors:

- As a result of the excessive irradiation energy with glass, the aluminum foil overlay was completely ablated as shown in Fig. 3.25a, vaporizing the copper foil top surface (Fig. 3.26), which hence resulted in the reduction of induced

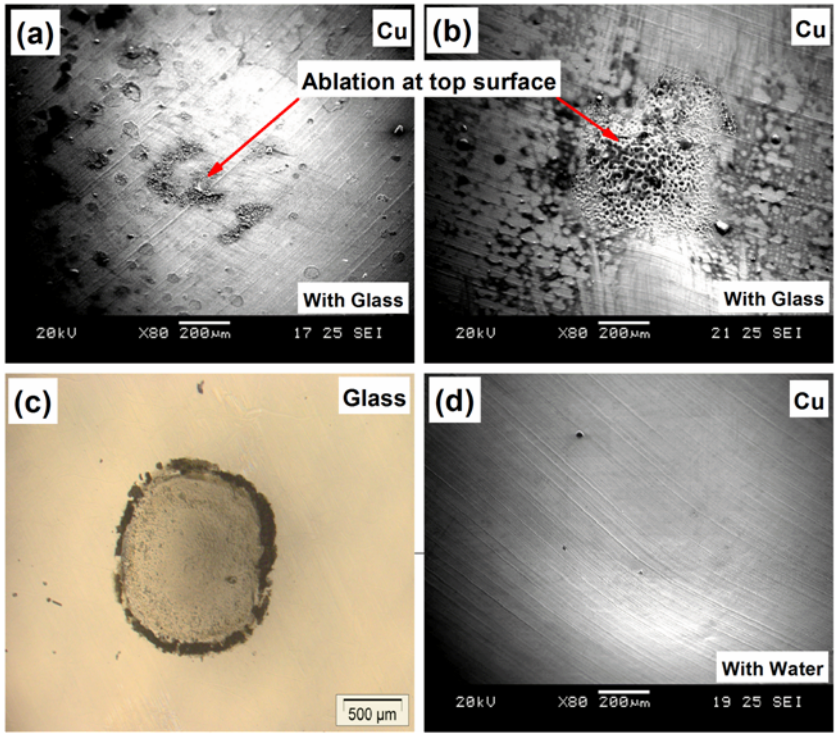

Figure 3.26: Surface integrity of copper top surface with glass and water confinements in FPLSF (a) Damaged copper surface at 13.6 J/cm^2 laser fluence with glass (b) Damaged copper surface at 20.9 J/cm^2 laser fluence with glass (c) Damage of fused silica glass at 20.9 J/cm^2 (d) Copper top surface at 20.9 J/cm^2 with water confinement

shock pressure and hence the reduction in the crater depth.

- Partial vaporization of overlay with water confinement as seen in Fig. 3.25b caused the shockwave propagation through the aluminum foil. As detailed previously, this will result in the enhancement of shock pressure amplitude due to the impedance mismatch effects. There will be no impedance mismatch in case of glass due to the complete vaporization.

- With glass confinement, the accurate sealing between foil and glass is not maintained throughout the foil forming duration as the confinement breaks off once the foil starts deforming. In case of water, perfect confinement exists during the entire laser irradiation and foil deformation. This behavior with water is expected to result in highly confined plasma and higher shock pressure subsequently, which will be examined further in the next chapter.

Contrarily, deeper craters were attained with glass confinement for the fluence of

20.9 J/cm^2 due to the corresponding shockwave structure formation. Furthermore, the vaporization of copper foil top surface at 20.9 J/cm^2 (Fig. 3.26b) with glass confinement caused a reduction of foil thickness. Thinner foils result in an increase of material velocity and deformation depth.

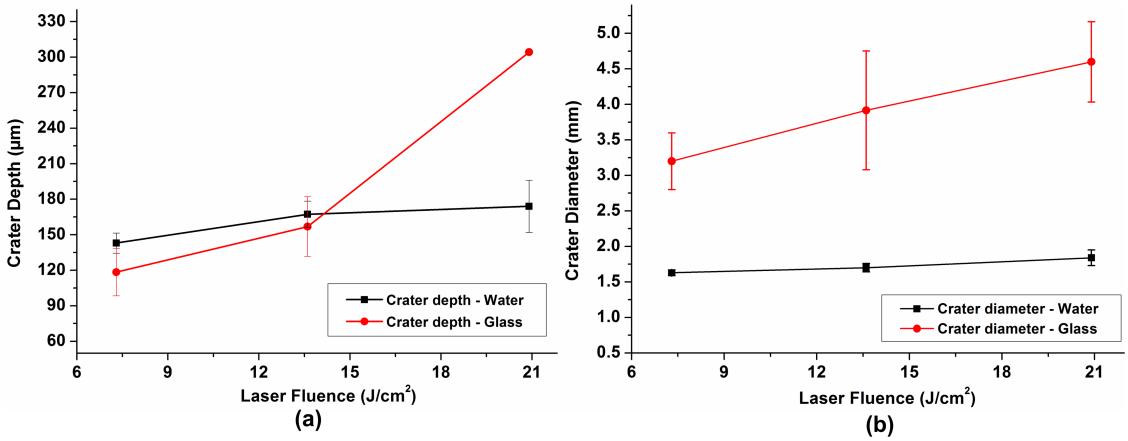

Figure 3.27: Comparison of dimensions of craters formed by FPLSF using water and glass confinements (a) Crater depth (b) Crater diameter

In FPLSF, the diameter of the crater has been proportional to the laser beam properties. As the same beam with uniform spatial intensity profile was used in this experiment, the variation in crater diameter for the increase in laser fluence is expected to be minimum, which was adhered with the water confinement as shown in Fig. 3.27b. Conversely, the crater diameter with glass confinement ranged between 3 mm to 4.5 mm, which is much higher than the laser beam size (0.6 mm) and the crater diameter with water (1 mm to 2 mm). The larger crater diameter with glass is a resultant of the corresponding larger vaporization area as witnessed from Fig. 3.25a. Free plasma expansion at successive laser pulses with glass confinement could also induce the larger deformation diameter. In addition, the increase in laser fluence resulted in larger change in crater diameter with glass. This behavior is explained as follows:

- The increase in crater diameter with fluence is attributed to the corresponding change in vaporization behavior of aluminum foil. As seen from Fig. 3.25, the effective vaporization area of the aluminum overlay increased in large proportion along with laser fluence for glass confinement. Whereas, with

water, despite an increase in vaporization depth, the area of vaporization remained closer to the beam size.

- At higher laser fluences, the formation of shockwave structures on copper foil with glass confinement is the reason for an excessively large crater diameter whereas only uniform hemispherical craters were formed with water confinement at all fluences.

3.10.4.2 Confinement thickness

The effect of confinement layer thickness has been tested where water confinement with other processing conditions are similar to the previous case. It is noted that the reduction in absorbed laser intensity and the refraction effects with the increased confinement thickness were not considered.

Fig. 3.28 illustrates the change in depth and diameter of the deformation craters with respect to the confinement layer thickness for two different laser fluences. It is observed from Fig. 3.28a that, for an increase in confinement thickness from 4 mm to 8 mm, the crater depth increased from 143 μm to 205.5 μm for 7.3 J/cm^2 whereas from 167.3 μm to 205 μm for 13.6 J/cm^2. Similarly, an increase in crater diameter was observed along with the confinement thickness as seen in Fig. 3.28b. It is noted that the crater size increased along with the confinement thickness in spite of the corresponding reduction in incident laser intensity.

Morales et al. [172] identified the shockwave propagation within the confinement layer to be influenced by the confinement thickness. Whereas, Ocana et al. [173] observed an increase in plasma pressure along with the increase in confinement thickness. The increase in crater size in FPLSF along with the increase in confinement thickness can be attributed to the aforementioned increase in plasma pressure. Even though a correlation of confinement thickness with the plasma confinement and the shock pressure could be derived from these literature findings, a detailed investigation of laser-induced plasma is required to understand the observed experimental results in this analysis.

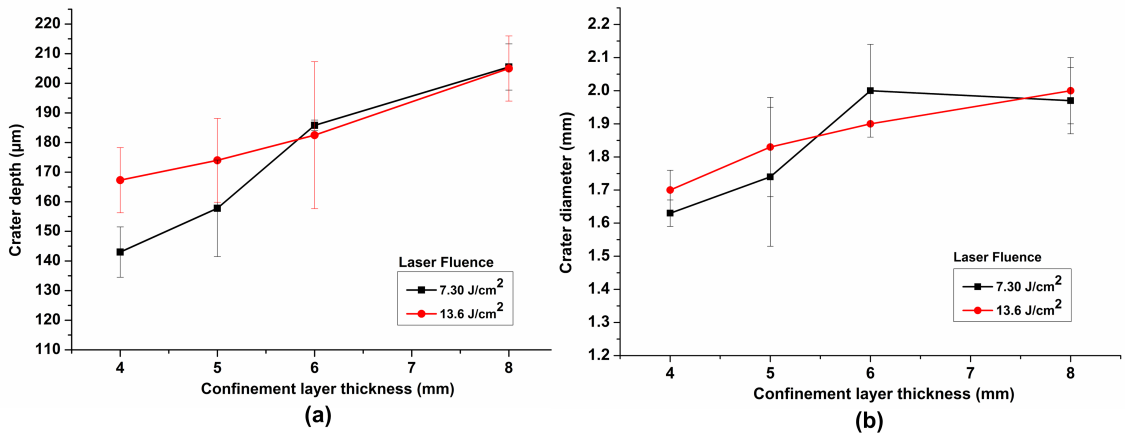

Figure 3.28: Effect of confinement layer thickness on the crater formation (a) Crater depth (b) Crater diameter

3.10.5 Flexible Pad

3.10.5.1 Pad material

To study the effect of flexible pad material (hardness) on the metal foil deformation, the following three different rubber materials, silicone rubber (SR), natural rubber (NR), and polyurethane rubber (PU) have been tested. Thickness of the flexible pad was kept constant as 900 µm in this study. The analysis is compared for different metal foils including copper, nickel and stainless steel. The other processing conditions were as follows: confinement - water (4 mm); ablative overlay - aluminum (15 μm); laser fluence - 13.6 J/cm^2, number of laser pulses - 45.

Fig. 3.29 presents the experimental observations of the effect of flexible pad material on the deformation characteristics of metal foil including crater depth, foil thinning at the formed crater center (measurement method in 5.1), and top and bottom surface hardness at the crater center (measurement method in 5.2.2). As noticed from the stress-strain curve at Fig. 6.7, the three materials are sorted according to their hardness as follows: polyurethane rubber > natural rubber > silicone rubber for strain levels greater than 0.5, whereas silicone rubber is observed to be stiffer than natural rubber for strain smaller than 0.5.

The effect of flexible pad material on the crater depth for three different foil materials is shown in Fig. 3.29a. For similar processing conditions, the crater depth

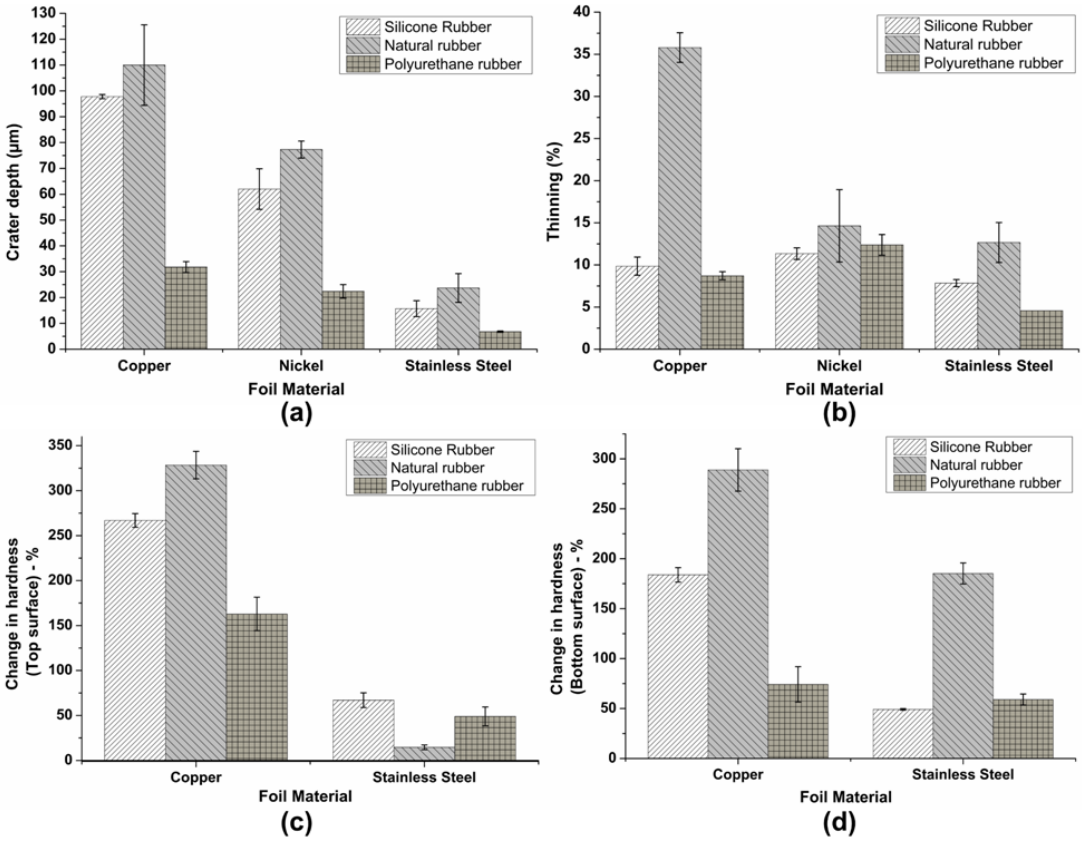

Figure 3.29: Experimental investigation of the effect of flexible pad material on (a) Crater depth (b) Foil thinning at crater center (c) Crater top surface hardness at center (d) Crater bottom surface hardness at center

produced with silicone rubber, natural rubber, and polyurethane rubber pads on copper foil was 97.8 μm, 110 μm, and 31.8 μm, respectively. It is evident that the maximum and minimum crater depths were achieved with natural rubber and polyurethane rubber respectively. The similar tendency was repeated for other foil materials tested, nickel and stainless steel. Thus, it is clear that a reduction in crater depth has been observed with an increase in flexible pad hardness, irrespective of the foil material tested. It is obvious that the increase in pad hardness increases the restriction to the metal foil deformation, thereby reducing the deformation of the foils. Despite minor changes, the flexible pad material was found to have no significant influence on the crater diameter as the lateral dimensions of the crater is controlled mainly by the laser beam profile which was maintained constant in this study.

As a result of metal foil plastic deformation in FPLSF, the foil experiences a

reduction in thickness, which ranged between 4% to 35% across different combinations of metal foils and flexible pad materials. Fig. 3.29b compares the experimental results of the effect of flexible pad material on the foil thinning at the center of the crater. The maximum thinning was observed with natural rubber, softest of the three pads tested, irrespective of the deformed metal foil (35%, 14.6%, and 12.7% for copper, nickel, and stainless steel, respectively). Despite a minor variation with nickel, the minimum thinning of foils was experienced with the hardest polyurethane rubber pad (8.7% for copper and 4.6% for stainless steel). Thus, it is evident that the thinning decreased with the increase in flexible pad hardness for copper and stainless steel metal foils. The same behavior can also be identified with nickel foil considering the corresponding standard deviation of thinning (1.2%).

The influence of flexible pad material on the hardness at the center of top and bottom crater surfaces of the deformed metal foils is illustrated in Figs. 3.29c and 3.29d. For increase in pad hardness, a reduction in hardness at the top surface was observed for copper foil as shown in Fig. 3.29c. For stainless steel foil, except an inconsistency with the natural rubber pad, the similar behavior can be observed between silicone rubber and polyurethane rubber. Similar to the top surface, the hardness at the bottom surface of the crater decreased with an increase in pad hardness for both the metal foils. Therefore, it is evident that the hardness at both the top and bottom foil surfaces increases as a result of FPLSF irrespective of the metal foil and the flexible pad.

The experimental observation of reduction in thinning and crater surface hardness with the increase in pad hardness is an intriguing behavior. During the deformation in FPLSF, the shockload acts on the top surface of the metal foil during its entire duration. Meanwhile, bottom surface of the foil will be experiencing resistance against the deformation from the flexible pad. With increase in flexible pad hardness, there will be more resistance to the foil deformation causing compression of the foil in the thickness direction. In addition, once the compression of the flexible pad reaches the saturation limit, restriction to further compression

will cause shockwaves to be directed back towards the foil. Thus, the foil is expected to experience more compression and hence increase in thinning and surface hardness with the increase in rubber hardness. Contrary to this hypothesis, both the thinning and surface hardness reduced along with the hardness of the flexible pad in this analysis. Though the observed behavior of flexible pad on thinning and hardness correlate with induced plastic deformation (crater depth), examining the stress-strain distribution along the metal foil and flexible pad is required to address the pertinent uncertainties. Finite element analysis of the process in chapter 6 will explore the flexible pad effect in detail.

3.10.5.2 Pad thickness

The effect of flexible pad thickness on deformation characteristics of metal foil in FPLSF is analyzed using various pad materials and metal foils. Fig. 3.30 compares the experimental observation of crater depth, foil thinning at crater center, and the top and bottom surface hardness at the crater center between two flexible pad thicknesses, 900 µm and 3000 µm for different foil materials and flexible pads.

For increase in pad thickness from 900 µm to 3000 µm, the crater depth increased from 110 μm to 112.7μm for copper foil, whereas a large increase from 23.7 μm to 55.9 μm occurred for stainless steel foils with natural rubber pad. The behavior of pad thickness has been identical with silicone rubber despite a discrepancy on copper foil. Thus, it can be identified that the crater depth increased along with the increase in pad thickness.

The experimental results for the pad thickness effect on foil thinning is shown in Fig. 3.30b. For increase in pad thickness 900 µm to 3000 µm, thinning on stainless steel foil increased from 7.8 % to 8.8 % with silicone rubber pad, and from 12.7 % to 17.8 % with natural rubber pad. Similar behavior was observed with copper foil despite an error with natural rubber pad. Thus, the results indicate an increasing trend for thinning along with the pad thickness, though the change was minimum. Contrarily, the hardness at both the top and bottom surfaces of

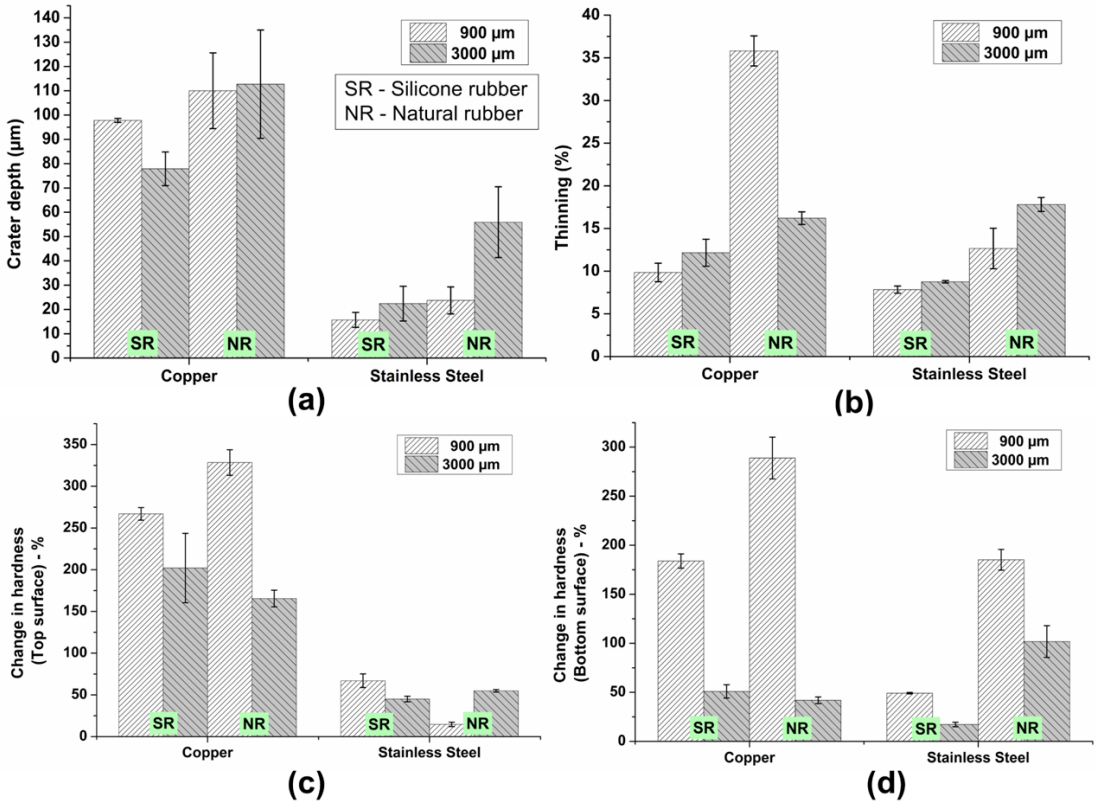

Figure 3.30: Experimental investigation of the effect of flexible pad thickness on (a) Crater depth (b) Foil thinning at crater center (c) Crater top surface hardness at center (d) Crater bottom surface hardness at center [SR – Silicone rubber; PU – Polyurethane rubber]

the crater experienced a reduction with increased pad thickness as evidenced from Fig. 3.30c and Fig. 3.30d respectively.

In summary, the increase in flexible pad thickness caused an increase in crater depth and thinning but with a reduction in surface hardness. Therefore, it is inferred that an optimum pad thickness exists to maximize the feature deformation with enhanced surface hardness.

Following aspects pertinent to the flexible pad thickness addresses the possible causes for the observed behavior:

- The flexible pad is compressed when the foil deforms due to the shockwave propagation. Once the pad attains its maximum compression, further deformation will not be possible. Then, the pad will induce a counter pressure, which acts in the direction opposite to the shock pressure, towards the metal foil. This counter pressure will restrict the deformation of the foil. The

amplitude of the counter pressure depends upon the pad thickness and the mechanical properties of the flexible pad.

- When the pad thickness is small, elastic waves propagating in the rubber will induce a rarefaction wave when the plastic wave is still propagating in the metal foil. This rarefaction wave could lead to the reduction in amplitude of the plastic wave and hence the reduction in the metal foil deformation.

The examination of shockwave interactions for the change in flexible pad thickness will be performed using finite element analysis.

3.11 Summary

This chapter introduced the Flexible Pad Laser Shock Forming (FPLSF) process which is a mold-free microforming technique using the laser-induced shockwaves and a flexible pad to induce plastic deformation on metal foils. Using FPLSF, microcraters of depth ranging between 80 µm and 130 µm and radius ranging between 485 µm and 616 µm were formed on copper foils of 25 µm thickness for the laser fluence varying between 7.3 J/cm^2 and 20 J/cm^2. It was observed that the formed craters were in hemi-spherical shape for the square-shaped laser beam with flat-top intensity profile. The deformation depth and diameter of the craters were found to be largely influenced by the laser fluence and beam profile respectively. Hence, it is understood that, various deformation crater profiles can be achieved using FPLSF by controlling the laser processing parameters with the help of a flexible pad. Fabrication of crater arrays on copper foils was demonstrated to examine the reproducibility of FPLSF. In addition, deformation craters with smaller depth and diameter were produced using a laser system with different laser processing variables.

The different mechanisms involved in FPLSF, laser-target interaction, plasma formation and expansion, shockwave formation and propagation, plastic deformation of metal foils and elastic deformation of flexible pad, were discussed briefly

in this chapter. Also, some significant inferences derived from the experimental results were discussed, which require further investigation for better process understanding.

The major advantages with FPLSF technique are determined to be the improvement in process flexibility, reduction in process cycle time, elimination of expensive micromold fabrication, and increased tribological properties due to the frictionless forming.

An efficient process controllability and predictability mandate an extensive process knowledge, characterized by the understanding of various process variables and the process mechanisms involved in the process. As a first step, a detailed parametric study to understand the influence of different process variables including substrate material, laser fluence, number of pulses, and the material and thickness of ablative overlay, confinement layer, and flexible pad, was conducted in this chapter.

The succeeding portions of this thesis are dedicated in studying the underlying process mechanisms.

Chapter 4

Investigation of Laser-Induced Plasma in FPLSF

The principal mechanism behind the induced shock pressure is the formation and propagation of plasma upon laser irradiation. Laser-induced plasma significantly influences the magnitude and the duration of shockwaves and hence plastic deformation of metal foil.

As observed from Chapter 3, the comparison of formed crater shapes between water and glass confinements in FPLSF revealed a significant difference in shapes at higher laser fluences. Hemispherical craters were formed on copper foil with water confinement, whereas shockwave ripples were formed with glass confinement. This behavior was attributed to the difference in plasma and shockwave propagation between different confinement layers. However, further analysis of plasma characteristics is required to understand the effect of confinement layer on deformation crater shapes.

Furthermore, the effect of confinement layer thickness on plastic deformation of metal foil is found to be influenced by the plasma characteristics, as discussed in section 3.10.4.2. The dependency of plasma confinement on the confinement thickness and shockwave velocity has also been established in the literature [172, 173]. However, in spite of the efforts to understand the influence of confinement layer

thickness, the above-mentioned research works analyzed the effect using numerical analysis of plasma dynamics. The effect of confinement thickness on the plasma behavior has been rarely examined using experimentation.

Therefore, in order to understand the process mechanisms involved in FPLSF, it is necessary to study the formation and expansion of plasma with respect to different process parameters such as laser fluence, confinement medium, and confinement layer thickness.

In this chapter, the time evolution of plasma was studied using a high-speed camera as detailed in section 4.1. The plasma evolution was characterized by measuring the plasma size using the plasma images acquired by a high speed camera. A correlation between the plasma size and the depth and diameter of the craters formed by FPLSF has been performed to study the effect of laser-induced plasma on the plastic deformation of metal foils. The influence of different process parameters such as laser fluence, number of laser pulses, confinement layer medium and its thickness on the plasma propagation has been analyzed in detail.

4.1 Plasma visualization using high speed camera

Photron FASTCAM SA5 high-speed camera has been used to capture the formed plasma in this study. The camera has a maximum exposure time of 1 μs and a wide range of frame rates [from 50 to 150000 fps (frames/sec)], out of which 5000 fps was used mainly in order to capture the full plasma image as observed in 4.1b. The plasma images were captured at the maximum frame rate (150000 fps) of the camera as well to understand the evolution of plasma. The camera was positioned at an angle of β (35°) to the path of the laser beam as illustrated in 4.1a. The entire evolution of laser-induced plasma from its formation to the disappearance was recorded for the analysis.

The shape and size of the plasma change with the observation angle (β) of the

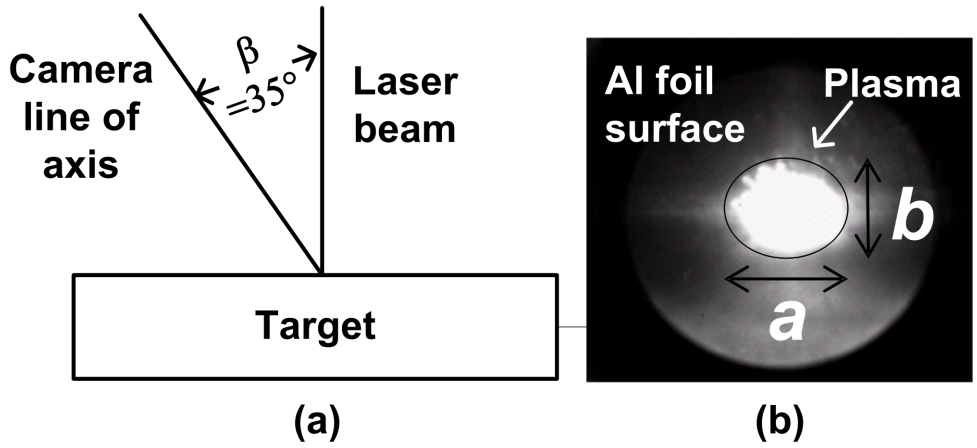

Figure 4.1: Measurement method for the plasma diameter (a) Orientation of camera with the laser beam (b) Image of plasma acquired by high speed camera

camera. Therefore, in this analysis, change factor of plasma size was used instead of the absolute plasma sizes. The plasma images were acquired at regular time intervals (200 µs) by the high speed camera from which the plasma diameter and its change factor were estimated. The plasma was seen as a bright spot in the acquired image as shown in 4.1b. The area of actual illumination ($A = \pi ab$) was calculated from the minor and major axes lengths as the plasma shape is observed to be approximately elliptical. As the camera line of axis is 35° (β) inclined to the laser beam axis, the actual illumination area (A) has to be projected to a plane perpendicular to the camera axis to calculate the projected illumination area ($A_p = Acos\beta$). From A_p, the projected illumination diameter ($D = \sqrt{(4 * A_p/\pi)}$) was calculated, assuming that the projected shape of the plasma is circular. From this projected diameter (D), the plasma diameter (D_P) was calculated by making a comparison with the initial projected diameter (D_0) corresponding to the laser beam spot size of 0.6 mm ($D_P = 0.6 * D/D_0$). The change in plasma size at different time periods with respect to initial plasma size was characterized by the change factor (D/D_0).

4.2 Evolution of laser-induced plasma

The plasma evolution typically comprises the following processes in sequence: plasma formation, expansion, decay, and disappearance. The evolution of plasma for single laser pulse irradiation of 7.3 J/cm^2 laser fluences was analyzed using the plasma images acquired at the frame rate of 150000 fps. Water with 4 mm thickness was used as the confinement layer.

Figure 4.2: Evolution of plasma for single pulse irradiation at 7.3 J/cm^2 laser fluence (Camera frame rate = 150000 fps)

Fig. 4.2 shows the sequence of plasma images with respect to time. The time difference between two successive frames has been 6.67 μs at the camera frame rate of 150000 fps. It can be observed that the plasma was visible at 6.67 μs whereas it disappeared at 13.3 μs. Since there is a possibility of plasma formation instantly after the firing of laser pulse and the plasma disappearance anytime before 13.3 μs, the plasma lifetime, starting from plasma formation, expansion, decaying to vanishing for single pulse irradiation is approximated to be less than 13.3 μs.

In comparison with the literature, Tanski et al.[130] observed a total plasma lifetime of 80 ns, which was slightly more than the laser pulse duration of 55 ns during UV laser irradiation of stainless steel. In their experiment, the plasma expanded until 22 ns (after the laser peak position) and then the plasma started decaying. However, in an experiment by Barthelemy et al. [116], for a 10 ns pulse width using XeCl excimer laser pulse irradiation on aluminum target, the plasma lifetime lasted longer than 500 ns, i.e. 50 times the pulse duration. In that case, significant plasma expansion occurred during the first 10 ns to 100 ns, after which the plasma decayed [116]. In our experiments, the exact plasma lifetime and plasma evolution phases starting from plasma formation, expansion, decay to vanishing upon a laser pulse have been difficult to observe due to the larger time

interval of 6.67 μs between two frames as compared to the laser pulse duration of 38 ns. Typically, high speed camera is used for the qualitative characterization of plasma dynamics. Since this study dedicates more emphasis on the extent of plasma propagation to understand the correlation between the plasma expansion and the metal foil deformation, this characterization technique is applicable for the subsequent analyses.

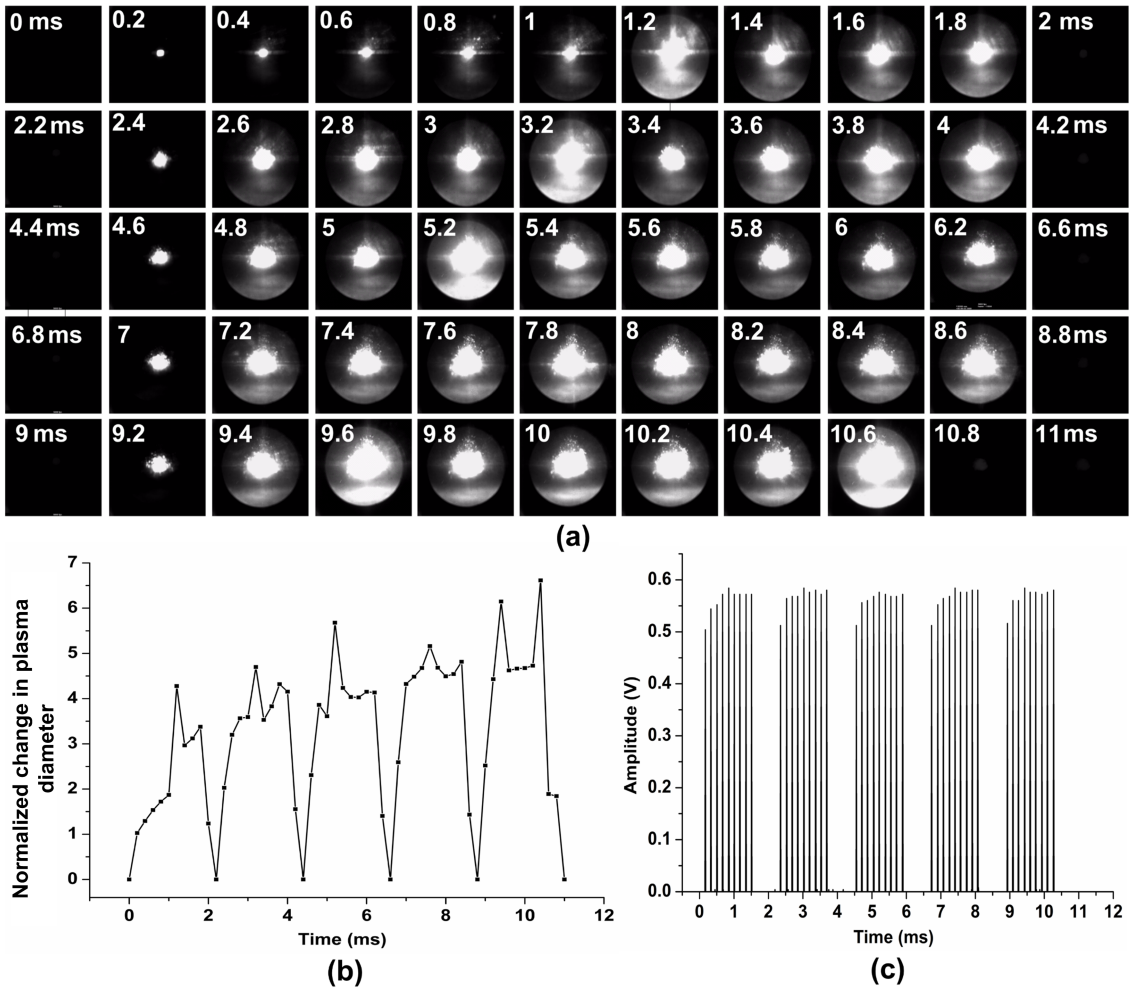

Figure 4.3: Evolution of plasma for 45 pulses laser irradiation at 7.3 J/cm^2 laser fluence (a) Sequence of plasma images captured at regular time intervals by high speed camera (b) Change factor of plasma diameter with respect to time (c) Voltage amplitude of laser pulses measured using photodetector

The analysis of plasma evolution for 45 pulses laser irradiation at a frequency of 6 KHz with 7.3 J/cm^2 laser fluence is shown in Fig. 4.3. In this analysis, 45 pulses were applied through 5 cycles with 9 pulses in each cycle. It can be witnessed from Fig. 4.3c which illustrates the time profile of laser pulses measured by a

photodetector. Fig. 4.3a shows the sequence of plasma images taken at regular time intervals by high speed camera with a frame rate of 5000 fps. The change in plasma size with time is illustrated in Fig. 4.3b. It is revealed from the plasma images that, in each cycle, the plasma was smaller at the first pulse, then increased gradually and reached the maximum size during the fifth or sixth laser pulse. After attaining the maximum, the plasma decreased in size during the subsequent pulses. In continuous irradiation of 45 pulses with the frequency of 6000 Hz, the plasma lifetime for one laser pulse of 13.3 μs was 12.5 times shorter than the pulse repetition time of 166.67 μs. Thus, there was no interference of plasma evolution from subsequent laser pulses as the plasma formed with each pulse completely vanished before the next laser pulse. The increased plasma expansion along with the number of pulses can be related to the increment in absorption of laser beam by the previously ablated rougher surface.

The plasma behavior was similar when direct irradiation conditions were used, as shown in Fig. 4.4. Thus, it is evident from Fig. 4.4 that plasma remained only at the aluminum foil surface. As no confinement layer existed, the plasma expanded freely in the axial direction, which had been ionized during the subsequent pulses. This tendency can be seen from Fig. 4.4 at 0.8 ms where the plasma spread further axially to the regions away from the irradiated surface. The axial displacement is observed to increase at subsequent pulses. However, there was no occurrence of plasma shielding, where the active plasma region will be detached from the target surface completely. Breakdown of air molecules is found to occur during the later pulses due to the increased presence of ejected particles, which can be witnessed at Fig. 4.4 after 7 ms. The aforementioned behaviors were not experienced with water confinement as plasma expansion is confined along the surface and the ejected particles are diluted by the water confinement.

It is evident from Fig. 4.3 that the plasma propagation occurred along the irradiated surface of the aluminum foil. It is also observed that the radial propagation of plasma along the surface was approximately circular even though the laser

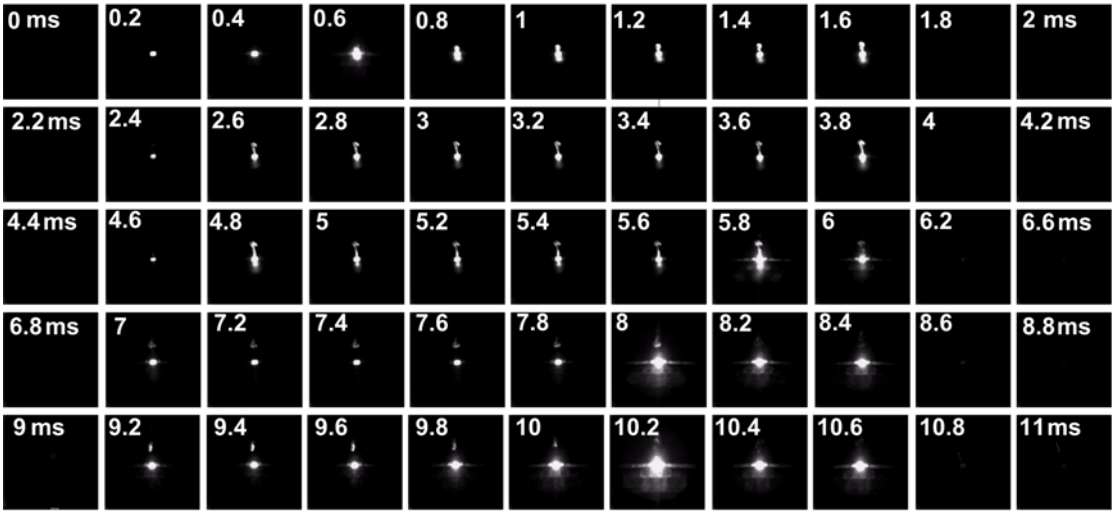

Figure 4.4: Plasma evolution at 7.3 J/cm^2 laser fluence with no confinement layer at the frame rate of 5000 fps

beam was square-shaped. This behavior is consistent with the literature in which the shape of the laser-irradiated plasma plume and the shockwave were observed to be hemi-spherical while expanding both in ambient air [116, 130] and in water [126]. The propagation of plasma in the axial direction has been restricted by water confinement in one direction and metal foil in the other direction.

This study further analyzes the correlation between the plasma expansion and the plastic deformation of metal foils.

4.3 Effect of laser fluence on plasma behavior

Fig. 4.5 compares the plasma evolution for single pulse irradiation at two laser fluences, 7.3 J/cm^2 and 20.9 J/cm^2. Water with 4 mm thickness was used as the confinement layer. It can be observed that the lifetime of plasma for single laser pulse (lesser than 13.3 μs) remained the same irrespective of the laser fluence. However, the effect of fluence can be noticed when the experiment were conducted at 45 pulses. Fig. 4.6 compares the plasma image at different laser fluences for the time duration of 9.4 ms. It can be identified from Fig. 4.6 that the plasma behavior varied significantly at 20.9 J/cm^2 fluence. At lower fluences (7.3 J/cm^2 and 13.6 J/cm^2), radial plasma propagation occurred along the interface between

the water and aluminum foil. Whereas, at higher fluence (20.9 J/cm^2), the plasma was seen both at the water-air interface and the water-aluminum foil interface. This observation confirms the occurrence of dielectric breakdown at the water-air interface at higher intensities [125]. The dielectric breakdown phenomenon occurs due to one or more of the following mechanisms: cascade ionization, multiphoton ionization, and the surface impurities [108, 152].

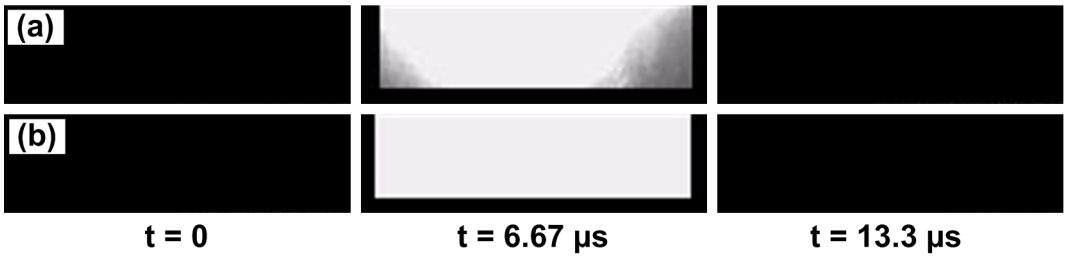

Figure 4.5: Comparison of plasma evolution at different laser fluence (a) 7.3 J/cm^2 (b) 20.9 J/cm^2

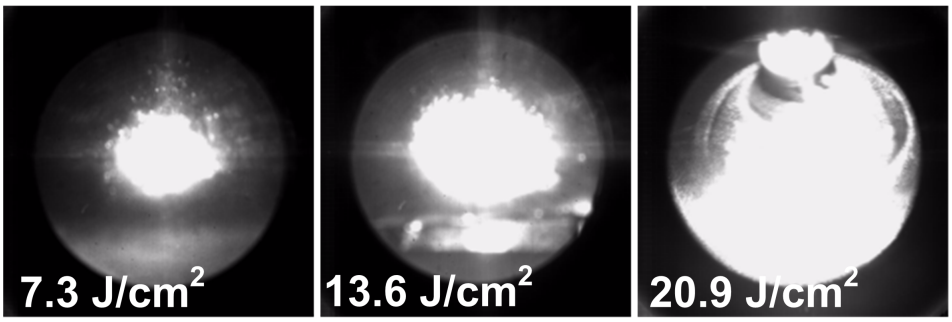

Figure 4.6: Effect of laser fluence on the evolution of laser-induced plasma at 9.4 ms

Fig. 4.7 compares the change in plasma diameter with time at different laser fluences. It is obvious that the plasma diameter increased with the increase in laser fluence. As the fluence increased, the vaporization area and depth of the aluminum foil increased (Fig. 3.25), leading to the increase in plasma diameter. The correlation between the change factors of crater size and plasma size with increase in laser fluence is illustrated in Fig. 4.8. The peak laser-induced shock pressure was calculated using Fabbro's model (Eqn. 2.8) and plotted in Fig. 4.8b.

When the laser fluence was increased by the order of 2.86 times from 7.3 J/cm^2 to 20.9 J/cm^2, the maximum plasma diameter increased accordingly by the order

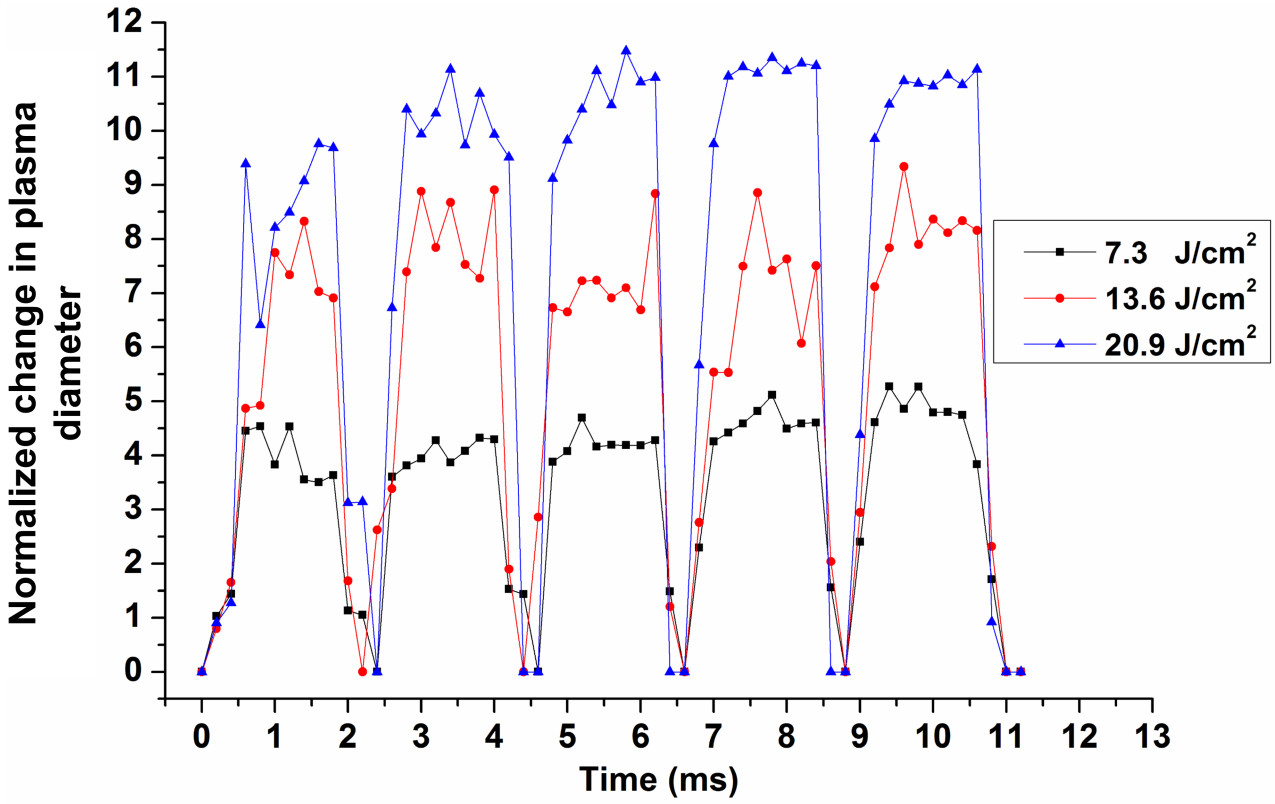

Figure 4.7: Change factor of plasma diameter with respect to time at different laser fluences

of 2.18 times (Fig. 4.8b). Consecutively, it is observed that the change factor of maximum shock pressure (1.69 times) was smaller than that of plasma diameter. The change factor of crater depth was calculated to be 1.47 times, which correlates well with that of maximum shock pressure. Interestingly, it can be noted from Fig. 4.8 that the change factor has been descending in the order of laser fluence (2.86), maximum plasma diameter (2.18), maximum shock pressure (1.69), and crater depth (1.47). With increase in laser fluence, the shock pressure, i.e. the forming load, increased, resulting in increased plastic deformation of foils and thus deeper craters. Meanwhile, the crater diameter increased only by a small amount in the order of 1.13 times (Fig. 4.8b) as the crater diameter is influenced mainly by the laser beam size which has been constant throughout the analysis.

It can be observed from Fig. 4.8b that both the plasma diameter and pressure increased simultaneously with increase in laser fluence. It is interesting to observe that, even though the plasma propagated to a larger distance of about 7 mm,

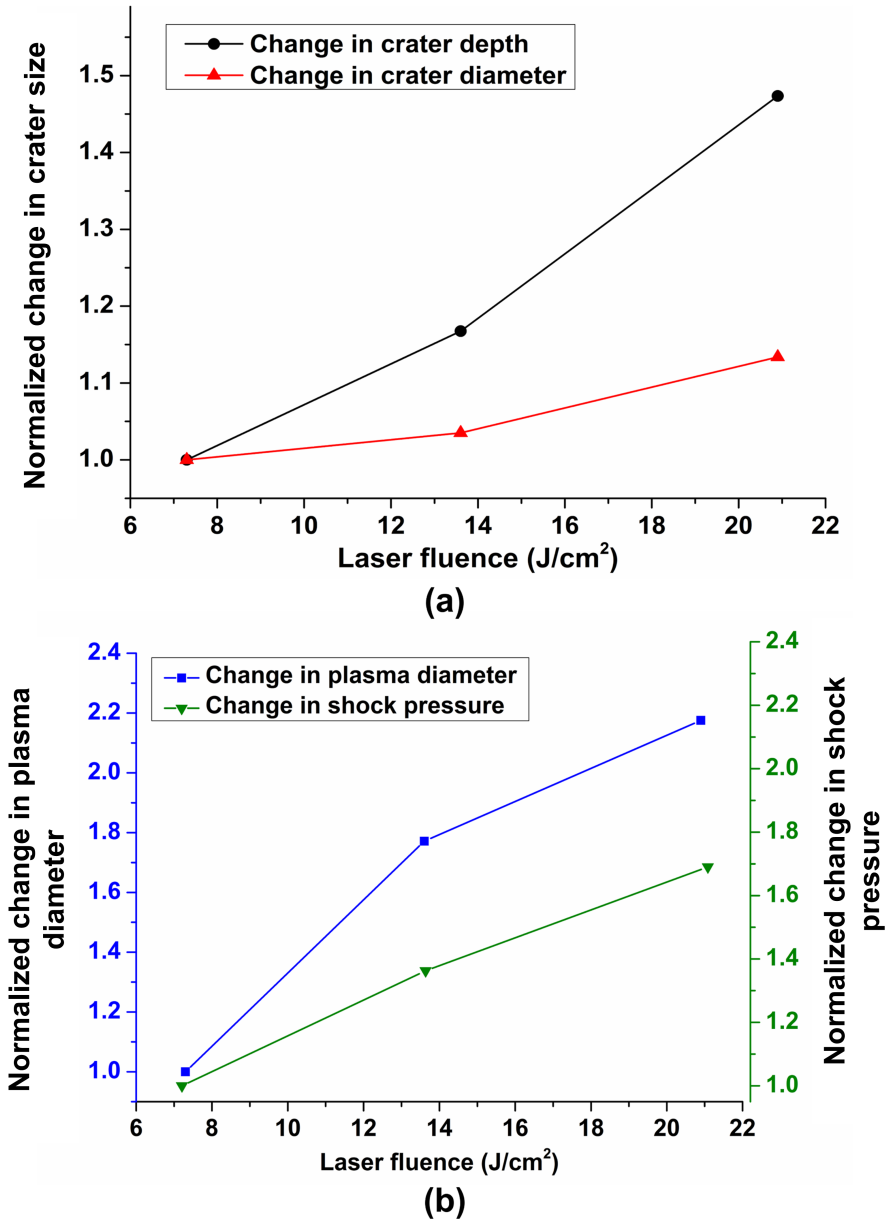

Figure 4.8: Comparison of change factor of crater size with the change factor of maximum plasma diameter and theoretical shock pressure at different laser fluences

the crater diameter (1 mm) was not increased significantly. As the distance from the center of irradiation increases, the plasma density is reduced correspondingly. Therefore, at foil positions distant from the irradiation spot, the plasma density was less and hence the resultant shock pressure was insufficient to induce the plastic deformation. It is revealed from the analysis that the expansion of plasma is associated with the increase in plasma density while the laser fluence is increased.

The measured plasma diameter at 20.9 J/cm^2 could be slightly larger than the actual diameter. This could be due to the scattering of light by the shockwave

propagating at the top surface (as seen in Fig. 4.6).

4.4 Effect of confinement medium on plasma behavior

The influence of confinement layer materials such as fused silica glass and deionized water on the plasma evolution has been analyzed at laser irradiation of 45 pulses. The major difference observed between the glass and water confinement mediums is the occurrence of dielectric breakdown phenomenon at higher laser fluence. Fig. 4.9 compares the images of plasma at 20.9 J/cm^2 laser fluence with water and glass confinement layers. Plasma observation at the water top surface in Fig. 4.9a indicates that the dielectric breakdown of water occurred at the interface between the air and water top surface. Whereas, with the glass confinement, dielectric breakdown occurred at the interface between the bottom surface of glass and the ablative overlay as shown in Fig. 4.9b. The damage of glass can be attributed to the reflectivity of the target and the collision of metal plasma with the rear surface of the glass [19].

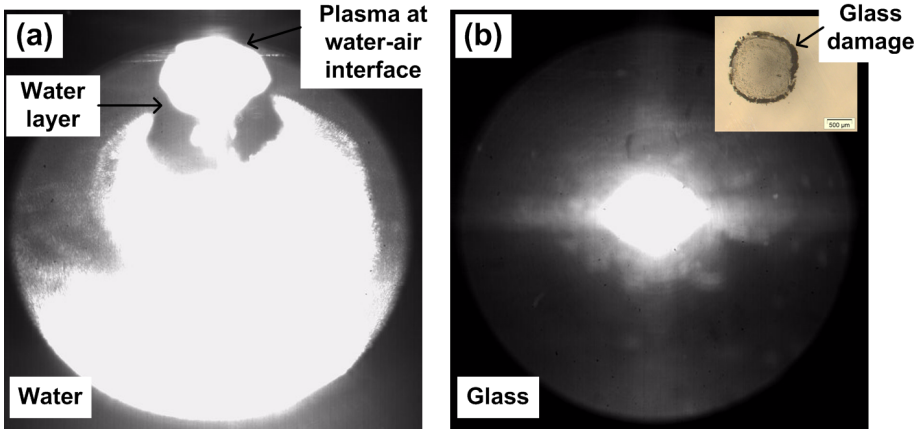

Figure 4.9: Comparison of dielectric breakdown mechanism between water and glass confinements at 20.9 J/cm^2 laser fluence (a) Water confinement (b) Glass confinement

The correlation between the change factor of crater size and the change factor of maximum plasma diameter for water and glass confinements is illustrated in Fig.

4.10. For 2.86 times increase in laser fluence, the plasma diameter increased by the order of 3.28 times in glass whereas it increased only by 2.18 times in water as shown in Fig. 4.10b. Correspondingly, the change factor of crater depth was higher in glass (2.57 times) than in water (1.47 times) as shown in Fig. 4.10a. The increase in crater diameter too was higher with glass (1.44 times) than with water (1.13 times). Furthermore, the actual crater depth and diameter were higher with glass at higher laser fluences. This larger crater size in glass was observed to be mainly influenced by the propagation characteristics of plasma. It can be inferred from the results that the expansion of plasma is more restrictive in glass, causing smaller plasma diameter. Thus, plasma was confined to a narrow region resulting in higher density of plasma in glass. The denser plasma caused higher shock pressure (forming load) and hence deeper craters were produced with glass confinement. Meanwhile, as the plasma expansion proceeded to a larger distance in water, the plasma density and pressure were reduced. The diameter of plasma during the first pulse was approximately constant between water and glass confinements. The maximum plasma diameter occurred at the time period ranging between 7 ms to 10.6 ms.

During the parametric study of confinement layer medium in section 3.10.4.1, shockwave structures were noticed on copper foil with glass as the confinement layer. This effect was attributed to the plasma and shock wave propagation behaviors. One of the hypotheses has been the shockwave propagation from irradiated surface, which is explained as follows:

- The shockwave begins its propagation towards the metal foil from the irradiated surface both axially and radially. Since the copper foil itself is ablated with the glass confinement (as illustrated in Fig. 3.17c), the shockwave structures could have formed on copper surface. This hypothesis was verified for possible shockwave structures as loading is started from the partial irradiated top surface. Fig. 4.11 shows the aluminum and copper foil surfaces with water as the confinement for the partial vaporization condition (laser

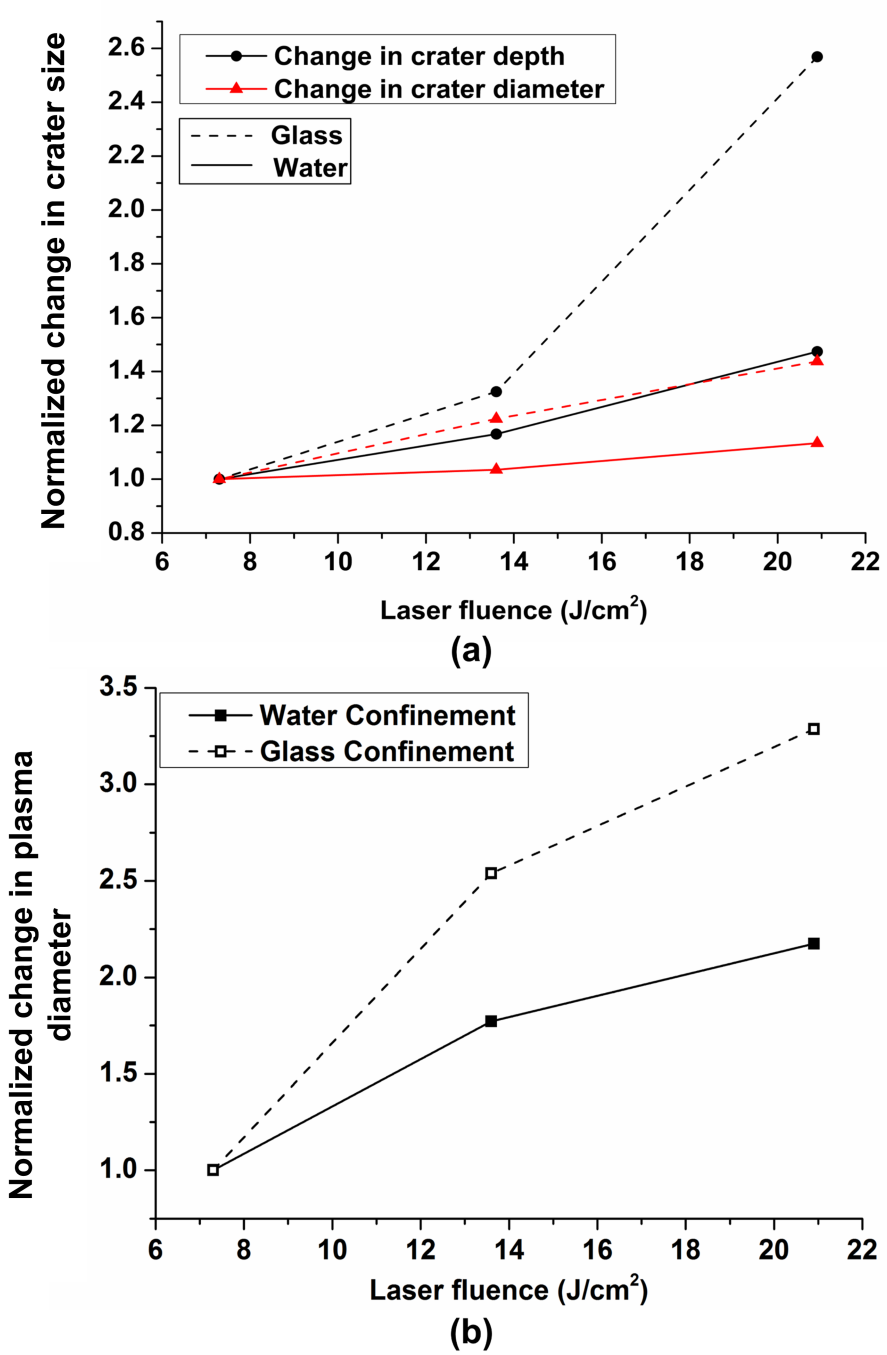

Figure 4.10: Comparison of the change factor of crater size and the change factor of maximum plasma diameter between water and glass confinement layers

fluence of 13.6 J/cm^2). Contrary to the claim, there was no shockwave structures on aluminum foil as witnessed from Fig. 4.11a. Thus, the formation of shockwave ripples could be a characteristic of glass confinement. To verify this claim further, shockwave propagation behavior between water and glass confinement layers for aluminum and copper foils are compared, as shown

in Fig. 4.12. It can be observed from Fig. 4.12b that entire thickness of the aluminum foil overlay was vaporized. Despite this complete vaporization, shockwave pattern was formed on aluminum foil in addition to that on copper foil. The similar behavior was not observed with water confinement (Fig. 4.12a) despite the complete vaporization of aluminum foil over its thickness. Thus, it is clear that the shockwave patterns on metal foil is resulted entirely by glass confinement.

Formation of shockwave ripples with glass confinement is attributed to one or two of the following behaviors:

1. Upon irradiation, two shockwaves propagate axially in both directions (towards metal foil and confinement layer) extending the plasma interface [160]. In case of water confinement, water is receptive to the shockwave and the propagation of shockwaves is experienced, as seen in Fig. 4.6. Meanwhile, as the glass remains stationary, the shockwaves are reflected back towards the metal foil resulting in a complex interaction between the shockwaves.

2. In addition, an significant difference in confinement is predicted between water and glass confinements.

    - *Water*: Once a portion of the material is vaporized from the ablative overlay upon the irradiation, the water flows into the displaced volume. Therefore, the formed plasma is always confined by water causing the plasma to propagate along the irradiated surface.
    - *Glass*: In case of glass confinement, the confinement is cut off from the irradiated area during the first instance of overlay vaporization. During the subsequent pulses, there will be no close confinement for the expanding plasma in the axial direction. The formed plasma is constricted by the ablative overlay drilled inner walls. This difference in plasma expansion with glass confinement could significantly affect the shockwave propagation and subsequent plastic deformation.

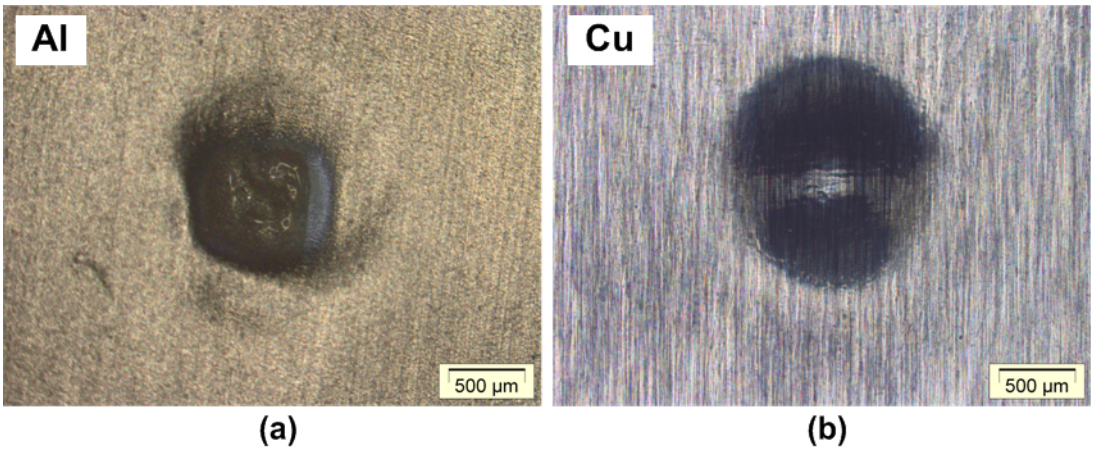

Figure 4.11: Shockwave propagation analysis at 13.6 J/cm^2 laser fluence with water confinement (a) Aluminum foil overlay (b) Copper foil

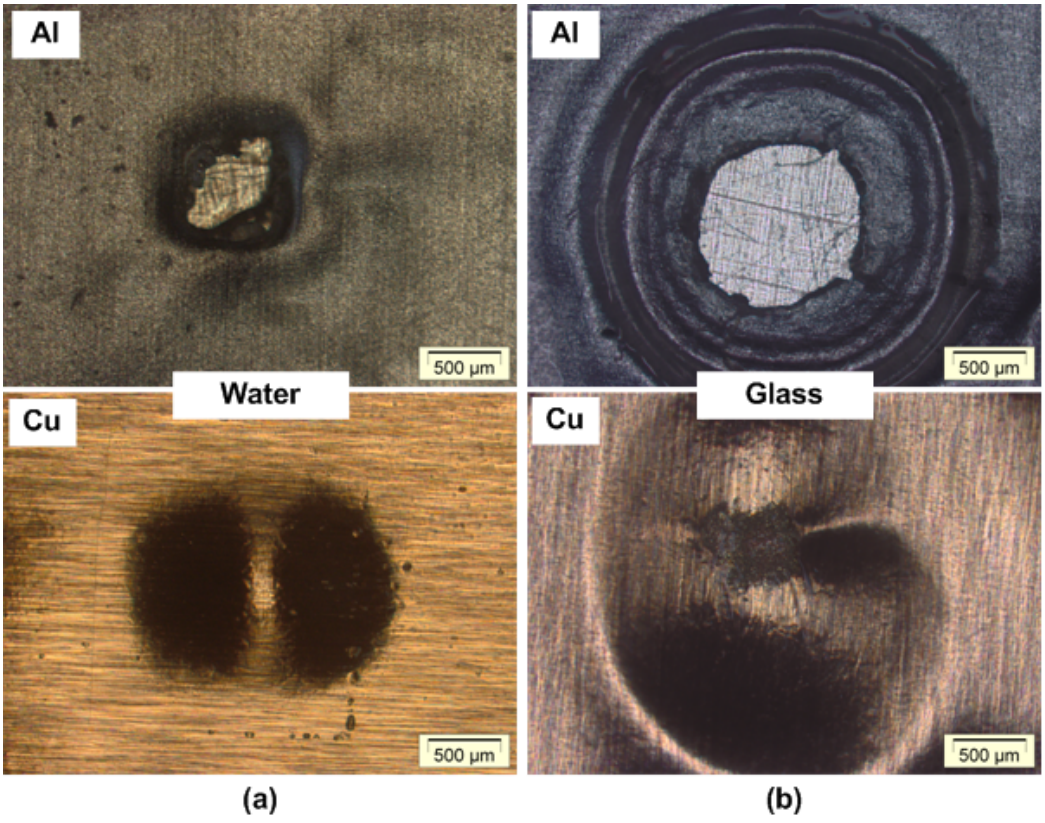

Figure 4.12: Comparison of shockwave propagation in aluminum foil overlay (top) and copper foil (bottom) in FPLSF between water and glass confinement layers at 20.9 J/cm^2 laser fluence (a) Water confinement (b) Glass confinement

The larger actual size and change factor of craters in glass confinement were attributed to higher transmittance, complete vaporization of aluminum foil overlay, shockwave propagation and vaporization in copper foil, and increased material velocity due to the reduced foil thickness with the glass confinement. The par-

tial vaporization with water confinement and subsequent shockwave attenuation further increased the difference. In addition to the above mentioned factors, the plasma analysis revealed that the dielectric breakdown behavior with water confinement, which will reduce the induced shock pressure causing further reduction in deformation sizes.

The difference between water and glass confinement as discussed above is compared in Table. 4.1.

Table 4.1: Difference in plasma behavior between water and glass confinements

Water Confinement	**Glass Confinement**
Larger plasma diameter.	Smaller plasma diameter.
No shockwave formation on copper foil.	Shockwave formation on copper foil at high laser fluences.
Plasma diameter is larger than the crater diameter.	Plasma diameter is smaller than the crater diameter, mainly due to the propagation of shockwaves in metal foils.
Breakdown of water at water-air interface at 20.9 J/cm^2.	No breakdown at glass-air interface at 20.9 J/cm^2.

4.5 Effect of confinement thickness on plasma behavior

The effect of confinement layer (water) thickness on the plasma propagation was analyzed at different thickness of 4 mm, 6 mm, and 7 mm. Two laser fluence levels, 7.3 J/cm^2 and 13.6 J/cm^2 and 45 laser pulses were used for the experimentation. A correlation between the change factors of crater size and plasma size for different confinement thicknesses is shown in Fig. 4.13. With constant laser fluence, a reduction in plasma diameter was observed when the confinement thickness was

increased from 4 mm to 7 mm (Fig. 4.13b). This behavior can be attributed to the absorption of laser energy within the confinement thickness.

It can be observed from Fig. 4.13a that both the crater depth and diameter increased with the increase in confinement thickness from 4 mm to 8 mm at both 7.3 J/cm^2 and 13.6 J/cm^2 fluences, despite a discrepancy with the crater diameter for 8 mm. As the laser energy experiences absorption within the confinement, reduction in crater size was expected with increase in confinement thickness. As mentioned earlier, Morales et al. [172] observed the influence of confinement thickness on plasma pressure as the arrival of shockwave before the occurrence of laser peak reduces the plasma pressure. For the confinement thickness (t) of 4 mm in FPLSF, the time (τ) taken by the shockwave to reach the water-air interface is calculated to be 2.4 μs considering the shock velocity (D) in water as 1650 ms^{-1}. As 2.4 μs is much longer than the pulse duration of 38 ns, this behavior could not be the reason for lesser shock pressure and crater depth at smaller confinement thickness. Ocana et al. [173] found numerically that the plasma pressure increases with increase in confinement thickness. In this study, reduction in plasma diameter was observed with the increase in confinement thickness (Fig. 4.13b). The correlation between plasma diameter and plasma pressure with increase in confinement thickness confirms that the reduction in plasma diameter increases the plasma density and pressure due to the confinement of plasma. Hence, the increase in crater depth and diameter is attributed to the reduction in plasma diameter with increase in confinement thickness.

4.6 Summary

This chapter studied the laser-induced plasma evolution in FPLSF using a high speed camera. Also, the influence of plasma evolution on the plastic deformation of metal foils is experimentally investigated. The plasma lifetime, starting from plasma formation, expansion, decay to vanishing for single pulse irradiation was found to be less than 13.3 μs irrespective of the confinement conditions. For 45

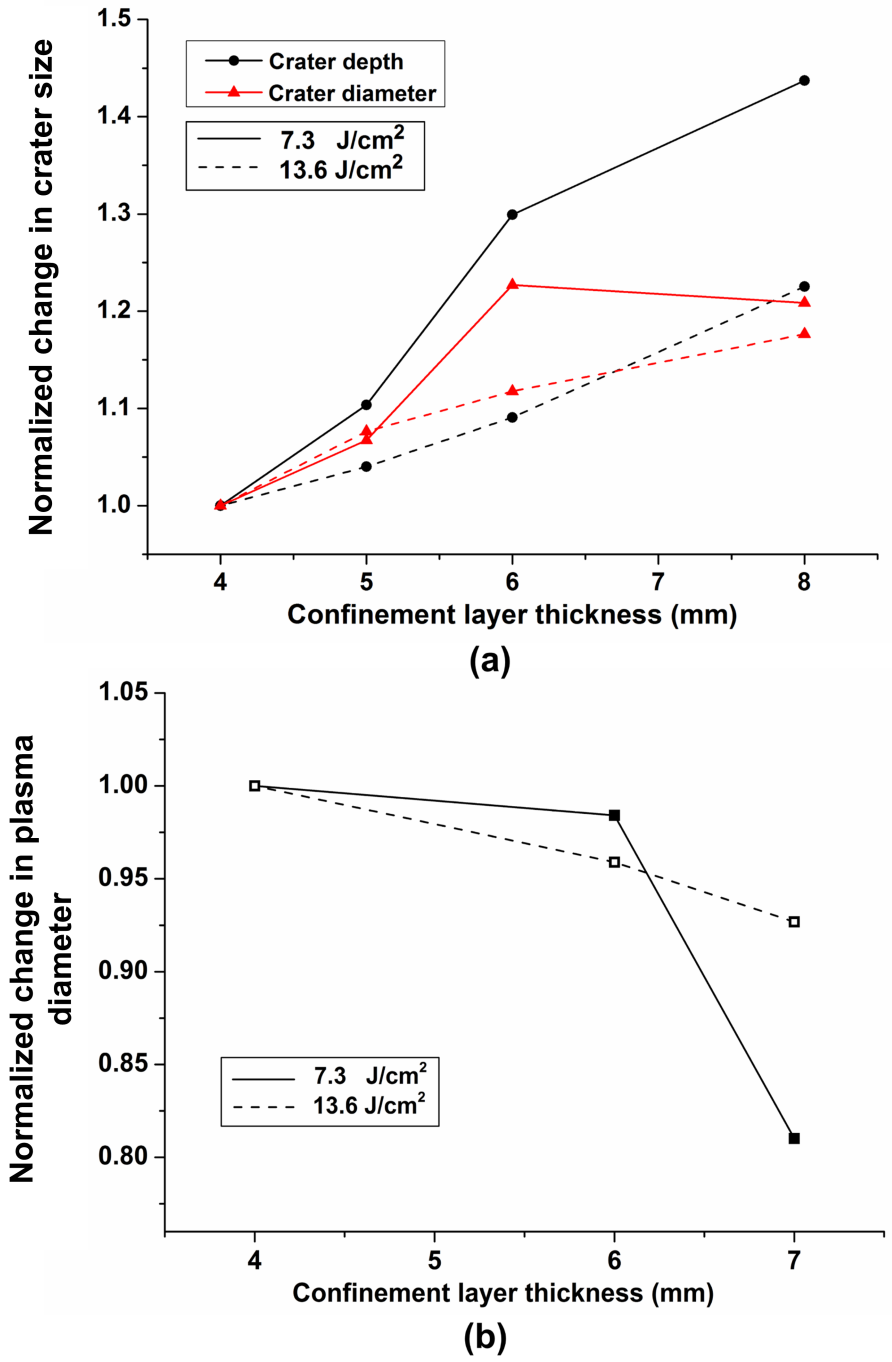

Figure 4.13: Correlation between change factors of crater size and plasma size at different confinement layer thicknesses

pulses irradiation as 5 cycles with 9 pulse train in each cycle (pulse duration - 38 ns, pulse frequency - 6 KHz), the plasma size increased gradually and attained its maximum at the fifth or the sixth cycle. No interference between the plasma evolution resulting from successive laser pulse irradiation were observed.

The laser fluence is found to have significant effect on the plasma evolution in

water confinement. For laser irradiation of 45 pulses, when the laser fluence was increased by 2.86 times, the change factors of maximum plasma diameter (2.18), maximum shock pressure (1.69), and crater depth (1.47) increased in the same order. It is understood from the results that the increase in laser fluence increased both the plasma size and plasma density.

A significant difference in plasma evolution characteristics was observed between water and glass confinement layers. At higher laser fluence, dielectric breakdown occurred at the water-air interface with water whereas it occurred at the glass-ablative layer interface with glass. The confined plasma in glass increased the plasma density and pressure resulting in deeper craters. The confinement behavior pertaining to water and glass varies considerably, resulting a change in plasma expansion and shockwave propagation characteristics. Accordingly, the deformation features on metal foils are affected such that the shockwave patterns were formed on the copper foil with glass confinement.

When the water confinement thickness was increased, increase in crater size was observed in spite of the laser energy absorption within the confinement. Though this behavior was attributed to the corresponding reduction in plasma size, a detailed analysis of plasma pressure will be required to understand the correlation between plasma evolution and confinement layer thickness.

Chapter 5

Plastic Deformation Analysis

This chapter studies the high strain rate plastic deformation characteristics of metal foils in FPLSF. The deformation behavior of metals at strain rates greater than $10^4 s^{-1}$ was discussed in chapter 2 associated with the processes including electromagnetic forming, explosive forming, and laser shock processes, where the high strain rate mechanisms are effective. The inference of results from other high strain rate processes on FPLSF, where the metal foils are deformed plastically at high strain rates under the laser shock loading, could be intricate due to the following observations:

(a) FPLSF uses hyperelastic flexible pad as support, which undergoes large elastic deformation along with the foil deformation. As evidenced from Chapter 5, the mechanical properties of the flexible pad influences the plastic deformation of metal foils significantly as the pad restricts the foil deformation, inducing compressive stresses on the bottom surface of the foil. These stress states are expected to affect the microstructures and mechanical properties of the deformed surfaces.

(b) In most of the high strain rate processes, severe compression of deforming metals occurs because of the process configurations. Meanwhile, the compression of the metal in the thickness direction is uncertain due to the existence of flexible pad in FPLSF.

(c) In high strain rate processes with mold patterns, the inertia effects play a significant role in improving the formability of the material. When the deforming material reaches the mold bottom, an additional compression through thickness is experienced due to the inertia. In case of FPLSF, the forming velocity of the foil is restricted by the flexible pad. Therefore, although FPLSF has similar loading rate, the improvement in material formability due to the inertia effects is questionable in FPLSF.

(d) At the end of laser shock loading in FPLSF, the flexible pad releases its elastic energy and retains its original position. The elastic recovery of rubber is found to influence the plastic deformation of foil by causing the displacement of the deformed foil upwards, as observed from the finite element analysis (as discussed in Chapter 6). The influence of high strain rate on the elastic release of the flexible pad may affect the deformed foils.

Therefore, it is essential to analyze the plastic deformation mechanisms involved in FPLSF in order to understand and predict the process behaviors.

In this chapter, the thickness distribution of the deformed foil along its cross section at different positions is analyzed initially. Then, the hardness at the crater cross-section and the top and bottom crater surfaces are measured and analyzed. A correlation between thinning and hardness behaviors was performed as well. The comparison of microstructure on copper foil before and after FPLSF is investigated by Electron BackScatter Diffraction (EBSD) technique. Quantitative characterization of the deformed microstructure at top and bottom crater surfaces after forming is analyzed using parameters such as grain size distribution, aspect ratio, and misorientation angle distribution. In addition, the microstructures at center and edge regions of the deformation crater are compared. The effect of laser fluence on the crater microstructure after FPLSF is also investigated. Finally, the evolution of textures in copper foils as a result of FPLSF is discussed. Following experimental conditions were used throughout this chapter: copper foil thickness - 25 μm; confinement - water (4 mm); ablative overlay - aluminum (15 μm); flexible pad -

silicone rubber (0.9 mm); Nd:YAG laser (wavelength -1064 nm, pulse duration - 38 ns, number of laser pulses - 45, pulse repetition rate - 6 KHz) .

5.1 Thinning

Thinning (%), a ratio at which thickness of the metal foil is reduced after forming, has been one of the major parameters to understand the process formability. To analyze the thickness distribution of deformed foils, the craters were cross-sectioned at 2 mm offset from the center of crater. The cut samples were first cold-mounted using Struers® Epofix resin and then manually polished up to the crater center sequentially using different grades of abrasives. For cutting, mounting, and polishing of samples, ASTM E3 standard [192] and preparation procedures suggested by Struers® [193] were adopted.

The thickness of the crater cross-section was measured at the center using an optical microscope. Thinning percentage of the metal is measured from Eqn. 5.1 ,

$$Thinning(\%) = \frac{t_0 - t_i}{t_0} * 100 \tag{5.1}$$

where t_0 and t_i are the foil thicknesses before and after forming respectively. The thickness was measured at different positions at the foil cross-section as shown in Fig. 5.1. The initial thickness of the copper foil (t_0) was measured as 31.8 µm with a standard deviation of 1.28 µm.

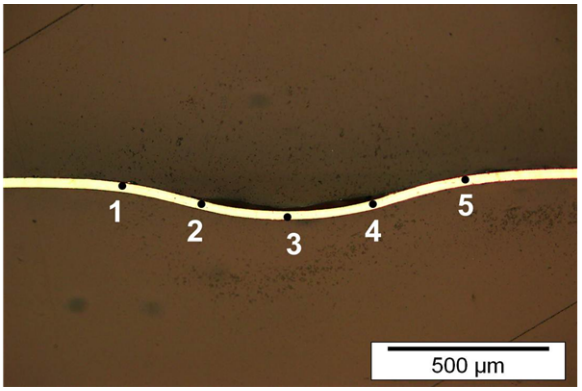

Figure 5.1: Thickness measurement positions along the crater cross-section

Fig. 5.2 illustrates the foil thinning with respect to laser fluence. Thinning of deformed foils is observed to vary from 7% to 25% after FPLSF for the laser fluence ranging between 7.3 J/cm^2 and 20.9 J/cm^2. It is evident that the maximum thinning of the deformation crater occurred at its center (location 3) and reduced gradually further away from the center. During plastic deformation of metal foils, the reduction in thickness occurs due to the combination of compressive strain in the axial direction and tensile strain in the radial/transverse directions. When the flexible pad is deformed during the shockwave loading, it induces axial compressive stress in the thickness direction of the foil. During FPLSF, the magnitude of axial and transverse strains at the crater center are larger than the corresponding strains at other foil positions, which is witnessed from the finite element analysis as discussed in chapter 6. The maximum thinning observed at the crater center is attributed to the above mentioned stress-strain behavior. The increase in thinning along with the laser fluence is a result of the corresponding increase in shock pressure and amount of plastic deformation.

Thinning at other foil locations 1, 2, 4, and 5 is mainly due to the tensile stresses in the transverse directions. It is observed from Fig. 5.1 that the edge portions (location 1 and 5) experienced minimum reduction in thickness. This behavior is contrary to the processes employing molds and punches, where thinning is maximum at the feature edges due to the restriction of material flow. In FPLSF, the material flow is not restricted at the edges as the flexible pad behind the edges assists the material flow by undergoing elastic deformation.

Another significant advantage with FPLSF is the increase in uniformity of thickness distribution. For all the laser fluences except 7.3 J/cm^2, the variation in thinning across different crater locations ranged between 6% and 8% which is less than the thinning variation of around 20% for the processes involving molds/dies [91, 194]. The minimum thickness variation was observed at 20.9 J/cm^2, which can be identified from the crater cross-section at different laser fluences at Fig. 5.3.

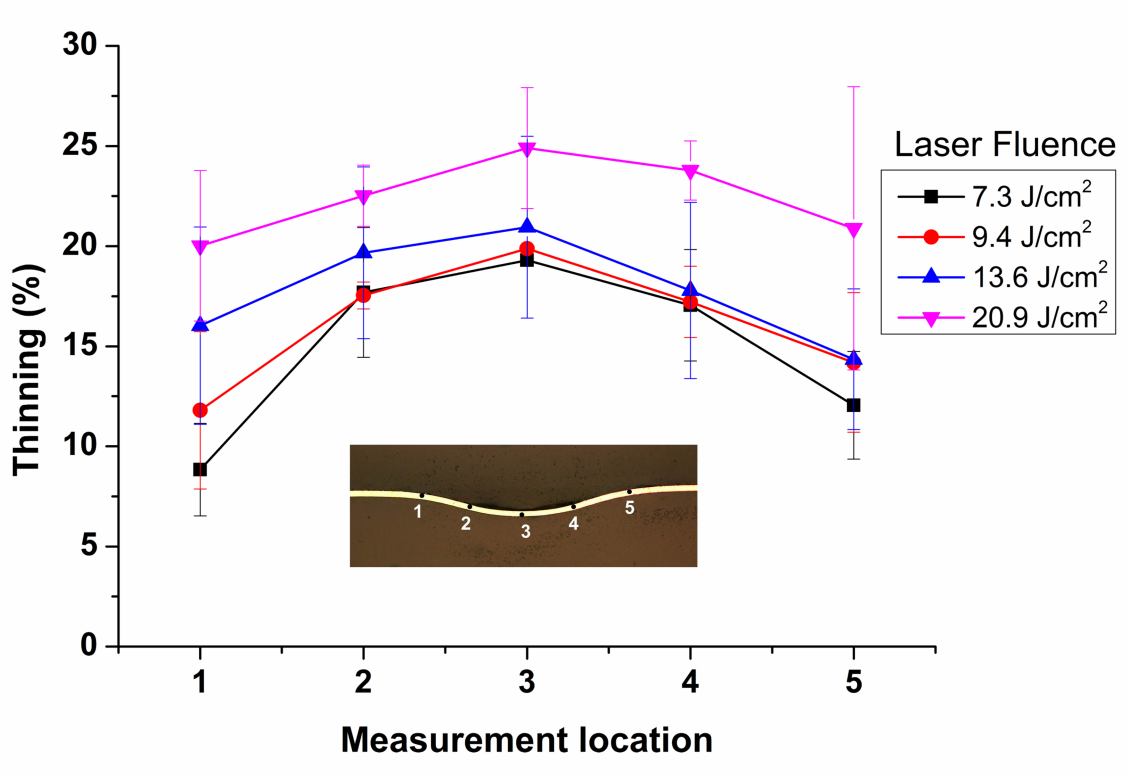

Figure 5.2: Effect of laser fluence on foil thinning at different positions along crater cross-section

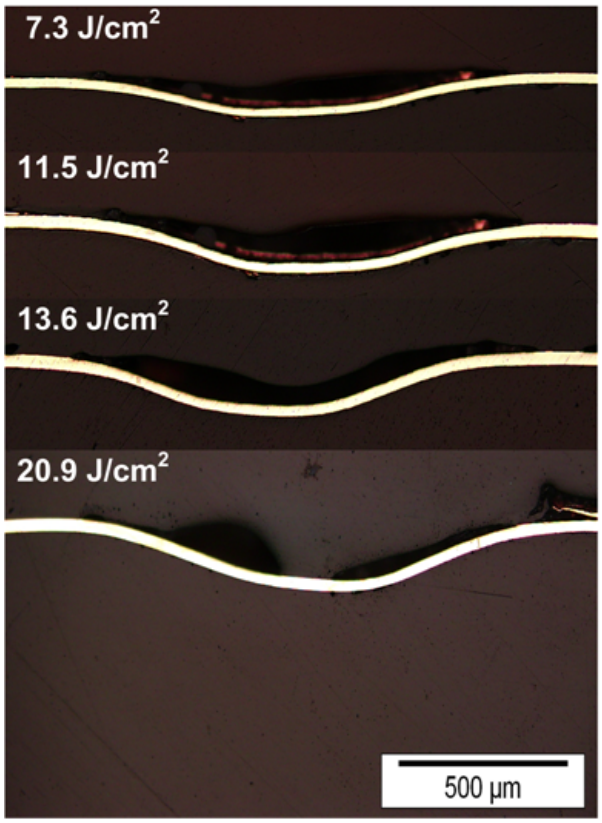

Figure 5.3: Crater cross-sections on copper foil with respect to laser fluence

The thinning behavior of metal foils during deformation in FPLSF with more uniform thickness distribution than other high strain rate processes can be associated with the flexible pad arrangement that provides a controlled deformation velocity of the metal foils.

5.2 Hardness

In this analysis, the hardness was measured at the cross-section and the surfaces to examine the effect of plastic deformation in FPLSF.

5.2.1 Cross-sectional hardness

The hardness of the sample at the different locations in the cross-section (see Fig. 5.1) was measured by Nanoindenter XP (maximum indentation depth of 1000 μm with 0.01 nm resolution and maximum 500 mN load with 50 nN resolution) using a Berkovich diamond indenter. Continuous Stiffness Measurement (CSM) method has been used to calculate the hardness and elastic modulus where the contact stiffness is measured continuously during the loading [195]. Indentation load was continuously recorded during the loading and unloading cycle of indentation. The hardness (H) is measured as a ratio of applied load (P) to the projected contact area (A) at that load, as $H = P/A$, where the projected contact area is calculated as a function of contact depth (h_c) which is a factor of penetration depth (h), load (P), stiffness ($S = dP/dh$), and a constant based on indenter geometry (ε) as follows, $h_c = h - (\varepsilon P/S)$. In this analysis, the load-displacement curve has been used to analyze the material behavior. As the indenter is a displacement controlled system, the maximum penetration depth was given as 1000 nm for this experiment. Typical indentation on the sample cross-section is shown in Fig. 5.4.

The sample preparation involves procedures similar to that of thinning characterization, but an additional fine polishing using silica suspended particles of size less than 1 μm was performed to produce a fine finish ideal for nanoindentation.

The load-displacement curves are compared between different process conditions and at different foil positions. Fig. 5.5 shows the $P - h$ curves pertaining to the indentation of deformation crater at different foil locations (Fig. 5.1) for the laser fluence of 13.6 J/cm^2. It can be observed from the crater profiles and thickness distribution that the deformation has been almost symmetric across the crater center. Thus, only one of the foil locations corresponding to the center (position 3), periphery (position 2 or 4), and edge (position 1 or 5) of the crater is subjected to the analysis.

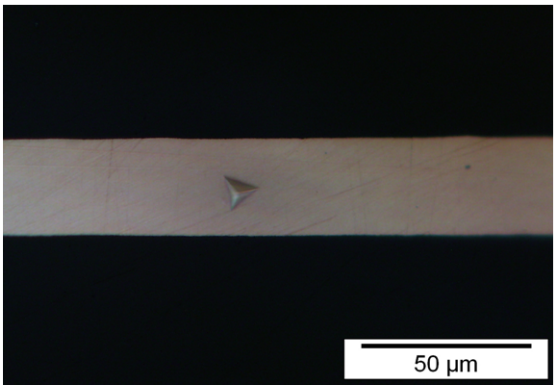

Figure 5.4: Nanoindentation on copper foil cross-section for maximum indentation depth of 1000 nm

It is obvious from Fig. 5.5 that the hardness of the material has increased after FPLSF, as the indentation load on the crater was much higher that on the copper foil before FPLSF. The required load to achieve a similar displacement is increased, indicating an improvement in hardening. The increase in slope of the load-displacement curve highlights the increased flow stress caused as a result of plastic deformation.

It can be identified from Fig. 5.5 that the hardening curve has been different between different regions across the foil. The maximum hardness was observed at the crater edges (location 5), followed by the crater center (location 3) and the periphery (location 4) regions. However, the difference in stiffness between the foil locations were observed to be smaller. This minor variation in hardness profiles

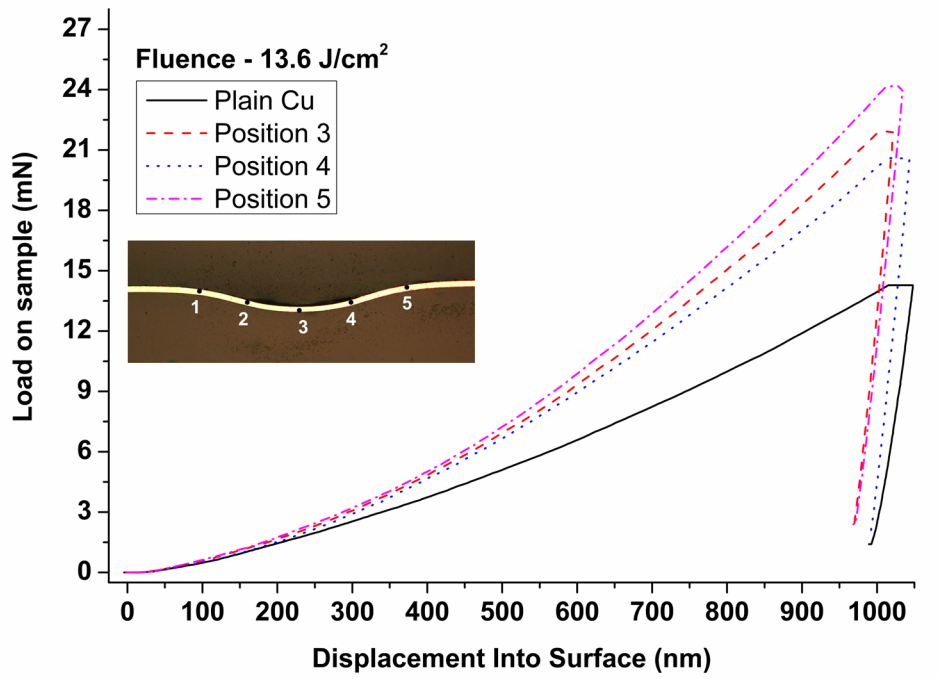

Figure 5.5: Comparison of load - displacement relationship before and after FPLSF at different foil positions for the laser fluence of 13.6 J/cm^2

between different foil locations correlates with the corresponding thinning behavior as seen in Fig. 5.2. The small variation in thickness distribution (less than 10%) between different crater locations indicates an uniform plastic deformation, which explains the observed hardness profile along the crater as well.

The observation of identical curves were more prominent when the fluence is 9.4 J/cm^2 as shown in Fig. 5.6a. Similarly, for 20.9 J/cm^2, though the hardness was observed to be smaller at foil position 5, it is similar between foil locations 3 and 4 [Fig. 5.6b].

The effect of laser fluence on cross-sectional hardness at foil position 3 is illustrated in Fig. 5.7. It is evident that the hardness enhancement increased along with the increase in laser fluence. The observed results are in correlation with the thinning results as observed in Fig. 5.2. The identical increase in hardness with fluence was also experienced at other crater regions; crater edges (location 5) and crater periphery (location 4), as shown in Fig. 5.8. The increase in shock pressure

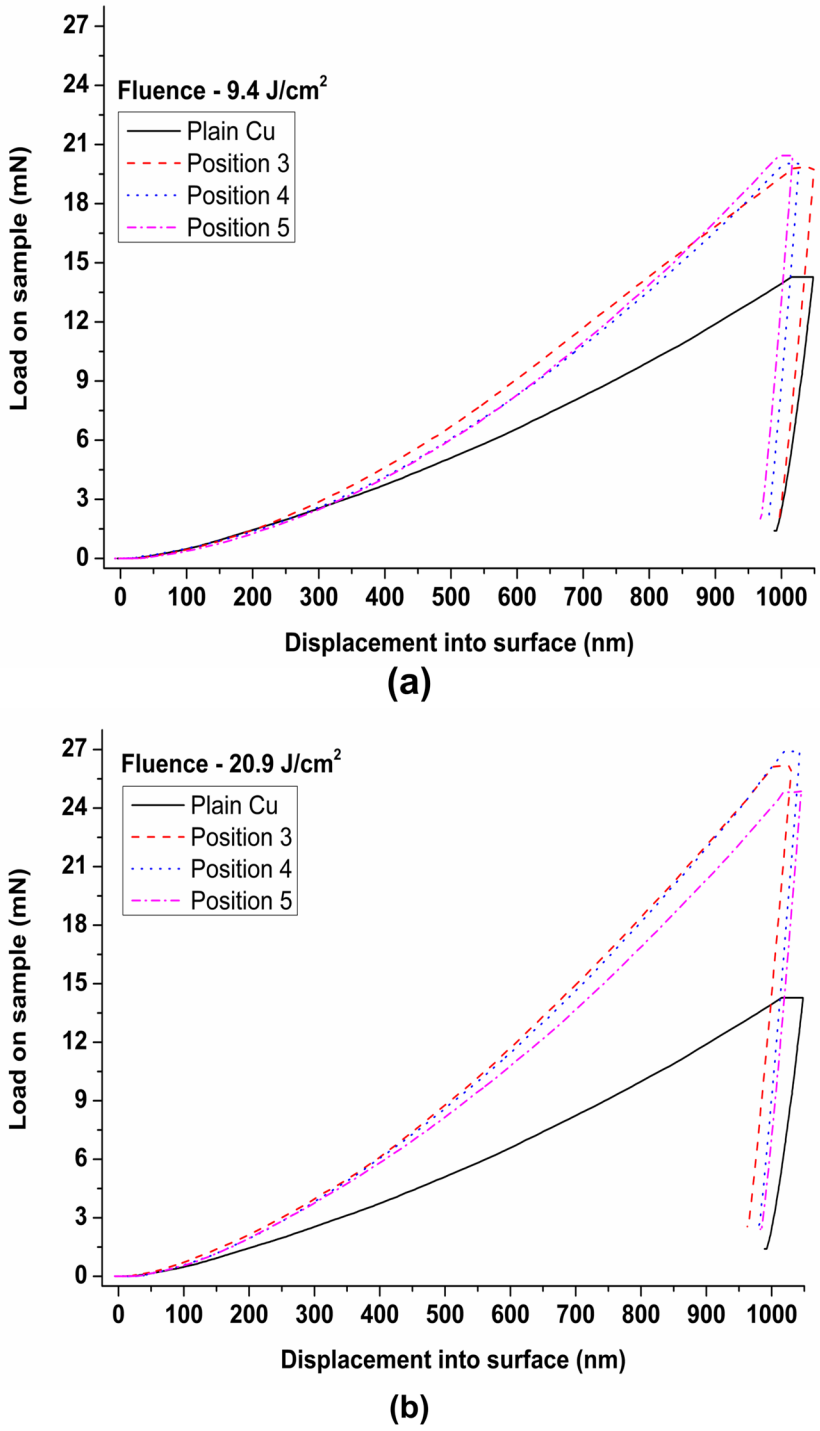

Figure 5.6: Comparison of load - displacement relationship before and after FPLSF at different foil positions for the laser fluence of (a) 9.4 J/cm^2 (b) 20.9 J/cm^2

and axial compression along with the laser fluence results in the increased plastic deformation of foils. As the foils experienced compression along the thickness (which is evidenced by the thinning analysis), the hardness at the cross-section is improved. It should be emphasized that the improvement in hardness will occur

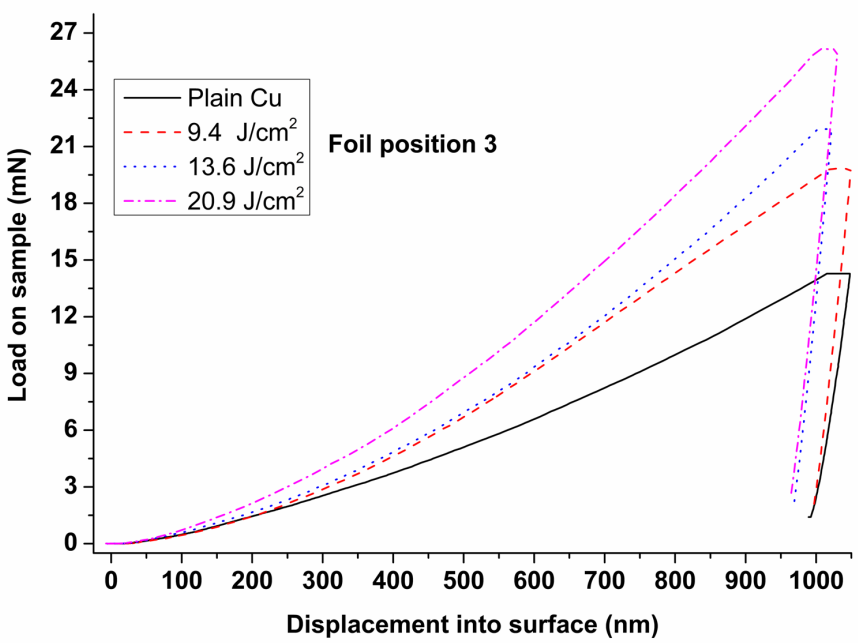

Figure 5.7: Comparison of load - displacement relationship with change in laser fluence at foil position 3

irrespective of the plastic deformation mechanism, strain hardening or adiabatic softening, experienced during the process due to the microstructural changes, which will be discussed further.

5.2.2 Surface hardness

In addition to the nanoindentation at the cross-section, hardness was also measured at the surfaces of the deformed features Vickers microindenter. Vickers Hardness (Kgf/mm^2) is calculated as follows, $HV = 1.8544F/d^2$ where F is the indentation load and d is the average projected length of the diagonal by the indentation, where d is determined manually using the in-built optical microscope. The indentation load of 50 Kgf was used.

The indentation was applied at the center of the crater for both the top and bottom surfaces as illustrated in Fig. 5.9. During the indentation of the top crater surface, the bottom portion was rested on a rigid support and the adjacent regions were firmly supported to avoid any deviation. Meanwhile, the indentation of the bottom crater surface required the crater to be filled with resin hardener in order

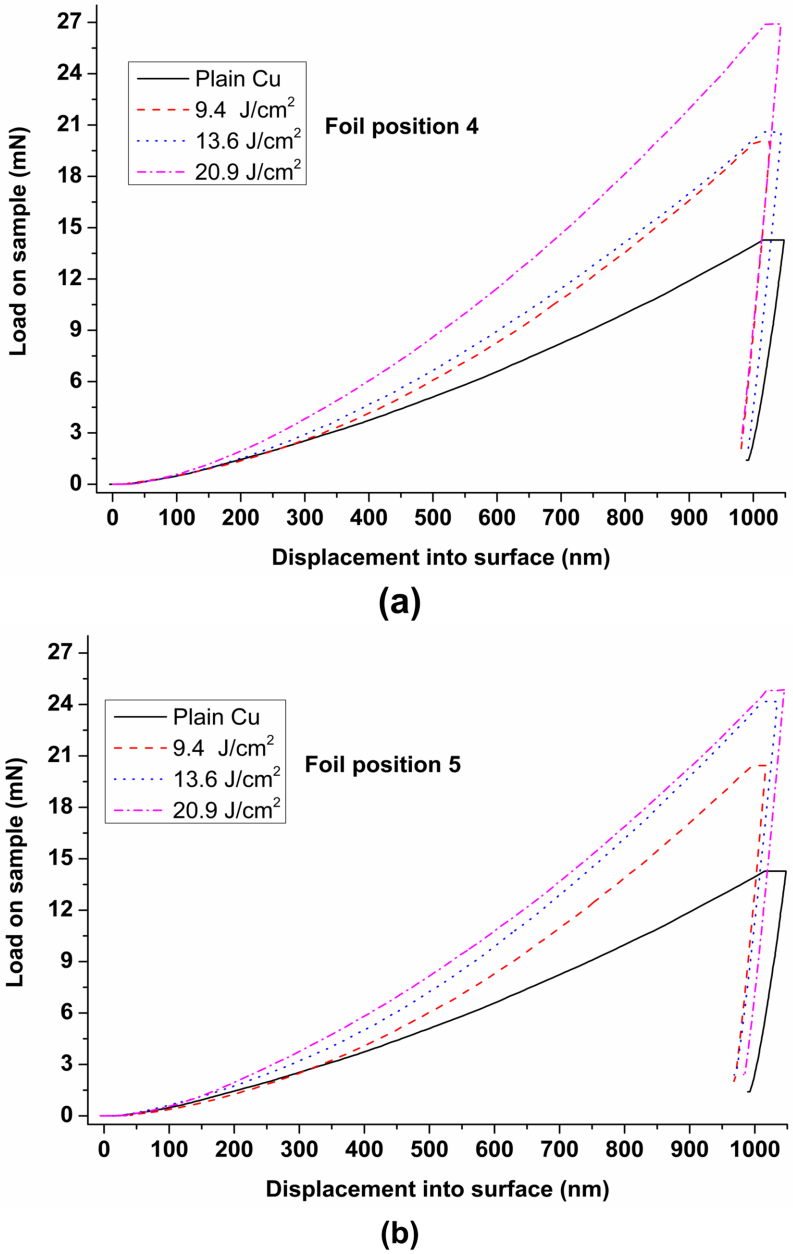

Figure 5.8: Comparison of load - displacement relationship with change in laser fluence at (a) Foil position 4 (b) Foil position 5

to avoid bending of craters during indentation, as shown in Fig. 5.9. The samples were mechanically polished before deformation, in order to eliminate the surface roughness effect on the measured microhardness. The measured surface hardness of the as received copper foil was 34.71 VH with a standard deviation of 2.56.

The hardness at the top and bottom surfaces of the deformation craters for varying laser fluence is compared at Fig. 5.10. As illustrated in Fig. 5.9, hardness was measured at the center. It is apparent that the hardness at both the surfaces

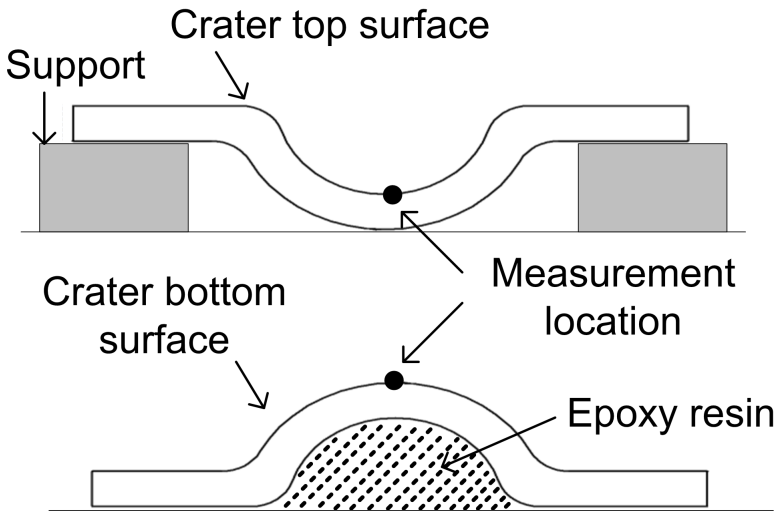

Figure 5.9: Schematic of surface hardness measurement method

increased after FPLSF, as a result of plastic deformation of the foils. The increase in hardness at the top surface after FPLSF ranged between 23% and 71% for the fluence varying between 7.3 J/cm^2 and 20.9 J/cm^2, highlighting an increasing trend along with the fluence. Meanwhile, the increase in hardness at the bottom surface remained nearly constant (39% - 48%) with the increase in laser fluence. The top crater surface was observed to be harder than the bottom crater surface except for the lower laser fluences (7.3 J/cm^2 and 9.4 J/cm^2). A correlation between the top surface hardness and the foil thinning behavior can also be observed from Fig. 5.10. Standard deviation of hardness varied between 1.52 to 3.1 for top surface where it varied from 3.9 to 5.2 at bottom surface.

The increase in hardness at the crater surfaces can be attributed to one or more of the following mechanisms:

(a) Strain hardening effect during plastic deformation, where the occurrence of dislocation motion and subsequent tangling is experienced, restricting further slip motion

(b) Adiabatic softening effect at high strain rates, due to which nucleation of new dislocations and subgrain formation occurs. The grain refinement at high strain rate leads to uniform and smaller grain sizes after forming leading to the increase the hardness of the surface [89].

(c) The compressive residual stresses induced at the top and bottom surfaces under shock loading which causes an increase of hardness in both top and bottom surfaces of the formed craters [83, 89].

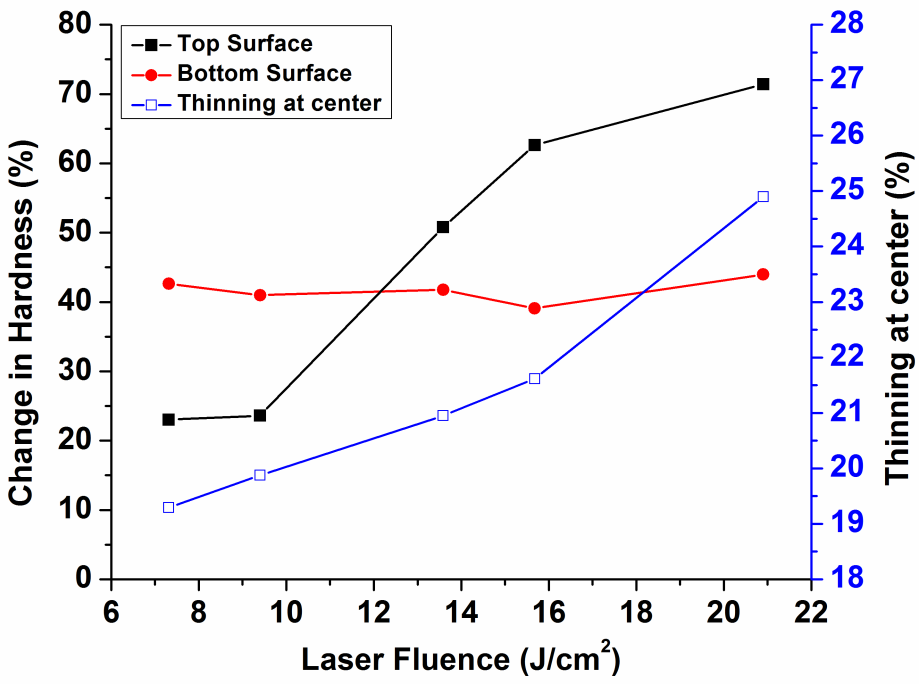

Figure 5.10: Correlation between surface hardness and thinning

In FPLSF, the process configuration could be a decisive factor in the plastic deformation and the subsequent mechanical properties of the deformed feature. Upon shockloading, the foil top surface experiences compression by the propagating shockwaves while the bottom foil surface experiences movement restriction from the flexible pad which undergoes concurrent elastic deformation. As a result, the amount of plastic deformation and the underlying mechanism could be varying between top and bottom crater surfaces, resulting in dissimilar microstructure and surface hardness profiles. The possible deformation mechanism in FPLSF is studied further using with microstructure analysis.

5.3 Microstructure analysis

5.3.1 Electron backscatter diffraction

Electron backscatter diffraction (EBSD) technique is a SEM based method to quantitatively characterize the crystal lattice orientation, texture, phase information, grain boundary characteristics, and microstructure [196–198]. A schematic of the pattern acquisition using EBSD is illustrated in Fig. 5.11 [199]. The working principle of EBSD system is briefed as follows [197]: The sample, which is polished precisely, is tilted to the incident electron beam. Typically, the beam penetrates to a narrow distance of 5 - 50 nm from the surface. When an electron beam is incident on the tilted crystalline specimen, the electrons are diffracted from the crystal planes which form a large cone as seen from Fig. 5.11. Diffraction of patterns are formed with the intersection of the cone with a phosphor screen, which is placed in the vicinity. Diffraction patterns consist of a set of Kikuchi bands, which are characteristic of the sample crystal structure and orientation. The identification of the bands is achieved automatically using Hough transformation from which the crystal orientation at each measurement point in the sample is identified.

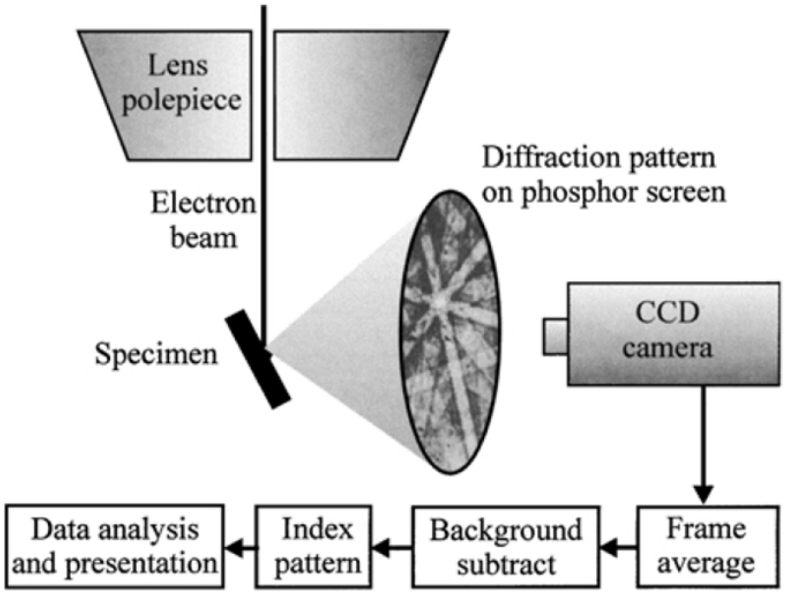

Figure 5.11: Schematic of electron backscatter diffraction pattern acquisition [199]

In this analysis, an EBSD system (Oxford Instruments HKL) attached to JEOL 7600F field emission SEM (FE-SEM) system was used. Channel 5 acquisition package was used to collect and analyze the EBSD data. The tilt angle and working distance of the sample were 70^{o} and 24 mm respectively. The required area on RD-TD plane (along the crater surface) of the sample was scanned at a step size ranging between 0.5 μm and 1 μm using the beam scanning mode.

The boundaries of the crystal grains are defined using misorientation angle, which is the difference in orientation between grains, through rotating the coordinate system of crystals into coincidence. Typically, the misorientation angle for the grain boundary (high-angle boundary) is found to be greater than 10^{o}, whereas the subgrain boundary (low-angle grain boundary) is lesser than 2^{o} [89, 198, 199]. In this analysis, misorientation angle of 10° and 2° were used to define the grain and subgrain boundaries, respectively. Inverse Pole Figure (IPF) maps help to identify the grains and their orientation by interpreting the crystallographic orientations with the sample coordinate system. Band contrast map highlights the degree of plastic deformation the grain experiences, with low contrast (darker region) indicating larger deformation and high contrast (bright region) indicating no deformation. The following quantitative parameters, grain size distribution, aspect ratio, and misorientation angle distribution are characterized from the analysis. Grain size is calculated using the mean line intercept method (ASTM E112 standard).

Prior to the analysis, a critical sample preparation procedure is required as the diffraction patterns are acquired from few nm deep at the surface. In addition to the mechanical polishing in sequence from coarse abrasives to the colloidal silica as described earlier, electropolishing of the samples was performed. Electropolishing removes the surface irregularities and the deformation layers. The following parameters were used for the electropolishing of copper foils: electrolyte - D2 (Struers A/S), area - 0.5 cm^2, voltage - $15V$, time - 10 to 20 sec.

5.3.2 Deformation mechanisms in FPLSF

The changes in microstructure of copper foils after forming are studied by comparing the inverse pole figures and band contrast maps of a plain copper foil surface with the top and bottom surfaces of the formed craters. The microstructure of the copper foil surface before and after FPLSF is shown in Fig. 5.12 and Fig. 5.13.

Fig. 5.12 shows that significant grain elongation occurred after FPLSF as a result of plastic deformation. Elongation of grains were experienced both at the top and bottom surfaces of the crater. Also, a significant increase in subgrain boundaries, which are represented as thin lines in 5.12c, was observed after forming. Nucleation of strain-free fine grains during forming is also evident from Fig. 5.12. Subsequently, an increase in high dislocation density regions was experienced after forming. This behavior is evident from the band contrast maps of the copper foil before and after FPLSF as shown in Fig. 5.13, where the darker regions represent the increase in the degree of plastic deformation.

The quantitative characterization of microstructure using grain diameter, aspect ratio, and misorientation angle is compared for copper foils before and after FPLSF in Figs. 5.14 and 5.15. It can be observed from Fig. 5.14a that the fraction of grains with diameter smaller than 1 µm increased after FPLSF, indicating the nucleation of new grains during plastic deformation. An increase in number of grains with aspect ratio less than 1.5 was observed after forming as seen from Fig. 5.14b, suggesting an increase in uniformity of grains. Typically, uniformity in grain size is achieved by grain refinement through recrystallization, recovery, or grain breakdown. Meanwhile, it is clear from Fig. 5.12 that the grain elongation has been predominant in FPLSF. Thus, the increase in uniformity (reduction in aspect ratio) could have resulted from the nucleation of new grains during the forming process.

Fig. 5.15 compares the misorientation angle distribution of copper before and after FPLSF. The fraction of low angle grain boundaries (misorientation angle $< 2.5^{o}$) is found to increase from 5 % at plain foils to 21 % after forming. As the

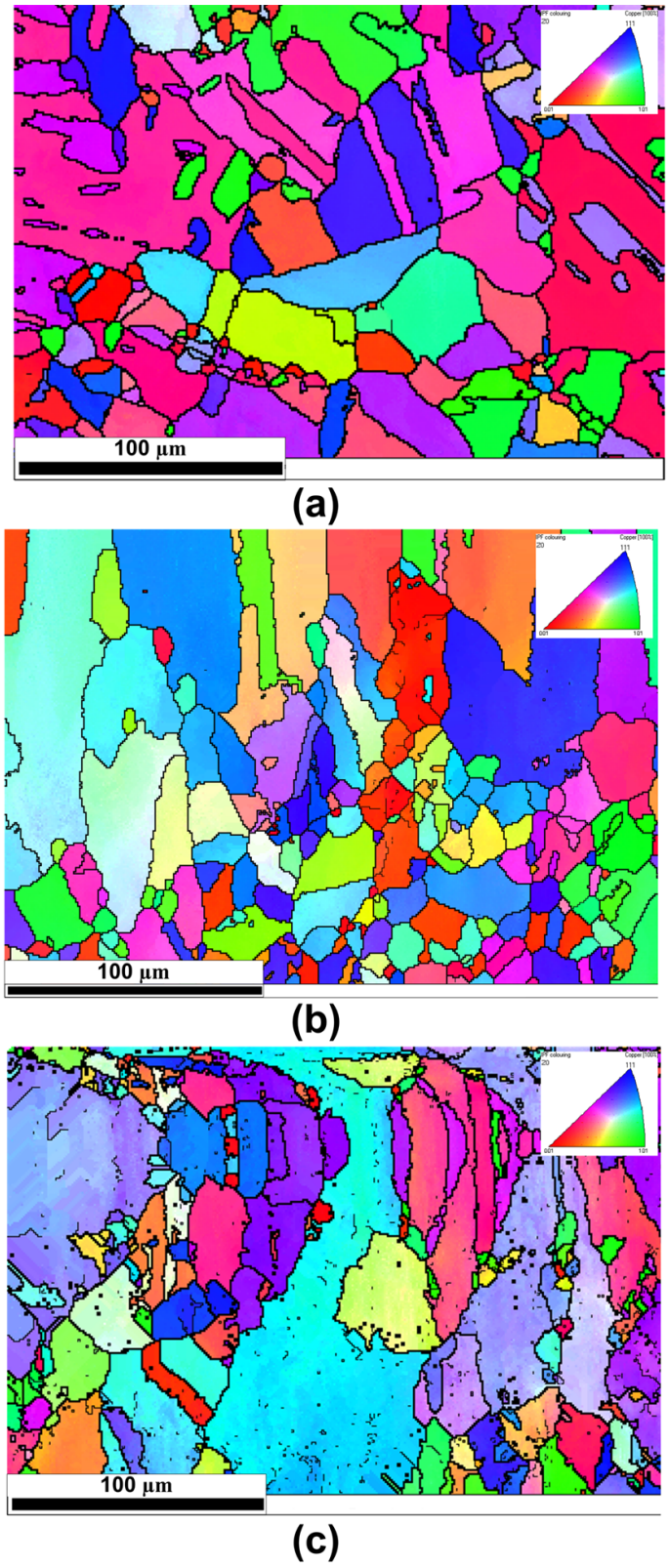

Figure 5.12: Comparison of microstructure of copper foil before and after FPLSF at 13.6 J/cm^2 fluence by inverse pole figure map (a) Copper foil surface before FPSLF (b) Top surface of the formed crater (c) Bottom surface of the formed crater

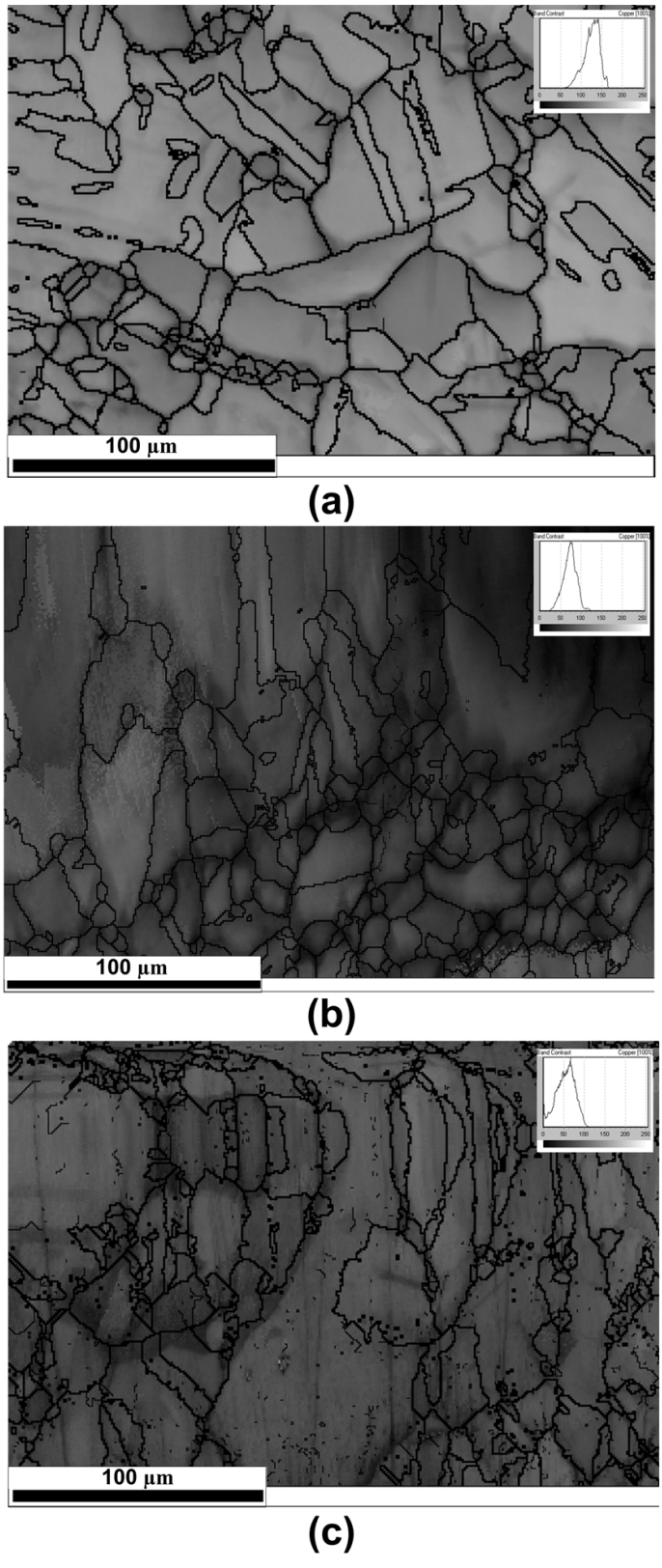

Figure 5.13: Comparison of microstructure of the copper foil before and after FPLSF at 13.6 J/cm^2 fluence by band contrast map (a) copper foil surface before FPSLF, (b) top surface of the formed crater, (c) bottom surface of the formed crater

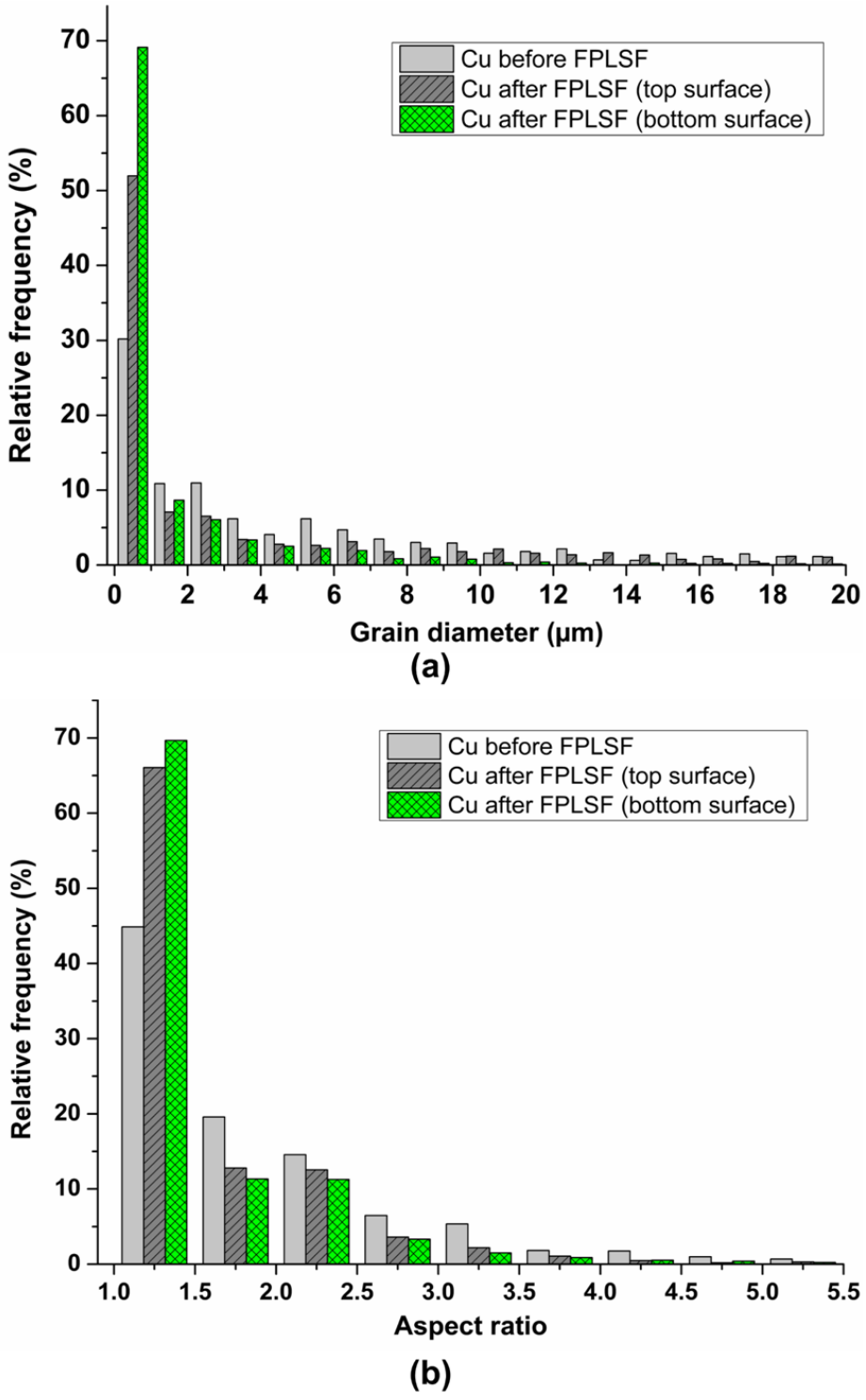

Figure 5.14: Comparison of grain size distribution of the copper foil surface before FPLSF with the top and bottom surfaces of the craters formed by FPLSF (a) grain diameter, (b) aspect ratio

smaller misorientation angle ($<2^{o}$) indicates the presence of subgrains and newly nucleated grains, the increase in substructures in the foil after FPLSF is evident. This observation also substantiates the reduction in grain size behavior observed

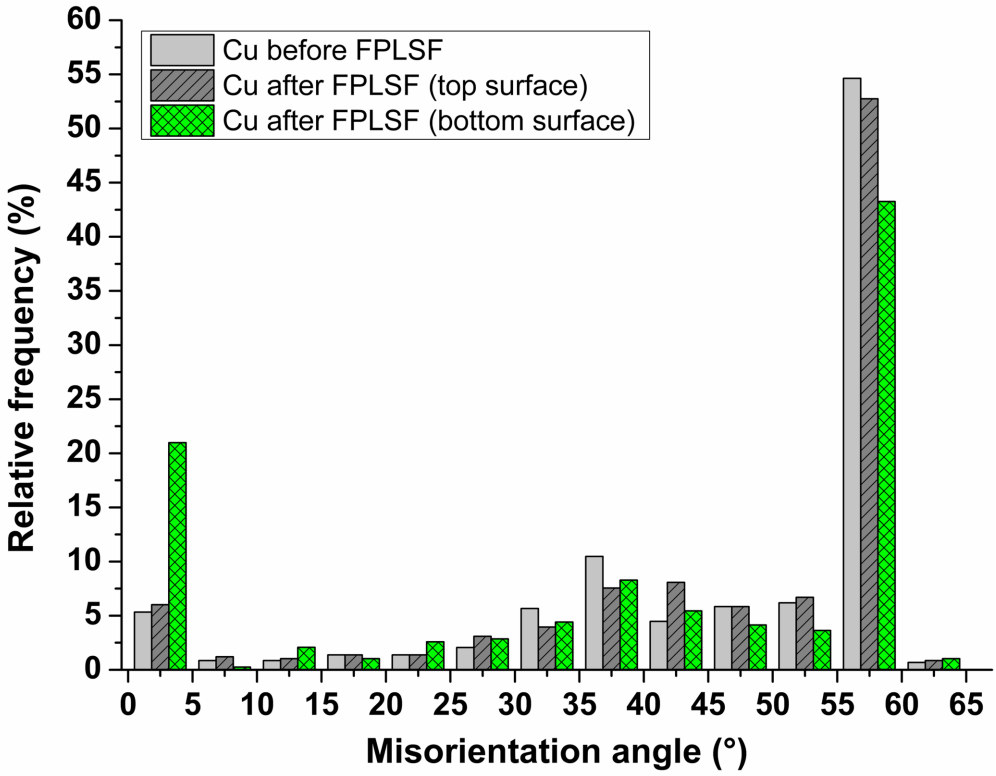

Figure 5.15: Comparison of misorientation angle distribution of the copper foil surface before FPLSF with the top and bottom surfaces of the craters formed by FPLSF

in Fig. 5.14a. Though the fraction of high angle grain boundaries was reduced after forming, an increase in high dislocation density regions is apparent from Figs. 5.13b and 5.13c. During the plastic deformation of copper foils with FPLSF, a significant increase in subgrain formation and dislocation density was experienced.

It is interesting to note that, although the loading conditions are similar between FPLSF and other high strain rate processes, the plastic deformation behavior as well as the microstructural changes are observed to be significantly different. Andrade et al. [136] observed the predominant subgrain formation in copper after shock loading. Similar subgrain structures were found by Cheng et al. [89] during laser dynamic forming of copper. The average size of the grains was approximately 0.1 to 0.5 μm after shock loading of copper [89, 136]. In case of FPLSF of copper, despite the subgrain formation, the average grain size was found to be greater than 1 μm. There was no refinement of grains during FPLSF as in other high strain rate processes. This difference in microstructure modification can be attributed

to the combination of several factors. Typically, the plastic deformation mechanism is influenced by a complex interaction between strain levels, strain rate, and applied pressure. The difference in mechanisms between FPLSF and other laser shock forming processes is attributed to the following behavior:

1. FPLSF configuration is considered as one of the major causes of the difference in process mechanisms. In other high strain rate processes, the deforming material is either bulk, as in laser shock peening, or sheets flowing into a die, as in explosive forming or laser dynamic forming. In both cases, there will be severe compression of the metal along the thickness direction due to the harder metal support or die resisting the displacement of the substrate. In FPLSF, the displacement is constrained by the flexible pad that absorbs the energy and undergoes larger elastic deformation, while allowing the metal foil deformation simultaneously. The deformation velocity is controlled in FPLSF using a flexible pad whereas large deformation velocity is experienced in processes using dies.

2. Large plastic strains ($\varepsilon > 4$) are required for the occurrence of dynamic recrystallization, where elongation of grains and subsequent breakdown to subgrains of 0.1 μm, followed by nucleation of new grains happen [136]. In FPLSF, the plastic strain levels experienced by the copper foil during deformation is around 0.5, as observed from the finite element analysis of FPLSF, as seen in the next chapter. These strain levels are considerably small in comparison to the plastic strains (3 to 4) suitable for the dynamic recrystallization conditions.

3. A significant difference in the deformation mechanism between copper specimen shocked using femtosecond (fs) and nanosecond (ns) lasers was experienced [134]. Dislocation slip occurring with ns lasers was suppressed by twinning and stacking faults with fs lasers as a result of increased shock pressure and strain rate. This result highlighted that the increase in strain

rate from $10^6 s^{-1}$ (for ns pulses) to $10^8 s^{-1}$ (for fs pulses) causes a significant change in the mechanisms involved in the plastic deformation. In FPLSF, the strain rate of the foil is significantly reduced ($\sim 10^4 s^{-1}$) due to the controlled displacement of metal foils induced by the flexible pad arrangement. The reduction in strain rate influences the deformation mechanisms significantly.

4. In high strain rate forming with dies, there will be additional material compression upon impact due to the inertia effects, increasing the plastic strain further. As the displacement is restricted in FPLSF, the compression of metal in the thickness direction due to the inertia effects is greatly reduced. It is understood that the importance of inertia effects on the formability and mechanical properties improvement in high strain rate forming processes is considerably larger than reported.

The combined effect of reduction in strain rate, strain levels, and inertia effects restricts the FPLSF process to experience high strain rate effects. From the observations of inverse pole figure maps, grain diameter, aspect ratio, and misorientation profiles, the strain hardening behavior appears to be more prominent than the adiabatic softening, which is a common behavior during high strain rate processes. Dislocation slip is predicted to be the dominant deformation mechanism rather than twinning or stacking faults in FPLSF due to the reduced strain rate and plastic strain. The results highlight that, in addition to strain rate, plastic strain magnitude and inertia effects also play a dominant role in the adiabatic softening mechanism.

5.3.3 Comparison between top and bottom surfaces

The microstructural difference between the top and bottom crater surfaces is analyzed. During FPLSF, the top surface of the metal foil is subjected to laser shock loading while the bottom surface is constrained by the flexible pad. Fig. 5.12 shows that the grains at the bottom surface experienced more elongation than at the top surface. Also, the presence of subgrain boundaries was prominent at the

bottom surface of the crater. Correspondingly, the bottom surface consisted of a large fraction grains with diameters less than 1 μm in comparison to the top surface which is observed from Fig. 5.14a. A significant increase in low angle grain boundaries after forming at the bottom surface (Fig. 5.15) confirms the larger amount of subgrain formation at the bottom surface. Comparison of aspect ratio (Fig. 5.14b) also shows that the grains appear to be more uniform at the bottom surface, largely due to nucleated fine grains.

Therefore, it is evident that the bottom surface contained high dislocation density regions, fine grains and substructures, whereas the top surface consisted mainly of high dislocation density regions. This phenomenon is expected since the bottom surface experiences an axial compression in the thickness direction due to the flexible pad throughout the foil deformation during shock loading while the top surface is subjected to the shock loading only. The larger compressive strain in the axial direction and tensile strain in the transverse directions at the bottom surface compared to those of top surface induces more elongation of grains at the bottom. The larger magnitude of plastic strain at the bottom surface is confirmed by the finite element analysis of FPLSF. The occurrence of larger plastic deformation at bottom surface induces nucleation of new grains concurrently with grain elongation. Meanwhile, the top surface experiences volumetric compression during plastic deformation. The compression of grains reduces the elongation of grains and increases the uniformity of grains as shown on Fig. 5.12b.

The larger increase in hardness at the top crater surface as a result of FPLSF as seen in Fig. 5.10 can be explained as follows:

- An increase in uniformity of grains was observed at the top crater surface (Fig. 5.12b). As the uniform grains leads to even distribution of load among the grains, an increase in the material strength is experienced.
- The compression of grains at the top surface as opposed to the grain elongation at bottom surface could cause significant difference in dislocation movement and substructure formation.

- The dislocation density is greater and approximately uniform across the grains at top surface in comparison to the bottom surface as it is concentrated on narrow regions at bottom during the deformation, which can be verified from the band contrast density (Fig. 5.13).

The presence of subgrain structures at the bottom surface indicate the simultaneous existence of high strain rate effects in narrow regions where the plastic strain and strain rates are higher, along with dominant strain hardening in most of the regions. The top surface reveals the evidences of merely the strain hardening effect. This difference in plastic deformation mechanism between top and bottom surfaces could be a significant factor in the dissimilar hardness behaviors of constant hardness at bottom surface and increasing hardness at top surface with increasing laser fluence, as observed in Fig. 5.10. The observed correlation between foil thinning and top surface hardness is a result of plastic deformation due to the strain hardening mechanism.

5.3.4 Comparison between center and edges of crater

The deformed craters obtained by FPLSF experienced different amount of plastic deformation between the center and edge portions as evidenced from the corresponding change in thickness (Fig. 5.2). Thus, the microstructure at the edge regions of the crater is analyzed with that of the center regions. Fig. 5.16 shows the inverse pole figure and band contrast maps of the crater edge region at the laser fluence of 13.6 J/cm^2. A substantial increase in high dislocation density regions was observed around a narrow thin portion along the crater edge. Meanwhile, the grain elongation was observed at the adjacent regions.

The grain diameter and aspect ratio are compared between crater center and crater edge regions in Fig. 5.17. The grain size distribution at the crater edge region appears to be similar to that of as received copper, but a reduction in average grain diameter and its standard deviation was observed. In the crater edge regions, the fraction of smaller grains (diameter < 1 μm) is 31% in comparison

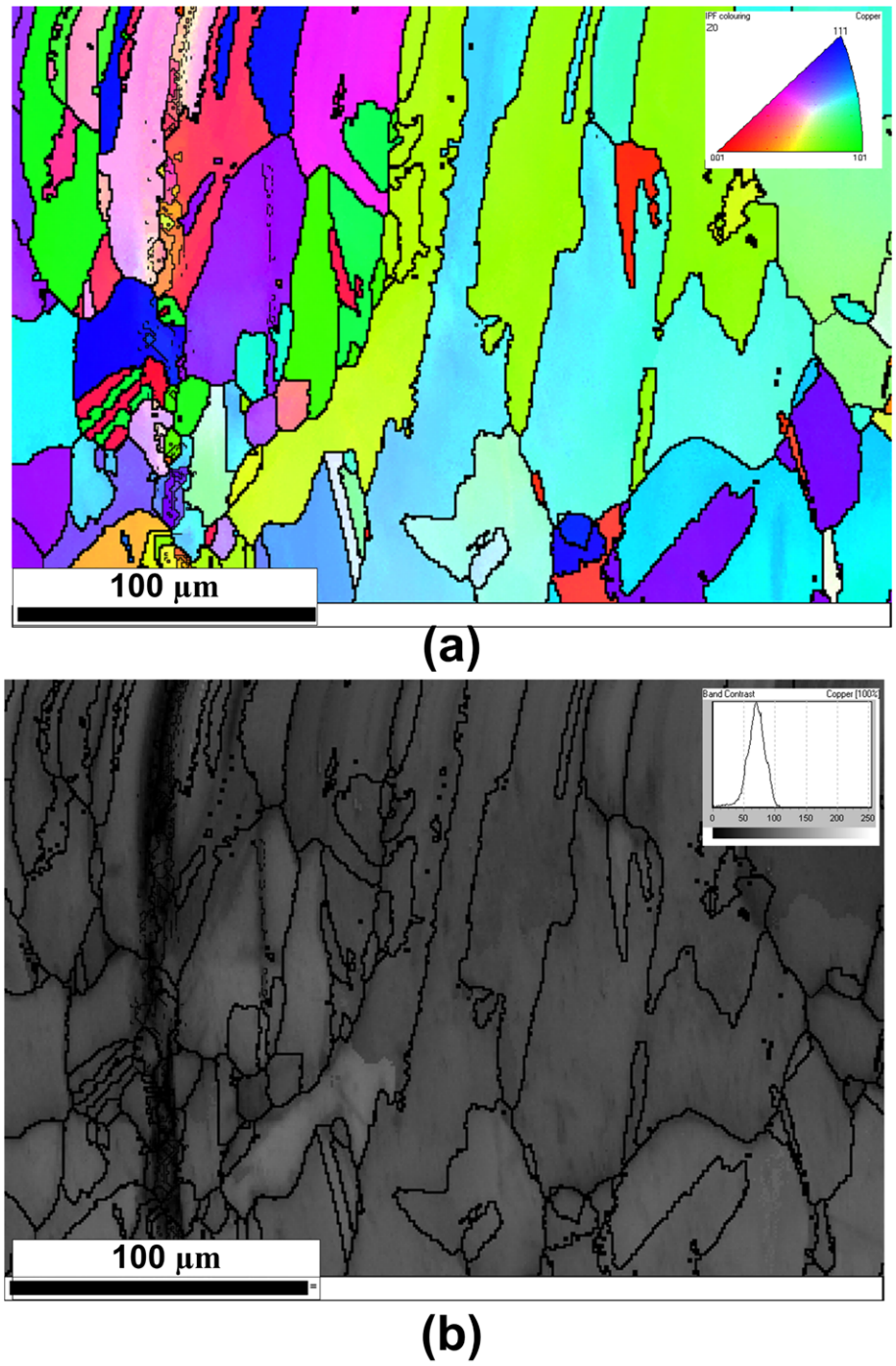

Figure 5.16: Deformation crater edge region at the bottom portion at 13.6 J/cm^2 fluence (a) Inverse pole figure map (b) Band contrast map

to 68.5% in the crater center, which highlights the presence of larger grains at the edges. The grains were more elongated at the crater edges than at the crater center as evidenced from Fig. 5.16 and Fig. 5.12. The subgrain formation and nucleation of new grains at the crater edges were not as significant as experienced at the crater center, which resulted in the increased diameter (more grains with

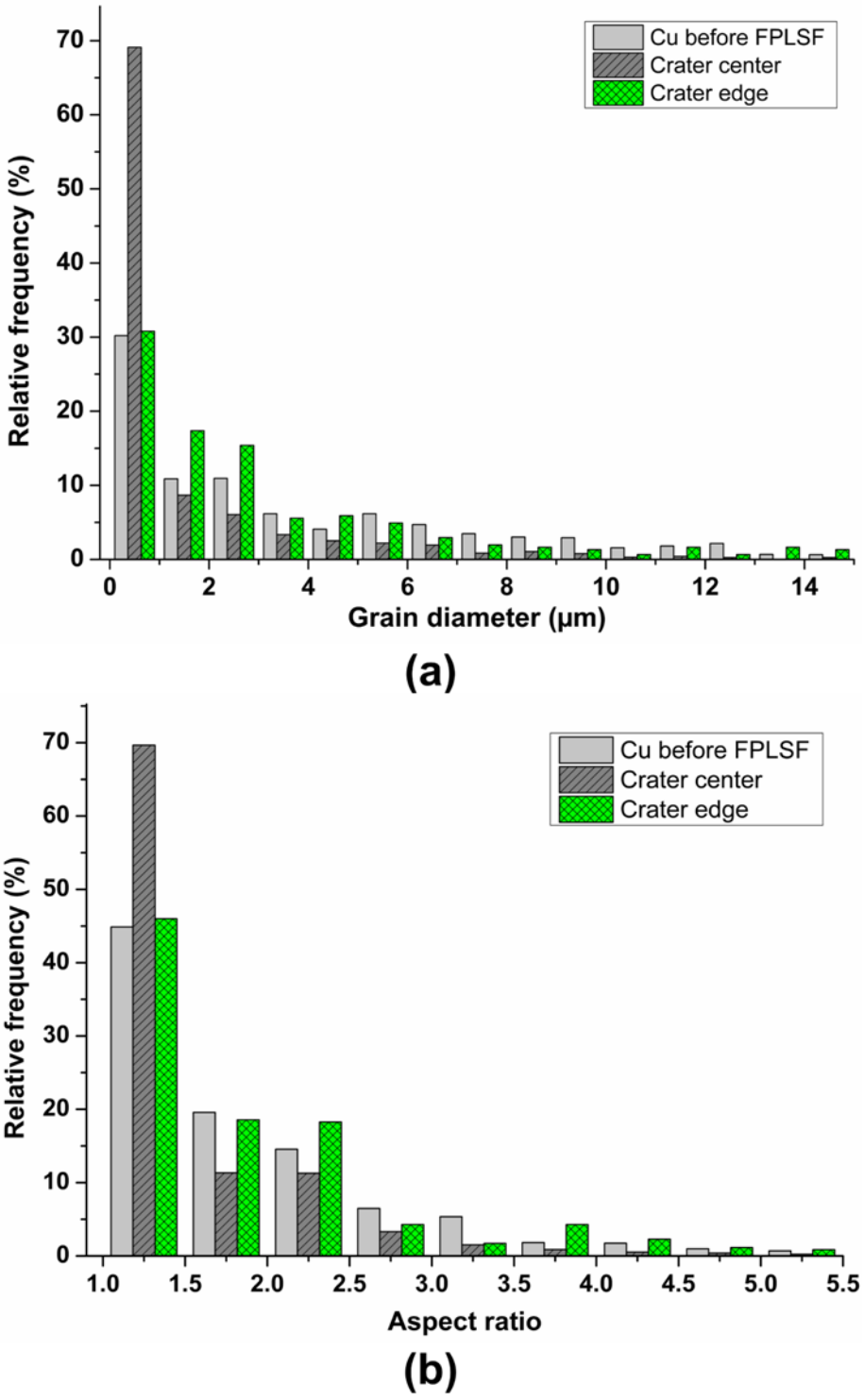

Figure 5.17: Comparison of grain size distribution between center and edge regions of the deformation crater (bottom side) by FPLSF (a) Grain diameter (b) Aspect ratio

diameter $> 1\ \mu m$) and less uniformity (aspect ratio > 1.5) of the grains at the edges. This effect can be compared with the misorientation angle distribution at Fig. 5.18, where the fraction of low angle grain boundaries (misorientation angle

$< 2.5^{o}$) at the edge (7%) is three times smaller, in comparison to the center (21%). The observed difference in microstructure between the center and edge portions of the crater is reasonable as the magnitudes of stress, plastic strain, and strain rate are comparatively smaller at the circumference than at the center.

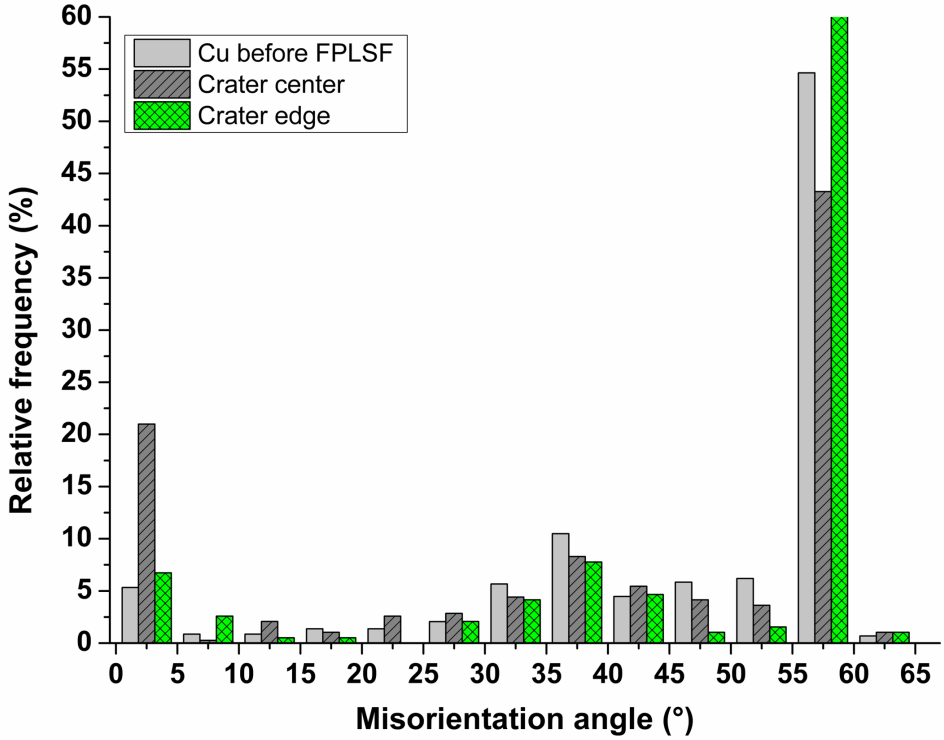

Figure 5.18: Comparison of misorientation angle distribution between center and edge regions of the deformation crater (bottom side) by FPLSF

In high dislocation density thin region along the crater circumference, few fine grains were observed as shown in Fig. 5.16. This behavior can be explained by finite element analysis (6.3). During plastic deformation, each side of the laser beam outer edge experiences a varying stress profiles. The region towards the crater center experiences a tensile stress whereas the opposite region experiences compression. The compressive strain in the narrow region could have resulted in the refinement of grains and the higher dislocation density region in Fig. 5.16, whereas the grain elongation is caused by the tensile stresses.

5.3.5 Effect of laser fluence

The effect of laser fluence on the microstructure of the formed crater is analyzed for two different fluences, 13.6 J/cm^2 and 20.9 J/cm^2. Fig. 5.19a shows the band contrast map of the crater bottom surface corresponding to 20.9 J/cm^2 fluence. It is evident from the comparison of Fig. 5.19a with Fig. 5.13c corresponding to 13.6 J/cm^2 fluence that, a substantial increase in high dislocation density regions was observed with an increase in laser fluence. The increase in laser fluence increases the shock pressure, and hence the plastic deformation of the foil. Fig. 5.20 compares the misorientation angle distribution between 13.6 J/cm^2 and 20.9 J/cm^2 fluences. With increase in laser fluence from 13.6 J/cm^2 and 20.9 J/cm^2, both increase in low angle boundaries ($< 2^o$) from 21% to 23% indicating the presence of subgrains, and high angle boundaries ($>55^o$) from 43.3% to 49.2% indicating high dislocation density regions were observed.

5.3.6 Texture Analysis

The surface textures generated on the deformed metal after forming influences the mechanical properties. Fig. 5.21 compares the inverse pole figure maps of the copper foil before and after FPLSF. It can be observed from 5.21c that, after FPLSF, a large number of grains in bottom surface along the rolling direction ($X0$) were oriented towards the (111) crystal plane , which is the densely packed crystallographic plane, favorable for slip to occur during plastic deformation in FCC crystals. The further plastic deformation could be relatively easier at the bottom surface than at the top surface due to the crystal lattice orientation favorable for dislocation slip. The texture formation could also explain for the lower hardness observed at the bottom surface compared to that of the top surface after FPLSF (as seen in Fig. 5.10). However, no significant texture formation was observed after FPLSF.

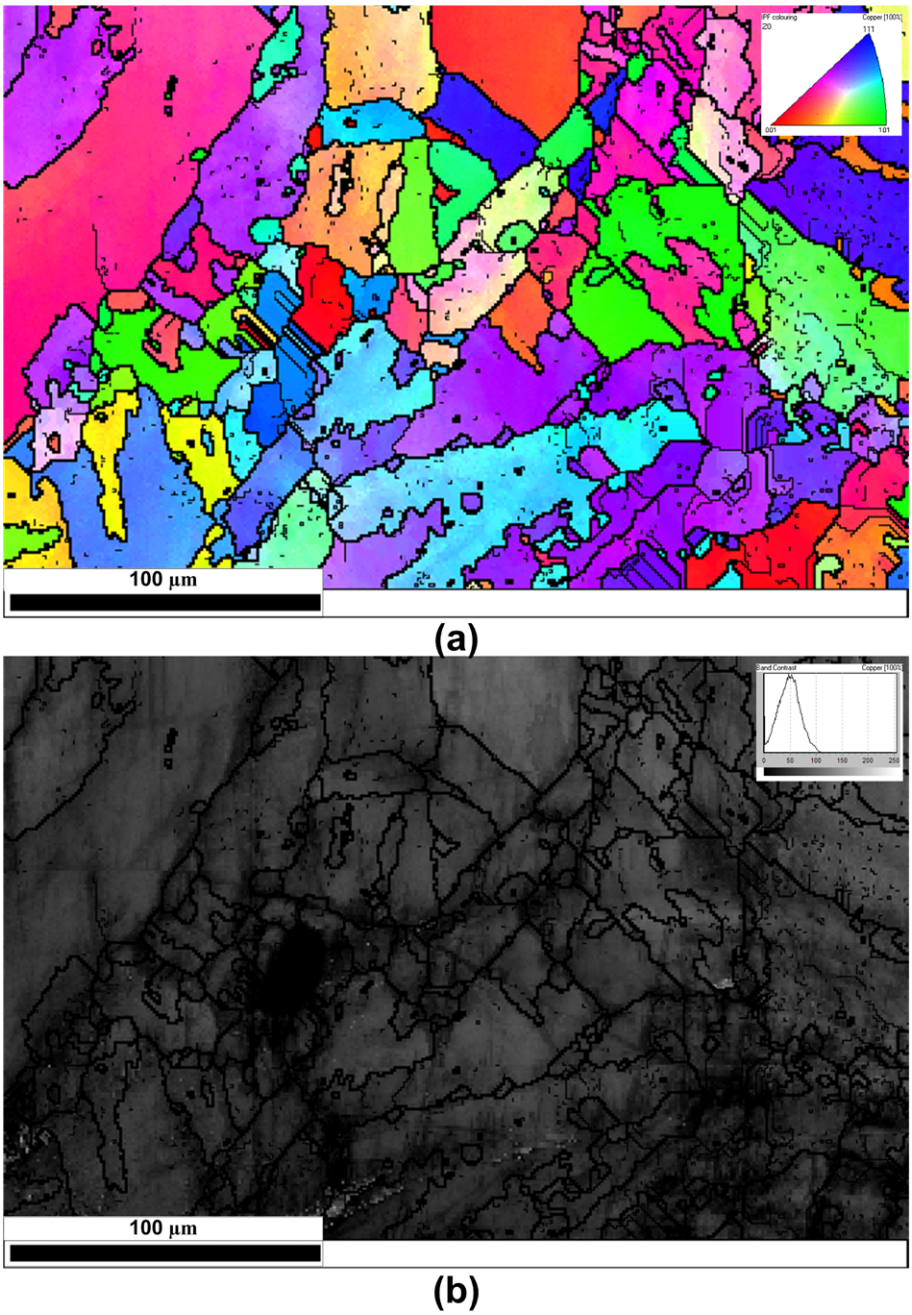

Figure 5.19: Crater microstructure at the bottom portion at 20.9 J/cm^2 fluence (a) Inverse pole figure map, (b) Band contrast map

5.4 Summary

This paper studies the high strain rate plastic deformation behavior of thin metal foils in FPLSF. The hemispherical crater formation during FPLSF is characterized using foil thinning, surface hardness of the craters, and qualitative and quantitative microstructural analysis in order to study the underlying plastic deformation

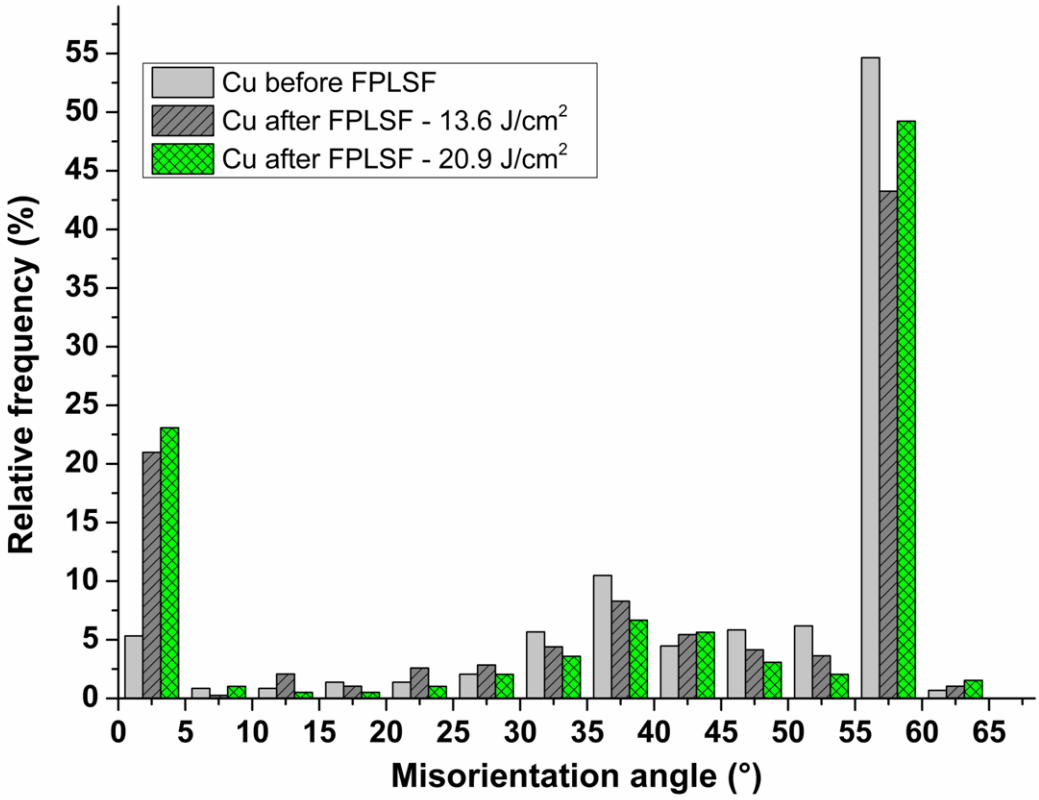

Figure 5.20: Effect of laser fluence on the misorientation angle distribution of crater surface after plastic deformation by FPLSF

mechanisms. The following conclusions were obtained from the results:

1. FPLSF produces uniform thickness distribution (variation less than 10%) across the deformed craters with maximum thinning at the crater center.

2. The microstructure of the copper foil surface after FPLSF consisted of sub-grains, nucleated fine grains, high dislocation density regions, and predominantly elongated grains. Correspondingly, reduction in grain size and aspect ratio together with increase in low grain angle boundaries were witnessed.

3. An improvement in surface hardness of the deformed features was realized. The larger surface hardness at the top surface in comparison to the bottom surface is attributed to the increase in grain uniformity and high dislocation density regions.

4. In FPLSF, strain hardening effect was observed to be the dominant plastic deformation mechanism, contradictory to the occurrence of adiabatic softening

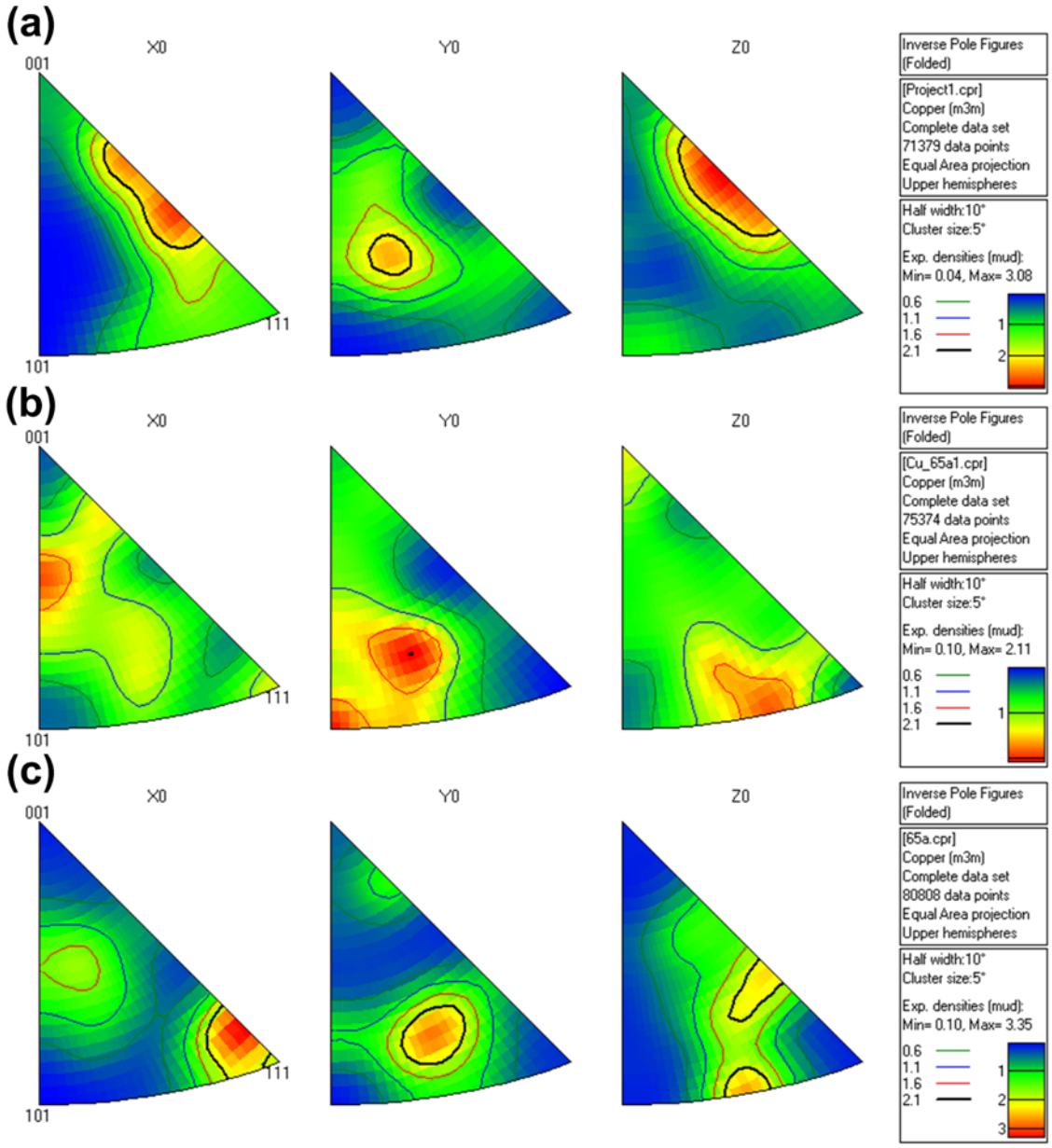

Figure 5.21: Comparison of texture of copper foil before and after FPLSF at 13.6 J/cm^2 fluence by Inverse pole figure mapping (a) Copper foil surface before FPSLF, (b) Top surface of the formed crater, (c) Bottom surface of the formed crater

known to occur at high strain rate deformations. This behavior is attributed to the FPLSF process configuration which induced a combined reduction of plastic strain, strain rate, and inertia effects.

5. Deformation behavior was observed to be different at the top and bottom surfaces, and also at the center and edge regions of the crater, causing a change in hardness and microstructure profile.

6. Increase in subgrain structures and high dislocation density regions are observed with increase in laser fluence

In addition to the process related benefits with FPLSF as discussed in chapter 4, improved process formability demonstrated by FPLSF results in deformation features with uniform thickness distribution and enhanced mechanical strength, which is favorable for the fatigue life of the microcomponents. The modeling and prediction of the developed process is paramount to deploy in the industry, which will be focused in the next chapter.

Chapter 6

Finite Element Analysis

The prediction of process behavior is a necessity for process design purpose. Also, in FPLSF, the deformation of the metal foil occurs at strain rates greater than 1 x 10^5 s^{-1}. At these process speeds, it is difficult to study the process evolution and the stress-strain distributions during the deformation process experimentally. Furthermore, it will be time-consuming and difficult to extensively investigate the wide range of various process variables experimentally to understand their influence on the metal foil deformation. Therefore, process simulation of FPLSF is necessary to predict the process outputs, analyze the process variables, and study the characteristics of high strain rate deformation of metal foil and flexible pad.

6.1 Finite element model setup

A commercially available finite element analysis software package, ABAQUS is used in this analysis. Explicit algorithm is typically used to model the high speed dynamic events for which implicit algorithm has convergence issues. Explicit method uses a large number of small time increments. In this modeling, explicit algorithm is used as FPLSF involves high speed shock loading, resulting in dynamic material response. As the shock loading profile is assumed to be identical to that of the laser beam profile, the square laser beam requires 3D modeling of the process. However, a quarter of the 3D model is sufficient and used for the simulation to reduce the

computational cost. The 3D finite element model consisting of metal foil, flexible pad, and metal support is shown in Fig. 6.1.

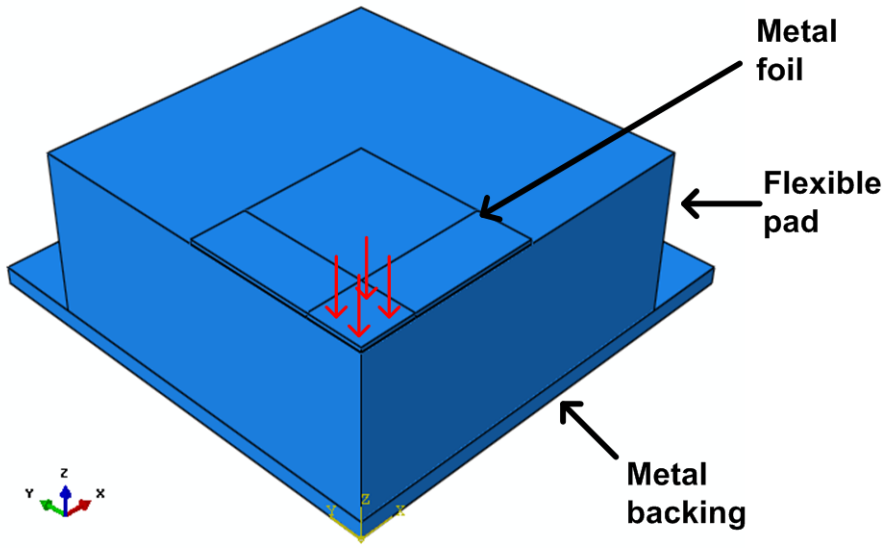

Figure 6.1: 3D finite element model of FPLSF process

The flexible pad is placed over the rigid metal support. Both the foil and the flexible pad are modeled as deformable solids, where the part dimensions (1 mm x 1 mm x 0.025 mm) correspond to the experimental setup. The metal foil and the flexible pad are defined using C3D8R elements, which are 8-node, linear brick elements with reduced integration and hourglass control. This process involves two contact interaction pairs: metal foil and flexible pad and metal support and flexible pad. The interaction between the contact surfaces are defined using surface to surface contact algorithm with kinematic contact formulation. Symmetric boundary conditions are applied on $x-0-z$ and $y-0-z$ surfaces for both the foil and flexible pad. A time period of 25 μs is modeled in this simulation. The other modeling parameters including loading conditions, material modeling, mesh density, and friction properties are discussed further below. Fig. 6.2 illustrates the foil locations at the center and circumference of the crater, where the stress and strain distributions are analyzed in detail.

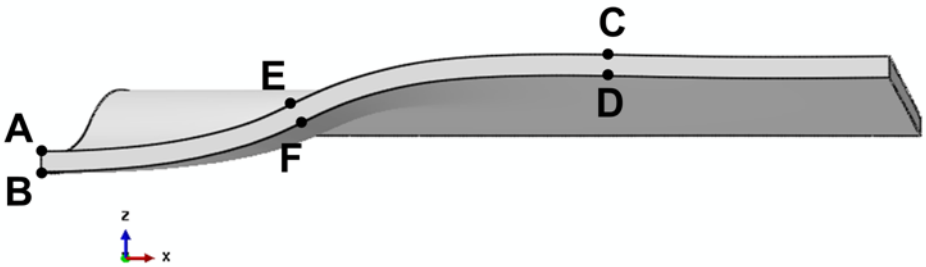

Figure 6.2: Measurement set positions in metal foil for analysis

6.1.1 Plastic deformation of metal foils

As FPLSF involve high strain rate (10^5 s^{-1}) plastic deformation, Johnson-Cook constitutive model (Equation 2.11), which is developed for materials subjected to high temperature, large strains, and high strain rates has been employed in this analysis [181]. The mechanical properties of the substrate metal foils, pure copper, pure nickel, and AISI 316 stainless steel, are presented in chapter 3 (Table 3.1). As the experiments are conducted at room temperature, the temperature effects are neglected from the analysis.

6.1.2 Laser-induced shock pressure

In laser shock processes, the laser-induced shock waves provides the deformation force, where the loading is given in terms of shock pressure. The loading area identical to the beam area has been used in laser shock processing [156, 200]. The spatial pressure profile is also assumed to be identical to the laser beam profile. However, Gulshan et al. [153] partitioned the loading area five regions from the center of irradiation in which the pressure magnitude increases from the center to the outer edge. As the flat top intensity profile is used in the experiments, spatial distribution of the pressure is maintained uniform across the loading area. Shock loading was applied on top of the metal foil in an area over 0.3 mm x 0.3 mm, as illustrated by arrows in Fig. 6.1. The selection strategy of the temporal profile and lifespan of the pressure pulse is discussed further in the next sections.

6.1.2.1 Pressure - Temporal profile

The temporal profile of the shock pressure is identified to be an influential factor. Though the pressure pulse profile depends on the laser pulse, different pulse profiles as illustrated in Fig. 6.3a have been used in the simulation of laser shock processes [148, 155]. Hu et al. [155] approximated the pressure pulse into a triangular ramp, where the pressure reaches its peak in the time duration equal to its FWHM and decays to zero in the same FWHM time period (Fig. 6.3a). This assumption was attributed to the shorter duration of the pressure pulse. A slightly different triangular pulse was used in the laser shock bulging simulation by Zheng et al. [201]. Nam [202] used a pressure pulse profile as indicated in Fig. 6.3a, which was adopted by Gulshan et al. [153] in the simulation of laser shock peening. However, the actual pressure pulse measured experimentally by Peyre et al. [176] was found to follow the Gaussian laser pulse distribution, as shown in Fig. 6.3b. Thus, in this analysis, pressure pulse according to the temporal profile of the laser pulse has been used.

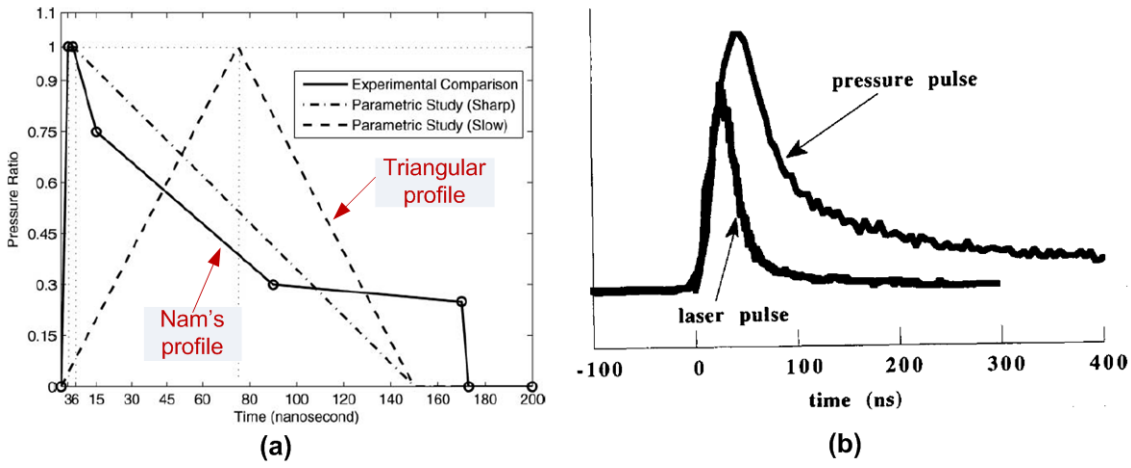

Figure 6.3: Shock pressure temporal profiles (a) Approximation of pressure profile for simulation [153] (b) Experimental measurement of temporal profiles of shock pressure and the laser pulse [176]

It can be identified from Fig. 6.3b that the shock pressure profile is identical to the laser pulse profile initially until the beam attains its peak. The pressure increases further and reaches its maximum, after which it is reduced at a faster

rate initially and then the decline becomes gradual. Typically the pressure pulse is characterized by FWHM (Full width at half maximum) to calculate its duration. Pence et al. [203] predicted the duration of pressure to be twice that of laser pulse using hydrodynamic modeling. Whereas, the pressure pulse, 3 to 4 times longer than the laser pulses was reported from the experimental investigations by Fabbro et al. [146]. According to the shock pressure modeling discussed earlier (section 2.7.1 in chapter 2), the pressure pulse duration is predicted to be 2 times longer than the laser pulse duration in confining conditions. Ocana et al. [204] used an 1D model, LSPSIM for the shock pressure estimation. However, in laser-induced shock pressure simulations, the Fabbro's shock pressure model [160] has been extensively used to define the pressure of shockwaves induced by the expanding plasma under confinement conditions [79, 90, 95]. Fabbro's model is used for the shock pressure estimation in this thesis.

In this thesis, the laser-induced shock pressure as a function of time was calculated by numerically solving the equations 2.6 and 2.7 using MAPLE code. The differential equations require the initial values of absorbed laser intensity, shock pressure, and the plasma interface thickness. The temporal profile of the laser intensity was Gaussian. The fraction of plasma internal energy to increase the thermal energy, α is set as 0.1 [90, 160]. The shock impedance values of the confinement mediums and the ablative overlay target used in this experiment are given in Table 3.2. Temporal distribution of shock pressure calculated from the Fabbro model for various laser intensities is shown in Fig. 6.4. Despite the application of 45 laser pulses during the experiments, single pressure pulse is applied on the metal foil surface during the simulation due to the minor change in deformation geometry (10%) observed experimentally between single and 45 laser pulses in addition to the complexity involved with the interaction of subsequent pressure pulses.

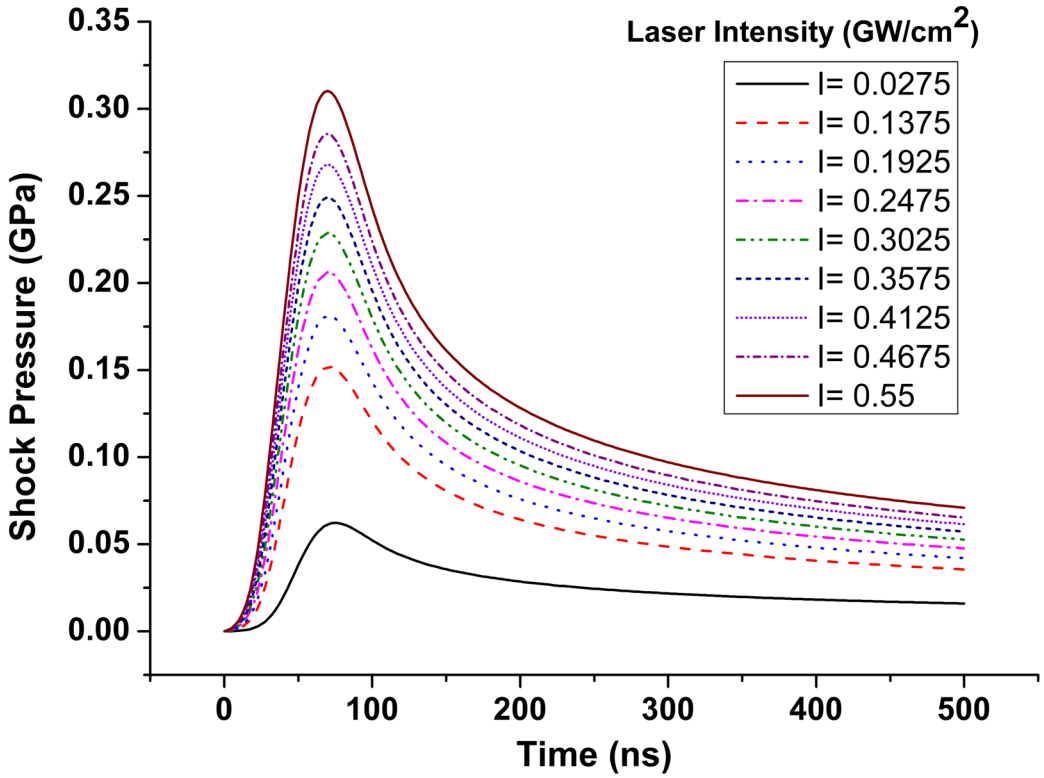

Figure 6.4: Temporal profile of laser-induced shock pressure

6.1.2.2 Shock pressure duration

The analytical formulation of shock pressure does not determine the lifetime of the pressure pulse, which extends well beyond the end of laser pulse as witnessed from Fig. 6.5. Experimental investigation of pressure pulse using quartz gauge by Peyre et al. [176] confirms the following observation (Fig. 6.3b) of longer pressure pulse span in comparison to the laser pulse duration, without specific information on its lifetime. Therefore, the shock pressure pulse lifespan was selected in this analysis by comparing the simulation results at different time periods with the experimental results.

In order to understand the effect of pressure lifespan on the deformation, the following durations are examined: 200 ns, 300 ns, 400 ns, 500 ns. In addition to the simulation conditions mentioned previously, laser fluence of 20.9 J/cm^2, Mooney - Rivlin material model for flexible pad, and an element size of 5 μm in each axis are used for this investigation. It is evident from Fig. 6.6 that the foil deformation increases with the extension of pressure application. It is interesting

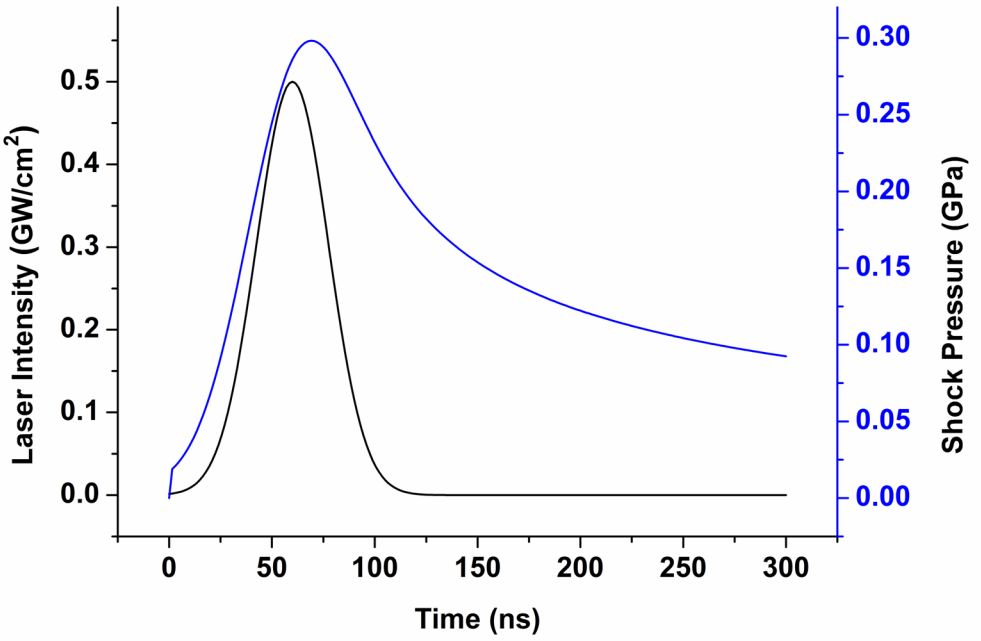

Figure 6.5: Comparison of the temporal profiles of laser beam and pressure pulse estimation using Fabbro's model [160]

to note that, despite the identical pressure magnitude, pressure pulse FWHM, and the peak pulse time, the foil deformation is affected by the time period until which the shock pressure persists. The simulation results with different pulse lifespans are compared with the experimental crater depth of 123.5 μm, and the pressure lifespan of 200 ns is found to have better agreement with the experiments. Thus, the pressure pulse lifespan of 200 ns has been used in this analysis.

6.1.3 Hyperelastic deformation of flexible pad

The flexible pads used in FPLSF possess hyperelastic material properties, experiencing large elastic deformation upon loading. Different models have been reported to define the hyperelastic material properties of the rubber, that has nonlinear elastic behavior when subjected to large strains [205]. The hyperelastic behavior is described through the strain energy density, which is the work done per unit volume to deform a material from stress-free state to a loaded state. The relationship between the stress and strain is defined by the strain energy density function (W) which is a scalar valued function relating strain energy density of a material to the

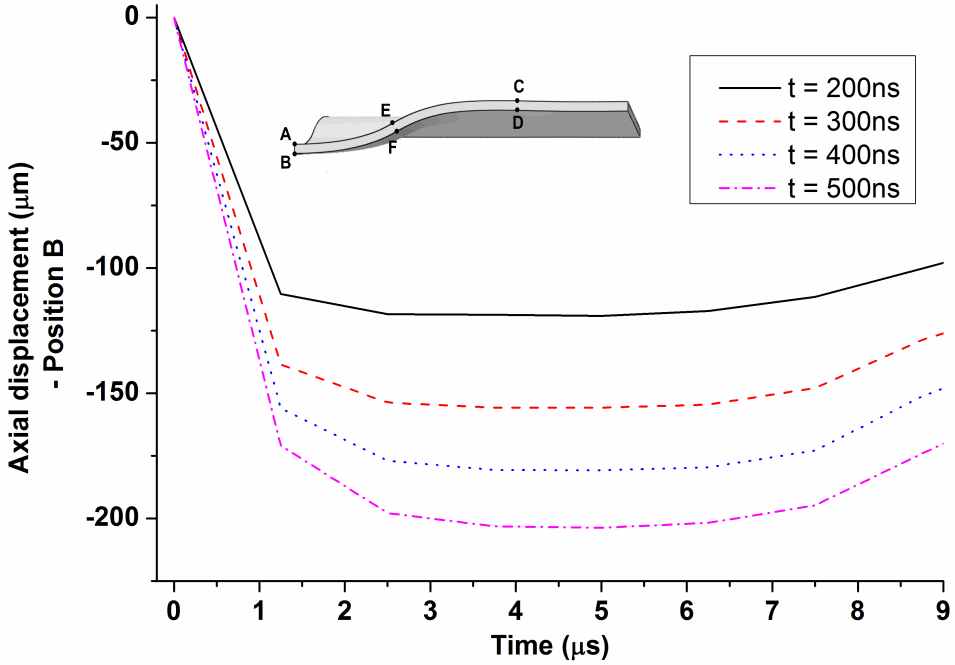

Figure 6.6: Sensitivity of pressure pulse lifespan on metal foil deformation at position B

deformation gradient tensor ($\mathbf{F}$), $W = W(\mathbf{F})$.

Modeling of soft rubber material was first initiated by Hencky [206]. Hencky expressed the relationship between the strain energy and the principal strains (e_i) as a function of $ln(1+e_i)$ rather than e_i. However, the prediction of rubber behavior beyond the stretch level using this model was found to be inconsistent. Mooney [207] then developed a strain energy model consisting of two new coefficients, G (rigidity modulus) and H compared to the previous elasticity theories. H can be measured from the coefficient of asymmetry as follows, $\alpha_a = H/G$. In this model, the stress component (σ_{ij}) is determined by the derivative of strain energy function (W) with respect to the strain component (ε_{ij}),

$$\sigma_{ij} = \frac{\partial W}{\partial \varepsilon_{ij}} \tag{6.1}$$

$$W = \sum_{k+m=1}^{n} C_{km} \left[(I_1 - 3)^k + (I_2 - 3)^m \right] + \frac{1}{2} K (I_3 - 1)^2 \tag{6.2}$$

where C_{km} represents the material constants, I_1,I_2, and I_3 are Cauchy-Green tensor invariants, and K is the bulk modulus. This model predicted the linear portion of the force-stretch curve accurately for two types of rubber, tread stock and gum stock with the following formulation of tensile force,

$$T = \frac{G}{2}P_2(\lambda) + \frac{H}{2}Q_2(\lambda) \tag{6.3}$$

where $P_2(\lambda)$ and $Q_2(\lambda)$ are functions of principal stretches. In order to fit the experimental curve, an empirical term '$C\lambda_m$' was added to Eqn. 6.3, in which m ranges from 17 to 25, which indicates the influence of empirical fit. No theoretical interpretation of the term '$C\lambda_m$' was provided however. The limitation with this formulation is the assumption of "traction in simple shear at any isotropic plane is proportional to the shear", which was proved to be erratic at higher stretches. Another issue with this model is that the stress at any point is merely a function of present strain, neither history nor rate of loading were considered in the formulation, irrespective of the strain limits, lower or higher. A simplified version of Mooney-Rivlin strain energy function for incompressible rubbers is given as,

$$W = \sum_{i=1}^{2} C_i(I_i - 3) \tag{6.4}$$

A reduced polynomial form, Yeoh model, eliminating the second tensor invariant from Eqn. 6.4 is expressed as [208],

$$W = \sum_{i=1}^{3} C_i(I_1 - 3)^i \tag{6.5}$$

A further simplification of strain energy function, Neo-Hookean model is depicted as, $W = C_1(I_1 - 3)$.

A different formulation for strain strain energy potential using principal stretches (λ_i) instead of tensor invariants in the models discussed earlier (Mooney-Rivlin, Yeoh, and Neo-Hookean) was devised by Ogden [209] as follows,

$$W = \sum_{i=1}^{N} \frac{2\mu_i}{\alpha_i^2}(\overline{\lambda}_1^{\alpha_i} + \overline{\lambda}_2^{\alpha_i} + \overline{\lambda}_3^{\alpha_i} - 3) + \frac{K_i}{2}(J-1)^2 \tag{6.6}$$

where μ is the shear modulus and J is the Jacobian of the deformation gradient, $J = det(F)$.

Martins et. al. [208] compared different hyperelastic material models such as Yeoh, Mooney-Rivlin, Ogden, Neo-Hookean, Humphrey, Martins, and Veronda-Westmann to define soft human tissues. The best correlation between the experiments and analytical modeling was experienced with Yeoh and Ogden models for analyzing the deformation behavior of soft tissues [208]. However, for smaller strain levels ($\varepsilon < 0.2$), poor predictability was demonstrated by all the material models. Mooney-Rivlin model has been widely used in various studies related to the rubber pad forming [45, 64, 65, 70, 210]. Few researchers have used Ogden model to describe the rubber material [60, 211]. Ali et al. [212] recommended the selection of material models based upon the magnitude of deformation with Neo-Hookean model for smaller strains, Mooney-Rivlin model for moderate strains, and Ogden model for larger strains.

Thus, in this FPLSF simulation, different hyperelastic material formulation, Mooney-Rivlin, Ogden, Neo-Hookean, and Yeoh models are compared to choose the model with better prediction capabilities. The properties of the material can be defined using the constants or the test data. In this analysis, uniaxial tension or the compression test data of the flexible pad materials was supplied as the input for the Mooney-Rivlin strain energy formulation. The stress-strain response of the flexible pad are determined using uniaxial tension and compression tests. Uniaxial tension tests were performed using Instron 5500R universal testing machine with a displacement loading at 500 mm/min. Dog-bone specimens for tension test were prepared as per the ASTM D412 standard [213] and the process is terminated with failure. Uniaxial compression test were performed with the loading speed of 0.5 mm/min and the test was terminated at the strain of 0.8. The specimen were prepared according to ASTM D395 standard [214]. The stress-strain relationship

for silicone rubber, natural rubber, and polyurethane rubber from uniaxial tension and compression tests is shown in Fig. 6.7.

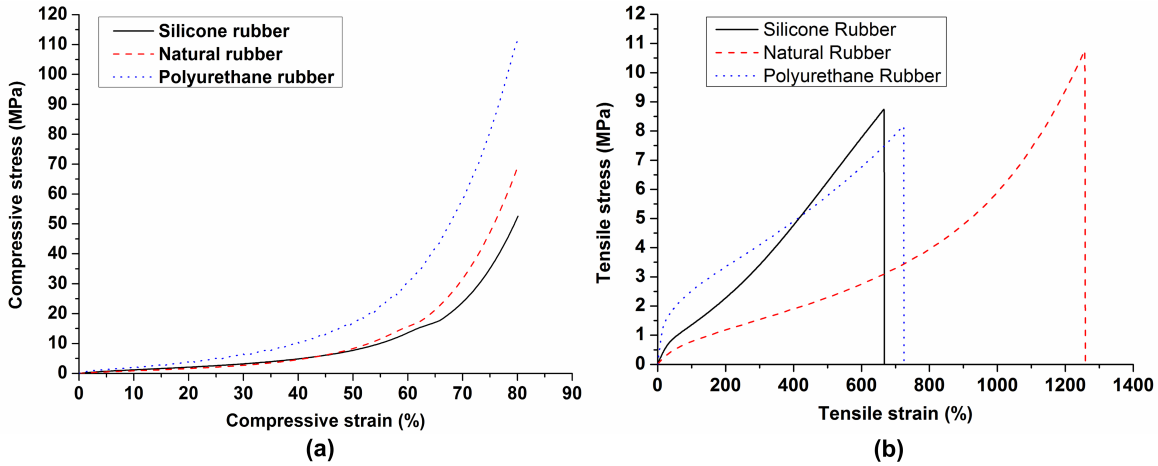

Figure 6.7: Experimental stress-strain behavior for different flexible pad materials (a) Uniaxial compression (b) Uniaxial tension

Silicone rubber flexible pad and copper metal foil are used for this analysis. It is evident from the axial displacement of foil position B at Fig. 6.8a that the deformation behavior of metal foil is predicted well with Mooney-Rivlin model, whereas the predicted crater depths are much higher than that of experiments. An excessive compression of pad with Neo-Hookean model was experienced, which can be verified from the constant equivalent strain of the metal foil at Fig. 6.8b. The investigation of Yeoh model (Eqn. 6.5) too indicated a poor agreement with experiments. Thus, Mooney-Rivlin model is used to define the hyperelastic deformation of flexible pad in FPLSF.

6.1.4 Mesh sensitivity

The selection of optimum mesh size for the analysis is based on the experimental agreement and the simulation cost. Initially, the different mesh densities of flexible pad were tested, which revealed no difference in the material response. Hence, the uniform mesh of 30 μm element size was chosen at all dimensions of the flexible pad. Further, the mesh size of the metal foil is analyzed as given in the Table. 6.1. The number of elements in each direction and the total number of elements in a

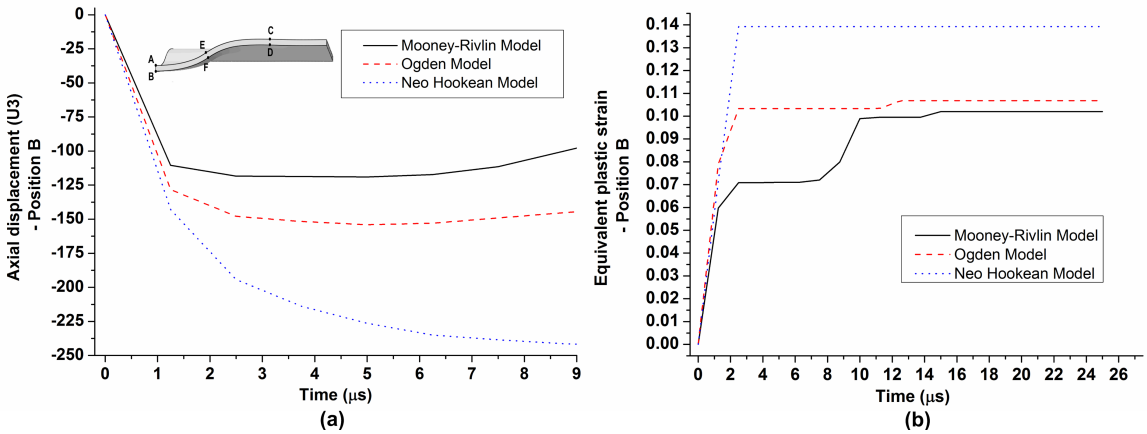

Figure 6.8: Effect of hyperelastic material model on the deformation behavior in FPLSF (a) Axial displacement (b) Equivalent plastic strain

combination are listed accordingly.

Table 6.1: Mesh sensitivity analysis

No	Element size in X direction (μm)	Element size in Y direction (μm)	Element size in Z direction (axial) (μm)	Total number of elements	Processing time ($minutes$)	Crater depth (μm)
I	10	10	12.5	2 x 10^4	39.4	110.7
II	10	10	10	2.5 x 10^4	62.75	109.4
III	10	10	5	5 x 10^4	102.1	107.4
IV	5	5	5	20 x 10^4	215.8	107.1
V	5	5	1	100 x 10^4	395.2	104.7
VI	2.5	2.5	2.5	160 x 10^4	502.5	105.2

Fig. 6.9a compares the axial displacement of the metal foil for different mesh combinations (which are indicated by the total number of elements in the graph). It can be observed that the axial deformation of the metal foil at position B varies only by a smaller amount with change in mesh density. The other foil positions also exhibit a similar behavior. The crater depth, which is presented in Table. 6.1, is calculated from the relative displacement of foil positions A and C corresponding to the crater center and non-deformed foil regions, respectively. The experimental observation of crater depth for corresponding laser fluence (20.9 J/cm^2) was 123.5 μm. In comparison with the experiments, the simulation with finer meshes (conditions V and VI in Table. 6.1) experiences more deviation. In addition, uneven

aberrations of axial plastic strains in the foil occur with finer meshes. Whereas, it can be observed from Fig. 6.9b that the equivalent plastic strain magnitudes are much lesser for the coarse meshes (conditions I and II). Furthermore, minor increase in strains, which is possible during the springback of rubber, are not predicted for coarse meshes. Thus the uniform mesh of 5 μm element size in all directions is identified to be an optimum mesh density and selected for further analysis.

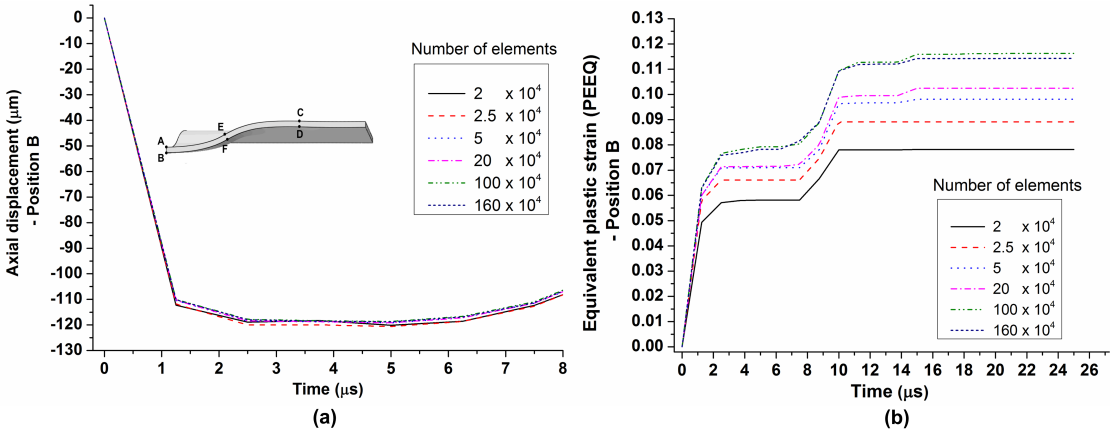

Figure 6.9: Comparison of foil deformation at position B at different mesh densities (a) Axial displacement (b) Equivalent plastic strain

6.1.5 Friction

Friction between the process components is one of the significant variables affecting the deformation properties in sheet metal forming, Peng et al. [46] observed in flexible forming process that, an increase in the coefficient of friction from 0 to 0.3 during the interaction between the rubber pad and the blank, causes no significant change in the stress distribution of the blank. Similarly, the friction coefficient was found to have no effect on the thickness distribution of the blank. Meanwhile, it is obvious that friction between the blank and the rigid die proved to be significant in processes with dies [10]. Ramezani et al. [60] used the friction coefficient between the rubber and blank as 0.25 whereas Liu et al. [194] and Dirikolu et al. [64] used 0.2 in lubricated conditions. Sala et. al [70] used 0.6 as the friction coefficient in non-lubricated conditions.

In this analysis, the friction between the contact surfaces is evaluated with the

following friction coefficients (μ): 0.2, 0.3, 0.4, and 0.6. Fig. 6.10 compares the deformation profile and equivalent plastic strain of the metal foil with change in friction coefficient. Despite a minor deviation with μ= 0.6, the friction between the surfaces has no considerable effect on the foil deformation, as the axial displacement (Fig. 6.10a) and plastic strain profiles (Fig. 6.10b) are identical with the change in friction properties. This behavior of friction effect in FPLSF can be comparable to the rubber pad forming process, as the flexible pad displaces along with the blank, reducing the effect of friction in the process response. A friction coefficient of 0.4 is applied in this simulation to define the friction between the flexible pad with both the metal foil and metal support.

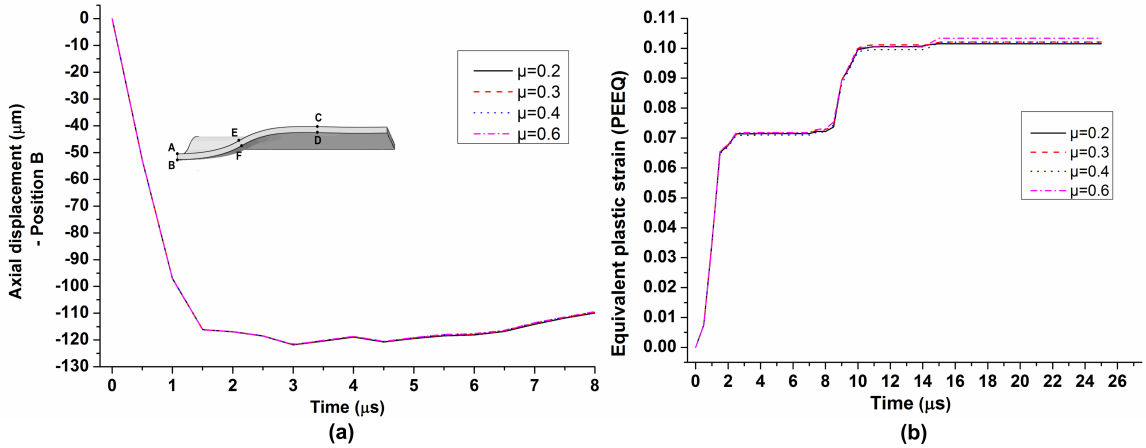

Figure 6.10: Sensitivity of friction coefficient on foil deformation at position B (a) Axial displacement (b) Equivalent plastic strain

6.2 Finite element model validation

The validation of the finite element model is performed using the comparison of the following deformation characteristics between experiments and simulations: shape, depth, and diameter of the deformation features. Fig. 6.11 compares the 3D and 2D geometry of the formed craters between experiments and simulation. SEM image of the formed crater on copper foil, which is hemispherical in shape, corresponding to the laser fluence of 13.6 J/cm^2 with silicone rubber (900 μm thick) as the flexible pad is shown in Fig. 6.11a. It can be observed from the axial displacement contour

of the metal foil (Fig. 6.11c) from simulations that the predicted crater shape has been hemispherical, which confirms with the experimental observations. The 2D ($x - z$ plane) profile of the crater from simulation (Fig. 6.11b) is compared with the surface profile measured by Talyscan surface profiler (Fig. 6.11d) indicating a similar crater profile.

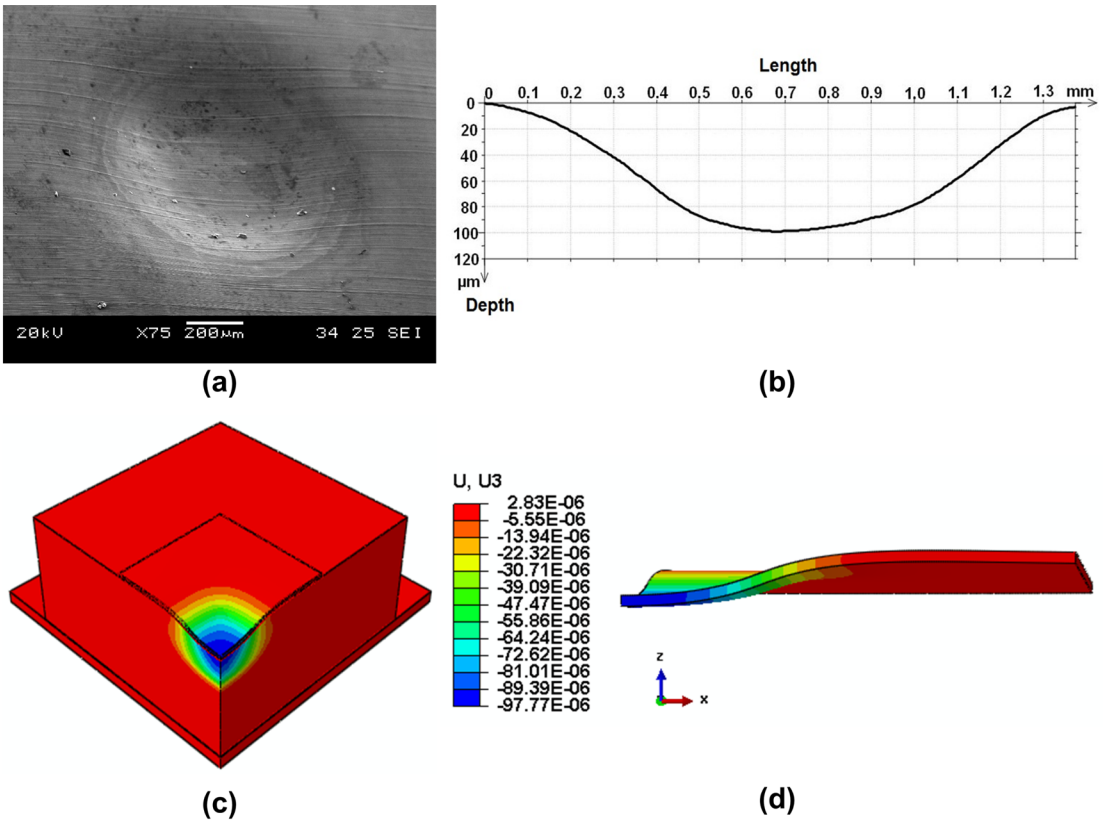

Figure 6.11: Comparison of deformation feature on copper foil between simulation and experiment at 13.6 J/cm^2 laser fluence: (a) SEM image of the deformation crater top surface (b) 2D surface profile at the center of crater, from experiments; (c) 3D Axial displacement (μm) contour (d) 2D (x-z plane) displacement (μm) profile of the foil, from simulations

From the simulations, the crater depth of 85.9 μm for the laser fluence of 13.6 J/cm^2 is predicted, whereas the corresponding crater depth from the experiments has been 97.8 μm. The difference in crater depth and crater diameter between simulation and experiment is found to be 12% and 4.8% respectively. This discrepancy is attributed to a number of factors including limitations with shock pressure modeling, non-inclusion of strain rate effects in the modeling of flexible pad deformation, and approximations in pressure pulse duration, loading area, and the

number of pulses, which are detailed in section 6.5 at later part of this chapter. The agreement between the experiments and simulation is reasonably sufficient for this study, as this thesis focuses on examining the time-resolved stress-strain distributions during the process and analyzing the generic qualitative behavior of process parameters on the deformation characteristics using the process simulation. Thus, the developed finite element model is used for the further analysis.

6.3 Deformation analysis

The evolution of crater formation in FPLSF is analyzed in detail using the finite element analysis. The high strain rate deformation of metal foils and hence the crater formation consists of various process stages. Copper foil (25 μm thick) and silicone rubber (900 μm thick) are used as the substrate and flexible pad materials, respectively. Fig. 6.12 illustrates the axial displacement profile of copper foil and flexible pad (silicone rubber) at different time periods during the process simulation for the laser fluence of 13.6 J/cm^2. The crater formation in metal foil can be classified into the following sequences:

1. Metal foil deformation phase (up to 1.8 μs)
2. Flexible pad elastic deformation due to inertia (1.8 μs – 4.1 μs)
3. Flexible pad elastic recovery (4.1 μs – 9 μs)
4. Foil detachment from the flexible pad (after 9 μs).

The different process stages are also illustrated in Fig. 6.13 that compares the axial displacement of foil and flexible pad at the center position of their top surfaces.

Stage 1: When the loading is initiated, there is no significant deformation of the foil until 40 ns. The shockwave starts from the top surface, propagates through the foil thickness, and reflects back from its bottom surface during which the next shockwave starts propagating from the top surface. The maximum von Mises stress occurs at the center of the foil thickness near the loading area circumference at this

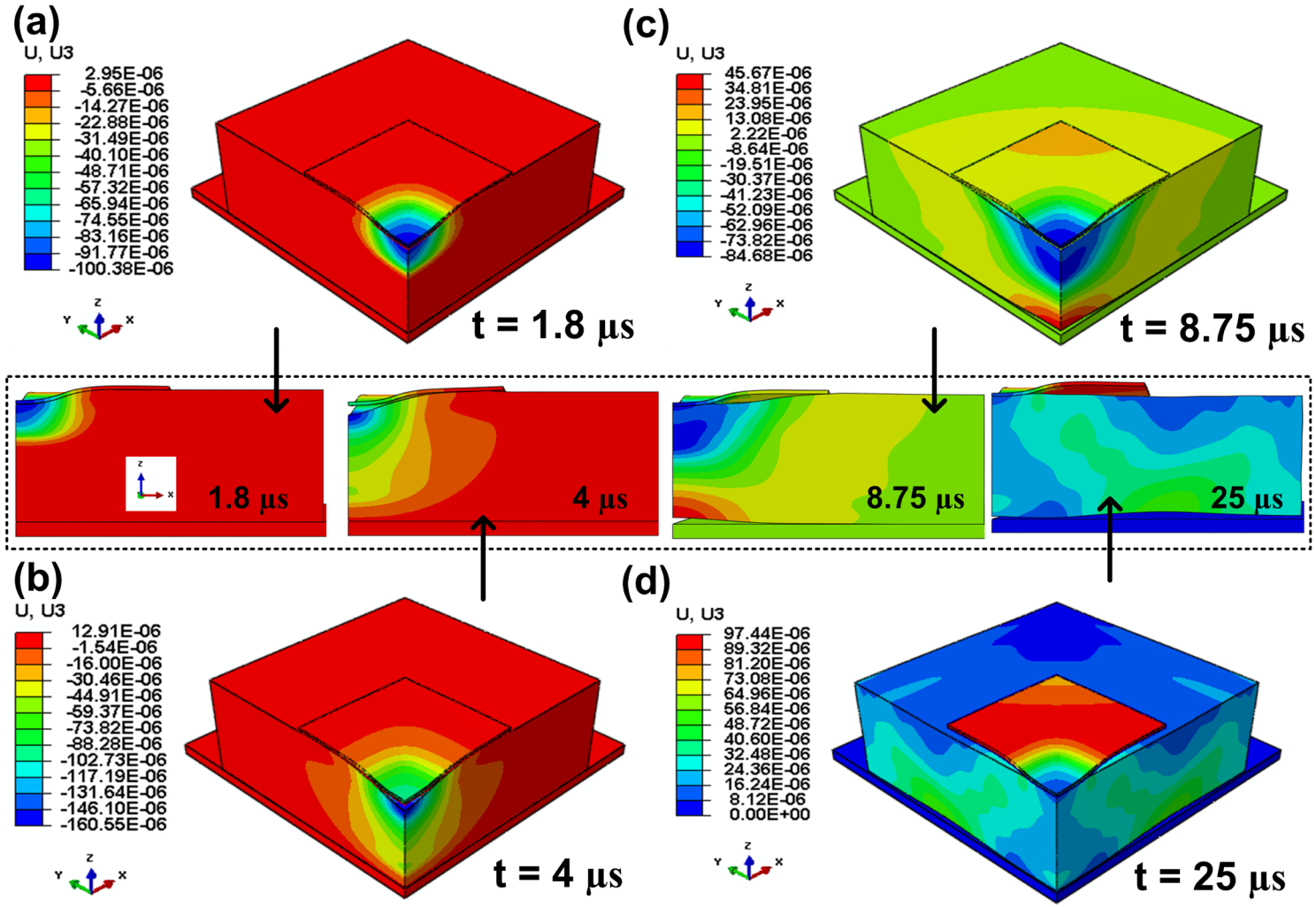

Figure 6.12: Axial displacement (m) contours with respect to time (a) t = 1.8 μs (b) 4 μs (c) 8.75 μs (d) 25 μs

period, which can be compared by the early rise of equivalent plastic strain at E and F compared to other positions from Fig. 6.14. Then the maximum von Mises stress moves away from the circumference to the adjacent regions along foil positions E and F after 110 ns. With increase in time, the stress moves further away from the circumference. Though the displacement at foil position A starts at 50 ns, it is very minimal until 220 ns, after which it increases gradually. Deformation at B starts at 180 ns and increases gradually after 250 ns. Simultaneously, the shockwaves propagate in the transverse directions along the loading surface. It is interesting to observe that the foil deformation continues until 1.8 μs though the load duration ends at 200 ns. During this entire stage (until 1.8 μs), the displacement of foil and flexible pad are similar which can be verified from Figs. 6.12a and 6.13.

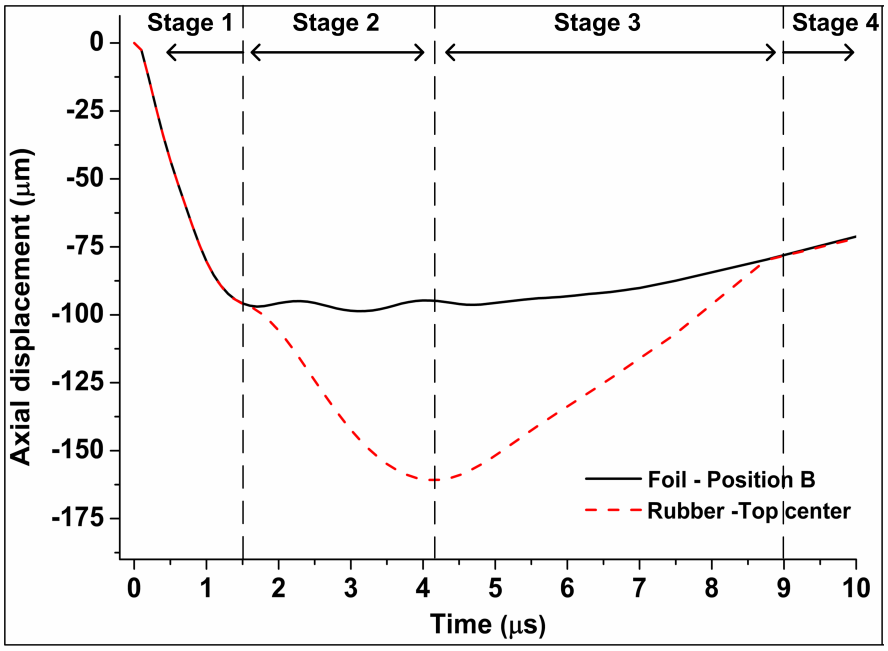

Figure 6.13: Comparison of axial displacement (μm) of foil position B and center of flexible pad top surface

Stage 2: The foil deformation attains its saturation after 1.8 μs and the increase in displacement has been kept minimal until it reaches its peak at 3.1 μs. Meanwhile, the flexible pad continues its deformation as seen in Figs. 6.12b and 6.13. The maximum principle stress at this stage is located near the crater edges with the foil, whereas it occurs at a distance of 300 μm from the pad top in the

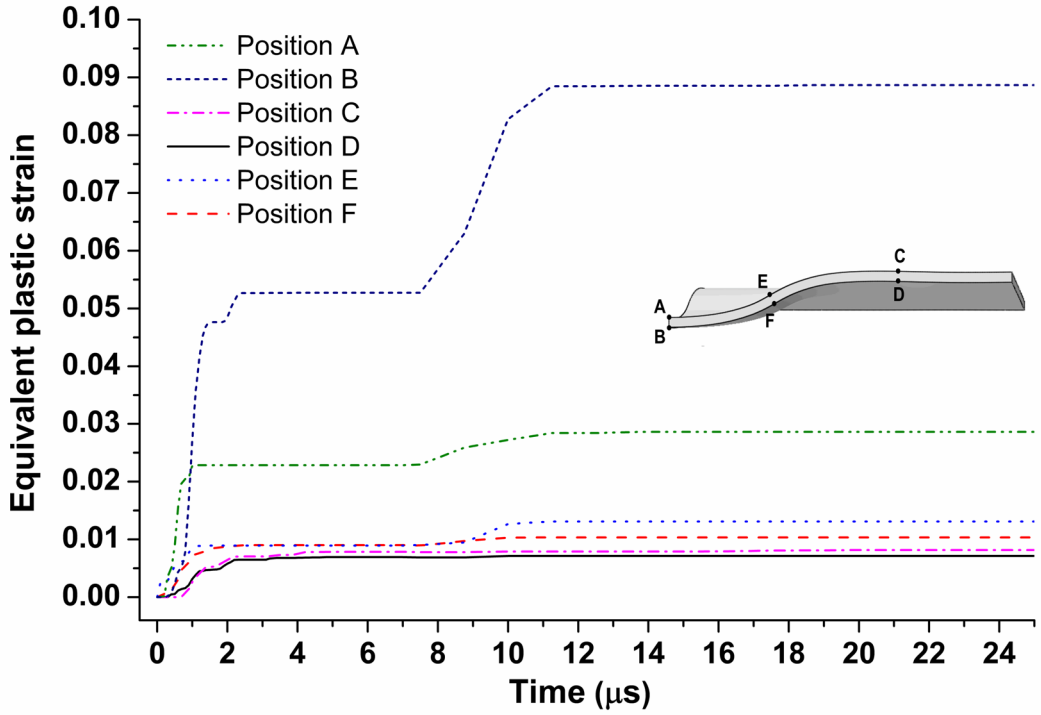

Figure 6.14: Equivalent plastic strain with respect to time for different foil positions

flexible pad spreading over a distance of 90 μm. During this stage, the elastic deformation of flexible pad is continued due to the inertia till the shockwave reaches the bottom of the pad.

Stage 3: In this stage, the shockwaves propagating in the flexible pad reach the bottom surface at 4.1 μs. The shockwaves then retract back forcing the pad in the opposite direction. The pad comes into contact with the foil at 8.75 μs as shown in 6.12c. Once the flexible pad contacts the foil at the center, both the foil and pad are found to have axial displacement in the upward direction. At this stage, a small plastic deformation occurs only at the foil position B causing a reduction in obtained crater depth. This behavior can be witnessed from the rapid increase in equivalent plastic strain at B after 8 μs in Fig. 6.14. However, the shape of the crater still remains hemispherical as seen in 6.12c.

Stage 4: The displacement of flexible pad and foil continues upwards at this stage as the foil is gradually detached from the flexible pad. However, the foil does not experience any plastic deformation. The formed crater on the metal foil which is completely detached from the pad at 25 μs can be seen Fig. 6.12d.

6.4 Effect of process parameters

The parametric study of significant process variables is performed to understand their influence on the plastic deformation characteristics of the metal foil. It is also required to correlate the stress-strain distribution with the experimental observations as discussed in the previous chapters.

6.4.1 Effect of metal foil material

The influence of metal foil material on the plastic deformation during FPLSF is analyzed for the following materials: copper, nickel, and stainless steel. It is obvious from Fig. 6.15 that copper experiences the maximum displacement followed by nickel and stainless steel, which is in correlation to the mechanical properties (yield strength, strain hardening coefficient, and tensile strength) of the materials as indicated in Table. **??**.

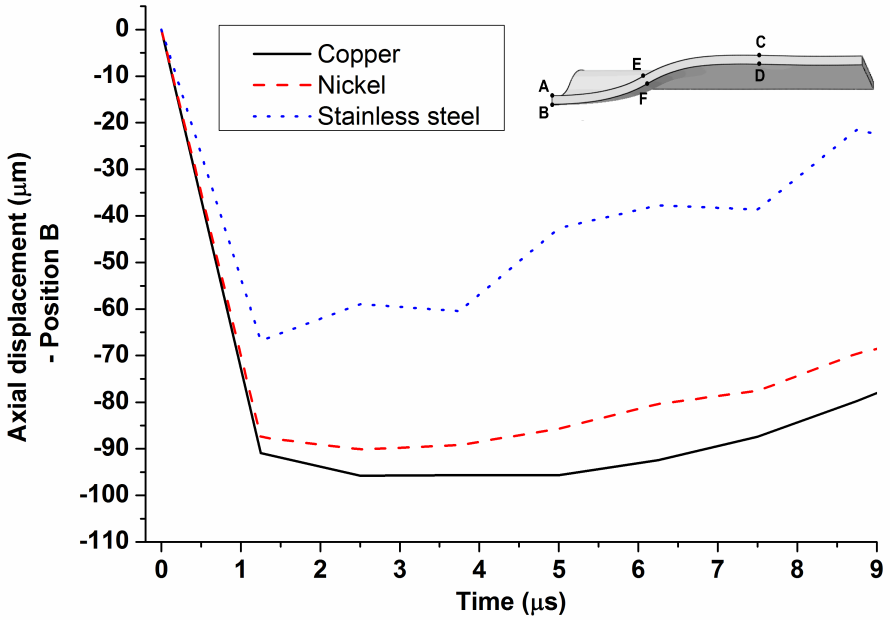

Figure 6.15: Comparison of axial displacement (μm) of foil position B between different metal foils

6.4.2 Effect of metal foil thickness

The thickness of the metal foil plays a major role in the deformation characteristics. This analysis will also be helpful to determine the FPLSF process capability, in terms of competent substrate thickness range, within which absolute foil deformation of the entire substrate without damages is accomplished.

Fig. 6.16 compares the axial displacement and equivalent plastic strain of foil position B between four different thicknesses of copper foil. It is obvious that the deformation increases with a reduction in foil thickness. However, for much smaller thicknesses (10 μm), the foil experiences structural damage by means of an irregular bend around the edges during deformation, as indicated in Fig. 6.17a. Additionally, the shape of the deformation features with 10 μm thick foil is observed to be different than that with thicker foils. The feature shape with 10 μm has been identical to a square box (Fig. 6.17a), instead of the hemispherical crater shape as observed with 25 μm (Fig. 6.17b). This square-box feature geometry can be correlated with the square loading profile in this analysis. Meanwhile, the thicker foils experience smaller deformation and no detachment of the foil from the flexible pad was observed. Due to the rigidity provided with the thicker foils, no plastic deformation in the opposite direction occurs (as explained in section 6.3 for 25 μm thickness) during the elastic recovery of flexible pad, which can be witnessed from the corresponding equivalent plastic strain at Fig. 6.16b and crater profiles at Figs. 6.17c and d. At thicker foils, the maximum von Mises stress occurs at the center portion of the foils at 1.25 μs in comparison to the edges of the loading area at lesser thicknesses. With increase in thickness, the area of deformation increases with reduction in axial displacement. Thus, it can be concluded that the formation of perfect hemispherical craters with flat top intensity profile is influenced significantly by the metal foil thickness.

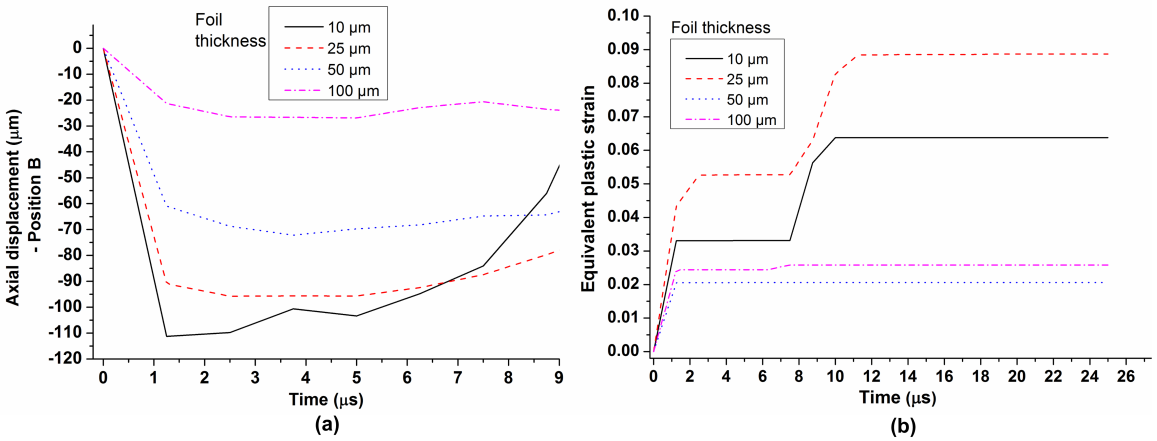

Figure 6.16: Effect of metal foil thickness on foil deformation at position B (a) Axial displacement (μm) (b) Equivalent plastic strain

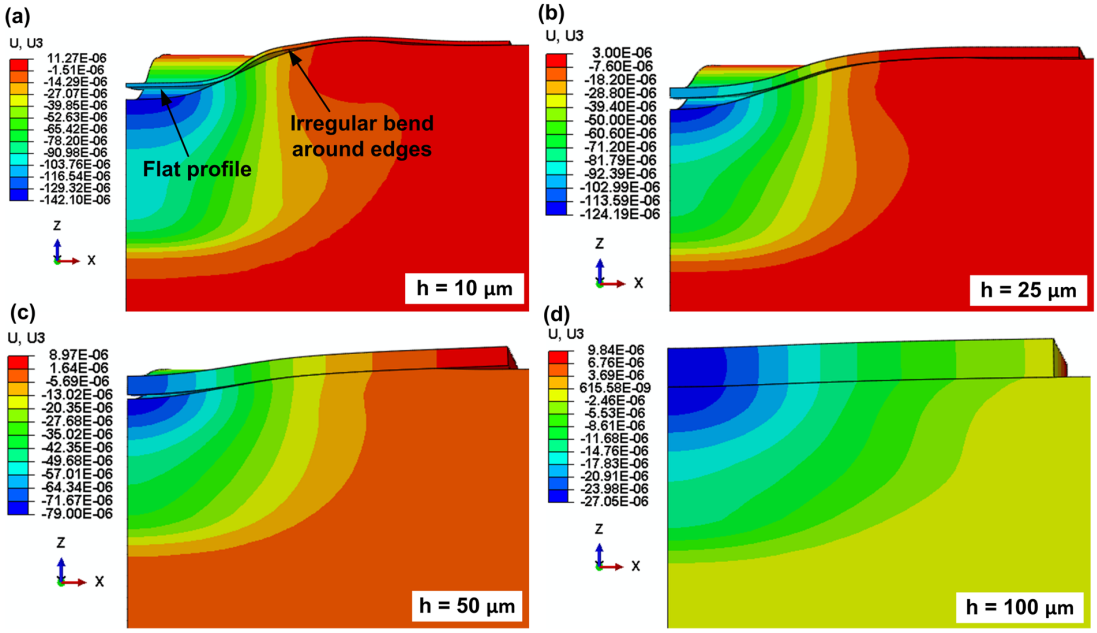

Figure 6.17: Comparison of crater formation through axial displacement (m) between different metal foil thicknesses (a) 10 μm (b) 25 μm (c) 50 μm (d) 100 μm

6.4.3 Effect of flexible pad material

To study the effect of flexible pad material on the metal foil deformation, the following three different rubber materials, silicone rubber (SR), natural rubber (NR), and polyurethane rubber (PU) have been tested on copper foil. The thickness of the flexible pad is kept constant as 900 µm in this study.

Fig. 6.18 compares the evolution of crater formation between flexible pad materials through the axial displacement contour at different time periods of the forming

process. It can be observed from Fig. 6.18 that the initiation and time duration of four different stages of the FPLSF process vary significantly with the flexible pad material, which can be attributed to the corresponding change in propagation speed and direction of the shockwaves within the flexible pad. The flexible pad detaches from the foil at 1.4 μs with polyurethane rubber compared to 1.8 μs for silicone rubber and natural rubber, which can be verified from Fig. 6.19 where the axial displacement of foil position B (center of crater bottom surface) and the center of the flexible pad top surface are compared between flexible pad materials. It is evident that the propagation of shockwave is faster with polyurethane rubber, which is stiffer than other materials tested. Correspondingly, the elastic recovery of rubber too is faster with polyurethane rubber. This behavior can be witnessed from Fig. 6.20 where the equivalent plastic strain raises sharply at foil position B after 7.5 μs for silicone and natural rubbers and after 5.6 μs for polyurethane rubber, the time at which the flexible pad comes in contact with the foil. However, there is no change in the amount of equivalent plastic strain with the change in the flexible pad material.

The experimental investigation of flexible pad material (section 3.10.5.1 in chapter 3) indicated an increase in deformation depth with increase in flexible pad hardness. The simulation results are found to be consistent with that of experiments, where the foil deformation is maximum with natural rubber and minimum with polyurethane rubber. The deformation gradient of the foil is also larger with natural rubber. The experimental observation of reduction in thinning and surface hardness with increase in pad increase requires an examination of stress and strain distributions in the metal foil and flexible pad during the deformation process, which is achieved through finite element analysis.

Fig. 6.21 compares the transverse and axial stress distributions between silicone rubber and polyurethane rubber at the center of the crater top and bottom surfaces for copper foils during FPLSF. A schematic illustration of these stress profiles at different time periods is presented in Fig. 6.22. Before the foil deformation is

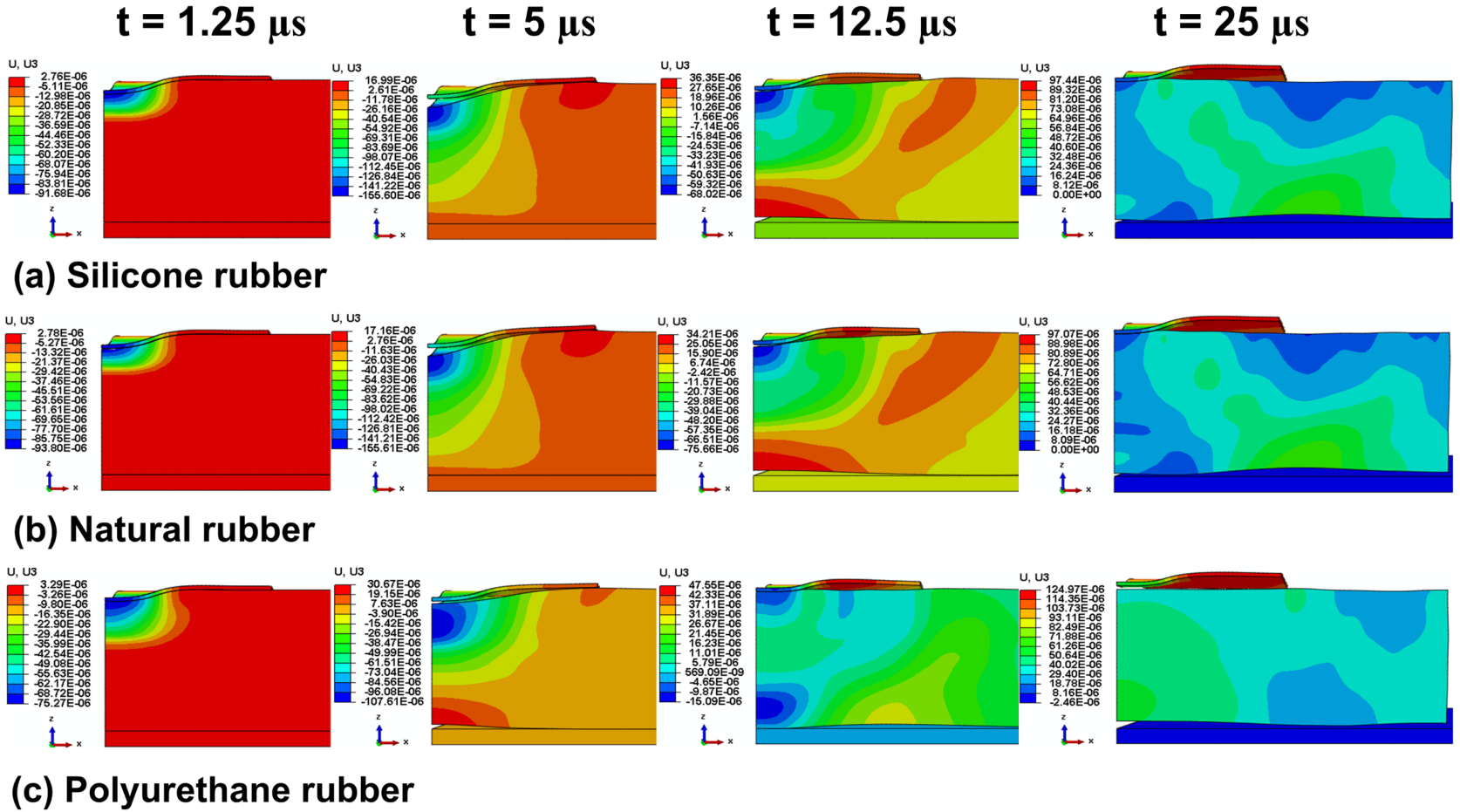

Figure 6.18: Finite element analysis of the effect of flexible pad material on axial displacement (m) contour at different time duration for (a) Silicone rubber (b) Natural rubber (c) Polyurethane rubber

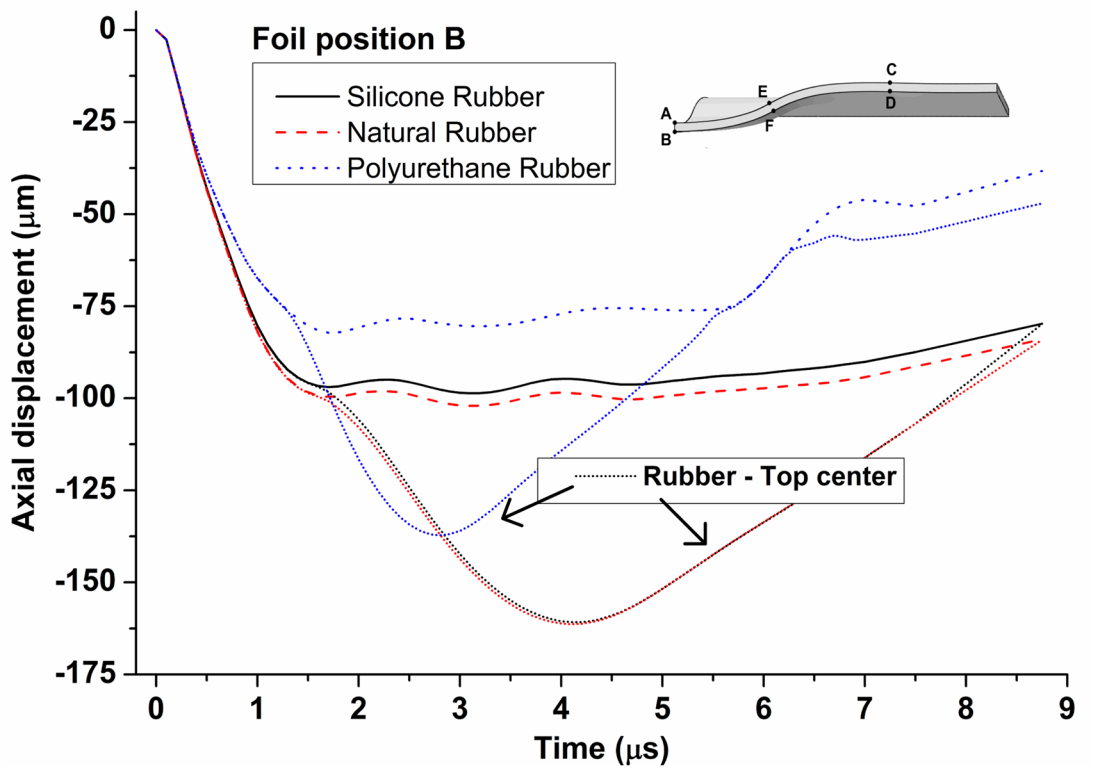

Figure 6.19: Comparison of axial displacement (μm) of foil position B and Rubber top center between different flexible pad materials

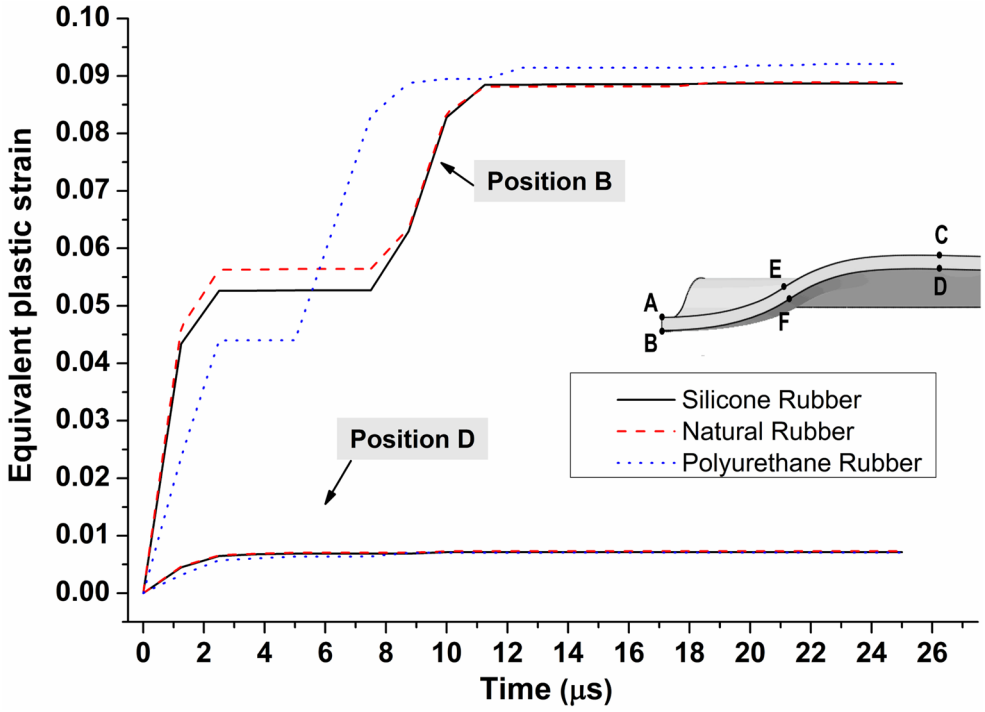

Figure 6.20: Comparison of equivalent plastic strain between foil positions B and D between different flexible pad materials

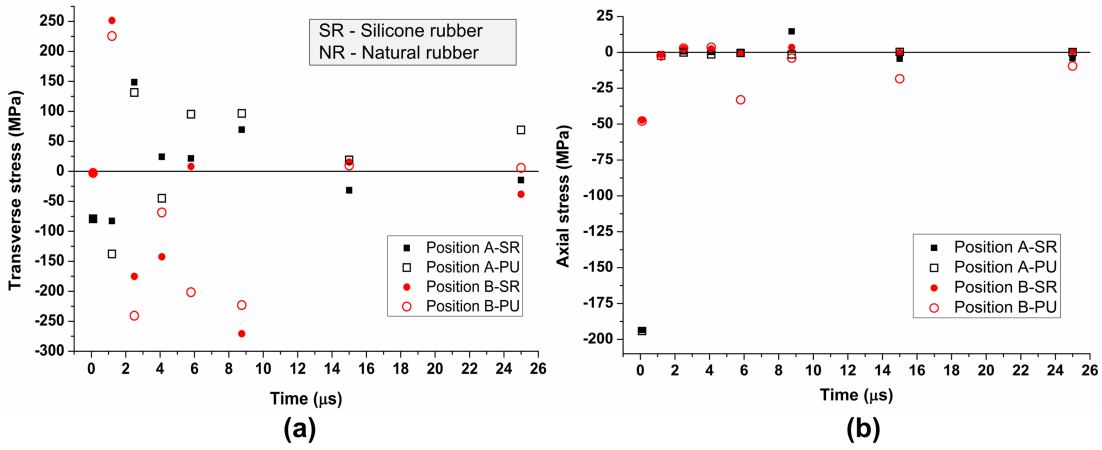

Figure 6.21: Effect of flexible pad material on stress distribution at foil positions A (top surface) and B (bottom surface) (a) Transverse stress (b) Axial stress [SR – Silicone rubber; PU – Polyurethane rubber]

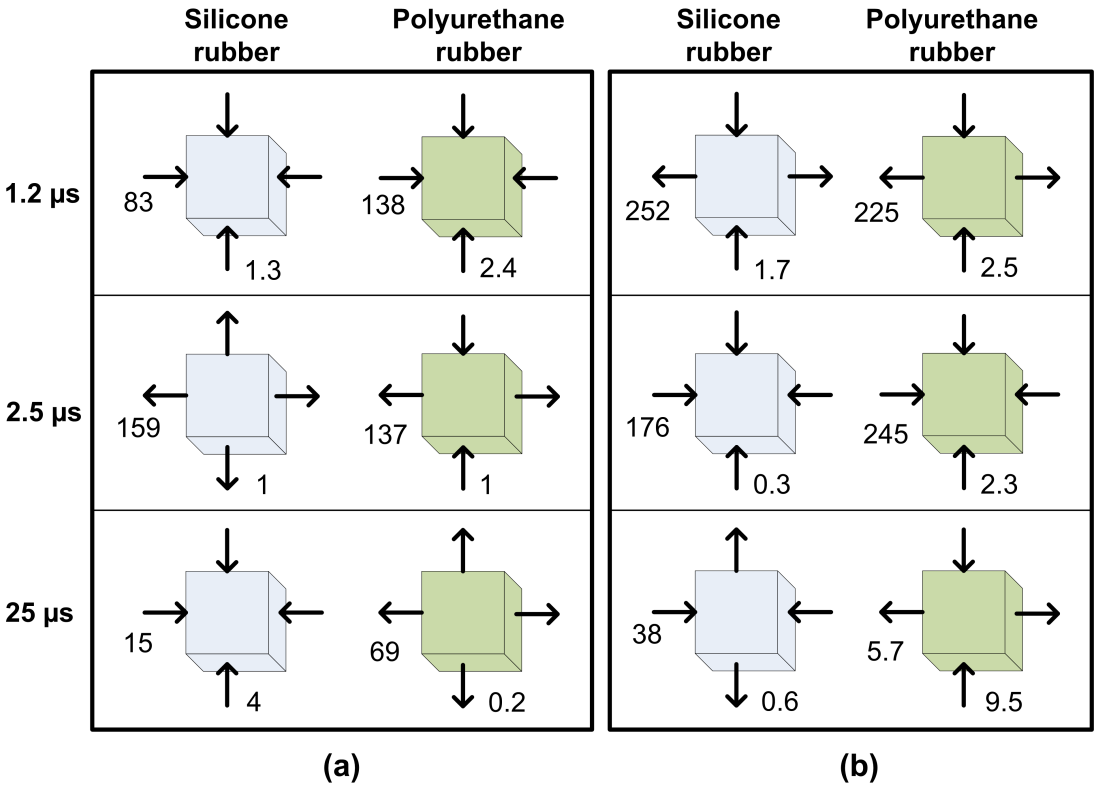

Figure 6.22: Effect of flexible pad material on stress distributions (unit as MPa) of the metal foil during deformation at (a) Position A (top surface) (b) Position B (bottom surface)

started (at 100 ns), both the axial and transverse stresses at foil positions A and B are compressive and remain identical for both pad materials. With silicone rubber as the flexible pad, the transverse stresses are tensile up to 10 μs before turning to compressive at foil position A, whereas it remains compressive throughout the

analysis after being tensile at 1.2 μs (when the foil is in contact with the flexible pad) at foil position B. With increase in pad hardness, more compression at A (top) and less tension at B (bottom) along transverse directions (Fig. 6.21a), and increased axial compression both at A and B (Fig. 6.21b) are experienced during the deformation stage. For all processing conditions, the magnitude of axial stress is much lesser than that of transverse stresses as evident from Fig. 6.21.

Finite element simulation predicted the similar trend of thinning with the change in flexible pad material. The following discussion explains the observed experimental behavior of foil thinning:

1. Experimental results indicated the maximum thinning at the center of the crater. This behavior is in correlation to the maximum axial and transverse strains at the center in comparison to the strains at other foil positions.

2. An increase in thinning along with flexible pad hardness was expected as an increased foil compression by the pad is likely to occur. The reversal of trend with experiments can be substantiated using the finite element analysis as follows:

   (a) Thinning of metal foils occurs due to the combined compressive axial strain and tensile transverse strains. As the axial strain remains compressive and transverse strains remain tensile throughout the deformation (Fig. 6.23), foil thinning occurs during FPLSF. The reduction of thinning with increase in pad hardness can be attributed to the subsequent reduction in the magnitude of both the axial compression and transverse tensile strains as evident from Fig. 6.23.

   (b) It is realized from Fig. 6.18 that, though the final crater depth is controlled by the flexible pad, the displacement of flexible pad continues even after the foil deformation is ceased. Therefore, there will be no axial compression of foil as anticipated once the pad departs the bottom surface of the foil regardless of the pad material.

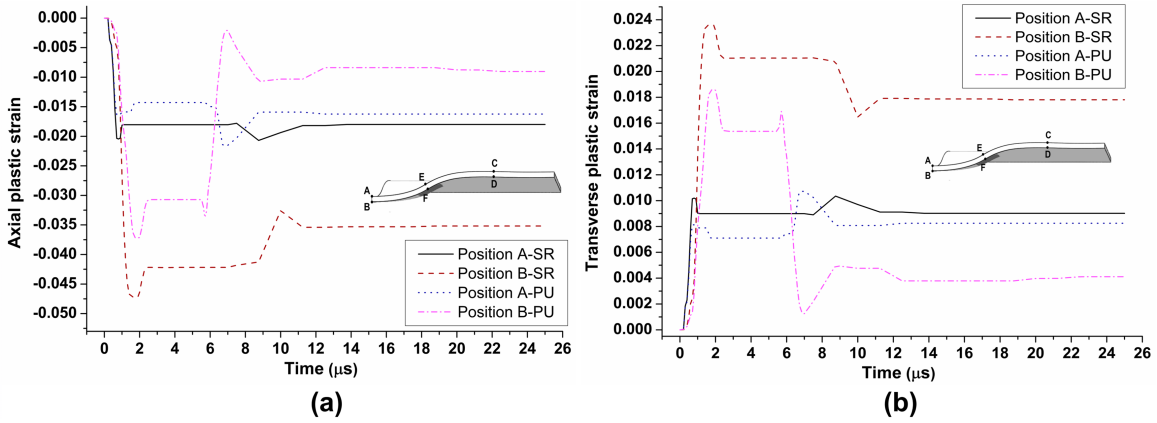

Figure 6.23: Effect of pad material on strain distribution at foil positions A and B (a) Transverse strain (b) Axial strain [SR – Silicone rubber; PU – Polyurethane rubber]

Similarly, the observation of reduction in surface hardness with increase in pad hardness is attributed to the following factors:

1. The residual stresses at both the center of top and bottom surfaces after the process turns from compressive (with silicone rubber) to tensile (with polyurethane rubber) with increase in pad hardness (Fig. 6.22 at 25 μs). As the compressive residual stress is a crucial factor for the surface hardness enhancement, the reduction in hardness with polyurethane rubber is comprehensible.

2. Reduction in axial compressive strain and transverse tensile strains are observed (Fig. 6.23) with increase in pad hardness, together with lesser plastic deformation, which could have resulted in the reduction of surface hardness.

6.4.4 Effect of flexible pad thickness

The finite element analysis of the effect of flexible pad thickness on the foil deformation is performed at the different thickness levels: 300 μm, 600 μm, 900 μm, 1200 μm, 1500 μm, 2000 μm, and 3000 μm. Silicone rubber is used as the flexible pad. Fig. 6.24 compares the evolution of crater formation between different thicknesses of the flexible pad. The crater depth with the change in pad thickness is plotted in Fig. 6.25a. For increase in pad thickness, the crater depth increases drastically

from 300 μm to 900 μm, whereas it increases gradually for thicknesses greater than 900 μm. Despite the significance of pad thickness on final crater depth, it is interesting to observe that the maximum displacement at foil positions A and B at 1.25 μs remains unchanged, which can be witnessed from the identical axial displacement (Fig. 6.24 at 1.25 μs for all thicknesses) and the identical axial plastic strain in Fig. 6.25b. The constant displacement with the change in pad thickness is attributed to the fact that, the displacement of the foil depends upon the shock pressure and flexible pad properties, which are kept constant in the analysis.

A significant difference in the behavior of flexible pad elastic recovery is found to occur with the change in pad thickness. During foil deformation stage, the disengagement of flexible pad from the metal foil is accompanied by the propagation of axial compressive shockwave through the pad thickness starting from the top surface. Subsequent formation of tensile shockwave at 5 μs at the top surface center of the flexible pad is shown in Fig. 6.26a, which is identical at all the flexible pad thicknesses. As a result, contact between pad and foil is established at foil position B, causing an upward displacement of the contact region. During this stage, the compressive wave in the axial direction is reflected back from the pad bottom, forcing the pad to dissociate from the metal backing. Concurrent propagation of transverse tensile shockwave causes the flexible pad to establish contact with the foil initially at the crater center (position B) and then to the circumference (position F) and the non-deformed area (position D). Fig. 6.26b shows the contact formation between flexible pad and foil for 900 μm thickness. The above-mentioned phenomenon is similar for the pad thickness ranging between 900 μm and 1500 μm. If the flexible pad is thicker than 1500 μm, the contact is established only between foil positions B and F as shown in Fig. 6.26b for 3000 μm, as the compressive shockwave takes longer time to reach the bottom surface. Correspondingly, no compression of foil position B was noticed from Fig. 6.25b for pad thicknesses greater than 1500 μm. Therefore, it is evident that the interaction between different shockwaves, axial rarefaction wave with the transverse tensile

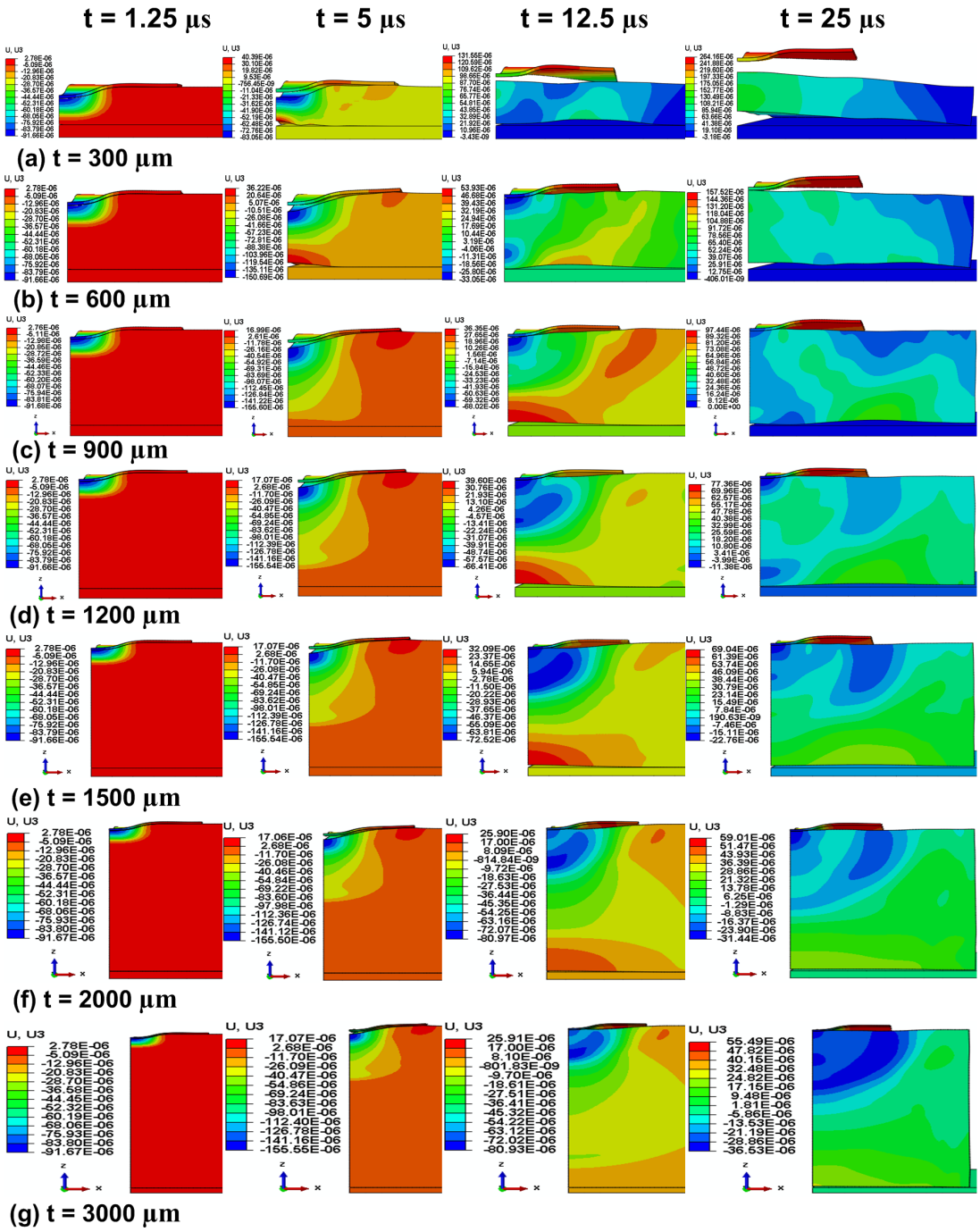

Figure 6.24: Finite element analysis of the effect of flexible pad thickness on axial displacement (m) contour at different time duration (a) 300 μm (b) 600 μm (c) 900 μm (d) 1200 μm (e) 1500 μm (f) 2000 μm (g) 3000 μm

shockwaves, during flexible pad elastic recovery has a decisive role in the final deformation crater geometry. As the flexible pad thickness influences the axial rarefaction wave, it is a significant factor for the crater depth, crater shape, foil thinning, and crater surface hardness in FPLSF.

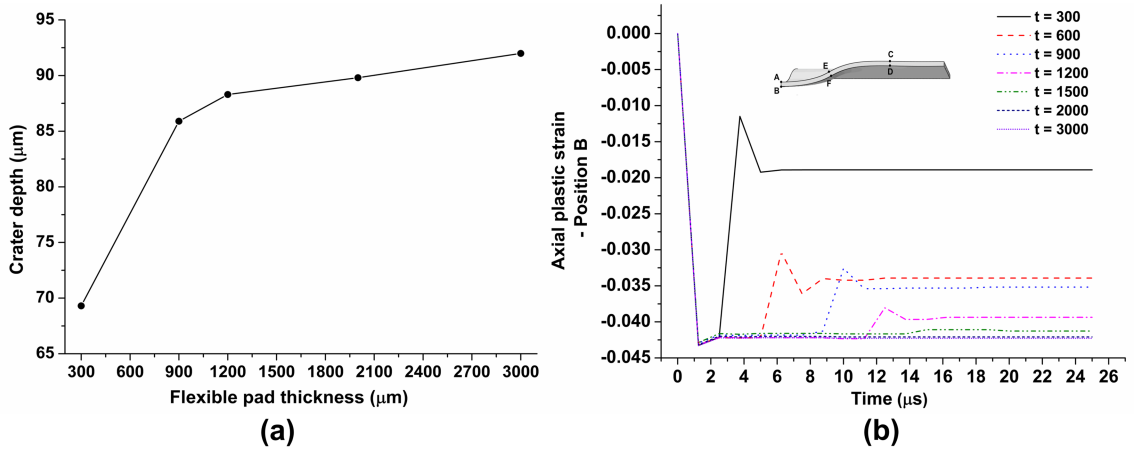

Figure 6.25: Finite element analysis flexible pad thickness influence in FPLSF (a) Change in crater depth with respect to the flexible pad thickness (b) Evolution of axial plastic strain at foil position B with variation in pad thickness

The change in elastic recovery of flexible pad with thickness results in the observed change in crater depth (Fig. 6.25a) despite the constant maximum displacement. The smaller crater depth with 300 μm can be attributed to the following behavior occurring during the process: when the pad thickness is small, the shockwave reaches the pad bottom rapidly. As a result, the flexible pad is detached from the metal backing and displaced in the upward direction. The retracting pad contacts the center portion of the deformed crater and induces more plastic deformation in the opposite direction, which is evident from the corresponding larger axial plastic strain shown in Fig. 6.25b.

Experimental analysis of flexible pad thickness (section 3.10.5.2 in chapter 3) indicated a reduction in surface hardness with increase in flexible pad thickness. This behavior is examined by the finite element analysis as follows:

1. It can be noticed from Fig. 6.25b that the amount of plastic deformation at the foil center during the elastic recovery of the pad reduces with the increase in pad thickness, and almost no deformation is observed at that stage for pad thicknesses greater than 2000 μm.

2. With increase in pad thickness, the magnitude of compressive residual stresses remains approximately constant at the center of top surface (Fig. 6.27a), whereas the residual stresses turns from compressive to tensile at the bottom

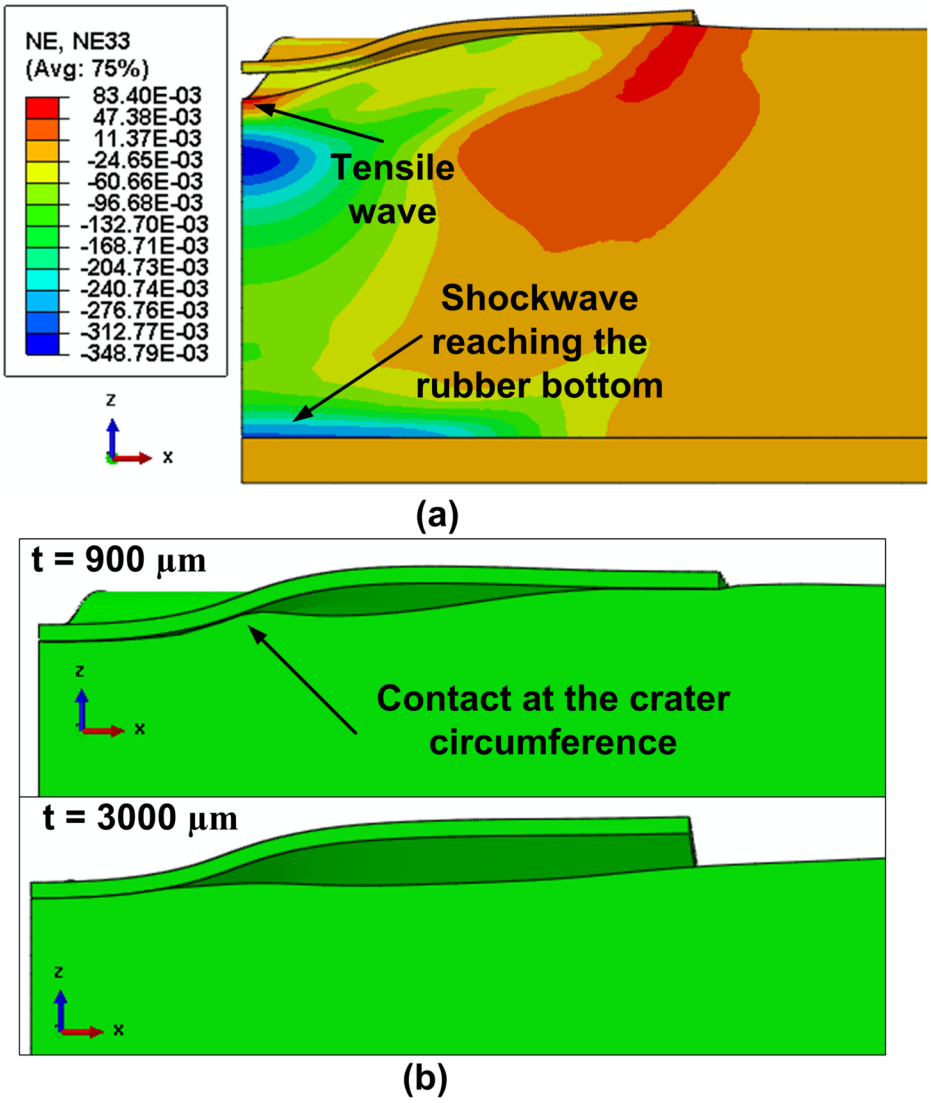

Figure 6.26: (a) Axial strain contour indicating different shockwaves at 5 μs (thickness - 900 μm) (b) Comparison of contact evolution between foil and flexible pad during elastic recovery of rubber for pad thicknesses 900 μm and 3000 μm

surface center (Fig. 6.27b).

As both the magnitude of plastic deformation and compressive residual stresses is reduced with increase in pad thickness, the surface hardness will be experiencing a reduction as observed during the experiments.

Therefore, while comparing the effect of pad thickness on the crater depth with that on the surface hardness, it is realized that, an optimum thickness of flexible pad has to be selected in order to achieve maximum feature deformation and maximum surface hardness of formed features.

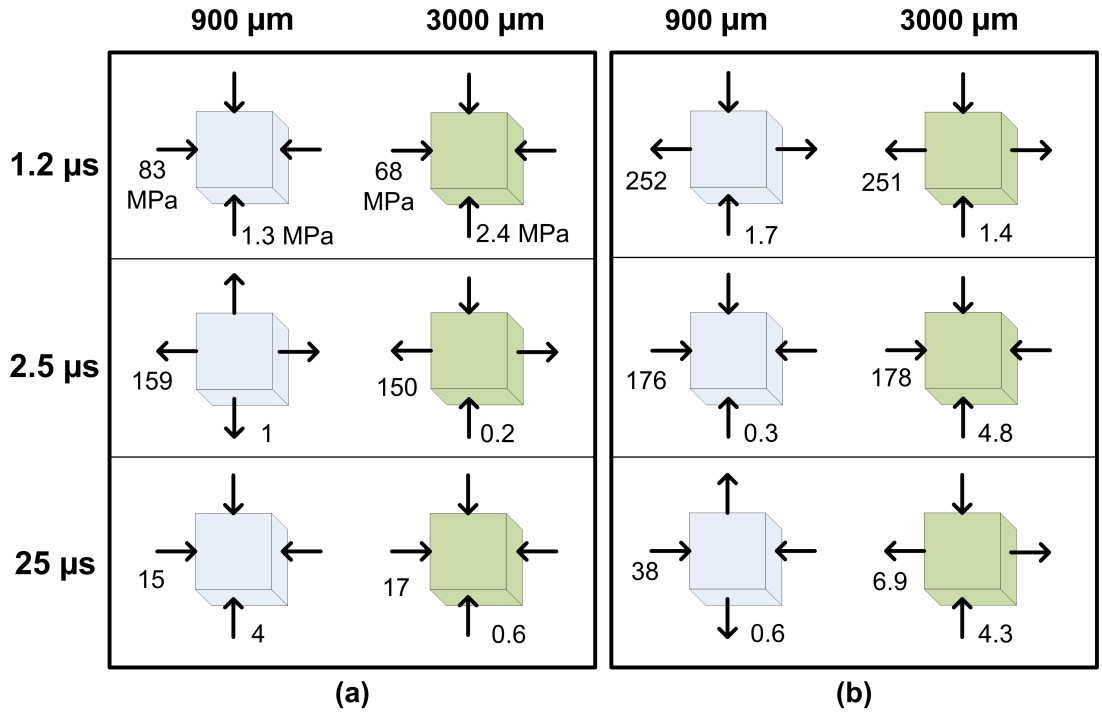

Figure 6.27: Effect of flexible pad thickness on stress distributions (unit as MPa) of the metal foil during deformation at (a) Position A (top surface) (b) Position B (bottom surface)

6.4.5 Effect of laser fluence

The comparison of deformation crater depth between experiments and simulation is analyzed at different laser fluences ranging from 7.3 J/cm^2 to 20.9 J/cm^2 as shown in Fig. 6.28. The relative error between experiments and simulation is found to be 10% to 20% for the given range of laser fluences, which is in acceptable range for the behavioral study.

It can be observed from Fig. 6.28 that, for laser fluences less than 7.3 J/cm^2, crater formation is predicted by the simulation despite no actual crater formation. This discrepancy resulted from the assumption of Fabbro's model that the supplied laser energy is sufficient for the irradiation of target surface. For the laser fluence of 5.2 J/cm^2, plastic deformation of copper foils is observed with simulations as the peak shockpressure calculated from Eqn. 2.8 for the 5.2 J/cm^2 fluence (167 MPa) is greater than the yield strength of copper (90 MPa). Whereas, the laser energy was insufficient to vaporize the aluminum foil ablative overlay during experiment for the

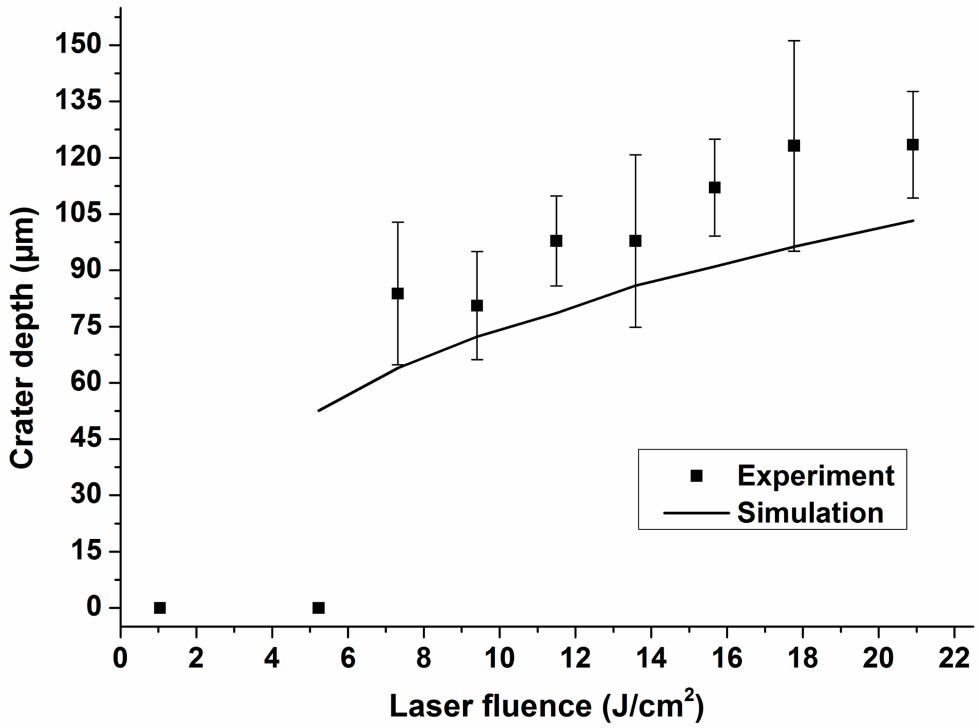

Figure 6.28: Comparison of crater depth between experiment and simulation for different laser fluence

corresponding laser fluence and hence no craters were produced. Thus, the finite element model of FPLSF is proven to predict the crater formation reliably for laser fluences greater than the fluence threshold limit for ablative overlay vaporization.

6.5 Discussions

Though the finite element modeling of FPLSF assists in studying the deformation behavior and the process parameters effectively, few discrepancies with the existing modeling approach are identified:

- Despite an agreeable correlation (less than 20%) between experiments and simulation is noted, the range of deviation is uniform with the change in laser fluence as seen in Fig. 6.28.
- Though the finite element analysis predicts the deformation of foils with natural rubber and silicone rubber reasonably well, over-prediction of deformation depth was observed for polyurethane rubber. Similar behavior was noted for

the stainless steel foil irrespective of the flexible pad material.

- The foil thinning is under-predicted with the simulation despite the trend of pad hardness and thickness influence on thinning is coherent.

These discrepancies can be attributed to several aspects including material modeling, shock loading conditions, and process conditions. The following discussion addresses these disagreements and highlights some relevant concerns:

- Mooney-Rivlin strain energy formulation (Eqn. 6.2) is employed in this analysis to define the hyperelastic deformation of flexible pad. The material properties of flexible pad are defined using quasi-static compression or tension tests. Previously, Mooney - Rivlin model has been used to predict the deformation of rubber successfully, but in quasi-static loading conditions [45, 64, 65, 70, 210]. In FPLSF, the strain rates involved in the deformation of rubber is observed to be greater than 1 x 10^5 s^{-1}. The effect of strain rate on the rubber deformation could have significant influence on the stress-strain relationships. As the Mooney-Rivlin formulation does not consider the history or rate of loading, there is a possibility of inaccurate prediction of dynamic material response of flexible pad. This high strain rate effect could cause significant deviation in rubber deformation between the simulation results and the actual experiments. Due to this, the predicted elastic deformation of rubber is lesser than the actual case, causing the corresponding reduction in metal foil deformation.

- As mentioned earlier, uniaxial tension and compression tests (Fig. 6.7) are used to define the flexible pad properties in this analysis. However, the material experiences different deformation modes such as uniaxial, biaxial, and volumetric tension or compression during its deformation in FPLSF. The difference in stress-strain behavior between actual FPLSF process and the limited testing conditions could lead to the discrepancies in the foil material plastic deformation. Test data at corresponding strain rates and other deformation modes might be required for better prediction.

- The simulation has been performed with single pulse whereas the actual experiments were conducted with 45 pulses. The deformation geometry with single pulse was found to be 10% smaller than with 45 pulses. This factor can be comparable to the 10 to 20 % variation between experimental and simulation results.

- Despite the prediction of pressure pulse to sustain for longer time ($> 3\ \mu s$) after the end of laser pulse by Fabbro's shock pressure model, the total lifespan of the shock pressure pulse have been approximated as 200 ns in this analysis based on the better correlation with experiments. Meanwhile, it is observed from this finite element analysis (Fig. 6.6) that the shock pressure duration plays a significant role in the deformation of metal foils. If the pressure pulse lifespan longer than the assumed 200 ns is applied, the deformation depth will be increased obviously. An experimental measurement of shock pressure pulse will be required to determine the pressure pulse span.

- Due to the partial ablation of overlay material, the shockwaves are initiated from the overlay surface, which then propagates into the overlay before contacting the metal foil (as discussed in chapter 3). Thus, when the shockwave reaches the substrate, the impacting area will be larger than the irradiated beam area. Due to the approximation of loading area similar to the beam area considered in this simulation, the prediction of deformation profiles might be inaccurate.

- The attenuation of the shockwaves is an another effect of the partial ablation of overlay during the experiments. This shockwave attenuation is not considered in the shock pressure calculation using Fabbro's model (Eqn. 2.7). Thus, the shockpressure used in the simulation should be higher than that with experiments, which hence should result in increased deformation. However, the reversal of this trend (Fig. 6.28) observed earlier, highlights the possible occurrence of impedance mismatch effect. These two contrasting behaviors, shockwave attenuation and pressure enhancement due to the impedance mis-

match, as a result of partial ablation of ablative overlay, is expected to influence the process outputs. If the pressure increase by impedance effects exceeds the shockwave attenuation, the pressure pulse magnitude will be higher. However, these behaviors are not taken into account in the shock pressure calculation, which could result in the process simulation discrepancies.

6.6 Summary

This chapter demonstrates the development of a finite element model to study the deformation characteristics of metal foil in FPLSF. The prediction of deformation feature depth, diameter and shape from the FE model correlates sufficiently well with the experimental results. Then, a time-resolved analysis of stress and strain distributions at different positions along the foil is performed. The crater formation in FPLSF is identified to be comprised of various sequential process stages: metal foil and flexible pad deformation, inertial pad displacement, elastic recovery of pad, and the foil detachment from pad. Furthermore, several process variables, laser fluence, material and thickness of the metal foil and flexible pad are investigated using the finite element analysis. The following significant conclusions can be made from the analysis:

- Different deformation feature shapes are obtained with the change in the thickness of foil substrate for identical pressure pulse profiles, highlighting the significance of foil thickness in realizing the required deformation features.
- The flexible pad material (hardness) have significant influence on the plastic deformation of the metal foils. The initiation and time duration of four different stages of FPLSF process vary significantly with the flexible pad material, which can be attributed to the corresponding change in the propagation speed and direction of the shockwaves within the flexible pad.
- Similarly, the flexible pad thickness influences the deformation feature geometry through a difference in elastic recovery behavior of the flexible pad.

An optimum flexible pad thickness is necessary to achieve maximum feature deformation and surface enhancement of formed features.

- The difference in the geometry and surface characteristics of the deformation features with change in flexible pad hardness and thickness is attributed to the magnitude and direction of strain distribution during the deformation phase, additional plastic deformation during the elastic recovery of the pad, and the residual stress distributions at the deformed feature.

Finally, the limitations with the existing finite element modeling approach are outlined, some of which are common to the simulation of laser shock processes.

Chapter 7

Conclusions and Future Work

This chapter summarizes the conclusions of this research work and highlights possible directions for further improvement.

7.1 Conclusions

In this work, a new, non-contact microforming technique, Flexible Pad Laser Shock Forming (FPLSF), to fabricate microfeatures on thin metallic foils has been developed and successfully demonstrated. FPLSF uses laser-induced shock waves and a flexible-pad arrangement to induce plastic deformation of metal foils. Hemispherical craters of depth ranging from 15 μm to 300 μm, and radius between 150 μm and 1 mm were formed on 25 μm thick copper, nickel, and stainless steel foils using a Q-switched Nd:YAG laser irradiation. The crater formation in FPLSF comprised of various sequential process stages: laser irradiation of ablative overlay, plasma formation and expansion, shockwave propagation, metal foil and flexible pad deformation, and elastic recovery of flexible pad. In order to acquire the process knowledge, several FPLSF parameters, were studied in detail. The most significant parameters to control the deformation depth and diameter were identified to be laser fluence and beam profile. Also, single laser pulse was sufficient to produce the craters as more than 90% and 75% of the final depth and diameter were achieved during the first pulse itself, in comparison to 45 pulses. Ablative over-

lay was found to affect the foil deformation based on two mechanisms, impedance mismatch effects and shockwave attenuation. In addition to controlling the depth and diameter, confinement medium influences the shape of deformation features. At higher laser fluences ($20.9 J/cm^2$), shockwave ripples were formed on copper foils with glass confinement whereas hemispherical craters were formed with water confinement. Understanding of the above mentioned process behaviors required detailed investigation of laser-induced plasma characteristics.

The laser-induced plasma evolution in FPLSF was investigated using a high speed camera. Plasma characteristics was found to correlate with the observed parametric behaviors for laser fluence, number of pulses, and especially confinement medium. For an increase in laser fluence, the plasma diameter and pressure increases simultaneously, in correlation to the increase in feature size. Upon multiple pulse irradiation, no interference between the plasma evolution resulting from successive laser pulse irradiation is observed. The relationship between plasma evolution and plastic deformation behavior is compared in Table. 7.1.

Table 7.1: Comparison of deformation features and plasma observation for confinement thickness parameter

Parameter	**Deformed feature profiles**	**Plasma visualization**
Confinement medium	Uniform hemispherical craters with water and shockwave ripple structures with glass confinements.	Dielectric breakdown at different interfaces (water-air for water and glass-ablative layer for glass).
	Deeper craters with water.	Smaller plasma diameter, hence increased plasma density.
Confinement thickness	Increase in crater depth and diameter along with confinement thickness.	Reduction in plasma diameter, which leads to increased plasma pressure.

A significant advantage with FPLSF is that the deformed features has uniform thickness distribution with variation less than 10%. In addition, the top and bottom surfaces of the deformed features are strengthened by 20 to 70% after FPLSF. The hardness and thickness distribution were also found to be influenced by the

process variables, as indicated in Table. 7.2. As mechanical properties are closely related to the microstructure, the underlying plastic deformation mechanism was studied using a detailed microstructure analysis. The microstructure of copper foil surface after forming consisted of subgrains, nucleated fine grains, high dislocation density regions, and predominantly elongated grains. A corresponding reduction in grain size and aspect ratio together with an increase in low grain angle boundaries were witnessed. Higher surface hardness observed at the top crater surface in comparison to the bottom surface, was attributed to the increase in grain uniformity and high dislocation density regions. In FPLSF, strain hardening effect is observed to be the dominant plastic deformation mechanism contradictory to the occurrence of adiabatic softening at high strain rate processes such as explosive forming, electromagnetic forming, and laser shock peening. This difference in mechanism is due to the combined reduction of plastic strain, strain rate, and inertia effects resulting from the FPLSF process configuration. Deformation behaviors are observed to be different at top and bottom surfaces, and also at center and edge regions of the crater, causing a change in hardness and microstructure profile.

Finally, a finite element model was developed to study the high velocity deformation characteristics of metal foil and flexible pad in FPLSF. FE model correlated reasonably well with the experimental results to perform a qualitative process analysis. A time-resolved analysis of stress and strain distributions at different positions along the foil was performed. Furthermore, several process variables, laser fluence, material and thickness of the metal foil and flexible pad are analyzed numerically. The significance of foil thickness in realizing the required deformation features is highlighted through the observation of different feature shapes with thickness variation for identical process conditions. The hardness and thickness of the flexible pad demonstrate significant influence on the plastic deformation of metal foils. An optimum flexible pad thickness is necessary to achieve maximum feature deformation and surface enhancement of formed features. The difference in the geometry and surface characteristics of the deformation features with change in flexible pad

Table 7.2: Summary of some of the main conclusions

Process conditions	**Formability analysis**			**Microstructure analysis**	**Finite element analysis**
	Crater depth	**Hardness**	**Thinning**		
Forming effect in FPLSF	$\sim 15\ \mu m$ to 300 μm	Improvement in both surfaces.	Thinning $\sim$ 4 to 35% at center.	Grain elongation, subgrains, high dislocation density, nucleation of new fine grains, uniform grain size.	Not Applicable (N.A)
Deformation feature - Top vs bottom surface	N.A	Hardness at top greater than bottom.	N.A	Increase in grain size uniformity and high dislocation density at top surface.	Higher stresses at bottom. Transverse stresses at top is compressive, as opposite to bottom. Axial compression at both surfaces.
Deformation feature - Center and edge	N.A	Minor variation in hardness.	Maximum at center. Variation across crater less than 10%.	More elongation at edges. Large high dislocation density over a narrow region at edges.	Maximum von Mises stress at the edge. Varying stress profiles on both sides of the loading edge.
Increase in laser fluence	Increases	Increases	Increases, but more uniform across sample.	Increase in high dislocation density and subgrain structures.	Increase in stress and strain magnitudes.
Increase in flexible pad hardness	Decreases	Decreases (both at top and bottom)	Decreases	N.A	Reduction in axial compressive and transverse tensile strains. Change in residual stress from compressive to tensile.
Increase in flexible pad thickness	Increases	Decreases (both at top and bottom)	Increases	N.A	Reduction in compressive residual stresses. Change in elastic recovery behavior.

hardness and thickness is attributed to the magnitude and direction of strain distribution during the deformation phase, additional plastic deformation during the elastic recovery of pad, and the residual stress distributions at the deformed feature.

A holistic summary of results from different studies conducted in this thesis is shown in Table. 7.2 through comparing deformation profiles, mechanical properties, underlying microstructures, and the stress-strain distribution (from finite element analysis) for several process conditions in FPLSF.

7.2 Major Contributions

- The developed process, FPLSF, adds significant flexibility in the sheet metal micro-manufacturing domain, as the process is reliable, accurate, flexible, and fast enough to be used for mass customization and mass production environment. FPLSF has clear advantage in micromanufacturing due to the elimination of expensive micromold fabrication, improvement in process flexibility, reduction in process cycle time, and an increased tribological properties due to the frictionless forming.
- The detailed investigation of process deformation mechanisms in FPLSF enriches the process knowledge and modeling in the field of High-strain-rate forming.
- Analysis of laser-induced plasma in this work provides significant insights to other relevant processes including laser shock peening, laser peen forming, and laser shock forming where the plasma influence is prominent.
- The exploration of high strain rate loading behavior of hyperelastic materials (flexible pad) in FPLSF identifies new directions to the relevant, conventional quasi-static rubber pad forming process.

7.3 Future Work

The following recommendations are made to improve the developed process as well the knowledge domain of high-strain rate forming and laser-induced shock processing in general:

- To enhance the flexibility of FPLSF to fabricate different feature shapes, a new method of using mask patterns along with FPLSF is proposed. The schematic of the setup is shown in Fig. 7.1. The mask with required feature geometry will be positioned in the beam path, which will result in ablative overlay vaporization of area identical to the mask pattern. In this arrangement, 2D profile of the deformation features on metal foil will replicate the mask patterns, whereas feature depth will be controlled by FPLSF process variables.

- Process mechanisms involved in FPLSF were broadly classified into laser-induced shockwave formation and plastic deformation of metal foils in earlier parts of this thesis. However, in real case, these different behaviors occur simultaneously during FPLSF. Therefore, a holistic approach involving all the relevant physical behaviors in FPLSF, laser irradiation of ablative overlay, plasma formation and expansion under confinement, shockwave propagation, plastic deformation of metal foil, and hyperelastic deformation of flexible pad, is required for improved process prediction. An analytical formulation directly relating input process variables (laser conditions, ablative overlay and confinement parameters) to the output foil deformation characteristics (depth, diameter, surface hardness) shall be developed.

- Impedance mismatch behavior between successive layers influences the shock pressure propagation. This impedance mismatch effect can be tested by positioning flexible pad on both sides of the metal foil, as shown in Fig. 7.2a, to investigate its influence on plastic deformation of metal foils. Further, different layers of flexible pad materials can be stacked (Fig. 7.2b) according

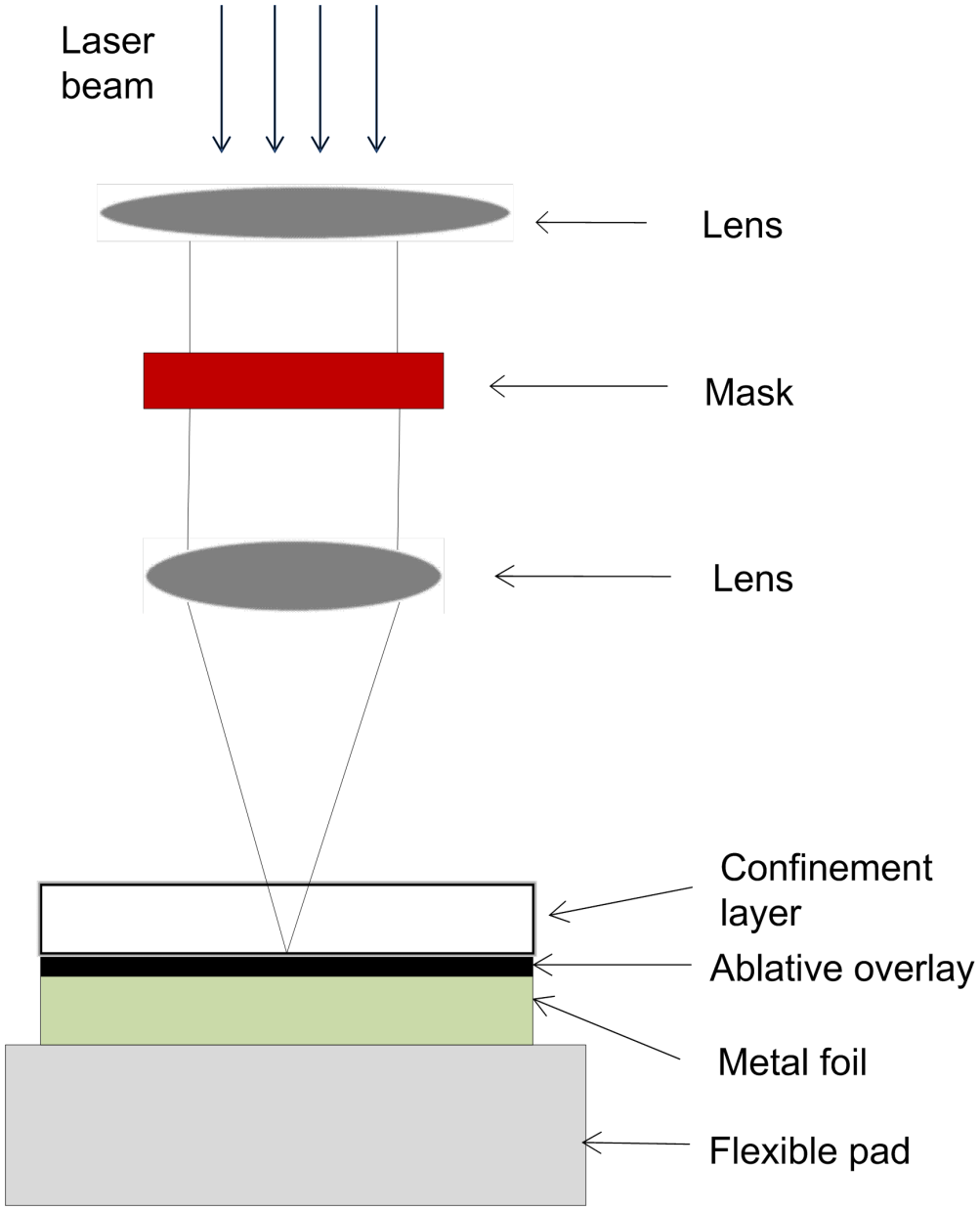

Figure 7.1: Schematic of FPLSF using mask patterns

to their impedance such that $Z_I > Z_{II} > Z_{III}$ and examined for its effect on foil deformation. The correlation between shock impedance of flexible pad and metal foil deformation characteristics can be derived through the above mentioned experimental schemes.

- The shock pressure duration plays an influential role in the plastic deformation of metal foils as discussed earlier. However, the uncertainty with the exact shock pressure duration resulted in the underestimation of metal foil deformation in FPLSF process simulations. Therefore, the measurement of

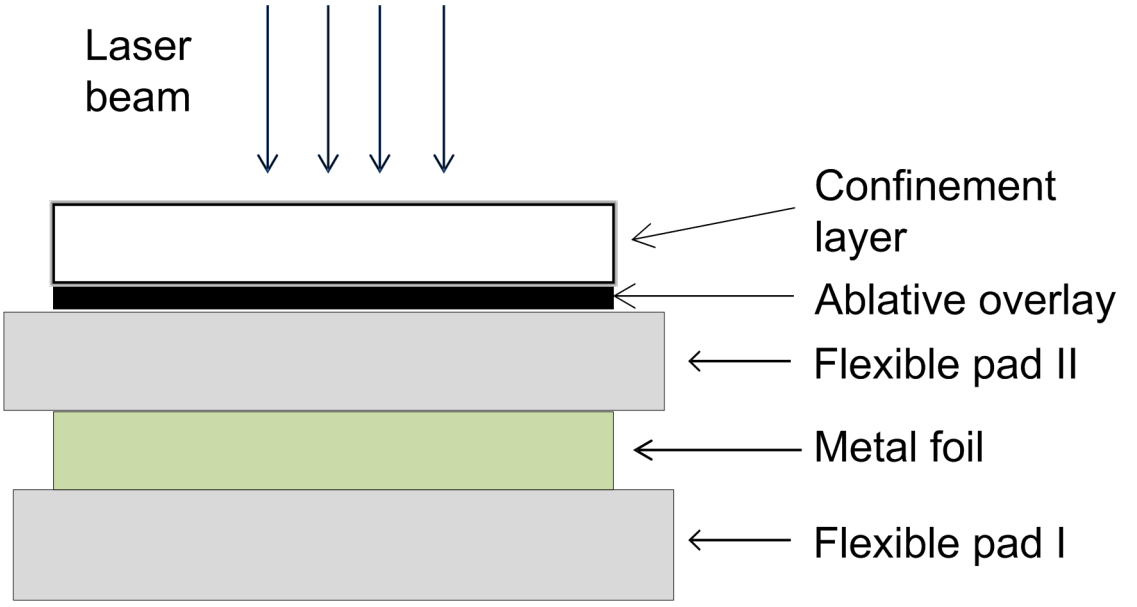

(a) Modified FPLSF schematic I – Flexible pad over metal foil

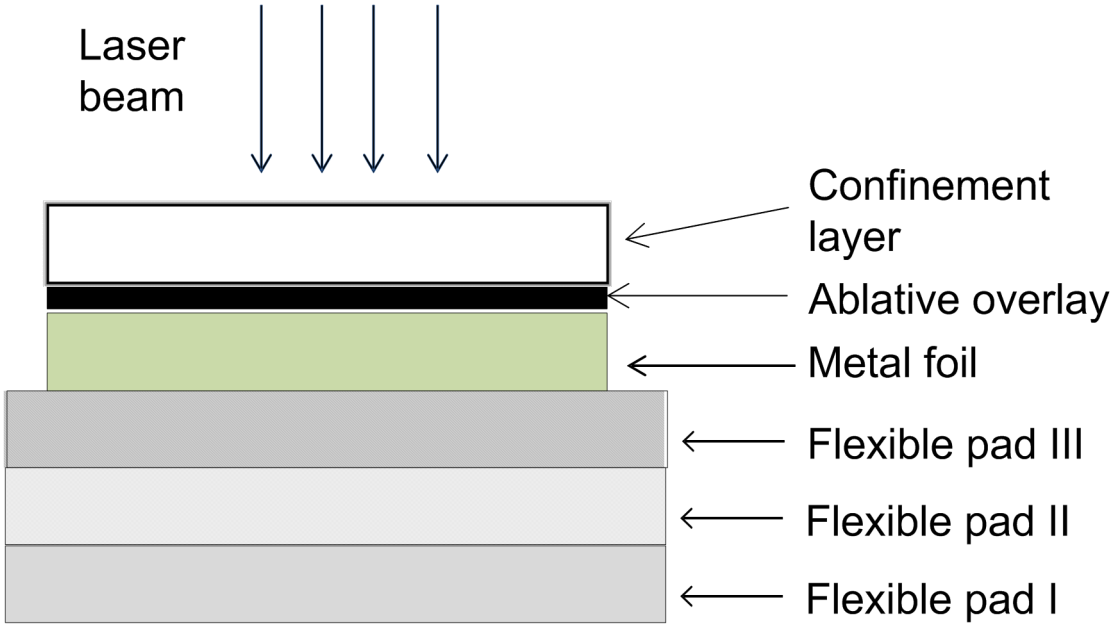

(b) Modified FPLSF schematic II – Flexible pad layering

Figure 7.2: Effect of impedance mismatch behavior in FPLSF (a) Modified FPLSF schematic with additional flexible pad over metal foil (b) Stacking of flexible pads with different acoustic impedance

shock pressure profile becomes necessary for the reliable prediction of process outcomes. In addition, the temporal analysis of shock pressure will address the questions pertaining to the correlation between the plasma existence and

the shock pressure. Along with the existing results on plasma formation and propagation, the shock pressure analysis will enhance the knowledge on the underlying process variables, especially, ablative overlay and confinement layer, which are also commonly used in most of the laser shock processes.

- Deployment of Fabbro's shock pressure model, which was originally developed for laser shock processing with bulk substrates, to the sheet metal forming as in FPLSF, especially in conditions of partial ablation of sacrificial overly, poses prediction issues. Thus, the corresponding modification of the pressure model is required.
- The application of loading area identical to that of laser beam proves erroneous in FE analysis. The correction of loading profiles in consideration with the spherical shockwave propagation, both in direct application and through overlay thickness conditions, is suggested to improve simulation predictions.
- Determining the stress strain relationship of hyperelastic flexible pad materials at high strain rates using Split Hopkinson bar test is suggested for FPLSF, which will also be helpful to understand the effect of strain rate on the hyperelastic material deformation in general.
- The microstructure analysis using EBSD is limited by its inability to identify the various deformation modes including twinning, stacking faults, and dislocation cells. Transmission Electron Microscopy (TEM) analysis of the deformed features is required to understand the underlying deformation modes in FPLSF.

Appendix A

Plastic Deformation - Texture Analysis

Typically, the texture on the deformation structures are analysed using the pole figure maps. It is found from A.1that, no significant textures were formed on copper after FPLSF. Similarly, no change in textures were observed between center and edge regions of the craters as noticed in A.2. Change in fluence also had no formidable effect on the texture [A.3].

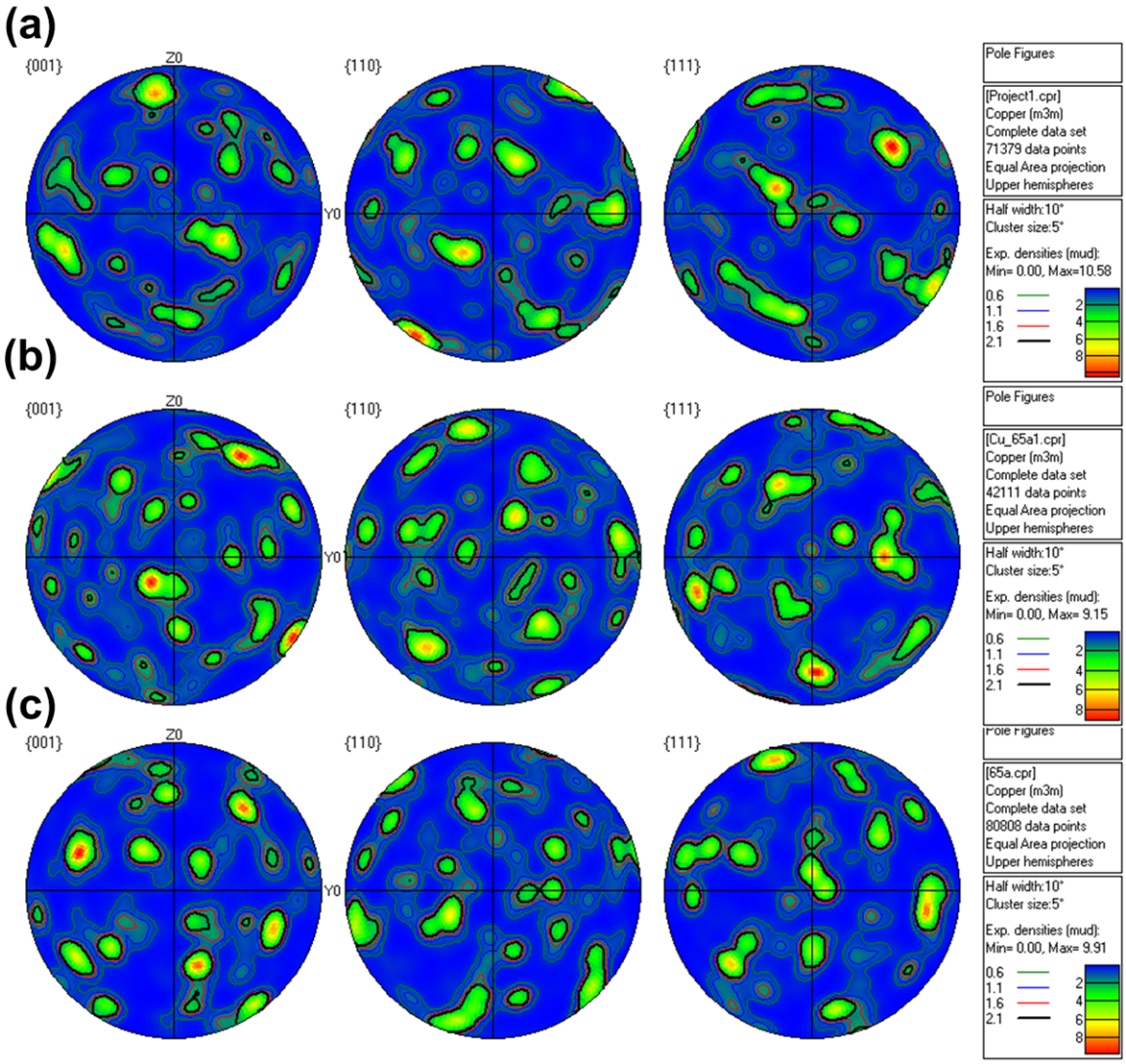

Figure A.1: Comparison of copper foil texture before and after FPLSF at 13.6 J/cm^2 fluence (a) Copper foil surface before FPSLF (b) Top surface of the formed crater (c) Bottom surface of the formed crater

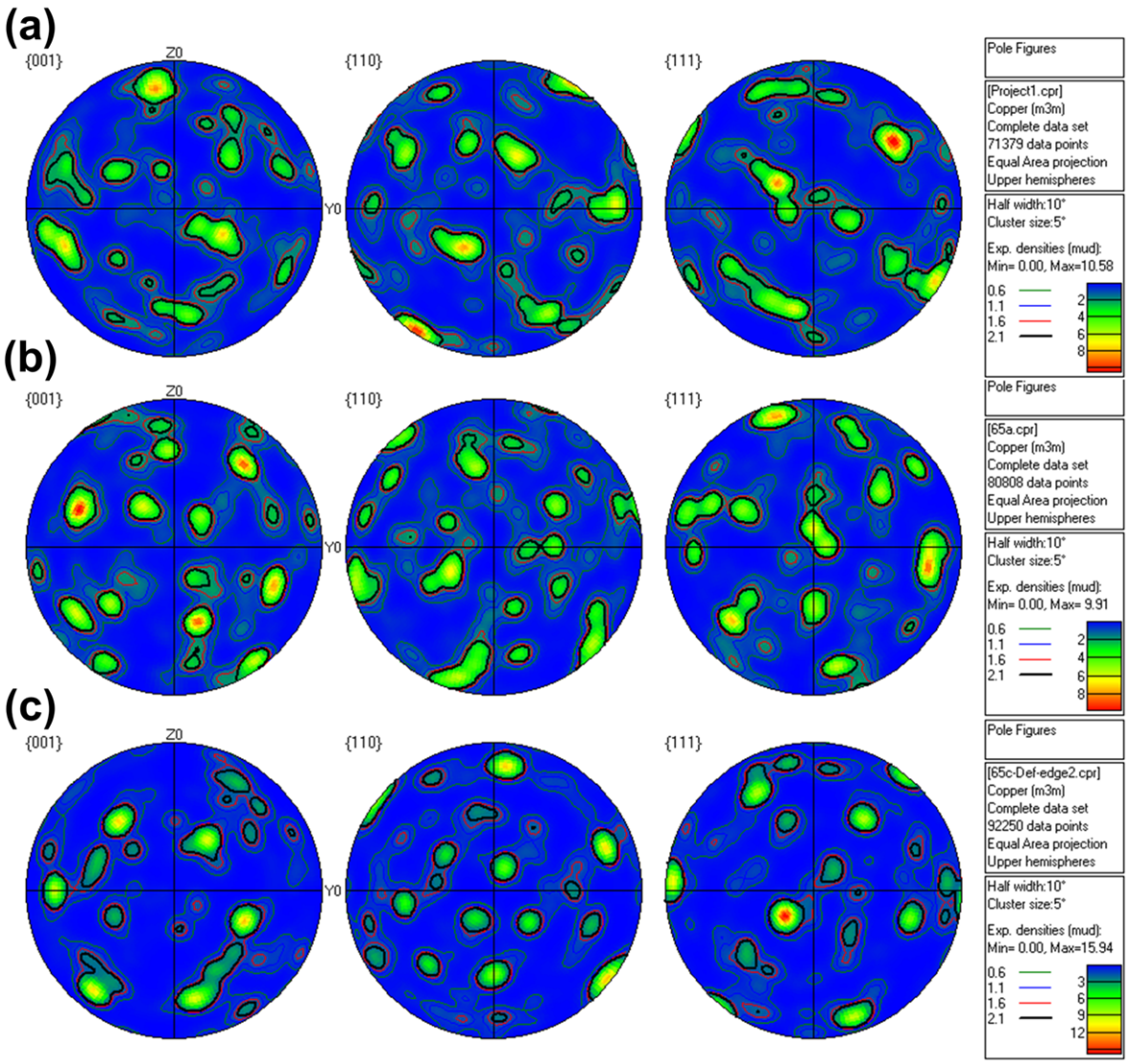

Figure A.2: Comparison of copper foil texture after FPLSF at 13.6 J/cm^2 fluence between crater center and edge portions (a) Copper foil surface before FPSLF (b) Crater center (c) Crater edge

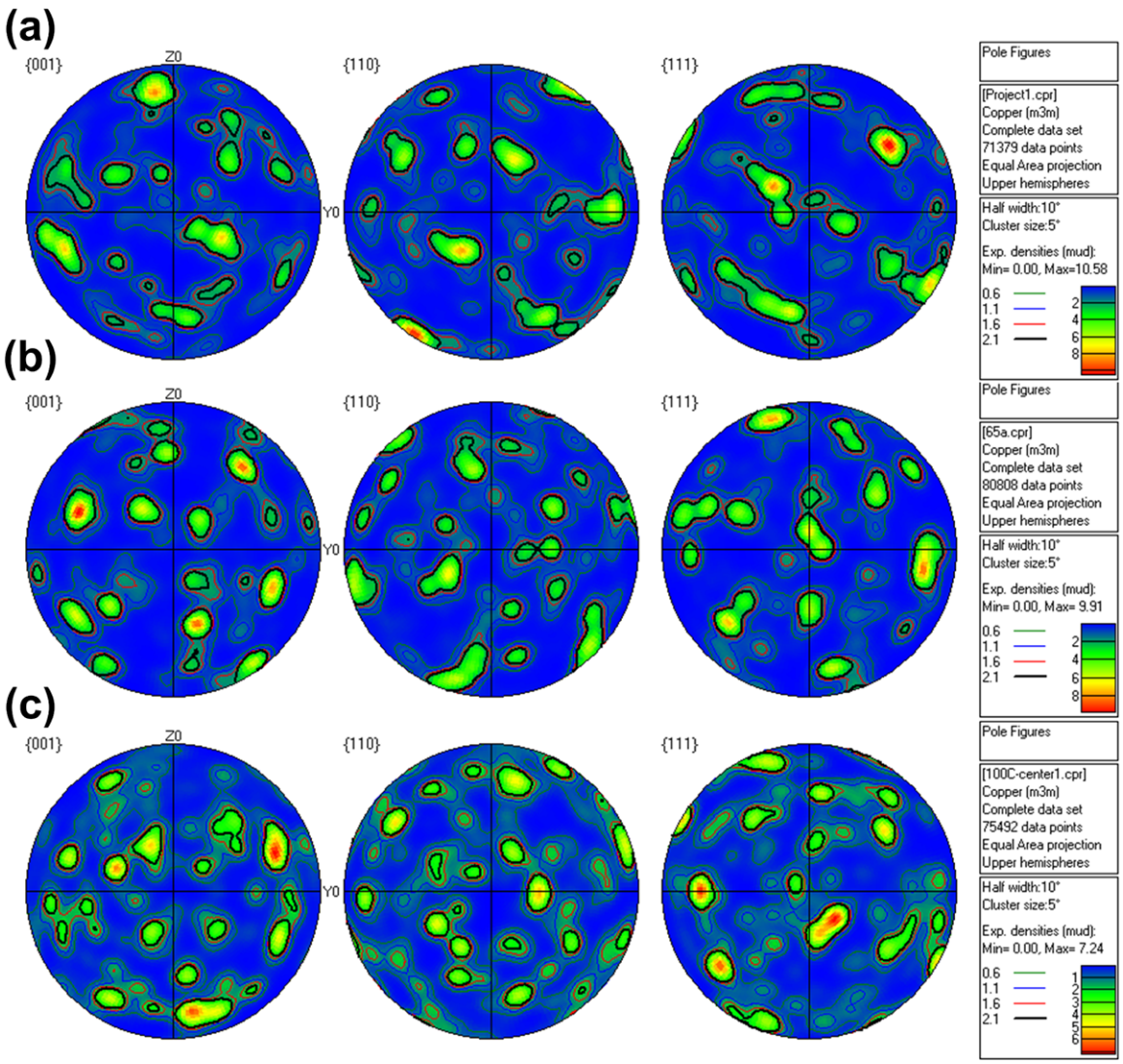

Figure A.3: Effect of laser fluence on copper foil texture (a) 13.6 J/cm^2 (b) 20.9 J/cm^2

Bibliography

[1] VK Jain, Ajay Sidpara, R Balasubramaniam, GS Lodha, VP Dhamgaye, and R Shukla. Micromanufacturing: A review-Part I. *Proceedings of the Institution of Mechanical Engineers, Part B: Journal of Engineering Manufacture*, 2014.

[2] Kornel F Ehmann, David Bourell, Martin L Culpepper, Thom J Hodgson, Thomas R Kurfess, Marc Madou, Kamlakar Rajurkar, and Richard E DeVor. International assessment of research and development in micromanufacturing. Technical report, DTIC Document, 2005.

[3] V. K. Jain. *Micromanufacturing processes*. Boca Raton, FL : CRC Press, 2012, c2013., 2012.

[4] Serope Kalpakjian and Steven R. Schmid. *Manufacturing processes for engineering materials*. Pearson Education, Upper Saddle River, N.J., 5th edition, 2008.

[5] Yi Qin, Andrew Brockett, Jie Zhao, Akhtar Razali, Yanling Ma, and Colin Harrison. Forming of micro-sheet-metal components. In *Micromanufacturing Engineering and Technology*, pages 130–145. William Andrew Publishing, Boston, 2010.

[6] Yi Qin, A. Brockett, Y. Ma, A. Razali, J. Zhao, C. Harrison, W. Pan, X. Dai, and D. Loziak. Micro-manufacturing: research, technology outcomes and development issues. *The International Journal of Advanced Manufacturing Technology*, 47(9):821–837, 2010.

[7] U Engel and R Eckstein. Microforming-from basic research to its realization. *Journal of Materials Processing Technology*, 125-126(0):35 – 44, 2002.

[8] B. Y. Joo, S. I. Oh, and Y. K. Son. Forming of micro channels with ultra thin metal foils. *CIRP Annals - Manufacturing Technology*, 53(1):243–246, 2004.

[9] Su dong Moon, Namsuk Lee, and Shinill Kang. Fabrication of a microlens array using micro-compression molding with an electroformed mold insert. *Journal of Micromechanics and Microengineering*, 13(1):98, 2003.

[10] M. Geiger, M. Kleiner, R. Eckstein, N. Tiesler, and U. Engel. Microforming. *CIRP Annals - Manufacturing Technology*, 50(2):445–462, 2001.

[11] E. Brousseau, S. Dimov, and D. Pham. Some recent advances in multi-material micro- and nano-manufacturing. *The International Journal of Advanced Manufacturing Technology*, 47(1):161–180, 2010.

[12] L. F. Thompson, C. G. Willson, and M. J. Bowden. *Introduction to microlithography*. ACS professional reference book. American Chemical Society, Washington, DC, 2nd edition, 1994. ISBN 0841228485 (alk. paper).

[13] L. Alting, F. Kimura, H. N. Hansen, and G. Bissacco. Micro engineering. *CIRP Annals - Manufacturing Technology*, 52(2):635–657, 2003.

[14] Yi. Qin. Micro-forming and miniature manufacturing systems-development needs and perspectives. *Journal of Materials Processing Technology*, 177: 8–18, 2006.

[15] Akhtar Razul Razali and Yi Qin. A review on micro-manufacturing, micro-forming and their key issues. *Procedia Engineering*, 53(0):665 – 672, 2013.

[16] Mikell P. Groover. *Fundamentals of modern manufacturing : materials, processes, and systems*. Prentice Hall, Upper Saddle River, N.J., 1996. ISBN 0133121828.

[17] J. Jeswiet, M. Geiger, U. Engel, M. Kleiner, M. Schikorra, J. Duflou, R. Neugebauer, P. Bariani, and S. Bruschi. Metal forming progress since 2000. *CIRP Journal of Manufacturing Science and Technology*, 1(1):2–17, 2008.

[18] Y. Saotome and A. Inoue. Superplastic micro-forming of microstructures. In *Micro Electro Mechanical Systems, 1994, MEMS '94, Proceedings, IEEE Workshop on*, pages 343–348, 1994 1994.

[19] Yong Li, Ting He, and Zhixin Zeng. Numerical simulation and experimental study on the tube sinking of a thin-walled copper tube with axially inner micro grooves by radial forging. *Journal of Materials Processing Technology*, 213(6):987 – 996, 2013.

[20] Yasunori Saotome and Hiroyuki Iwazaki. Superplastic backward microextrusion of microparts for micro-electro-mechanical systems. *Journal of Materials Processing Technology*, 119(1-3):307–311, 2001.

[21] Chunju. WANG, Debin. SHAN, Bin. GUO, and Lining. ZHOU, Jian. SUN. Key problems in microforming processes of microparts. *Journal of Materials Science & Technology*, 23(2):2, 2007.

[22] Neil Krishnan, Jian Cao, and Kuniaki Dohda. Study of the Size Effect on Friction Conditions in Microextrusion-Part I: Microextrusion Experiments and Analysis. *Journal of Manufacturing Science and Engineering*, 129(4): 669–676, 2007.

[23] J. Bohm, A. Schubert, T. Otto, and T. Burkhardt. Micro-metalforming with silicon dies. *Microsystem Technologies*, 7(4):191–195, 2001.

[24] Hiroshi Ike and Miroslav Plancak. Coining process as a means of controlling surface microgeometry. *Journal of Materials Processing Technology*, 80-81: 101–107, 1998.

[25] Karl-Heinrich Grote and Erik K. Antonsson. *Springer Handbook of Mechanical Engineering*. Berlin, Heidelberg : Springer Berlin Heidelberg, 2009., 2009. ISBN 9783540307389.

[26] Shiro Kobayashi, Soo-Ik Oh, and Taylan Altan. *Metal forming and the finite-element method*. Oxford series on advanced manufacturing. Oxford University Press, New York, 1989.

[27] F. Vollertsen, D. Biermann, H. N. Hansen, I. S. Jawahir, and K. Kuzman. Size effects in manufacturing of metallic components. *CIRP Annals - Manufacturing Technology*, 58(2):566–587, 2009.

[28] M. W. Fu and W. L. Chan. A review on the state-of-the-art microforming technologies. *The International Journal of Advanced Manufacturing Technology*, 67(9-12):2411–2437, 2013/08/01 2013.

[29] Fritz Klocke. *Manufacturing Processes 4 : Forming*. RWTHedition. Berlin, Heidelberg : Springer Berlin Heidelberg : Imprint: Springer, 2013., 2013.

[30] C.S. Namoco Jr., T. Iizuka, K. Narita, N. Takakura, and K. Yamaguchi. Effects of embossing and restoration process on the deep drawability of aluminum alloy sheets. *Journal of Materials Processing Technology*, 187-188(0): 202 – 206, 2007.

[31] F Forouhandeh, S Kumar, SN Ojha, and R Balasubramanian. Recent developments in microhydroforming. *Advances in Mechanical Engineering*, 2013, 2013.

[32] Francisco Chinesta, Elias Cueto, Ulf Engel, Andrzej Rosochowski, Stefan Geibdorer, and Lech Olejnik. Microforming and nanomaterials. In *Advances in Material Forming*, pages 99–124. Springer Paris, 2007. ISBN 978-2-287-72143-4.

[33] VK Jain, US Dixit, CP Paul, and Arvind Kumar. Micromanufacturing: A

review-part II. *Proceedings of the Institution of Mechanical Engineers, Part B: Journal of Engineering Manufacture*, 2014.

[34] F. Vollertsen, H. Schulze Niehoff, and Z. Hu. State of the art in micro forming. *International Journal of Machine Tools and Manufacture*, 46(11):1172–1179, 2006.

[35] Yasunori Saotome, Kaname Yasuda, and Hiroshi Kaga. Microdeep drawability of very thin sheet steels. *Journal of Materials Processing Technology*, 113 (1-3):641–647, 2001.

[36] F. Vollertsen, Z. Hu, H. Schulze Niehoff, and C. Theiler. State of the art in micro forming and investigations into micro deep drawing. *Journal of Materials Processing Technology*, 151(1-3):70–79, 2004.

[37] Feng Gong, Bin Guo, Chunju Wang, and Debin Shan. Micro deep drawing of micro cups by using dlc film coated blank holders and dies. *Diamond and Related Materials*, 20(2):196 – 200, 2011.

[38] Chen Chi-Han, Gau Jenn-Terng, and Lee Rong-Shean. An experimental and analytical study on the limit drawing ratio of stainless steel 304 foils for microsheet forming. *Materials & Manufacturing Processes*, 24(12):1256 – 1265, 2009.

[39] K. Manabe, T. Shimizu, H. Koyama, M. Yang, and K. Ito. Validation of fe simulation based on surface roughness model in micro-deep drawing. *Journal of Materials Processing Technology*, 204(1-3):89 – 93, 2008.

[40] R Erhardt, F Schepp, and D Schmoeckel. Micro forming with local part heating by laser irradiation in transparent tools. *Sheet Metal*, pages 497–504, 1999.

[41] Yasuo Marumo, Hiroyuki Saiki, and Liqun Ruan. Influence of resin dies and resin auxiliary sheets on deep drawability of metal foil. *Journal of Materials Processing Technology*, 162-163(0):530–533, 2005.

[42] J. Jeswiet, F. Micari, G. Hirt, A. Bramley, J. Duflou, and J. Allwood. Asymmetric single point incremental forming of sheet metal. *CIRP Annals - Manufacturing Technology*, 54(2):88–114, 2005.

[43] Muammer Koc and Sasawat Mahabunphachai. Feasibility investigations on a novel micro-manufacturing process for fabrication of fuel cell bipolar plates: Internal pressure-assisted embossing of micro-channels with in-die mechanical bonding. *Journal of Power Sources*, 172(2):725–733, 2007.

[44] Jung-Chung Hung and Chih-Chia Lin. Fabrication of micro-flow channels for metallic bipolar plates by a high-pressure hydroforming apparatus. *Journal of Power Sources*, 206(0):179 – 184, 2012.

[45] Yanxiong Liu and Lin Hua. Fabrication of metallic bipolar plate for proton exchange membrane fuel cells by rubber pad forming. *Journal of Power Sources*, 195(11):3529–3535, 2010.

[46] Linfa Peng, Jun Ni, Dong'an Liu, Peng Hu, and Xinmin Lai. Fabrication of metallic bipolar plates for proton exchange membrane fuel cell by flexible forming process-numerical simulations and experiments. *Journal of Fuel Cell Science and Technology*, 7(3):031009–031009, 2010.

[47] Chang-Youl Son, Yong-Phil Jeon, Yong-Tae Kim, and Chung-Gil Kang. Evaluation of the formability of a bipolar plate manufactured from aluminum alloy Al 1050 using the rubber pad forming process. *Proceedings of the Institution of Mechanical Engineers, Part B: Journal of Engineering Manufacture*, January 30, 2012 2012.

[48] S. S. Lim, Y. T. Kim, and C. G. Kang. Fabrication of aluminum 1050 micro-channel proton exchange membrane fuel cell bipolar plate using rubber-pad-forming process. *The International Journal of Advanced Manufacturing Technology*, 65(1-4):231–238, 2013.

[49] Chul Kyu Jin, Min Geun Jeong, and Chung Gil Kang. Fabrication of titanium bipolar plates by rubber forming and performance of single cell using tin-coated titanium bipolar plates. *International Journal of Hydrogen Energy*, (0):–, 2014.

[50] S. L. Semiatin, editor. *ASM handbook; v.14B: Metalworking; sheet forming.* Book News, Inc., 2006.

[51] Francisco Chinesta, Elias Cueto, and Torgeir Welo. Sheet metal forming advances in material forming. pages 175–191. Springer Paris, 2007.

[52] Frank Vollertsen and Zhenyu Hu. Analysis of punch velocity dependent process window in micro deep drawing. *Production Engineering*, 4(6):553–559, 2010.

[53] Kinuko Fujimoto, Ming Yang, Masanao Hotta, Hiroshi Koyama, Shizuka Nakano, Kazuo Morikawa, and Julie Cairney. Fabrication of dies in micro-scale for micro-sheet metal forming. *Journal of Materials Processing Technology*, 177(1-3):639 – 643, 2006.

[54] Jie XU, Chun ju WANG, Bin GUO, De bin SHAN, Y. SUGIYAMA, and S. ONO. Surface finish of micro punch with ion beam irradiation. *Transactions of Nonferrous Metals Society of China*, 19, Supplement 2(0):s526 – s530, 2009.

[55] M. Geiger, F. Vollertsen, and R. Kals. Fundamentals on the manufacturing of sheet metal microparts. *CIRP Annals - Manufacturing Technology*, 45(1): 277–282, 1996.

[56] J. Fleischer and J. Kotschenreuther. The manufacturing of micro molds by conventional and energy-assisted processes. *The International Journal of Advanced Manufacturing Technology*, 33(1):75–85, 2007.

[57] R. Neugebauer, K. D. Bouzakis, B. Denkena, F. Klocke, A. Sterzing, A. E.

Tekkaya, and R. Wertheim. Velocity effects in metal forming and machining processes. *CIRP Annals - Manufacturing Technology*, 60(2):627–650, 2011.

[58] Wenwu Zhang and Y. Lawrence Yao. Microscale laser shock processing–modeling, testing, and microstructure characterization. *Journal of Manufacturing Processes*, 3(2):128–143, 2001.

[59] J. Z. Zhou, J. C. Yang, Y. K. Zhang, and M. Zhou. A study on super-speed forming of metal sheet by laser shock waves. *Journal of Materials Processing Technology*, 129(1-3):241–244, 2002.

[60] Maziar Ramezani, Zaidi Mohd Ripin, and Roslan Ahmad. Sheet metal forming with the aid of flexible punch, numerical approach and experimental validation. *CIRP Journal of Manufacturing Science and Technology*, 3(3): 196–203, 2010.

[61] S. Thiruvarudchelvan. Elastomers in metal forming: A review. *Journal of Materials Processing Technology*, 39(1-2):55–82, 1993.

[62] S. Thiruvarudchelvan. The potential role of flexible tools in metal forming. *Journal of Materials Processing Technology*, 122(2-3):293–300, 2002.

[63] Linfa Peng, Peng Hu, Xinmin Lai, Deqing Mei, and Jun Ni. Investigation of micro/meso sheet soft punch stamping process - simulation and experiments. *Materials & Design*, 30:783–790, 2009.

[64] M. Husnu Dirikolu and Esra Akdemir. Computer aided modelling of flexible forming process. *Journal of Materials Processing Technology*, 148(3):376–381, 2004.

[65] Xiao Wang, Daozhong Du, Hu Zhang, Zongbao Shen, Huixia Liu, Jianzhong Zhou, Hui Liu, Yang Hu, and Chunxing Gu. Investigation of microscale laser dynamic flexible forming process - simulation and experiments. *International Journal of Machine Tools and Manufacture*, 67(0):8–17, 4// 2013.

[66] Hisaki Watari, Hiroshi Ona, and Yu Yoshida. Flexible punching method using an elastic tool instead of a metal punch. *Journal of Materials Processing Technology*, 137(1-3):151–155, 2003.

[67] Antonio Del Prete, Gabriele Papadia, and Barbara Manisi. Computer aided modelling of rubber pad forming process. *Key Engineering Materials*, 473: 637–644, 2011.

[68] Pratapkumar Nagarajan and Donggang Yao. Uniform shell patterning using rubber-assisted hot embossing process. I. Experimental. *Polymer Engineering & Science*, 51(3):592–600, 2011.

[69] M. Ramezani and Z.M. Ripin. Analysis of deep drawing of sheet metal using the marform process. *The International Journal of Advanced Manufacturing Technology*, 59(5):491–505, 2012.

[70] Giuseppe Sala. A numerical and experimental approach to optimise sheet stamping technologies: part II – aluminium alloys rubber-forming. *Materials & Design*, 22(4):299–315, 2001.

[71] Al-Qureshi H.A. Analysis of simultaneous sheet metal forming operations using elastomer technique. *Journal of Materials Processing Technology*, 125-126(0):751–755, 2002.

[72] V. Psyk, D. Risch, B. L. Kinsey, A. E. Tekkaya, and M. Kleiner. Electromagnetic forming–a review. *Journal of Materials Processing Technology*, 211 (5):787–829, 2011.

[73] G Zittel. A historical review of high speed metal forming. *4th International Conference on High Speed Forming*, 2010.

[74] Desiree Risch, Verena Psyk, and A. Erman Tekkaya. Investigation on a deep drawing and in-process electromagnetic calibration. *steel research international*, 80(5):329–334, 2009.

[75] J Shang, L Wilkerson, S Hatkevich, and GS Daehn. Commercialization of fuel cell bipolar plate manufacturing by electromagnetic forming. In *4th International Conference on High Speed Forming*, 2010.

[76] Glenn S.Daehn. *High Velocity Metal Forming*, volume 14B, Metalworking:Sheet Forming of *ASM Handbook*. ASM International, 2006.

[77] He Fengman, Tong Zheng, Wang Ning, and Hu Zhiyong. Explosive forming of thin-wall semi-spherical parts. *Materials Letters*, 45(2):133–137, 2000.

[78] V. S. Balanethiram and G. S. Daehn. Hyperplasticity: Increased forming limits at high workpiece velocity. *Scripta Metallurgica et Materiala*, 30(4): 515–520, 1994.

[79] Wenwu Zhang and Y. Lawrence Yao. Micro scale laser shock processing of metallic components. *Journal of Manufacturing Science and Engineering*, 124(2):369–378, 2002.

[80] Wenwu Zhang, Y. Lawrence Yao, and I. C. Noyan. Microscale laser shock peening of thin films, part 1: Experiment, modeling and simulation. *Journal of Manufacturing Science and Engineering*, 126(1):10–17, 2004.

[81] Charles S. Montross, Tao Wei, Lin Ye, Graham Clark, and Yiu-Wing Mai. Laser shock processing and its effects on microstructure and properties of metal alloys: a review. *International Journal of Fatigue*, 24(10):1021–1036, 2002.

[82] J. D. O'Keefe, C. H. Skeen, and C. M. York. Laser-induced deformation modes in thin metal targets. *Journal of Applied Physics*, 44(10):4622–4626, 1973.

[83] M. Zhou, Y. K. Zhang, and L. Cai. Ultrahigh-strain-rate plastic deformation of a stainless-steel sheet with tin coatings driven by laser shock waves. *Applied Physics A: Materials Science & Processing*, 77(3):549–554, 2003.

[84] Ming Zhou, Yongkang Zhang, and Lan Cai. Laser shock forming on coated metal sheets characterized by ultrahigh-strain-rate plastic deformation. *Journal of Applied Physics*, 91(8):5501–5503, 2002.

[85] Chaojun Yang, Zhen Ye, Jinzhong Lu, and Yinfang Jiang. Laser shock forming of sus304 stainless steel sheet with elliptical spot. *The International Journal of Advanced Manufacturing Technology*, 56(9):987–993, 2011.

[86] H. Schulze Niehoff and F. Vollertsen. Non-thermal laser forming of sheet metal. In *1st International conference on High Speed forming*, 2004.

[87] Frank Vollertsen, Hendrik Niehoff, and Hanna Wielage. On the acting pressure in laser deep drawing. *Production Engineering*, 3(1):1–8, 2009.

[88] Hanna Wielage and Frank Vollertsen. Undercuts by laser shock forming. *AIP Conference Proceedings*, 1353(1):1309–1312, 2011.

[89] Gary J. Cheng, Daniel Pirzada, and Zhou Ming. Microstructure and mechanical property characterizations of metal foil after microscale laser dynamic forming. *Journal of Applied Physics*, 101(6):063108–7, 2007.

[90] Huang Gao, Chang Ye, and Gary J. Cheng. Deformation behaviors and critical parameters in microscale laser dynamic forming. *Journal of Manufacturing Science and Engineering*, 131(5):051011, 2009.

[91] Ji Li, Huang Gao, and Gary J. Cheng. Forming limit and fracture mode of microscale laser dynamic forming. *Journal of Manufacturing Science and Engineering*, 132(6):061005, 2010.

[92] Cunjiang Yu, Huang Gao, Hongyu Yu, Hanqing Jiang, and Gary J. Cheng. Laser dynamic forming of functional materials laminated composites on patterned three-dimensional surfaces with applications on flexible microelectromechanical systems. *Applied Physics Letters*, 95(9):091108–3, 2009.

[93] H. Gao, R. Tang, T. Ma, H. Jiang, H. Yu, and G. J. Cheng. Direct Integration of Functional Structures on 3-D Microscale Surfaces by Laser Dynamic Forming. *Microelectromechanical Systems, Journal of*, PP(99):1–1, 2013.

[94] J Li, R J Zhang, H Q Jiang, and G J Cheng. Scalable nano-patterning of graphenes using laser shock. *Nanotechnology*, 22(47):475303, 2011.

[95] Huixia Liu, Zongbao Shen, Xiao Wang, and Hejun Wang. Numerical simulation and experimentation of a novel laser indirect shock forming. *Journal of Applied Physics*, 106(6):063107, 2009.

[96] Huixia Liu, Zongbao Shen, Xiao Wang, Hejun Wang, and Maoke Tao. Micromould based laser shock embossing of thin metal sheets for mems applications. *Applied Surface Science*, 256(14):4687–4691, 2010.

[97] M. Zhou, T. Huang, and L. Cai. The novel nanosecond laser micromanufacturing of three-dimensional metallic structures. *Applied Physics A: Materials Science & Processing*, 90(2):293–297, 2008.

[98] J. L. Ocana, M. Morales, J. J. Garcia-Ballesteros, J. A. Porro, O. Garcia, and C. Molpeceres. Laser shock microforming of thin metal sheets. *Applied Surface Science*, 255(10):5633–5636, 2009.

[99] Kenneth Edwards, Stuart Edwardson, Chris Carey, Geoff Dearden, and Ken Watkins. Laser micro peen forming without a tamping layer. *The International Journal of Advanced Manufacturing Technology*, 47(1):191–200, 2010.

[100] Edwards K R., Dearden G., Watkins K G., and Edwardson S P. Laser peen forming of thin sheet ferrous materials. In *Photon06 Conference Manchester*, 2006.

[101] J. Z. Zhou, H.X. Liu, C.J. Yang, X.G. Cao, J.J. Du, and M.X. Ni. Nontraditional forming process of sheet metal based on laser shock waves. *Key Engineering Materials*, 329:637–642, 2007.

[102] Ding Hua, Wang Yun, and Cai Lan. Laser shock forming of aluminum sheet: Finite element analysis and experimental study. *Applied Surface Science*, 256 (6):1703–1707, 2010.

[103] Y. K. Zhang, J.Z. Zhou, D.W. Zuo, J.C. Yang, and L. Cai. Study on technology of flexible forming of sheet metal based on laser shock waves. *Materials Science Forum*, 471-472:453–456, 2004.

[104] John Ion. *Laser processing of engineering materials: principles, procedure and industrial application*. Butterworth-Heinemann, 2005.

[105] E. Kannatey-Asibu. *Principles of laser materials processing*. Wiley series on processing of engineering materials. Hoboken, N.J. : Wiley, c2009., 2009. ISBN 9780470177983 0470177985.

[106] M. Cirisan, J. M. Jouvard, L. Lavisse, L. Hallo, and R. Oltra. Laser plasma plume structure and dynamics in the ambient air: The early stage of expansion. *Journal of Applied Physics*, 109(10):103301, 2011.

[107] Peter Schaaf. *Laser Processing of Materials : Fundamentals, Applications and Developments*. Springer Series in Materials Science: 139. Berlin, Heidelberg : Springer-Verlag Berlin Heidelberg, 2010. ISBN 9783642132810.

[108] Narendra B. Dahotre and Sandip P. Harimkar. *Laser Fabrication and Machining of Materials*. Boston, MA : Springer Science + Business Media, LLC, 2008. ISBN 9780387723440.

[109] AllanH Clauer, JohnH Holbrook, and BarryP Fairand. Effects of laser induced shock waves on metals. In *Shock Waves and High-Strain-Rate Phenomena in Metals*, chapter 38, pages 675–702. Springer US, 1981.

[110] Gulshan Singh. *Effective Simulation and Optimization of a Laser Peening Process*. Phd thesis, Wright State University, 2009.

[111] S. Amoruso, R. Bruzzese, N. Spinelli, and R. Velotta. Characterization of laser-ablation plasmas. *Journal of Physics B: Atomic, Molecular and Optical Physics*, 32(14):R131, 1999.

[112] D. I. Rosen, J. Mitteldorf, G. Kothandaraman, A. N. Pirri, and E. R. Pugh. Coupling of pulsed 0.35-μm laser radiation to aluminum alloys. *Journal of Applied Physics*, 53(4):3190–3200, 1982.

[113] Jr C. R. Phipps, T. P. Turner, R. F. Harrison, G. W. York, W. Z. Osborne, G. K. Anderson, X. F. Corlis, L. C. Haynes, H. S. Steele, K. C. Spicochi, and T. R. King. Impulse coupling to targets in vacuum by KrF, HF, and CO_2 single-pulse lasers. *Journal of Applied Physics*, 64(3):1083–1096, 1988.

[114] M. Beck, P. Berger, and H. Hugel. The effect of plasma formation on beam focusing in deep penetration welding with CO_2 lasers. *Journal of Physics D: Applied Physics*, 28(12):2430, 1995.

[115] N. Kumar, S. Dash, A. K. Tyagi, and Baldev Raj. Dynamics of plasma expansion in the pulsed laser material interaction. *Sadhana*, 35(4):493–511, 2010/08/01 2010.

[116] O. Barthelemy, J. Margot, and M. Chaker. Characterization of the expansion of an aluminum laser-induced plasma in ambient air by fast photography. *Plasma Science, IEEE Transactions on*, 33(2):476–477, 2005.

[117] Xiao Chen, Rong-Qing Xu, Jian-Ping Chen, Zhong-Hua Shen, Lu Jian, and Xiao-Wu Ni. Shock-Wave Propagation and Cavitation Bubble Oscillation by Nd:YAG Laser Ablation of a Metal in Water. *Applied Optics*, 43(16): 3251–3257, 2004.

[118] Ronald M. Gilgenbach and Peter L. G. Ventzek. Dynamics of excimer laser-ablated aluminum neutral atom plume measured by dye laser resonance absorption photography. *Applied Physics Letters*, 58(15):1597–1599, 1991.

[119] A Gupta, B Braren, KG Casey, BW Hussey, and Roger Kelly. Direct imaging of the fragments produced during excimer laser ablation of YBa2Cu3O7- δ. *Applied physics letters*, 59(11):1302–1304, 1991.

[120] H. Nose, H. Maeda, and M. Nakahara. Observation and application of laser induced shock wave. In *Advanced Information Networking and Applications, 2004. AINA 2004. 18th International Conference on*, volume 2, pages 215–218 Vol.2, 29-31 March 2004 2004.

[121] K. Watanabe, H. Torikai, Q. S. Yang, A. Sasoh, Y. Sano, and N. Mukai. Shock wave phenomena in underwater laser peening. In *Shock Waves*, chapter 159, pages 1039–1042. Springer Berlin Heidelberg, 2005.

[122] Hiroyuki Hirahara, Masaru Fujinami, and Masaaki Kawahashi. Optical measurement of a laser induced micro shock wave on a metal surface. *Journal of Fluid Science and Technology*, 3(8):965–974, 2008.

[123] J. Noack, D. X. Hammer, G. D. Noojin, B. A. Rockwell, and A. Vogel. Influence of pulse duration on mechanical effects after laser-induced breakdown in water. *Journal of Applied Physics*, 83(12):7488–7495, 1998.

[124] N. Seto. High-speed simultaneous observation of plasma and keyhole behavior during high power CO_2 laser welding: Effect of shielding gas on porosity formation. *Journal of Laser Applications*, 12(6):245–50, 2000.

[125] L. Berthe, R. Fabbro, P. Peyre, L. Tollier, and E. Bartnicki. Shock waves from a water-confined laser-generated plasma. *Journal of Applied Physics*, 82(6):2826–2832, 1997.

[126] L. Marti-Lopez, R. Ocana, J. A. Porro, M. Morales, and J. L. Ocana. Optical observation of shock waves and cavitation bubbles in high intensity laser-induced shock processes. *Applied Optics*, 48(19):3671–3680, 2009.

[127] L. Marti-Lopez, R. Ocana, E. Pineiro, and A. Asensio. Laser peening induced

shock waves and cavitation bubbles in water studied by optical schlieren visualization. *Physics Procedia*, 12, Part A(0):442–451, 2011.

[128] Franco Docchio, Pietro Regondi, Malcolm R. C. Capon, and John Mellerio. Study of the temporal and spatial dynamics of plasmas induced in liquids by nanosecond Nd:YAG laser pulses. 1: Analysis of the plasma starting times. *Applied Optics*, 27(17):3661–3668, 1988.

[129] B. Yilbas, A. Arif, S. Shuja, M. Gondal, and J. Shirokof. Investigation into laser shock processing. *Journal of Materials Engineering and Performance*, 13(1):47–54, 2004.

[130] M. Tanski, M. Kocik, R. Barbucha, K. Garasz, and J. Mizeraczyk. Time-resolved observation of the ablation plasma plume dynamics during nanosecond laser micromachining. In *Photonics and Optoelectronics (SOPO), 2012 Symposium on*, pages 1–4, 2012.

[131] Krzysztof A Nowakowski. *Laser beam interaction with materials for microscale applications*. PhD thesis, Worcester Polytechnic Institute, 2005.

[132] William D. Callister. *Materials science and engineering : an introduction / William D. Callister, Jr.* New York : John Wiley & Sons, c2007., 2007. ISBN 0471736961.

[133] William F. Smith and Javad Hashemi. *Foundations of materials science and engineering*. Dubuque, IA : McGraw-Hill, 2010., 2010.

[134] Y.X. Ye, Y.Y. Feng, Z.C. Lian, and Y.Q. Hua. Plastic deformation mechanism of polycrystalline copper foil shocked with femtosecond laser. *Applied Surface Science*, 309(0):240 – 249, 2014.

[135] Aderopo Adesola. *Damage Evolution in AA2099 and AA6061 Aluminum Alloys Under Quasi-static and Dynamic Mechanical Loading*. PhD thesis, University of Saskatchewan, 2011.

[136] U. Andrade, M. A. Meyers, K. S. Vecchio, and A. H. Chokshi. Dynamic recrystallization in high-strain, high-strain-rate plastic deformation of copper. *Acta Metallurgica et Materialia*, 42(9):3183–3195, 1994.

[137] F. Yazdani, M. N. Bassim, and A. G. Odeshi. The formation of adiabatic shear bands in copper during torsion at high strain rates. *Procedia Engineering*, 1(1):225–228, 7// 2009.

[138] Y. Yang, X.M. Li, S.W. Chen, Q.M. Zhang, F. Jiang, and H.G. Zheng. Effects of pre-notches on the self-organization behaviours of shear bands in aluminum alloy. *Materials Science and Engineering A*, 527:5084–5091, 2010.

[139] Mark Colgan and John Monaghan. Deep drawing process: analysis and experiment. *Journal of Materials Processing Technology*, 132(1-3):35–41, 2003.

[140] Gao Huang and G. J. Cheng. Laser-Induced High-Strain-Rate Superplastic 3-D Microforming of Metallic Thin Films. *Microelectromechanical Systems, Journal of*, 19(2):273–281, 2010.

[141] Xinmin Luo, Chunzhi Yuan, Xudong Ren, Yongkang Zhang, and Kangmin Chen. Laser shock deforming and induced microstructure evolution of austenitic stainless steel sheet. *International Journal of Materials and Structural Integrity*, 4(1):87–98, 2010.

[142] L.E. Murr. Residual microstructure - mechanical property relationships in shock-loaded metals and alloys. In MarcA. Meyers and LawrenceE. Murr, editors, *Shock Waves and High-Strain-Rate Phenomena in Metals*, pages 607–673. Springer US, 1981.

[143] M.A. Meyers, F. Gregori, B.K. Kad, M.S. Schneider, D.H. Kalantar, B.A. Remington, G. Ravichandran, T. Boehly, and J.S. Wark. Laser-induced shock compression of monocrystalline copper: characterization and analysis. *Acta Materialia*, 51(5):1211 – 1228, 2003.

[144] Huang Gao and Gary J. Cheng. 3D microscale laser dynamic forming: Multi-scale modeling and experimental validation. *Journal of Applied Physics*, 109 (10):103511–13, 2011.

[145] George T. (Rusty) Gray. High-strain-rate deformation: Mechanical behavior and deformation substructures induced. *Annual Review of Materials Research*, 42(1):285–303, 2012.

[146] R. Fabbro, P. Peyre, L. Berthe, and X. Scherpereel. Physics and applications of laser-shock processing. *Journal of Laser Applications*, 10(6):265–279, 1998.

[147] C. S. Montross, V. Florea, and M. V. Swain. The influence of coatings on subsurface mechanical properties of laser peened 2011-T3 aluminum. *Journal of Materials Science*, 36(7):1801–1807, 2001.

[148] Fei Wang, Zhenqiang Yao, and Xueping Zhang. Experimental and numerical simulation research on laser shock forming of thin metal sheet of brass. *Optical Engineering*, 47(2):024302–6, 2008.

[149] F. Wang, Z. Q. Yao, J. Hu, and Q. L. Deng. Experimental research and numerical simulation of laser shock forming of TA2 titanium sheet. *Acta Metallurgica Sinica (English Letters)*, 19(5):347–354, 2006.

[150] Kangmei Li, Yongxiang Hu, and Zhenqiang Yao. Experimental study of micro dimple fabrication based on laser shock processing. *Optics & Laser Technology*, 48(0):216–225, 6// 2013.

[151] J. P. Romain and P. Darquey. Shock waves and acceleration of thin foils by laser pulses in confined plasma interaction. *Journal of Applied Physics*, 68 (4):1926–1928, 1990.

[152] D. Devaux, R. Fabbro, L. Tollier, and E. Bartnicki. Generation of shock waves by laser-induced plasma in confined geometry. *Journal of Applied Physics*, 74(4):2268–2273, 1993.

[153] Gulshan Singh, Ramana V. Grandhi, and David S. Stargel. Modeling and parameter design of a laser shock peening process. *International Journal for Computational Methods in Engineering Science and Mechanics*, 12(5): 233–253, 2011.

[154] Jean-Eric Masse and Garard Barreau. Laser generation of stress waves in metal. *Surface and Coatings Technology*, 70(2-3):231–234, 1995.

[155] Yongxiang Hu, Zhenqiang Yao, and Jun Hu. 3-D FEM simulation of laser shock processing. *Surface and Coatings Technology*, 201(3-4):1426–1435, 2006.

[156] K. Ding and L. Ye. Three-dimensional dynamic finite element analysis of multiple laser shock peening processes. *Surface Engineering*, 19(5):351–358, 2003.

[157] Jian Zhong Zhou, Hui Xia Liu, Yong Kang Zhang, Ming Zhou, Xing Quan Zhang, and Ji Chang Yang. Experimental and numerical simulation of sheet bulging induced by laser shock peening. volume 5627, pages 386–392, Beijing, China, 2005. SPIE.

[158] Ji Li and Gary J. Cheng. Multiple-pulse laser dynamic forming of metallic thin films for microscale three dimensional shapes. *Journal of Applied Physics*, 108(1):013107–8, 2010.

[159] Schulze H Niehoff and F Vollertsen. Laser induced shock waves in deformation processing. *Metalurgija*, 11(3):183–194, 2005.

[160] R. Fabbro, J. Fournier, P. Ballard, D. Devaux, and J. Virmont. Physical study of laser-produced plasma in confined geometry. *Journal of Applied Physics*, 68(2):775–784, 1990.

[161] Zhigang Che, Shui-li Gong, Shikun Zou, Ziwen Cao, and Qunxing Fei. Investigation on the key techniques of confined medium and coating layer for

laser shock processing on aeroengine blade. In *Proceedings of the 36th International MATADOR Conference*, pages 527–530. Springer London, 2010. ISBN 978-1-84996-432-6.

[162] C. Carey, W.J. Cantwell, G. Dearden, K.R. Edwards, S.P. Edwardson, J.D. Mullett, C.J. Williams, and K.G. Watkins. Effects of laser interaction with graphite coatings. In *Laser Assisted Net Shape Engineering 5, Lane 2007*, pages 673–686, 2007.

[163] C. Rubio-Gonzalez, G. Gomez-Rosas, J. L. Ocana, C. Molpeceres, A. Banderas, J. Porro, and M. Morales. Effect of an absorbent overlay on the residual stress field induced by laser shock processing on aluminum samples. *Applied Surface Science*, 252(18):6201–6205, 2006.

[164] Xin Hong, Shengbo Wang, Dahao Guo, Hongxing Wu, Jie Wang, Yusheng Dai, Xiaoping Xia, and Yanning Xie. Confining medium and absorptive overlay: Their effects on a laser-induced shock wave. *Optics and Lasers in Engineering*, 29(6):447–455, 1998.

[165] TC Kaushik and BK Godwal. Numerical study of the impedance mismatch effect in laser-irradiated layered targets. *Journal of Applied Physics*, 64(10): 4889–4895, 1988.

[166] Alessandra Benuzzi, Michel Koenig, Jyothi Krishnan, Bernard Faral, Wigen Nazarov, Mauro Temporal, Dimitri Batani, Laura Muller, Flavia Torsiello, Tom Hall, and Nicolas Grandjouan. Dynamics of laser produced shocks in foam–solid targets. *Physics of Plasmas*, 5(8):2827–2829, 1998.

[167] P. Peyre and R. Fabbro. Laser shock processing: a review of the physics and applications. *Optical and Quantum Electronics*, 27(12):1213–1229, 1995.

[168] M. Morales, J. A. Porro, J. J. Garca-Ballesteros, C. Molpeceres, and J. L. Ocana. Effect of plasma confinement on laser shock microforming of thin metal sheets. *Applied Surface Science*, 257(12):5408–5412, 2011.

[169] K. L. Choo, Y. Ogawa, G. Kanbargi, V. Otra, L. M. Raff, and R. Komanduri. Micromachining of silicon by short-pulse laser ablation in air and under water. *Materials Science and Engineering: A*, 372:145–162, 2004.

[170] Arvi Kruusing. Underwater and water-assisted laser processing: Part 1-general features, steam cleaning and shock processing. *Optics and Lasers in Engineering*, 41(2):307–327, 2004.

[171] Y.X. Ye, Y.Y. Feng, X.J. Hua, and Z.C. Lian. Experimental research on laser shock forming metal foils with femtosecond laser. *Applied Surface Science*, 285, Part B(0):600 – 606, 2013.

[172] M. Morales, J. A. Porro, M. Blasco, C. Molpeceres, and J. L. Ocana. Numerical simulation of plasma dynamics in laser shock processing experiments. *Applied Surface Science*, 255(10):5181–5185, 2009.

[173] J. L. Ocana, M. Morales, C. Molpeceres, and J. A. Porro. Laser shock processing of metallic materials: Coupling of laser-plasma interaction and material behaviour models for the assessment of key process issues. *AIP Conference Proceedings*, 1278(1):902–913, 2010.

[174] Emil Egerer and Ulf Engel. Process characterization and material flow in microforming at elevated temperatures. *Journal of Manufacturing Processes*, 6(1):1–6, 2004.

[175] Chang Ye, Sergey Suslov, Bong Joong Kim, Eric A. Stach, and Gary J. Cheng. Fatigue performance improvement in aisi 4140 steel by dynamic strain aging and dynamic precipitation during warm laser shock peening. *Acta Materialia*, 59(3):1014–1025, 2011.

[176] P. Peyre, R. Fabbro, P. Merrien, and H. P. Lieurade. Laser shock processing of aluminium alloys. application to high cycle fatigue behaviour. *Materials Science and Engineering: A*, 210(1-2):102–113, 1996.

[177] Benxin Wu and Yung C. Shin. A self-closed thermal model for laser shock peening under the water confinement regime configuration and comparisons to experiments. *Journal of Applied Physics*, 97(11):113517, 2005.

[178] Yunfeng Cao, Benxin Wu, and Yung C. Shin. Parametric study on single shot and overlapping laser shock peening on various metals via modeling and experiments. *Journal of Manufacturing Science and Engineering*, 132 (6):061010–061010, 2010.

[179] Benxin Wu and Yung C. Shin. Two dimensional hydrodynamic simulation of high pressures induced by high power nanosecond laser-matter interactions under water. *Journal of Applied Physics*, 101(10):103514, 2007.

[180] Hongtao Ding and Yung C. Shin. Dislocation density-based modeling of subsurface grain refinement with laser-induced shock compression. *Computational Materials Science*, 53(1):79–88, 2012.

[181] *A constitutive model and data for metals subjected to large strains, high strain rates and high temperatures*, 1983.

[182] D. J. Steinberg, S. G. Cochran, and M. W. Guinan. A constitutive model for metals applicable at high-strain rate. *Journal of Applied Physics*, 51(3): 1498–1504, 1980.

[183] R Pratap and A Arunkumar. Material selection for MEMS device. *Indian Journal of Pure and Applied Physics*, 45:358–367, 2007.

[184] Anil Kurella and Narendra B Dahotre. Review paper: surface modification for bioimplants: the role of laser surface engineering. *Journal of biomaterials applications*, 20(1):5–50, 2005.

[185] Gyuyeol Bae, Yuming Xiong, S. Kumar, Kicheol Kang, and Changhee Lee. General aspects of interface bonding in kinetic sprayed coatings. *Acta Materialia*, 56(17):4858 – 4868, 2008.

[186] N. Tounsi, J. Vincenti, A. Otho, and M.A. Elbestawi. From the basic mechanics of orthogonal metal cutting toward the identification of the constitutive equation. *International Journal of Machine Tools and Manufacture*, 42(12): 1373 – 1383, 2002.

[187] ASM International. *Atlas of stress-strain curves*. Materials Park, OH : ASM International, 2002.

[188] W. M. Steen. *Laser material processing*. Springer, London ; New York, 3rd edition, 2003.

[189] L.M. Vilhena, M. Sedlacek, B. Podgornik, J. Vizintin, A. Babnik, and J. Mozina. Surface texturing by pulsed nd:yag laser. *Tribology International*, 42(10): 1496 – 1504, 2009.

[190] A. Amanov, I.S. Cho, Y.S. Pyoun, C.S. Lee, and I.G. Park. Micro-dimpled surface by ultrasonic nanocrystal surface modification and its tribological effects. *Wear*, 286-287(0):136 – 144, 2012.

[191] I. Etsion. State of the art in laser surface texturing. *Journal of Tribology*, 127(1):248–253, 2005.

[192] ASTM International. ASTM E3 - Standard Guide for Preparation of Metallographic Specimens, 2003.

[193] Struers A/S Elisabeth Weidmann, Anne Guesnier. Metallographic preparation of copper and copper alloys.

[194] Yanxiong Liu, Lin Hua, Jian Lan, and Xi Wei. Studies of the deformation styles of the rubber-pad forming process used for manufacturing metallic bipolar plates. *Journal of Power Sources*, 195(24):8177–8184, 2010.

[195] *The Nano Indenter XP Users Manual*. MTS Systems Corporation, 2002.

[196] Angus J. Wilkinson and T. Ben Britton. Strains, planes, and EBSD in materials science. *Materials Today*, 15(9):366–376, 2012.

[197] Adam J. Schwartz, Mukul Kumar, and B. L. Adams. *Electron backscatter diffraction in materials science*. Kluwer Academic, New York, 2000.

[198] Ehab A. El-Danaf, Mahmoud S. Soliman, and Abdulhakim A. Almajd. EBSD investigation of the microstructure and microtexture evolution of 1050 aluminum cross deformed from ECAP to plane strain compression. *EBSD-Untersuchung der Mikrostruktur- und Mikrotexturentwicklung einer von ECAP- bis zweiachsig komprimierten 1050-Aluminiumlegierug*, (10): 3291, 2011.

[199] F.J. Humphreys. Review grain and subgrain characterisation by electron backscatter diffraction. *Journal of Materials Science*, 36(16):3833–3854, 2001.

[200] Y.B. Guo. *Numerical Simulations - Applications, Examples and Theory*, chapter Laser Shock Peening: Modeling, Simulations, and Applications. InTech, 2011.

[201] Chao Zheng, Sheng Sun, Zhong Ji, Wei Wang, and Jing Liu. Numerical simulation and experimentation of micro scale laser bulge forming. *International Journal of Machine Tools and Manufacture*, 50(12):1048–1056, 2010.

[202] Taeksun Nam. *Finite Analysis of Residual Stress Field Induced by Laser Shock Peening*. PhD thesis, The Ohio State University, 2002.

[203] Chelsey Pence, Hua Ding, Ninggang Shen, and Hongtao Ding. Experimental analysis of sheet metal micro-bending using a nanosecond-pulsed laser. *The International Journal of Advanced Manufacturing Technology*, 69:319–327, 2013/05/10 2013.

[204] Jose L. Ocana, Miguel Morales, Carlos Molpeceres, Jorge Torres, Juan A. Porro, Gilberto Gomez, and Carlos Rubio. Predictive assessment and experimental characterization of the influence of irradiation parameters on surface deformation and residual stresses in laser-shock-processed metallic alloys, 2004.

[205] Allan F. Bower. *Applied mechanics of solids*. Boca Raton : CRC Press, c2010., 2010.

[206] H Hencky. The elastic behavior of vulcanized rubber. *Rubber Chemistry and Technology*, 6(2):217–224, 1933.

[207] M. Mooney. A theory of large elastic deformation. *Journal of Applied Physics*, 11(9):582–592, 1940.

[208] P. A. L. S. Martins, R. M. Natal Jorge, and A. J. M. Ferreira. A comparative study of several material models for prediction of hyperelastic properties: Application to silicone-rubber and soft tissues. *Strain*, 42(3):135–147, 2006.

[209] R. W. Ogden. Large deformation isotropic elasticity - on the correlation of theory and experiment for incompressible rubberlike solids. *Proceedings of the Royal Society of London. Series A, Mathematical and Physical Sciences*, 326(1567):565–584, 1972.

[210] Pratapkumar Nagarajan and Donggang Yao. Uniform shell patterning using rubber-assisted hot embossing process. II. Process analysis. *Polymer Engineering & Science*, 51(3):601–608, 2011.

[211] CR Siviour, WG Proud, DA Salisbury, and RE Winter. High strain rate compressive behaviour of a silicone elastomer. In *Proceedings of the XIth International Congress and Exposition*, Orlando, Florida USA, 2008. Society for Experimental Mechanics Inc.

[212] Aidy Ali, M. Hosseini, and B. B. Sahari. A review of constitutive models for rubber-like materials. *American Journal of Engineering and Applied Sciences*, 3(1):232–239, 2010.

[213] ASTM International. ASTM D412 - 06a Standard Test Methods for Vulcanized Rubber and Thermoplastic Elastomers-Tension, 2013.

[214] ASTM International. ASTM D395-03 Standard Test Methods for Rubber Property-Compression, 2003 (2008).

List of Publications

Journals

1. Nagarajan, B., S. Castagne, Z. Wang, and H. Zheng, Investigation of laser-induced plasma evolution in flexible pad laser shock forming with high speed camera, Applied Surface Science, 2014. 308(0): p. 221 - 229.

2. Nagarajan, B., S. Castagne, and Z. Wang, Mold-free fabrication of 3D micro-features using laser-induced shock pressure. Applied Surface Science, 2013. 268(0): p. 529-534.

3. Nagarajan, B., S. Castagne, Z. Wang, and H. Zheng, Influence of flexible pad in plastic deformation of metal foils in flexible pad laser shock forming – Experimental and finite element analysis, International Journal of Material forming, under review.

4. Nagarajan, B., S. Castagne, Z. Wang, and H. Zheng, Plastic deformation analysis in Flexible Pad Laser Shock Forming, Materials Science and Engineering - A, under review.

Conference Proceedings

1. B. Nagarajan, S. Castagne, Z.K. Wang, and H.Y. Zheng, Finite element analysis of the effect of flexible pad on the deformation of metal foils in Flexible Pad Laser Shock Microforming, Key Engineering Materials, 2014, pp. 581-588.

2. Nagarajan, B., S. Castagne, and Z.K. Wang, Investigation of Copper Foil Thinning Behavior by Flexible-Pad Laser Shock Forming. Key Engineering Materials, 2013. 535: p. 306-309.

3. Nagarajan, B., S. Castagne, and Z. Wang, Influence of Process Parameters on the Deformation of Copper Foils in Flexible-Pad Laser Shock Forming. in 8th International Conference on Micro Manufacturing, 2013. University of Victoria, Victoria, BC, Canada.

4. Nagarajan, B., S. Castagne, Z. Wang, C. Keat Lai, X. Wang, and H. Zheng, The Effects of Ablative Coating Thickness at Various Laser Intensities and Multiple Laser Pulses on Thin Copper Sheet Formability in High Strain Rate Laser Shock Forming, AIP Conference Proceedings , 2011. 1353(1): p. 511-516.